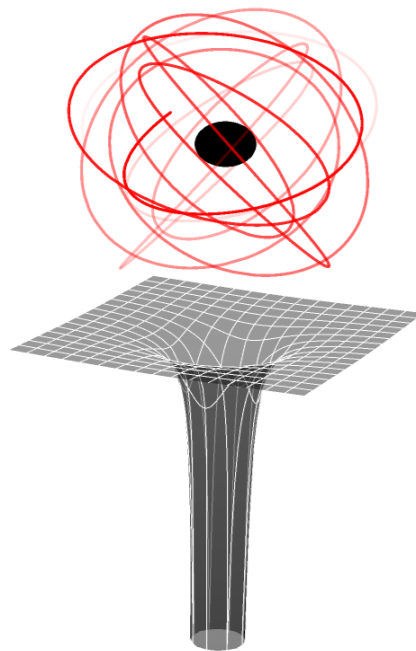




Utrecht
University



Black Holes beyond Relativity: the Onset of Chaos in Stellar Inspirals



MSC. THESIS - THEORETICAL PHYSICS

INSTITUTE FOR THEORETICAL PHYSICS - UTRECHT UNIVERSITY

Author:

Justus van der Velden
5933889

Supervisors:

Dr. Tanja Hinderer
Banafsheh Shiralilou MSc.
Dr. Tomislav Prokopec

JULY 2022

Abstract

With general relativity's incompatibility with quantum field theory forming our generation's primary challenge in high energy theoretical physics research, the upcoming LISA gravitational wave experiment will provide exciting new avenues to test for novel theories of gravity. One method of testing general relativity in the strong-field regime is the study of the dynamics and orbital evolution of a stellar-mass object's inspiral into a supermassive black hole in different gravity theories and searching for observable differences. In this thesis, a theoretical framework is presented in which to study the potentially chaotic properties of these extreme mass-ratio inspirals. The derivations, advantages and disadvantages of different formulations of black hole solutions in general relativity are considered. A treatment of orbits in the Kerr spacetime is performed in a broad range of scenarios. The framework is then employed to determine the existence and nature of the onset of chaotic features in the orbital dynamics of general relativity and Einstein-dilaton Gauss-Bonnet theory, a proposed theory of modified gravity derived from string theory. By employing numerical integration methods, we find that high-accuracy approximations of the metric tensor are required to determine whether chaotic features exist in modified gravity. By using approximate analytical black hole solutions, we find that the radial width of these features and hence the deviations from Kerr are of order $r \approx \mathcal{O}(10^{-4})$ or smaller in Boyer-Lindquist coordinates. An investigation into a coordinate-independent quantification of chaotic features is performed and applied to the findings. The results are then presented in the context of astrophysical challenges and experimental implications, based on which we conclude that future work is needed to conclusively determine whether these features are detectable.

Summary for non-physicists

In physics, the best theoretical model which explains how massive objects attract one another is Einstein's theory of general relativity. This theory gives very accurate and well-tested predictions for phenomena ranging from planetary orbits to the evolution of the cosmos. However, we know that this theory breaks down at the quantum level. This motivates us to explore alternatives to general relativity. In this thesis, we explore how one could look for alternatives using orbits of relatively low-mass black holes around much more massive black holes. Because gravity is very strong in these systems, we believe that potential deviations from the predictions of general relativity could become measurable there, if they exist. In the near future, we can use gravitational wave astronomy to perform experiments on such systems. Indeed, if gravity is not accurately described by general relativity, we expect to find distinct signs of chaos in gravitational wave signals coming from such a black hole system. We quantify the size and nature of these potential chaotic features in the case of an alternative theory of gravity. We find that the upper bound on the size of these effects is very small indeed. Nevertheless, we also conclude that looking for these signals in upcoming experiments is a good test of general relativity, granting us further insight into the nature of gravity.

Contents

1	Introduction and motivation	1
2	General relativity and dynamical systems	3
2.1	Summary of general relativity	3
2.1.1	Motion through curvature	3
2.1.2	Determining $g_{\mu\nu}$	5
2.1.3	Black holes	5
2.1.4	Symmetries of spacetime	6
2.1.5	Uniqueness of black hole solutions and the no-hair theorem	6
2.1.6	The extreme mass-ratio approximation	7
2.1.7	Gravitational waves	8
2.2	Introduction to dynamical systems and chaos	9
2.2.1	Hamilton-Jacobi mechanics	9
2.2.2	Integrability, action-angle variables and resonance	10
2.2.3	Poincaré maps and fixed points	12
2.2.4	Breaking integrability and the KAM theorem	13
2.2.5	Poincaré-Birkhoff theorem and chaotic features	14
3	Modifying gravity	17
3.1	Alterations to the Einstein-Hilbert action	17
3.2	Lovelock's theorem	18
3.2.1	Additional scalar fields	18
3.2.2	Higher order curvature terms	18
3.2.3	Higher dimensional theories	18
3.2.4	Non-local theories and breaking Lorentz invariance	19
3.2.5	Abandoning the principle of least action	19
3.3	Ostrogradski instabilities and ghosts	19
4	Stationary axisymmetric vacuum (SAV) solutions	22
4.1	The Weyl-Lewis-Papapetrou line element	22
4.2	Boyer-Lindquist coordinates	24
4.3	Prolate spheroidal coordinates	25
4.4	Factor structure coordinates	27
4.5	The event horizon of a Kerr black hole	29
5	Development of an orbital motion framework	30
5.1	Conserved quantities in SAV metrics	30
5.2	Defining an effective potential	32
5.2.1	Weyl coordinates	32

5.2.2	Prolate spheroidal coordinates	34
5.2.3	Boyer-Lindquist coordinates	37
6	The Kerr solution	40
6.1	Conservation of the Carter constant	40
6.2	Calculation of some curvature invariants	42
6.3	Innermost stable circular orbits	43
6.4	The Kerr effective potential	44
6.4.1	Computing J_{BL} and J_{PS}	44
6.4.2	Visualising the effective potential	47
6.4.3	Sensitivity to orbital parameters	48
6.4.4	Keplerian variables in Kerr spacetime	50
6.4.5	Contours of the phase space	52
6.5	Numerical evaluation of geodesics	53
6.5.1	Choice of coordinate system	53
6.5.2	Orbital stability	57
6.6	Three-dimensional orbits	58
6.6.1	Visualising the black hole	58
6.6.2	Restoring the ϕ component	59
6.6.3	Polar orbits	60
6.6.4	Zoom-whirl orbits	62
6.7	Resonant behaviour in Kerr spacetime	63
6.7.1	Resonant orbits	63
6.7.2	Rotation curve	65
7	Scalar Gauss-Bonnet gravity	68
7.1	Introduction to Scalar Gauss-Bonnet and Einstein-dilaton Gauss-Bonnet theory	68
7.1.1	Relation to string theory	69
7.2	EDGB as a modified gravity theory	69
7.2.1	Quadratic curvature and a scalar field	69
7.2.2	The scalar-curvature coupling	69
7.2.3	Instabilities and ghosts	70
7.2.4	The existence of black holes	70
7.3	Finding black hole solutions	71
7.3.1	Varying the action	71
7.3.2	Derivation of the static black hole equations	73
7.3.3	Solving for Γ and Λ	75
7.3.4	From static to rotating black hole	75
7.4	Accuracy of the line element at zero coupling	76
7.4.1	Effective potential deviation	77
7.5	The effect of α on the innermost root radius	80
7.6	Conserved quantity deviation	80
8	The search for chaos	83
8.1	Goals and considerations	83
8.1.1	Choice of coordinate system	83
8.1.2	Choice of parameters	84
8.1.3	Choice of resonances	85
8.1.4	Numerical considerations	86
8.1.5	The importance of iteration time	87

8.2	Verifying the framework	88
8.3	Chaotic features at $\mathcal{O}(\chi^2, \alpha^2)$	89
8.3.1	1/2 resonance	89
8.3.2	2/3 resonance	93
8.3.3	Kerr expansion	95
8.3.4	Conclusions at second order	96
8.4	Chaotic features at $\mathcal{O}(\chi^5, \alpha^7)$	97
8.5	Effects of the chosen coordinate system	101
8.5.1	The coordinate dependence of plateau size	101
8.5.2	Performance benchmark of different coordinate systems	102
8.6	Alternatives to plateau width	103
8.6.1	Phase space volume as an invariant measure of chaos	104
8.6.2	Application to higher order results	108
9	Astrophysical implications	110
9.1	Sagittarius A* and S4714	110
9.2	Gravitational wave astronomy	111
9.2.1	Measuring spacetime with interferometry	111
9.2.2	Orbital response to Birkhoff islands	113
9.2.3	Modelling the EMRI signal	114
9.3	Time dilation as an observable	115
9.3.1	Orbital period	115
9.3.2	The periodicity of time dilation	116
9.4	Environment effects near a supermassive black hole	118
10	Conclusions	120
10.1	Summarised conclusions	120
10.2	Elaborated conclusions	120
11	Points of discussion	123
11.1	Implications of findings	123
11.2	Sensitivity to line element choice	124
11.3	Software, hardware and numerical limitations	124
11.4	Suggestions for further research	125
11.4.1	Sweep of the orbital parameter space	125
11.4.2	Alternate definitions of chaos	125
11.4.3	Predictors of the magnitude of features	126
11.4.4	Other gravity theorems	126
12	Acknowledgments	127
A	A compact form of R_{GB}^2	128
B	Conserved quantities in the exact Kerr spacetime	129
C	Spin dependence of plateau width in second order Kerr spacetime	130
D	Evolution of \mathcal{A}_r and \mathcal{A}_θ	132
E	UU Gemini versus SURFsara Lisa computing cluster performance	133

Chapter 1

Introduction and motivation

Whether it is after watching the 2014 film *Interstellar* or via one of the first courses in your physics graduate programme, it is near impossible to have never heard of the best theory of gravity we have at our disposal. *General relativity* (GR) is among the most accurate and well-tested theories of modern science [1]. When first published by Albert Einstein over a hundred years ago, it ended a two century paradigm of Newtonian gravity. Although the Newtonian take on dynamics is accurate on a day-to-day scale, physicists of the nineteenth century realised that several natural processes were in contradiction with the absolute framework proposed by Isaac Newton in the seventeenth century. Mercury's orbital precession is one famous example of a discrepancy in Newtonian physics and Michelson and Morley's failure to prove the existence of aetherial wind was another nail in the coffin of the old theory of gravity. This mounting evidence spurred Einstein and others to completely reimagine our perception of dynamics and lead to a description of the universe which is accurate on scales ranging from planetary systems to the entire universe. Even after its general acceptance, evidence supporting GR kept on coming. GR has survived tests ranging from measurements of gravitational redshift to the density of pulsars [2] and has even found its way into some modern technological applications: GPS satellites would not function at all if uncorrected for gravitational time dilation [3]. Indeed, one does not even need to leave Earth orbit for general relativity to make itself indispensable.

Despite all of this, it looks like cracks are starting to appear in GR's explanation of gravity. This is because it is not the *only* modern physical theory with incredible predictive power. Around the same time as GR, quantum mechanics was in its infancy. After a century of development, it has evolved into another candidate for the most influential physical theory of all time: *quantum field theory* [4][5]. Experiments such as the Large Hadron Collider have performed extensive tests of the Standard Model and have yet to find any solid discrepancy in its predictions. This, however, is a problem, since GR and quantum field theory are inherently incompatible. The nature of quantum field theory makes it impossible to encode gravity as we understand it as part of its framework and GR provides no satisfactory descriptions of nature at the subatomic scale. This conundrum is the primary focus of a great deal of modern theoretical research. One way of approaching this incompatibility is by re-examining the validity of general relativity. What if GR has only survived experiments because we have not tested it in extreme enough cases? One possible explanation is that GR is only a part of the equation. A solution to the incompatibility of relativity and quantum field theory could come from an altered version of GR; a theory of *modified gravity*. Some modified gravities can be derived from proposed successors of quantum field theory such as string theory or loop quantum gravity, but they can also be viewed as stand-alone evolutions of the relativistic framework.

When the first ever gravitational waves were detected by the LIGO and Virgo collaborations [6], it simultaneously provided further confirmation of relativity through the existence of gravitational waves and an avenue to challenge relativity like never before. Through gravitational wave astronomy, researchers are now in a position to test gravity in, for example, regions near black holes and the Big Bang, which we consider the *strong-field regime* of gravity. Perhaps the subtleties of an underlying theory beyond relativity have eluded us up till now because they only appear in very strong gravitational fields. Indeed, many efforts are being made to search for effects unexplained by relativity in the region near black holes, the most extreme gravitational wells in the observable universe. Using for instance LIGO/Virgo, KARGA and via upcoming third generation detectors such as the Einstein Telescope and the Cosmic Explorer, predictions of GR can be put to the test near black holes and neutron stars of varying masses. In particular, the launch of the *Laser Interferometer Space Antenna* (LISA) will allow us to study the largest black holes known to exist [7].

Astronomers believe that at the heart of almost every galaxy lies a *supermassive black hole* [8]. Supermassive black holes are of almost incomprehensible proportions, having masses varying from hundreds of millions to tens of billions of solar masses [9]. Since they are not the only residents of the central clusters of galaxies, they are often orbited by a myriad of stellar-mass objects such as (neutron) stars or smaller black holes. These supermassive black hole systems can be exploited for the search for a theory beyond relativity. We call such a system an *extreme mass-ratio inspiral* (EMRI). We will consider systems where the ratio between the orbiting body and the central body is of $\mathcal{O}(10^{-5})$ or smaller an EMRI.

This thesis concerns itself with testing general relativity in just such a scenario. In particular, we will use extreme mass-ratio systems to investigate whether observable differences exist between the orbits of EMRIs in GR and a modified theory of gravity known as Einstein-dilaton Gauss-Bonnet theory. As will be extensively treated in this manuscript, such deviations from general relativity are expected to be characterised by the *onset of chaos* in their orbital dynamics. We will aim to find these chaotic features in Einstein-dilaton Gauss-Bonnet gravity and determine when, where and in what magnitude they can appear in extreme mass-ratio inspirals at the heart of a galaxy.

In Chapters 2 and 3, we provide the background knowledge required to understand the concepts behind this project, assuming working knowledge of (quantum) field theory and special relativity. In Chapter 4, the derivation and classification of the rotating black hole solution to the Einstein field equations is treated from first principle in several coordinate systems, elucidating the differences and similarities between different parametrisations of these compact objects. In Chapter 5, we then develop a framework which provides a characterisation of the full parameter space of orbits around rotating black holes, derived in several coordinate systems independently of one another. This orbital framework is applied to the Kerr solution from general relativity in Chapter 6, where several classes of orbits are parameterised and the behaviour of this spacetime for a diverse range of parameters is examined up to their relevance to the project. The modified theory of gravity which will be tested in this thesis, Einstein-dilaton Gauss-Bonnet theory, will be introduced in Chapter 7. Afterwards, in Chapter 8, the orbital framework is specialised to the search for chaotic features in Einstein-dilaton Gauss-Bonnet gravity, which requires both careful physical and numerical considerations. Finally, in Chapter 9, the results of this search are put into a broader astrophysical context, where we treat the experimental challenges and physical interpretations of the findings.

Chapter 2

General relativity and dynamical systems

In order to study theories beyond general relativity, it is essential to understand general relativity itself. The study of general relativity is a broad field with many applications, the relevance of particular theoretical aspects depending on one's research needs. In this chapter, we will reiterate some of the fundamental concepts from general relativity up to their relevance for this project. We will also introduce some important aspects from dynamical systems theory and how one uses this framework in the search for deviations from general relativity. We will generally set $c = 1$ throughout this thesis, unless explicitly stated otherwise.

2.1 Summary of general relativity

General relativity attempts to explain the motion of objects through the universe as a geometric theory. Let us discuss some of the basic concepts which are the most important to us, as well as define the most general conventions and notations as used in this manuscript.

2.1.1 Motion through curvature

The most fundamental relationship in general relativity is given through the *Einstein field equations*. These equations govern the response of the *curvature* of spacetime to the presence of *matter and energy* and determine how objects move through spacetime. Curvature is quantified using several different tensors and scalars; let us briefly reiterate how one defines these basic quantities.

In essence, a spacetime is fully determined by its *metric tensor* $g_{\mu\nu}$. This is a coordinate-independent quantity and is related to the infinitesimal *line element* ds^2 . The line element and metric tensor are related via [1][2]

$$ds^2 \equiv g_{\mu\nu} dx^\mu dx^\nu, \quad (2.1)$$

where we will in this thesis always consider spacetimes with four dimensions, such that dx^μ has four independent components. Furthermore, we employ the $(-, +, +, +)$ convention.

The study of motion requires a well-defined operator to measure change. In a curved spacetime, it is desirable to define the *covariant derivative* ∇_μ of some four-vector w_μ as

$$\nabla_\mu w_\nu \equiv \partial_\mu w_\nu - \Gamma_{\mu\nu}^\lambda w_\lambda. \quad (2.2)$$

Much like any covariant derivative, this is defined in such a way that the derivative of a vector transforms as a 2-tensor. Note that the operator itself is invariant under coordinate transformations. $\Gamma_{\mu\nu}^\lambda$ is the *Christoffel symbol*, which is a connection¹ uniquely determined by the form of $g_{\mu\nu}$. It can be derived by for instance varying the action of a test particle [1] or directly from concepts in differential geometry [10] and is given by

$$\Gamma_{\mu\nu}^\lambda \equiv \frac{1}{2}g^{\lambda\rho}(\partial_\mu g_{\nu\rho} + \partial_\nu g_{\rho\mu} - \partial_\rho g_{\mu\nu}). \quad (2.3)$$

Using the Christoffel symbol, we can introduce *geodesics*. Geodesics are the paths followed by unaccelerated *test particles* through spacetime, where one should note that gravity is not considered an 'acceleration' in general relativity; gravity is encoded in the metric itself. A test particle is a massive or massless object which travels through a gravitational field without affecting the field itself². Mathematically, a geodesic is a curve along which a vector in the tangent space³ satisfies the parallel transport equation, for details of which a reader is referred to any introductory book on general relativity [1][2][11]. Geodesics are defined as paths satisfying the *geodesic equation*:

$$\frac{d^2x^\mu}{d\lambda^2} + \Gamma_{\rho\sigma}^\mu \frac{dx^\rho}{d\lambda} \frac{dx^\sigma}{d\lambda} = 0, \quad (2.4)$$

where λ is an *affine parameter*, i.e. a timelike coordinate linearly constructed from *proper time* τ . Recall from special relativity that the proper time is the time as experienced by a non-accelerating observer in their rest frame⁴. It is defined via

$$d\tau^2 \equiv -ds^2. \quad (2.5)$$

Although the concept is much more abstract than just that, one can imagine objects following a geodesic curve to be 'freely falling' through spacetime, where the curvature of said spacetime might cause this falling not to be in a straight line.

Before we move on to the field equations, we will introduce some important tensors which are extensively used in this thesis. One can define the *Riemann tensor* as

$$R^\rho{}_{\mu\nu\sigma} \equiv \partial_\mu \Gamma_{\nu\sigma}^\rho - \partial_\nu \Gamma_{\mu\sigma}^\rho + \Gamma_{\mu\lambda}^\rho \Gamma_{\nu\sigma}^\lambda - \Gamma_{\nu\lambda}^\rho \Gamma_{\mu\sigma}^\lambda. \quad (2.6)$$

The Riemann tensor fully characterises the curvature of a given spacetime and is often used to quantify said curvature. It can be contracted with itself to obtain the *Ricci tensor* via

$$R_{\mu\nu} \equiv R^\lambda{}_{\mu\lambda\nu}. \quad (2.7)$$

This tensor can again be contracted with itself to obtain the *Ricci scalar* as

$$R \equiv R^\lambda{}_\lambda. \quad (2.8)$$

These curvature invariant quantities play an important role in the next section, where we introduce the derivation of the Einstein field equations.

¹A connection is a concept from differential geometry. For those interested in the mathematical aspects, connections and other concepts are more rigorously defined in for instance Ref. [10].

²The fact that particles affect the gravitational field is encoded in the Einstein field equations, which we will introduce shortly.

³The tangent space T_p consists of all possible vectors originating at point p on a manifold. The set of all T_p on a manifold is known as the *tangent bundle* [1].

⁴In the case of a black hole, it is the coordinate time measured at infinity.

2.1.2 Determining $g_{\mu\nu}$

All of the above describes how the motion of objects depends on the curvature of spacetime. But what is it that causes curvature in the first place? This question is equivalent to asking how $g_{\mu\nu}$ is determined. This is where the Einstein field equations become important. The field equations can be derived using the principle of least action. Let us start from the *Einstein-Hilbert action* S_{EH} , which will generate the curvature terms of the field equations. The full action is given by

$$S = S_{EH} + S_m = \frac{1}{16\pi G} \int \sqrt{-g} R \, d^4x + S_m, \quad (2.9)$$

where g is the determinant of the metric tensor and G is the gravitational constant. S_m is the 'matter action', the reason of which will become evident in the next equation. Recall how the Ricci scalar R is a double contraction of the Riemann tensor, which itself is uniquely dependent on the metric tensor $g_{\mu\nu}$ via the Christoffel symbol. By varying S with respect to $g_{\mu\nu}$, as explained in for example Ref. [1], one obtains the Einstein field equations as

$$G_{\mu\nu} \equiv R_{\mu\nu} - \frac{1}{2} R g_{\mu\nu} = 8\pi G T_{\mu\nu}, \quad (2.10)$$

where $T_{\mu\nu}$ is the *energy-momentum tensor*, which defines the distribution and flux of momentum and energy (and hence also matter) in a spacetime. The variation of S_m leads to the $T_{\mu\nu}$ term and is why S_m is called the matter action. The newly defined tensor $G_{\mu\nu}$ is referred to as the *Einstein tensor*. On the left hand side of this equation, one has quantities relating to the curvature of the spacetime as determined by $g_{\mu\nu}$, whereas the energy-momentum tensor on the right describes the distribution of matter and energy in spacetime. This relation is what is referred to when one speaks of the interplay between matter and spacetime as described by general relativity.

According to general relativity, any physical spacetime $g_{\mu\nu}$ must be a solution to the Einstein field equations. There are many such solutions, varying from flat spacetimes to descriptions of an expanding universe [12]. In this project, we are interested in a particular class of solutions: *black holes*.

2.1.3 Black holes

Especially useful solutions for $g_{\mu\nu}$ in the Einstein field equations are those describing spherically symmetric spacetimes, since these are used to describe gravitational systems such as orbiting planets around stars. In particular, one can assume a solution with $T_{\mu\nu} = 0$. This is because we would be interested in the shape of spacetime *outside* the central object, where the orbiting bodies would exist and no other matter is present. These kinds of solutions are called *vacuum solutions* and the unique spherically symmetric vacuum solution to the Einstein field equations is known as the *Schwarzschild metric*. It was discovered in 1916 [13] and is given by [1]

$$ds^2 = - \left(1 - \frac{2GM}{r} \right) dt^2 + \left(1 - \frac{2GM}{r} \right)^{-1} dr^2 + r^2 d\theta^2 + r^2 \sin^2 \theta d\phi^2, \quad (2.11)$$

where M is the black hole mass parameter. This line element is presented in Boyer-Lindquist coordinates, a concept which we will properly explain later, but which for the Schwarzschild case can be seen as a spherical-like coordinate system with radius r and angular coordinates θ, ϕ . This form of the metric corresponds to a spacetime with a single point mass M with no rotation or charge. It turns out that this solution is a very good model for gravitational motion of test particles around

a central object, at sufficient distance from the object. One property of the Schwarzschild metric is the fact that beyond the *event horizon*, a term we will properly define in Chapter 4, there exist no timelike or lightlike paths away from the centre of the object. Hence, if the object has a radius which is smaller than the event horizon corresponding to its mass and an orbiting particle crosses this horizon, it is impossible for that particle to escape the gravitational field of the central object. These kinds of objects are called *black holes*.

The Schwarzschild metric can thus be used to model orbits of test particles around a non-rotating black hole. If one considers rotating black holes, the metric becomes more complicated. The derivation of the rotating black hole metric will be shown in Chapter 4. The resulting line element corresponding to a rotating black hole is known as the *Kerr metric*, after its discoverer. If one also considers electric (or even magnetic!) charge, one obtains the *Kerr-Newman metric*, which looks very similar to the Kerr solution.

2.1.4 Symmetries of spacetime

For the study of spacetimes, one important aspect is the identification of *symmetries*. As mentioned above, the Schwarzschild metric displays spherical symmetry. There exists a more exact way of phrasing these symmetries by using *Killing vectors*. A Killing vector K_μ is a vector satisfying the Killing equation [1]:

$$\nabla_{(\mu}K_{\nu)} = 0. \quad (2.12)$$

A Killing vector generates an isometry, i.e. the metric is invariant under transformations along K_μ . In the Schwarzschild case for example, two Killing vectors are given by $K_1 = \partial_t$ and $K_2 = \partial_\phi$. It is important to note that the existence of a Killing vector is related to the existence of some *conserved quantity* in that spacetime, similarly to (but *not* directly the same as) Noether's theorem in other fields of physics. For example, contracting the angular Killing vector K_2 of the Schwarzschild metric with the four-momentum p_μ yields a conserved quantity, which we can identify as the *angular momentum* of the orbiting test particle:

$$\nabla_\mu(K_2^\lambda p_\lambda) = 0 \quad \Rightarrow \quad K_2^\lambda p_\lambda \equiv L_z = \text{constant}. \quad (2.13)$$

Such conserved quantities can also be derived elegantly using Hamilton-Jacobi theory, as we will show in Chapter 5. However, it is important to realise the relation between this method and the more general metric isometries generated by Killing vectors.

2.1.5 Uniqueness of black hole solutions and the no-hair theorem

In the above introduction to the Schwarzschild metric, we briefly mentioned how it is the *unique* spherically symmetric vacuum solution to the Einstein field equations. This is actually a very meaningful result and can be derived from *Birkhoff's theorem*, which states that all spherically symmetric vacuum solutions of the Einstein field equations are static and asymptotically flat [14].

Another theorem related to the uniqueness of black hole solutions in general relativity is the *no-hair theorem*. The (not generally proven⁵) no-hair theorem states that any black hole solution to the Einstein field equations in general relativity is completely characterised by three externally observable quantities: *mass*, *charge* and *spin*. The no-hair theorem was first proven for the relatively simple Schwarzschild metric in 1967 by Werner Israel [15] and then generalised to the charged case [16] and

⁵The no-hair theorem has as of 2022 not been mathematically proven in its most general form, although it *has* been proven to hold for black hole solutions in four dimensions.

the spinning case [17]. This theorem states that the Kerr-Newman solution (explicitly presented in Chapter 4) is not just the most general black hole solution allowed by general relativity, it is also the *unique* solution of this form. Indeed, setting the spin and charge of the Kerr-Newman metric to zero yields the Schwarzschild solution, which means that the Schwarzschild solution is just a special case of the Kerr-Newman metric. The uniqueness of the Kerr-Newman metric lies at the core of general relativity; hence, finding evidence for a black hole solution which is *not* described by the Kerr-Newman metric could be proof against the validity of general relativity. Thus, the search for theories beyond general relativity through black holes revolves around finding proof against the no-hair theorem.

Although the Kerr-Newman metric is the most general black hole solution in general relativity, we will set the electric charge of a black hole to zero. This is because we expect physical black holes in the universe to be (nearly) electrically neutral [18]. After all, if a black hole were charged, it would attract nearby oppositely charged matter and repel equally charged matter until equilibrium was achieved. Since the systems relevant to this thesis are supermassive black holes which are often surrounded by accretion disks from which charged material could be attracted by the black hole, we expect the effects of any black hole electric charge on the geodesics to be extremely small. Hence, the search for black holes in violation of general relativity is in our case reduced to finding rotating black holes which are not described by the Kerr solution. As for the magnetic charge of a black hole; in this thesis we will not dive into the highly contentious issue of the existence of magnetic monopoles. One could consider it comforting however that if magnetic monopoles turn out to exist, general relativity's black hole solutions would still work as a theory of gravity.

2.1.6 The extreme mass-ratio approximation

We have seen that geodesics of the Kerr metric model the orbits of massive or massless test particles around a rotating black hole. However, one might wonder how this is relevant to the extreme mass-ratio systems we are considering. After all, the full physical system of a massive object orbiting a supermassive black hole should also account for the effect of the *orbiting* object on the curvature of spacetime, not just the central black hole. However, in our system, the extreme mass-ratio causes the effects of the much lighter object on the gravitational field to be almost negligible. Efforts are being made to include corrections for these effects: for instance, work is being done on computing the effects of a test particle's mass on spacetime through a self-force approach [19]. In our case, the extreme mass-ratio causes these correction terms coming from the gravitational self-force of the orbiting body to become very small. The geodesic approximation is also convenient an analytical point of view; geodesics of Kerr spacetime without additional effects are uniquely defined by the metric tensor and a great deal of work has been performed on the properties of these geodesic orbits.

The geodesics introduced in this chapter are hence a good approximation of the orbits of stellar-mass objects around supermassive black holes. However, even when ignoring self-force terms, it is important to note that true stellar orbits would *not* follow geodesics precisely, since geodesics do not take into account the energy loss due to the generation of gravitational waves. Indeed, the full equations of motion consist of the geodesics as described by the Einstein field equations combined with the condition $\nabla_\nu T^{\mu\nu} = 0$ [20]. The resulting equations are known as the *MiSaTaQuWa equations* [21]. If one is to model the effects of energy loss of these orbits, one could start by making the values of the orbital energy and angular momentum explicitly dependent on time. Such a study was performed in Ref. [22]. This concept is called the *adiabatic approximation* and is sufficiently accurate if the rate of change of (otherwise) conserved quantities during one orbit is small.

It is beyond the scope of this project to incorporate these energy loss equations in the orbital evolution. However, interested readers are referred to for instance the sources cited above. For our purposes, it is important to qualitatively realise that the energy loss of orbits is an important component in the study of EMRIs for several reasons:

- It is orbital decay which allows orbits to slowly move closer to the black hole, allowing these orbits to cross regions where chaotic motion might be detectable.
- Gravitational waves, which of course carry energy, can only exist through this energy loss. It is these gravitational waves which will be actually detected by for instance LISA once it is launched, not the geodesics themselves. The modelling of gravitational waveforms is therefore a vital part of gravitational wave research.

2.1.7 Gravitational waves

A deep understanding of the physics of gravitational waves is required in order to measure any potential effects of modified gravity [23], since the computation of waveforms gravitational waves is a vital part of the study of extreme mass-ratio inspirals. Because of their importance, we will give a very basic introduction to how one derives the equations describing gravitational waves.

Recall that the equations of motion of some system are obtained by varying the gravitational action with respect to the metric. In general relativity, one can obtain gravitational wave equations by varying the Einstein-Hilbert action with respect to a metric of the form

$$\tilde{g}_{\mu\nu} = \eta_{\mu\nu} + h_{\mu\nu}, \quad (2.14)$$

where $\eta_{\mu\nu}$ is flat Minkowski spacetime and $h_{\mu\nu}$ is a small perturbation to this metric [1]. One can then substitute $\tilde{g}_{\mu\nu}$ in the Einstein field equations. The most straightforward way to obtain a solution to this is by using a linearised approach, i.e. expanding up to linear order in $h_{\mu\nu}$. The full derivation of how one obtains such solutions for $h_{\mu\nu}$ is not directly relevant to this thesis and can be read in for instance Ref. [1]. However, the upshot of such a computation is that one obtains the *linearised wave equation* given by

$$\nabla^\sigma \nabla_\sigma \bar{h}_{\mu\nu} = -16\pi T_{\mu\nu}, \quad (2.15)$$

where $\bar{h}_{\mu\nu} \equiv h_{\mu\nu} - \frac{1}{2}\eta_{\mu\nu}h$ and $h \equiv \eta_{\mu\nu}h^{\mu\nu}$. Setting $T_{\mu\nu} = 0$ allows one to compute the propagation of waves in a vacuum, whereas providing source terms in $T_{\mu\nu}$ allows one to model the generation of gravitational waves in for example black hole inspirals. By replacing the Einstein-Hilbert action with another action, one can derive the propagation and generation of gravitational waves in modified gravity.

Although helpful in calculations, linearisation is an assumption which is no longer valid in the strong-field regime. Hence, other, more accurate methods are being developed to tackle the generation of gravitational waves in this regime. One example is the post-Newtonian approach as used in for instance Ref. [23]. Using the resulting equations, it is possible to construct waveform models of gravitational radiation as emitted by several kinds of sources, such as binary black hole inspirals, including extreme mass-ratio inspirals. By matching the waveform models with experimental data, one can reconstruct the characteristics of the event which corresponds to the detected signal in a gravitational wave detector. In Chapter 9, we will dive deeper into the specifics of these detectors, as well as how they can be used to look for the onset of chaotic behaviour in extreme mass-ratio inspirals. However, we should first build an understanding of what we mean precisely by the onset of chaos in the context of black holes. This concept as well as a more general treatment of the dynamics of our system will be discussed in the next section.

2.2 Introduction to dynamical systems and chaos

General relativity provides a framework of spacetime as described in the previous section. However, we have not actually defined a way to generate equations of motion of orbiting particles in a concrete fashion from these basic principles. In this section, we will introduce how one computes the concrete equations of motion of test particles in a given spacetime, as well as some concepts from dynamical systems theory which are important in the search for chaos in modified gravity. A more thorough treatment of dynamical systems in the context of chaos is presented in for instance Ref. [24].

2.2.1 Hamilton-Jacobi mechanics

In this project, we will model the orbits around black holes by computing geodesics. Geodesics are defined as satisfying the geodesic equation as given in Eq. (2.4) and it is possible to compute the equations of motion directly by solving this equation. However, this is not a desirable way of approaching this problem, because Christoffel symbols can be cumbersome to calculate. If one uses *Hamilton-Jacobi theory*, one can compute the equations of motion from the *Hamiltonian* of the system, as well as straightforwardly prove the conservation of certain quantities in given spacetimes. In the context of general relativity, the Hamiltonian \mathcal{H} is given by [25][26][24]

$$\mathcal{H} = \frac{1}{2} g^{\mu\nu} p_\mu p_\nu, \quad (2.16)$$

where $p_\nu \equiv \mu \cdot u_\nu$ indicates the four-momentum of the test particle with mass μ . We will from now on set the test particle mass $\mu = 1$ by using natural coordinates.

Hamilton-Jacobi theory is built on the existence of conjugate sets of momentum and position coordinates. Let us define the position vector as q_μ with corresponding conjugate momentum vector p_μ . The equations of motion of the system are then fully determined by the Hamiltonian via the *Hamilton-Jacobi equations*, which can be written as [26][24]:

$$\dot{q}_\mu = [q_\mu, \mathcal{H}], \quad \dot{p}_\mu = -[p_\mu, \mathcal{H}], \quad (2.17)$$

where the dot indicates differentiation with respect to proper time τ and the square brackets indicate *Poisson brackets*, defined for general functionals X, Y as

$$[X, Y] \equiv \sum_\alpha \left\{ \frac{\partial X}{\partial q_\alpha} \frac{\partial Y}{\partial p_\alpha} - \frac{\partial X}{\partial p_\alpha} \frac{\partial Y}{\partial q_\alpha} \right\}, \quad (2.18)$$

where α runs over all four coordinate dimensions of the spacetime. We see that for a given metric tensor $g_{\mu\nu}$, it is straightforward to compute the equations of motion corresponding to the geodesics in that spacetime; one simply computes the Hamiltonian and then applies Eq. (2.17). Since in this project we will be varying $g_{\mu\nu}$ continually to find different properties of these geodesics, it is advantageous to use this particular framework. Of course, if one derives the equations of motion using another formalism, such as the Lagrangian formalism, one should obtain the same results. The underlying physics of the system should not be affected by the method used to obtain the equations of motion.

As briefly mentioned above, it is possible to use the Hamilton-Jacobi equations of motion to show the conservation of certain quantities. As we will discuss in Chapter 5, the momentum equation

can be straightforwardly used to show the conservation of energy and angular momentum in the class of spacetimes we are interested in. Although this conservation can in principle also be shown by finding the Killing vectors of a spacetime and computing the associated conserved quantity, the Hamiltonian method is more straightforward and does not require any additional calculation beyond the equations of motion themselves. This is another advantage of employing the Hamilton-Jacobi formalism.

2.2.2 Integrability, action-angle variables and resonance

We can now define what chaotic motion means in our context. To this end, we introduce the concept of *integrability* of the dynamics of a spacetime. This concept is central to this project and can be defined in several equivalent ways. We will follow the definition as provided in Ref. [25]. A metric's dynamics are said to be integrable if and only if the spacetime has as many degrees of freedom as independently conserved quantities. We further more require these conserved quantities to be *in involution* with one another. Two functionals X, Y are said to be in involution if they satisfy

$$[X, Y] = 0. \quad (2.19)$$

Since we will be considering four-dimensional spacetimes, this definition means that a solution to the Einstein field equations is integrable if and only if we can find four independently conserved quantities corresponding to that spacetime which are also in involution. It can be shown [25] that a spacetime with four such conserved quantities X, Y, Z, W defines a smooth four-dimensional manifold \mathcal{M} on which the geodesics exist. If one then (in our use case, reasonably) demands \mathcal{M} to be compact and connected⁶, it can be shown that this space is just a diffeomorphism of a four-torus \mathbb{T}^4 . Hence, we see that geodesics in an integrable four-dimensional spacetime are essentially just a coordinate transformation away from moving along a torus in four dimensions and that the integrability condition is equivalent to the existence of this diffeomorphism. This diffeomorphism would consist of transforming to a coordinate system referred to as *action-angle coordinates*. Let us denote these generalised action-angle variables with (θ_μ, J_μ) , where θ_μ indicates the position vector and J_μ the conjugate momenta. An action-angle coordinate system must then transform the coordinates in such a way that $\mathcal{H}(\theta_\mu, J_\mu) = \mathcal{H}(J_\mu)$, i.e. such that the Hamiltonian only depends on J_μ . Using the Hamilton-Jacobi equations in Eq. (2.17), this directly implies

$$\boxed{\begin{aligned} \dot{\theta}_\mu &= \dot{\theta}_\mu(J_\mu) = \frac{\partial \mathcal{H}}{\partial J_\mu} \\ \dot{J}_\mu &= 0. \end{aligned}} \quad (2.20)$$

Although it might not be immediately obvious, such a coordinate system has remarkable properties. From the conservation of J_μ and the independence of the four components of the conjugate momentum vector, we see that the conjugate momenta of this system are precisely the conserved quantities of this spacetime. This connection is why the conserved quantities are often referred to as *constants of motion* or *integrals of motion*. The J_μ coordinates are the "action" part of action-angle variables.

The position vector θ_μ now represents the four "angular" coordinates which determine the coordinates on the four-torus of a point in spacetime⁷, which is why these coordinates form the "angles"

⁶Compactness and connectedness are basic concepts from topology, for details on which interested readers are referred to any introductory textbook on the subject, or the accessible manuscript "Topology Without Tears" [27].

⁷Keep in mind that on a four-torus, a natural chart is given by four angles varying between 0 and 2π . This idea is most easily visualised by imagining a three-torus as an embedding in three-dimensional Cartesian space.

of action-angle variables. Since its components now only depend on the conserved quantities J_μ which are constant, we can define the *fundamental frequencies* ω_μ as

$$\omega_\mu \equiv \dot{\theta}_\mu(J_\mu). \quad (2.21)$$

When the conserved quantities are specified to particular values, these fundamental frequencies are constant and correspond to a specific geodesic. It can be shown that a set of conserved quantities yields a unique geodesic with corresponding fundamental frequencies, such that no two different orbital curves can be described by the same set of conserved quantities⁸. We also see that the torus on which a geodesic exists is uniquely determined by the values of J_μ . We can thus conclude that if we are given integrable metric as well as the values of the four corresponding conserved quantities, we have fully and uniquely determined the resulting geodesic, which when put in an appropriate coordinate system traces out a four-torus.

As an orbit evolves, it will form a curve on the four-torus. Depending on the fundamental frequencies corresponding to the orbit, the curve will either ergodically and densely fill out the full torus over infinite time (which is called *quasiperiodic* motion), or *periodically* trace over itself after some finite time. Periodic orbits happen when the fundamental frequencies of a geodesic are an *integer ratio* of one another. If this is the case, a so-called *resonance condition* is satisfied [28] and one refers to the orbit as a *resonant orbit*. If we define k_μ as a vector of four integers, the set of resonance conditions can mathematically be expressed as

$$\mathcal{R} = \{k_\mu \in \mathbb{Z}^4 \mid k_\mu k^\mu \neq 0 \text{ and } k_\mu \omega^\mu = 0\}. \quad (2.22)$$

The cardinality of \mathcal{R} indicates the number of satisfied resonance conditions of a given orbit. If there are $4 - 1 = 3$ satisfied resonance conditions, one for each of the spacelike coordinates, the orbit is *fully resonant*. However, for our analysis it will suffice for an orbit to be resonant in two of its fundamental frequencies. Hence, an orbit is considered resonant in coordinates x, y if their fundamental frequencies $\omega_x, \omega_y \in \omega_\mu$ satisfy the condition⁹

$$\nu \equiv \frac{\omega_x}{\omega_y} = \frac{m}{n}, \quad (2.23)$$

with $m, n \in \mathbb{N}$. Here we have defined ν as the *rotation number* corresponding to the orbit. This quantity forms the backbone of our analysis. If the rotation number of an orbit is rational, the orbit is resonant, meaning that it is periodic over some finite time τ . Likewise, an irrational value of ν corresponds to a non-resonant orbit, which is quasiperiodic. It is worth emphasising that we will not need a spacetime's dynamics to be integrable in order to compute rotation numbers; rather, we can use rotation numbers to identify whether a spacetime's dynamics are integrable or not. Indeed, one might wonder what happens if we do *not* have four conserved quantities, but for instance only three. One then has a metric whose dynamics are *non-integrable*. It turns out that geodesics then no longer foliate surfaces in \mathbb{T}^4 , but rather exhibit chaotic motion. Before we go into more detail however, let us first introduce a method to keep track the evolution of position coordinates and their conjugate momenta.

⁸Unlike the conserved quantities, the values of the fundamental frequencies do not necessarily uniquely determine the geodesics, as is explained in Ref. [25].

⁹Strictly speaking, our resonance condition allows the rotation number to take on negative values. However, we will define the rotation number to take on positive values only.

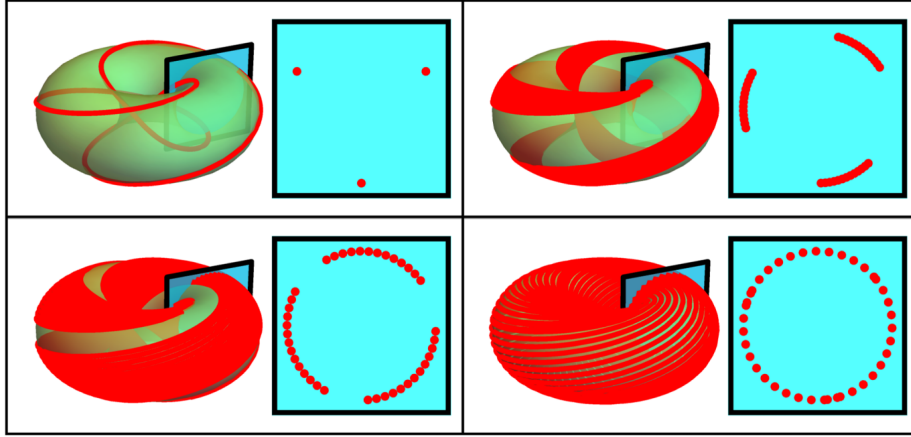


Figure 2.1: Illustration of two-dimensional Poincaré slices of a resonant orbit (top left) and non-resonant orbits [25]. In the resonant orbit, one can see how a geodesic traces over itself as it travels along the green two-torus. The corresponding Poincaré slice (cyan) shows how the piercings are always located in the same locations in the two-dimensional phase space, even as time goes to infinity. In this particular resonant orbit, we see three piercings, corresponding to a $2/3$ resonance. In the other pictures, we see non-resonant cases, where the two-torus is ergodically filled as time increases. The piercings of the corresponding Poincaré slice will accordingly ergodically fill a closed curve.

2.2.3 Poincaré maps and fixed points

Once one has the curve corresponding to a geodesic in spacetime, its position and conjugate momentum vectors will evolve as the proper time τ increases, precisely as governed by the Hamilton-Jacobi equations. The full eight-dimensional phase space of these orbits is difficult to visualise and, as will be shown in Chapter 4, unnecessary to characterise the orbital properties we are interested in. Hence, for the analysis of geodesics, one often takes a two-dimensional *slice* of the full phase space by considering a specific position coordinate and its conjugate momentum. Such a slice of the phase space is called a *Poincaré map* or *Poincaré slice*. Indeed, if one is investigating the resonance of an orbit in only two coordinates x, y , the four-torus along which the geodesic evolves is reduced to a two-torus. In Fig. 2.1, we see that as the geodesic evolves along this torus, it pierces the Poincaré slice repeatedly. In an integrable system, a geodesic will form closed curves in the Poincaré slice if the orbit is non-resonant. If it is a resonant orbit, the geodesic will pierce the slice at the same points periodically.

For a given set of conserved quantities, one can vary the initial conditions of the geodesics to obtain different curves in the Poincaré slice. Because we know that the geodesics are continuous and uniquely determined, it is not possible in spacetime with integrable dynamics for two of such curves to cross over each other. Accordingly, there exist closed "curves" in the Poincaré slice which consist of precisely *one* point in phase space. These are the *fixed points* of the phase space. The closed curves in the Poincaré slices of geodesics will always form around these fixed points. In a fixed point, the conjugate momentum is equal to zero. Let us give a simplified example to clarify this idea. If one imagines a spherical coordinate system (t, r, θ, ϕ) and finds a fixed point in the Poincaré slice corresponding to the radial coordinate r and its corresponding momentum p_r , one has that $p_r = 0$, such that the geodesic piercing the slice repeatedly at that fixed point *must* orbit at constant radius.

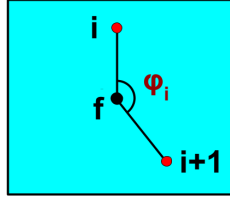


Figure 2.2: Illustration depicting the angle of advance φ_i between two successive piercings of the Poincaré slice as measured around fixed point f .

It turns out that one can use these piercings of the Poincaré slice to approximate the rotation number corresponding to the geodesic. The rotation number ν , defined in Eq. (2.23), can also be found by considering the angles between successive piercings of the Poincaré slice [25][29][30][31]:

$$\nu = \lim_{N \rightarrow \infty} \frac{1}{2\pi N} \sum_{i=1}^N \varphi_i, \quad (2.24)$$

where φ_i is the *angle of advance*¹⁰ between piercing i and $i + 1$ in the Poincaré slice one is considering, as illustrated in Fig. 2.2. Note that ν is just the average angle of advance of the piercings as a fraction of a circle, which is why it is called the *rotation number*.

In this project, we will mostly use the piercings of the Poincaré slice to compute ν . Of course, we are not able to complete an infinite amount of piercings; hence, the orbits will be evaluated for very long periods of time to approximate the true value of ν . Despite this, using this form of the rotation number is the most straightforward and least computationally expensive way for us to compute this quantity, in particular because we will numerically evaluate the equations of motion anyway for other components of the analysis as well. However, it is important to realise that the rotation number is intricately related to the fundamental frequencies of the geodesic, which form the mathematical foundation of this dynamical system.

2.2.4 Breaking integrability and the KAM theorem

Up till now, we have considered integrable dynamics, where there are precisely as many conserved quantities as there are degrees of freedom. However, this turns out to be a very special property which is possessed only by specific solutions to the Einstein field equations. The Kerr solution is in fact integrable¹¹, but if one perturbs the Kerr solution to obtain modified gravity theories, this integrability might be broken. In this section, we will discuss the theorems describing how this has an effect on the orbital dynamics from the previous section, as well as how one can identify the integrability of a spacetime without directly searching for conserved quantities.

Generally speaking, the existence of the four-tori described in the previous section depends on

¹⁰When computing the rotation number, it is important to always measure the angle along the same direction between successive piercings, rather than taking for instance the smallest of the two angles between the vectors of the piercings. This can be achieved by considering the determinant when computing the angle between the piercings.

¹¹Strictly speaking, the correct way to phrase this is by stating that the *dynamics* of the Kerr solution are integrable, rather than the Kerr solution itself. However, for the sake of brevity, we will from here on out denote a spacetime as (non-)integrable if its dynamics are (non-)integrable, where we understand that the latter is the more correct formulation.

the integrability of the underlying dynamics. In principle, we do not expect these tori to exist for non-integrable systems. However, it turns out that if a non-integrable Hamiltonian is similar enough to an integrable Hamiltonian, some of these tori might not be broken [25][32][28]. Since we expect any deviation from the integrable Kerr solution in a candidate modified gravity theorem to be (very) small, it is worth investigating what happens to the tori when a small perturbation is made to the Kerr solution.

Consider an integrable spacetime with a Hamiltonian in action-angle coordinates $\mathcal{H}_K(J_\mu)$. Now, let us add a perturbation \mathcal{H}_p to \mathcal{H}_K , such that we obtain a new Hamiltonian given by [25]

$$\mathcal{H}(\theta_\mu, J_\mu) = \mathcal{H}_K(J_\mu) + \epsilon \cdot \mathcal{H}_p(\theta_\mu, J_\mu), \quad (2.25)$$

for some constant ϵ . It is interesting to note that we do not specify what the nature of the perturbation \mathcal{H}_p is at this point. Sources of this perturbation can vary from the presence of an accretion disk or dark matter to the existence of quadratic curvature terms in the Einstein-Hilbert action, which is an example of modified gravity [28]. However, importantly for us, numerical inaccuracies such as performing a Taylor expansion or even the machine precision of a computer programme also cause a perturbation to the original Hamiltonian, as will become evident in Chapter 8.

Geodesics only foliate a four-torus if the spacetime is integrable, since only then a transformation to action-angle variables exists. However, if we let $\epsilon \ll 1$, such that the perturbation to an integrable Hamiltonian is very small, the *KAM theorem* [33][34][35] states that only the tori corresponding to resonant orbits will be destroyed, whereas if the rotation number of a geodesic is *irrational enough*, the torus will not be broken, but only slightly deformed [36]. A more exact formulation of which tori are preserved is given via *Arnold's criterion* in four dimensions:

$$k_\mu \omega^\mu > K(\epsilon) \cdot \left(\sum_{i=1}^4 |k_i| \right)^{-5}, \quad (2.26)$$

where $K(\epsilon)$ depends on the nature of the perturbation [28]. If Arnold's criterion holds, a particular torus is preserved. In order for the ratio of two natural numbers m/n to approach irrationality, we need m, n to be as large as possible. On the other hand, if the components of k_μ are small, Arnold's criterion is not satisfied and the torus is broken. This is precisely how the irrationality of ν and the breaking of the tori are related. One can now see that if a vector k_μ corresponding to a particular resonant condition has large enough components such the rotation number ν becomes close enough to an irrational number, Arnold's criterion is satisfied and the resonant orbit's torus is not broken. We have hence found a hierarchy in what kind of resonant tori will be destroyed by a perturbation to an integrable Hamiltonian: the torus of a resonant orbit with rotation number $\nu = m/n$ is more likely to be destroyed by a perturbation if m, n are small. These resonances are called *low-order resonances* and are given by for instance $\nu \in \{1/2, 2/3, 3/4, \dots\}$. Hence, if we are looking for signatures of perturbations to the Kerr metric, we should look for them around the low-order resonances, since we expect the tori of the integrable Kerr metric to be broken *first* around these geodesics.

2.2.5 Poincaré-Birkhoff theorem and chaotic features

The question remains how the breaking of tori affects the dynamics of the system. These effects are predicted by the *Poincaré-Birkhoff theorem* [25]. On a resonant torus, one in principle has an infinite number of periodic orbits. If the torus is broken, the theorem says that $\exists n \in \mathbb{N}$ such that $2n$ orbits will remain periodic, where half of them are stable and the other half are unstable. These

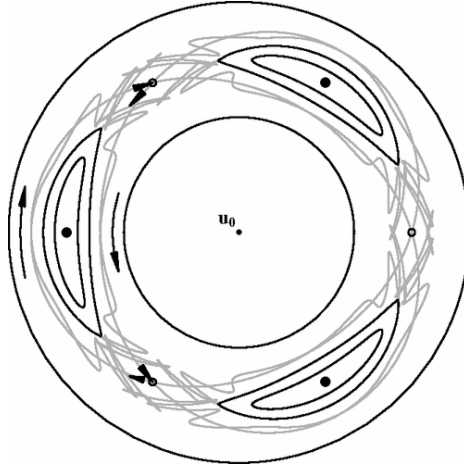


Figure 2.3: A schematic representation of a Birkhoff chain in a non-integrable spacetime's Poincaré slice [37]. u_0 indicates the original fixed point in the phase space, as it also appeared in the non-perturbed spacetime. The filled dots indicate the newly created stable fixed points, around which additional closed curves appear. The open points indicate the unstable fixed points, in equal number to the new stable points. Rather than closed curves, chaotic behaviour is visible in the curves near those points.

stable and unstable points on the torus form a so-called *Birkhoff chain* [37]. Around these stable points, additional closed curves in the phase space form, allowing nearby orbits to exist in an *island of stability*. In contrast to these islands of stability, unstable points are surrounded by a (very) thin veil of chaotic motion, causing the rotation number to become undefined at the original resonant curve. This shows up in the phase space as several closed curves *crossing over* one another, which as one might recall is topologically impossible in an integrable spacetime with an existing bijection to \mathbb{T}^4 . A schematic of this phenomenon is presented in Fig. 2.3.

If one performs an analysis of the rotation number in a perturbed metric, one can find evidence for both these stable and unstable points by analysing the rotation number. By varying the initial conditions of the differential equations describing geodesic motion, one is able to generate orbits with different orbital frequencies for the same set of conserved quantities. In this fashion, one can numerically analyse the behaviour of these frequencies near resonant values of ν . By making a plot of the value of the rotation number as a function of the initial conditions, one can compute the so-called *rotation curve*. In a fully integrable system, the rotation curve continuously and monotonically increases towards the fixed point in the phase space. However, in a perturbed system, the range of analysed geodesics might pass through one of the broken tori and thus through the Birkhoff chain surrounding that resonance. Depending on whether one passes through a stable or unstable orbit, one can then find either a *plateau* in the rotation curve, or a *discontinuity*. A plateau corresponds to an island of stability in the Birkhoff chain; in a small region around the location of the unperturbed resonance, the rotation number is fixed at the resonance value. A discontinuity in the rotation curve indicates an unstable point in the Birkhoff chain. Here, the rotation number becomes undefined at the original resonance, which is observed as a sudden jump in the rotation curve. An illustration of what this looks like is given in Fig. 2.4.

Both these types of features in the rotation curve result in detectable signals in gravitational waves.

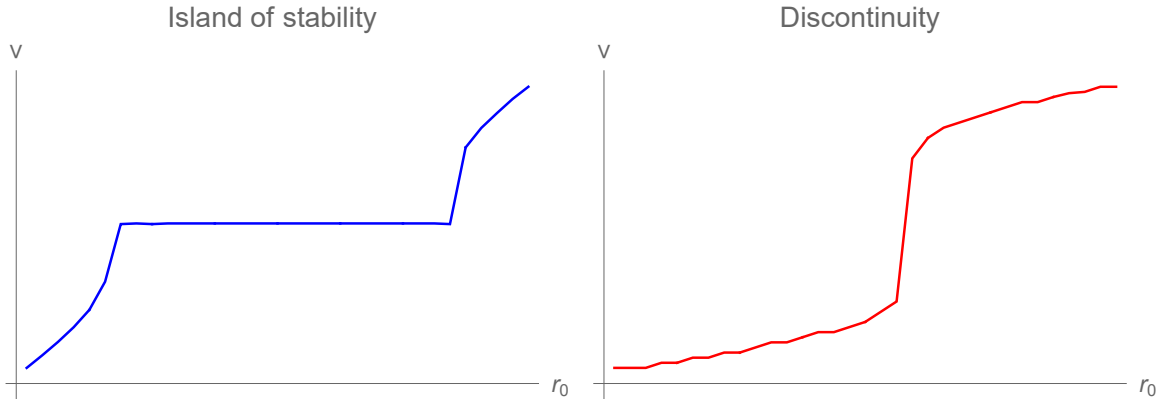


Figure 2.4: Examples of how the stable and unstable orbits caused by broken tori as predicted by the Poincaré-Birkhoff theorem could manifest in the rotation curve of orbits in a perturbed Kerr spacetime. On the horizontal axis, the initial radial coordinate of the geodesic is varied. If the spacetime were integrable, none of the above features would appear and the rotation curve would be completely smooth.

The orbital frequencies are not purely mathematical constructs; they are observable quantities which can be reconstructed from the gravitational waves emitted by EMRIs by using waveform models. It is through these measurements that one would look for islands of stability or discontinuities in the rotation curve. In a physical system, an orbiting stellar-mass object slowly loses energy, which causes it to pass through the potentially broken tori in a similar fashion to how we will vary the initial conditions of geodesics in this analysis. The hope is then that a rotation curve can be constructed from these observations and that any deviation from the Kerr solution in this regime of gravity can be (dis)proven. How this relates to actual gravitational wave observables and experiments will be treated in Chapter 9.

From a theoretical point of view, we are however not quite done. In this thesis, we will add a perturbation to the Kerr solution by computing geodesics in a theory of modified gravity. The established mathematical framework then tells us what kind of features to look for in the rotation curve. We have, however, not yet established whether we expect to find stable or unstable points in the rotation curve of modified spacetimes, how large we expect chaotic features to be, or whether these features will be reasonably detectable by future experiments. By performing an extensive numerical analysis, we will attempt to gain insight into these topics. First however, we will explore how one generally constructs a theory of modified gravity.

Chapter 3

Modifying gravity

Based on the previous chapters, it can be established that general relativity provides an expansive framework in which to model the effects of matter on spacetime. However, one of the underlying assumptions of general relativity is that it is a purely geometric theory, where the metric and connection are in principle not dynamical quantities. Although this is a mathematically pleasing idea and works well when describing for instance planetary dynamics, it is not necessarily true at all length scales. As stated in the introduction, it is known that general relativity provides no satisfactory description of gravity at the quantum level, even though quantum field theory and general relativity separately are considered very good models of nature. Indeed, if one attempts to apply a renormalisation scheme similar to the one developed for electroweak theory by 't Hooft and Veltman [38], it turns out that the coupling constant of quantum gravity has a negative mass dimension. Without going into too much detail, the physics behind the Standard Model tell us that this means that one would need an infinite amount of counterterms in the Lagrangian to obtain any meaningful dynamics from this interaction, rendering it physically unviable. This problem is known as the *non-renormalisability of general relativity*. This fact lies at the core of a great deal of modern physics research and incorporating gravity and quantum mechanics can be considered one of the greatest challenges in (theoretical) physics of our time.

The incompatibility of general relativity with quantum field theory motivates us to explore theories of gravity beyond the description as provided by Einstein. In this chapter, we will explore the general subject of modified gravity from a general relativity point of view and categorise some of the possible modifications through their general properties. It is also possible to approach this problem starting from other theories such as string theory or loop quantum gravity, but a full treatment of these theories lies beyond the scope of this thesis.

3.1 Alterations to the Einstein-Hilbert action

Recall from Chapter 2 that general relativity's field equations are derived from the Einstein-Hilbert action. The Einstein-Hilbert action as presented in Eq. (2.9) depends on the curvature of spacetime linearly. Since we know that this action appropriately describes gravity at planetary length scales, we require any modified gravity to effectively reduce to the Einstein-Hilbert action at large scales.

The study of modified gravities revolves around determining what modifications of the action yield meaningful results. However, one is not completely free in the choice of these modifications. In the following sections, we will discuss some of the problems which can arise when modifying gravity,

which in turn provide a form of classification of different modified gravity proposals. We will not outline specific modified gravity theories, but rather provide an outline of general aspects of modified gravity which will later be revisited when we choose a specific theorem to study.

3.2 Lovelock's theorem

When one seeks for an action that yield new gravity theorems, there are limitations on what one can find from the metric tensor by itself. These limits are encoded in *Lovelock's theorem* [14][39][40]. If the Lagrangian of an action depends only on the metric tensor such that $\mathcal{L} = \mathcal{L}(g_{\mu\nu})$, Lovelock's theorem states that in $3 + 1$ dimensions, the only possible symmetric and divergence free equations of motion at second order as obtained from $\mathcal{L}(g_{\mu\nu})$ are precisely the Einstein field equations. The consequences of Lovelock's theorem are that we must break one of the conditions of this theory in order to construct gravity theories which are meaningfully different from general relativity. Let us now discuss in what ways breaking these conditions can yield gravitational actions different from the Einstein-Hilbert action.

3.2.1 Additional scalar fields

Up till now, we have assumed that any modified action depends only on the spacetime curvature. Several modified gravities deal with Lovelock's theorem by introducing an additional *scalar field* into the gravitational action [14]. Such a theory is generally referred to as a *scalar-tensor theory* [5]. This kind of scalar dependency can be introduced in different ways. For instance, one could explicitly construct a scalar field ϕ_s from the corrections to S_{EH} , such that $R = R(\phi_s)$ and hence the two can be expressed in terms of one another. However, it is also possible to introduce an entirely independent scalar field, such that it has its own action and equation of motion. This scalar field can then be coupled to curvature terms, such that the full system of field equations from the action consists of four curvature equations and one scalar field equation. If one is willing to add scalar fields to the gravitational action, several additional classes of theories can be built which are different from the Einstein field equations.

3.2.2 Higher order curvature terms

Another method of bypassing Lovelock's theorem is by accepting higher order derivatives of curvature. The most straightforward generalisation we can construct is then given by

$$S_m = \int \sqrt{-g} f(R) d^4x, \quad (3.1)$$

where $f(R)$ represents some function of the curvature of spacetime such that $f(R) = R + \gamma R^n$, with $n \geq 2$ and γ constant [5]. Indeed, γ should be chosen such that the Einstein-Hilbert action is obtained at longer length scales. These classes of gravitational theories are known as *f(R) theories*. One advantage of these gravities is that for example R^2 gravity, where we add quadratic curvature terms, can be shown to be renormalisable in the quantum field theory picture [5]. Besides that, it is one of the more natural extensions of general relativity. However, the downside of using general $f(R)$ theories is the potential generation of ghosts and instabilities, as is elaborated on in Section 3.3.

3.2.3 Higher dimensional theories

Lovelock's theorem holds only in four-dimensional spacetimes. Hence, another way of generating solutions which differ from general relativity is by adding additional dimensions on top of the four

spacetime dimensions of general relativity. There is physical motivation for such extensions of gravity from several viewpoints. For instance, although general relativity was developed in $3 + 1$ dimensions, Riemannian geometry can in principle be applied to any D -dimensional theory. A prominent example of a physical theory using higher dimensions is of course (super)string theory [41]. Usually, higher dimensional theories restrict themselves to adding additional spacelike dimensions. However, work as also been performed on adding extra timelike coordinates [14].

The main problem with higher dimensional theories is that gravity does not seem to behave like a higher-dimensional force. For instance, from a superstring theory point of view, one could expect $D = 10$ dimensions. However, since the strength of the gravitational force from a point mass scales inversely with the number of dimensions, gravity on a solar system scale seems to be far too strong for this to be the case. Furthermore, if $D \neq 3 + 1$, there are no possible stable orbits allowed in the first place [14]. Hence, the effects of any additional dimensions should be (almost) negligible on planetary scales.

There are many theories which invoke higher dimensions to differentiate from the Einstein field equations. In addition to the aforementioned string theory, one could consider for instance Kalusa-Klein theory, which originated from an attempt to unify electrodynamics and gravity by Nordstöm [14][42]. One generally performs a dimensionality reduction to compactify higher-dimensional results into effects we can measure in the $3 + 1$ dimensions as observed by us.

3.2.4 Non-local theories and breaking Lorentz invariance

Gravitational actions exist which abandon the *locality* of general relativity, affecting the possible equations of motion. One should distinguish between kinematical and dynamical locality [43]. Kinematical locality is the concept of objects only acting on other objects in their direct vicinity, whereas dynamical locality is engrained in the action itself. For example, quantum mechanics is kinematically non-local, since the kinematics are not determined by explicit paths through spacetime but rather as a weighted average of all paths at once. However, relativistic quantum field theory is dynamically local. For us, dynamical (non-)locality is the interesting notion of locality.

Dynamical non-locality appears in the actions of several alternate gravities, such as certain string theories and loop quantum gravity [5][41]. These theories break Lorentz invariance at small length scales, which seems physically pathological. However, they do provide a method of generating renormalisable theories without introducing ghost fields and instabilities.

3.2.5 Abandoning the principle of least action

It is even possible to abandon the more fundamental concepts of dynamics in order to obtain different equations of motion. For example, one could give up on divergence-free field equations or even the symmetric exchange of indices in the metric tensor. However, if one attempts these changes, the variational principle is no longer applicable to derive the equations of motion [14]. These theories lie beyond the scope of this project and will not be considered further here.

3.3 Ostrogradski instabilities and ghosts

One problem which can arise when changing the Einstein-Hilbert action through higher derivative terms is related to the degrees of freedom in the Hamiltonian. In its most general form, the *theorem of Ostrogradski* states that if one has a Hamiltonian with a second (or higher) order time derivative,

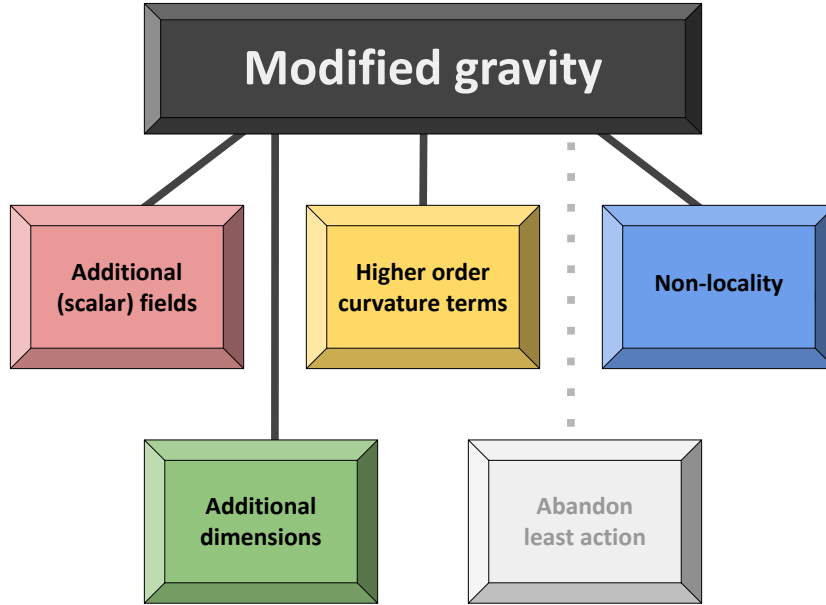


Figure 3.1: An overview of the classes of modified gravity as discussed in this chapter.

it is linearly unstable. These instabilities are referred to as *Ostrogradski instabilities* [5][44]. The consequences of this are best illustrated via an example using Euler-Lagrange mechanics. The following is a summarised version of the derivation performed by Ostrogradski as shown in Ref. [44].

Consider a system with a Hamiltonian including second order time derivatives. This results in some Lagrangian \mathcal{L} depending on variables including a second order derivative in time, i.e. $\mathcal{L} = \mathcal{L}(q, \dot{q}, \ddot{q})$. One can then apply the Euler-Lagrange equations to obtain

$$\frac{\partial \mathcal{L}}{\partial q} - \frac{d}{dt} \frac{\partial \mathcal{L}}{\partial \dot{q}} + \frac{d^2}{dt^2} \frac{\partial \mathcal{L}}{\partial \ddot{q}} = 0. \quad (3.2)$$

Under the assumption that \mathcal{L} depends non-degenerately on \ddot{q} , one then has that its derivative with respect to \ddot{q} still depends on \ddot{q} , such that any solution for $q(t)$ has the following dependencies:

$$q(t) = \mathcal{Q}(t, q_0, \dot{q}_0, \ddot{q}_0, q_0^{(3)}), \quad (3.3)$$

where $q^{(3)}$ is the third time derivative of q and q_0 and its higher order derivatives represent their respective initial values. Since we now have four initial conditions, we should also define four canonical coordinates. In the context of demonstrating the instabilities, one can pick

$$\begin{aligned} Q_1 &\equiv q, & Q_2 &\equiv \dot{q}, \\ P_1 &\equiv \frac{\partial \mathcal{L}}{\partial \dot{q}} - \frac{d}{dt} \frac{\partial \mathcal{L}}{\partial \ddot{q}}, & P_2 &\equiv \frac{\partial \mathcal{L}}{\partial \ddot{q}}. \end{aligned} \quad (3.4)$$

It turns out that one can solve for the coordinate P_2 by letting $q = Q_1$, $\dot{q} = Q_2$ and $\ddot{q} = a(Q_1, Q_2, P_2)$. Note that this solution only depends on three canonical coordinates, leaving one coordinate unused. This is due to the fact that \mathcal{L} only depends on three coordinates. However, as a result one can then reconstruct the Hamiltonian of the system as

$$\mathcal{H}(Q_1, Q_2, P_1, P_2) = P_1 Q_2 + P_2 \cdot a - \mathcal{L}. \quad (3.5)$$

There is a major problem with this Hamiltonian: the linear dependence on P_1 . Since this momentum could of course be negative independent of the sign of Q_2 , there is no lower bound on the total energy of the system. It thus is impossible to define a vacuum energy and hence any dynamical system of this form is inherently unstable. Furthermore, one can in principle freely and infinitely tap energy from the system through particles with negative energies [5]. In a quantum-mechanical context, such particles are states with negative norms and are referred to as *ghosts* [41][45] or *ghost modes* [46]. In some applications, such as the canonical formulation of QED, these ghosts are eliminated through gauge fixing. Generally however, one cannot simply ignore these unphysical states if they appear in a theory (of gravity).

Since this derivation does not depend on the actual form of \mathcal{L} , we see that the Ostrogradski ghost will appear if one has a higher order time derivative in the Hamiltonian with nothing to counter it. The Riemann tensor contains a time derivative and hence adding quadratic order curvature terms could introduce these instabilities into the modified gravity theory. Adding more terms does not necessarily solve the issue; in fact, having higher order time derivatives only makes it worse [44]. Because of this, some physicists working on gravities which display this instability aim to construct a model akin to an effective field theory, of which the low-energy limits hopefully provide meaningful descriptions of gravity. There are different, more involved ways of addressing these ghosts. For instance, if one is willing to discard S_{EH} entirely, one could construct alternative gravities consisting of just higher order curvature terms, some of which have no instability issues. However, discarding S_{EH} is contentious due to the copious amount of evidence supporting general relativity's predictions. Furthermore, one could introduce higher order spacial derivatives rather than temporal derivatives, avoiding the issue altogether. Additionally, adding an independent scalar field coupled to higher curvature terms can address the issue at the level of the equations of motion [46]. Finally, higher order derivatives might act on non-dynamical modes, which means that no ghosts should appear in that case. For a full discussion on the subject, readers are referred to for instance Ref. [14] or Ref. [5].

In the introduction, it was mentioned that the modification of gravity which will be considered in this thesis is Einstein-dilaton Gauss-Bonnet theory. When applying the above categorisation scheme, this theory falls under two categories; its action features higher-order curvature terms as well as a scalar field. Einstein-dilaton Gauss-Bonnet theory will be properly introduced in Chapter 7. Before diving into modified gravity, we should build a proper understanding of the parametrisations of black holes as provided by general relativity.

Chapter 4

Stationary axisymmetric vacuum (SAV) solutions

We have seen that the Kerr solution to the Einstein field equations parametrises spacetime around a rotating massive object as predicted by general relativity. The Kerr solution is part of a broader class of solutions known as *stationary axisymmetric vacuum solutions* (SAV solutions). These solutions have several interesting properties: stationarity refers to the line element being constant in time, axisymmetry implies a symmetry around one rotation axis (as opposed to spherical symmetry, where one imposes full rotational symmetry) and vacuum implies setting the energy-momentum tensor to zero. Setting $T_{\mu\nu} = 0$ is precisely what we need to characterise orbits near rotating black holes, since we aim to model geodesics *outside* of the compact object, where we assume no presence of additional energy or momentum. Intuitively, we can already realise that a Kerr black hole would fit well into this category; however, there are many subtleties when it comes to characterising SAV spacetimes. In this chapter, we will discuss some aspects of the derivation of SAV metrics and how they relate to the Kerr solution. We will provide an overview of several coordinate systems which can be used to describe SAV metrics, as well as which ones are the most appropriate for our analysis. From here on out, we will also set $G = M = 1$ for notational convenience, noting that we already had set $c = 1$ from the beginning.

4.1 The Weyl-Lewis-Papapetrou line element

Although the Einstein field equations in general relativity permit many different classes of solutions, the non-linearity of the equations means that most of these solutions are highly complicated and difficult to characterise. Therefore, a great deal of research has been conducted related to not just finding, but also characterising different solutions to the Einstein field equations. In the scope of this project, we are interested in SAV solutions to the Einstein field equations. In its most general form, one takes a four-dimensional line element in coordinates (x^0, x^1, x^2, x^3) given by

$$ds^2 = g_{\mu\nu} dx^\mu dx^\nu, \tag{4.1}$$

and identifies x^0 as the timelike coordinate. Since the metric tensor has 10 independent components [1], enforcing the Einstein field equations on this is not enough to find solutions. By adding further restrictions, we find different classes of solutions. Choosing different restrictions will lead to different classes of solutions. In the case of SAV solutions, we start by choosing x^3 as the axis of symmetry. SAV metrics must then be invariant under the following symmetry operations [47]:

Stationarity	Axial symmetry	Simultaneous reflection
$x^0 \rightarrow x^0 + a, a \in \mathbb{R}$	$x^3 \rightarrow x^3 + b, b \in \mathbb{R}$	$x^0 \rightarrow -x^0$ and $x^3 \rightarrow -x^3$

Another way of formulating stationarity and axial symmetry conditions is by demanding the existence of two commuting Killing vectors [47][48]. It can be shown using the Killing equation that this implies that

$$\partial_{x^0} g_{\mu\nu} = \partial_{x^3} g_{\mu\nu} = 0, \quad (4.2)$$

which means that the metric tensor should not explicitly depend on the timelike or axisymmetric components of the coordinate system.

By considering the above constraints and several other considerations, for details of which the reader is referred to for instance Ref. [47] or Ref. [48], Lewis proposed the following form of the SAV line element in 1932, building on Weyl's earlier work. This line element is called the *Weyl-Lewis-Papapetrou line element*. Let us relabel $x^0 = t, x^1 = \rho_W, x^2 = z_W$ and $x^3 = \phi$. The SAV line element is then given by

$$ds^2 = f dt^2 - 2m dt d\phi - (e^B d\rho_W^2 + e^C dz_W^2 + l d\phi^2), \quad (4.3)$$

for some functions f, B, C, l, m . By assuming $B = C$ and $fl + m^2 = \rho_W^2$, one obtains the SAV line element in *Weyl canonical coordinates*, or Weyl coordinates for short. It can be shown [48] that the line element can then be recast as

$$ds^2 = e^{-2U} (e^{2k} (d\rho_W^2 + dz_W^2) + R^2 d\phi^2) - e^{2U} (dt + A d\phi)^2, \quad (4.4)$$

where U, k, R and A are functions of *just* the components ρ_W and z_W of the metric, as demanded by the symmetries of SAV solutions. By exploiting the gauge freedom the harmonic function R (which is *not* to be confused with the Ricci scalar!) in the coordinates $R_{z_W z_W} + R_{\rho_W \rho_W} = 0$, we can set $R = \rho_W$ in this coordinate system [26].

When working with SAV solutions, it is important to realise that there is no one formulation which is by definition more useful than another. It turns out that every coordinate system lends itself to very specific problems. Weyl coordinates are a good example of this. A great advantage of this coordinate system is the common prefactor in the spatial components of the line element, i.e. $g_{\rho_W \rho_W} = g_{z_W z_W}$. As will be shown, this greatly simplifies the equations of motion of the system. However, the symmetries of this coordinate system which enable this simplicity of the field equations also make it very difficult to apply to the Kerr solution. Weyl coordinates display *cylindrical* symmetry, which means they are well adapted to solving those kinds of problems. However, the Kerr metric is an inherently *spheroidal* system. Because of this, it is extremely difficult to give an exact expression of the Kerr metric in Weyl coordinates: it is somewhat analogous to fitting a square peg in a round hole. As is explained on a more technical level in for instance Ref. [47], it is mostly due to the relation $fl + m^2 = \rho_W^2$ and the deceptively intricate relation between z_W and ρ_W that it is difficult to solve spheroidal problems with this coordinate system. Hence, we see that there is a clear motivation to use a coordinate system which has the same spheroidal symmetries as the Kerr solution. Luckily, there are several coordinate systems which do provide an exact and compact form of the Kerr metric.

4.2 Boyer-Lindquist coordinates

In 1963, Roy Kerr provided the first solution to the Einstein field equations which successfully parameterised the gravitational field around a rotating, massive object [49]. The solution was not derived in the Weyl form of the SAV metric; rather, Kerr realised that the spheroidal nature of the problem required a spheroidal coordinate system to solve. His solution is usually displayed in so-called *Boyer-Lindquist coordinates*, derived in 1966 [50]. Although Kerr actually used a different coordinate system to derive his solution, Boyer-Lindquist coordinates are commonly used because they are highly intuitive. The line element corresponding to the Kerr solution in Boyer-Lindquist coordinates is given by

$$ds^2 = - \left(1 - \frac{2r}{\Sigma} \right) dt^2 - \frac{2\chi \sin^2 \theta}{\Sigma} (dt d\phi + d\phi dt) + \frac{\Sigma}{\Delta} dr^2 + \Sigma d\theta^2 \quad (4.5)$$

$$+ \frac{\sin^2 \theta}{\Sigma} \left((r^2 + \chi^2)^2 - \chi^2 \Delta \sin^2 \theta \right) d\phi^2, \quad (4.6)$$

where

$$\Sigma = r^2 + \chi^2 \cos^2 \theta, \quad \Delta = r^2 - 2r + \chi^2, \quad (4.7)$$

and $\chi \in [0, 1]$ parametrises the spin per unit mass of the central black hole¹. When one sets $\chi = 0$, one obtains the traditional Schwarzschild solution corresponding to a non-spinning massive body, whereas $\chi = 1$ yields the so-called *extremal* Kerr black hole solution. In this coordinate system, we have $r \in [0, \infty]$, $\phi \in [0, 2\pi]$ and $\theta \in [0, \pi]$.

This form of the Boyer-Lindquist line element is the one as provided in Ref. [1] and is precisely equivalent to the form as provided in Ref. [48], as is easily verified using a symbolic programming language.

Although it is not feasible to derive a full Kerr line element expressed in Weyl coordinates for the reasons outlined in the previous section, there does exist an embedding of Weyl coordinates in Boyer-Lindquist coordinates:

$$\rho_W = \sqrt{r^2 - 2r + \chi^2} \sin \theta, \quad z_W = (r - 1) \cos \theta. \quad (4.8)$$

This relation will be used to depict the results of our calculations performed in Boyer-Lindquist coordinates in Weyl coordinates. A visualisation of the relation between these two coordinate systems is given in Fig. 4.1.

Boyer-Lindquist coordinates closely resemble a spherical coordinate system as often used in representations of 'traditional' 3-space spheroidal problems. This is one of the reasons why these coordinates are often used; they provide the user with some physical intuition of the behaviour of the metric. However, what is sacrificed for this intuition is the compactness of the line element itself. We no longer have a symmetry in the spacial components (r, θ) in the same way we had in Weyl coordinates. Furthermore, the line element itself is relatively convoluted, causing calculations to quickly become quite messy. Finally, the location of the event horizon changes with the spin value of the black hole, as will be shown later. However, there exists another coordinate system which strikes a compromise between all this, which we will now introduce.

¹Recall that we set the gravitational constant G , speed of light c and black hole mass M to 1 by using a natural coordinate system. The full formulation of the line element can be found in for instance Ref. [1] or via dimensional analysis. For other parametrisations discussed in this chapter, the reader is referred to Ref. [48].

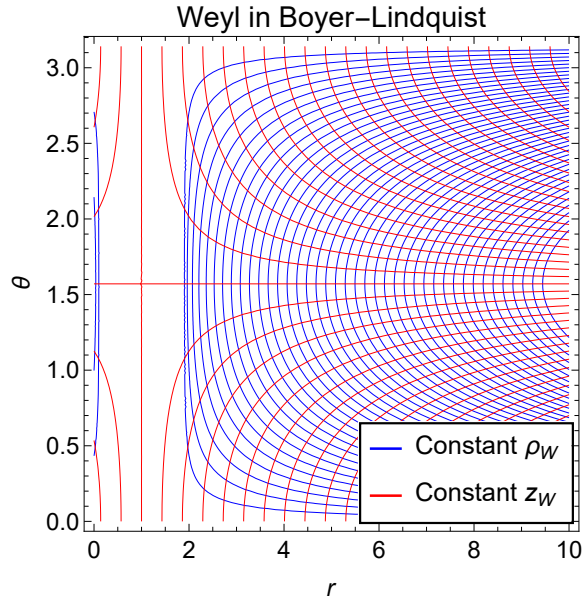


Figure 4.1: Weyl coordinates as a function of Boyer-Lindquist coordinates with $\chi = 1/2$. The effect of the event horizon is clearly visible.

4.3 Prolate spheroidal coordinates

In 1968, Ernst formulated a widely used form of the general SAV line element displaying the same spheroidal symmetries as the Kerr solution. Starting from the SAV line element in the form of Eq. (4.4) with $R = \rho_W$, Ernst introduced a complex potential method to solve for the Kerr black hole [47][48][51]. This complex potential in essence provides a relation between the characterising functions A and e^{-2U} . Starting from this *Ernst potential*

$$\mathcal{E} = -e^{-2U} + i\phi, \quad (4.9)$$

and including the relation

$$e^{4U} \nabla \phi = \frac{\hat{n} \times \nabla A}{\rho_W}, \quad (4.10)$$

where \hat{n} is the unit vector along ϕ , one can rephrase the field equations for the unknown functions in the line element as

$$(\xi \xi^* - 1) \nabla^2 \xi = 2\xi^* \nabla \xi \cdot \nabla \xi, \quad (4.11)$$

with

$$\xi = \frac{1 + \mathcal{E}}{1 - \mathcal{E}}. \quad (4.12)$$

Note that in the above expressions, the gradients are defined in the Boyer-Lindquist formulation. Finding different SAV line elements has now been reduced to solving Eq. (4.11) for ξ . This formulation does not just allow for finding the Kerr solution; it provides a complete classification scheme for many different SAV line elements satisfying the Einstein field equations, with each solution ξ corresponding to a different SAV line element [48][11]. In this framework, the Kerr solution is given by

$$\xi = px - iqqy, \quad (4.13)$$

with $p, q \in \mathbb{R}$ such that $p^2 + q^2 = 1$. In fact, we specifically require $q = \chi$ and $p = \sqrt{1 - \chi^2}$, again noting that we set the black hole mass to unity. Here, we have introduced a new coordinate system: *prolate spheroidal coordinates*. Weyl coordinates are related to prolate spheroidal coordinates via the following relations:

$$\rho_W = \sigma \sqrt{(x^2 - 1)(1 - y^2)}, \quad z = \sigma xy, \quad (4.14)$$

where $\sigma = p = \sqrt{1 - \chi^2}$ for the Kerr metric² [48][11]. The inverse relation is then given by

$$x = \frac{r_+ + r_-}{2\sigma}, \quad y = \frac{r_+ - r_-}{2\sigma}, \quad (4.15)$$

with

$$r_{\pm} = \sqrt{\rho_W^2 + (z \pm \sigma)^2}. \quad (4.16)$$

The line elements of the two coordinate systems are related via

$$\boxed{d\rho_W^2 + dz_W^2 = \sigma^2(x^2 - y^2) \left(\frac{dx^2}{x^2 - 1} + \frac{dy^2}{1 - y^2} \right)}, \quad (4.17)$$

where we note that the t and ϕ components of the metric are not transformed. Note that the domains of the variables in this system are $x \in [1, \infty)$ and $y \in [-1, 1]$. The equatorial plane is located at $y = 0$.

Whereas Boyer-Lindquist coordinates provided a messy form of the Kerr metric and Weyl coordinates did not allow for a straightforward solution at all, the Kerr solution in prolate spheroidal coordinates displays remarkable symmetry. From the solution for ξ given by the Ernst potential, one can determine [48] that for the Kerr metric we have

$$\boxed{\begin{aligned} e^{2U} &= \frac{p^2 x^2 + q^2 y^2 - 1}{(px + 1)^2 + q^2 y^2}, \\ e^{2k} &= \frac{p^2 x^2 + q^2 y^2 - 1}{p^2(x^2 - y^2)}, \\ A &= \frac{2q(1 - y^2)(px + 1)}{p^2 x^2 + q^2 y^2 - 1}. \end{aligned}} \quad (4.18)$$

One then obtains the full Kerr line element by substituting Eq. (4.17) and Eq. (4.18) in Eq. (4.4). Of course, one can also obtain the line element by transforming directly from Boyer-Lindquist coordinates. The transformation between Boyer-Lindquist coordinates and prolate spheroidal coordinates is given by

$$x = \frac{r - 1}{\sigma}, \quad y = \cos \theta, \quad (4.19)$$

where we again point out the unity of the black hole mass [48].

What made Weyl coordinates difficult to work with is precisely the strong point of prolate spheroidal coordinates. The inherent spheroidal symmetry of the Ernst equation causes its solutions to exhibit this symmetry as well, pairing well with the spheroidal symmetry of a rotating black hole. However,

²In literature, one might come across cases where σ is set to 1. This holds only for the static (Schwarzschild) solution and not for a general SAV metric, or even the Kerr solution. Setting $\sigma = p = 1$ directly implies $q = \chi = 0$ for the Kerr solution, transforming it into a Schwarzschild black hole.

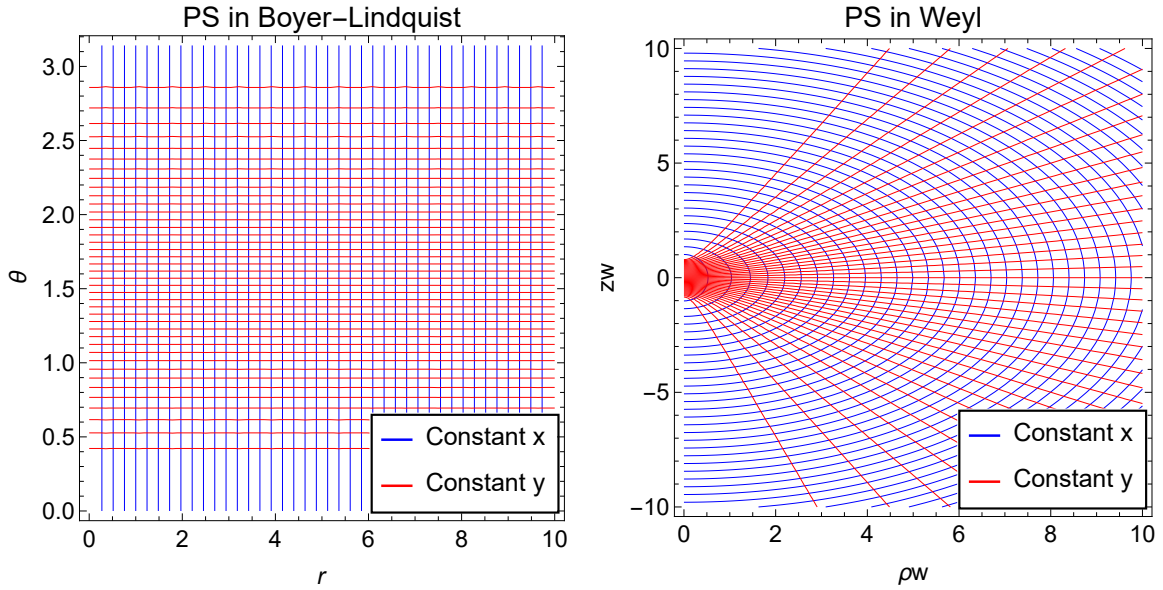


Figure 4.2: Prolate spheroidal coordinates in their relation to other coordinate systems with $\chi = 1/2$. Note how the shared spheroidal nature of Boyer-Lindquist and prolate spheroidal coordinates is visible in the right angles between the contours.

we have not totally lost the advantages of the Weyl formulation either. As can be seen from Eq. (4.17), g_{xx} are g_{yy} not exactly equal, but still very similar up to a factor:

$$\frac{g_{xx}}{x^2 - 1} = \frac{g_{yy}}{1 - y^2}. \quad (4.20)$$

Also, note that prolate spheroidal coordinates provide a more symmetric and slightly more concise form of the Kerr solution than Boyer-Lindquist coordinates. The relations between prolate spheroidal coordinates and the two other coordinate systems are depicted in Fig. 4.2.

We have seen that the Kerr solution is elegantly derived and parameterised using prolate spheroidal coordinates. Nevertheless, most textbooks and scientific works covering the Kerr metric use Boyer-Lindquist coordinates, due to their intuitive interpretation. However, there is another straightforward transformation we can compute to make prolate spheroidal coordinates more intuitive as well.

4.4 Factor structure coordinates

One of the main advantages of prolate spheroidal and Boyer-Lindquist coordinates in our analysis is that orbits will trace out rectangles in the (x, y) space, as will be shown later. It can be desirable to display orbits as compactly as possible in plots, while also retaining this rectangular form of the orbits. One can introduce *factor structure coordinates* as a function of prolate spheroidal coordinates, such that

$$x = \cosh \rho, \quad y = \cos z. \quad (4.21)$$

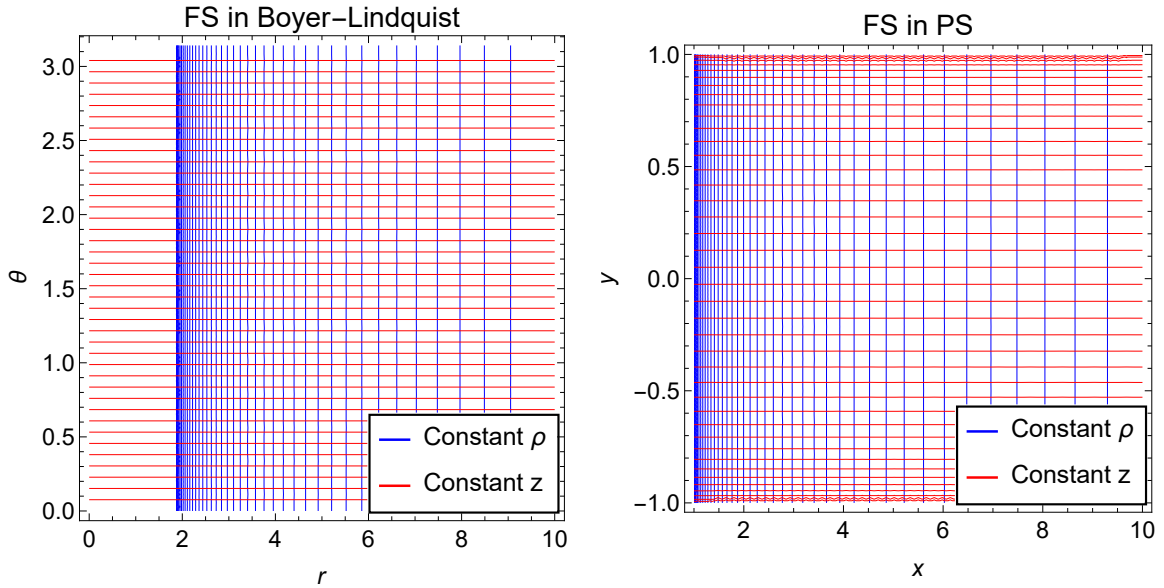


Figure 4.3: Factor structure coordinates in their relation to other coordinate systems with $\chi = 1/2$. The shared spheroidal nature of these coordinate systems is clearly visible, as well as the effect of the event horizon.

By applying this transformation (and the corresponding Hessian matrix), we find that the line element in this formulation can then be found by substituting

$$d\rho_W^2 + dz_W^2 = \sigma^2 \left((\cosh \rho)^2 - (\cos z)^2 \right) \left(\frac{\cosh \rho d\rho^2}{\cosh \rho^2 - 1} - \frac{\cos z dz^2}{1 - \cos z^2} \right), \quad (4.22)$$

in the general line element given in Eq. (4.4), as well as by applying to the $x \rightarrow \cosh \rho$ and $y \rightarrow \cos z$ to the functionals presented in Eq. (4.18).

As can easily be seen from the domain of x and y , the domains of factor structure coordinates are given by $\rho \in [0, \infty)$ and $z \in [0, \pi]$. In particular, we note the equatorial plane on $z = \arccos(0) = \pi/2$. In this form, even highly eccentric orbits can be displayed in a relatively compact plot, while also maintaining the symmetry advantages provided by the prolate spheroidal coordinate system. Furthermore, factor structure coordinates still trace out rectangular orbits in the (ρ, z) plane. The relation between factor structure coordinates and the other spheroidal coordinate systems is depicted in Fig. 4.3.

Nota bene: factor structure coordinates are hence *not* the same as Weyl coordinates, despite (confusingly) also using ρ and z . In this manuscript, we will always refer to Weyl coordinates using (ρ_W, z_W) and to factor structure coordinates using (ρ, z) , following the conventions of Ref. [26] and Ref. [31]. Because of this ambiguity, those wishing to do further reading on parametrisations of the Kerr solution are advised to take extra care regarding conventions, since there exist a great deal of variation in the treatment of this metric in literature.

4.5 The event horizon of a Kerr black hole

One of the most important surfaces of a black hole is the *event horizon*, which is famously the 'point of no return' from beyond which no timelike or lightlike paths exist out of the black hole. We would like to know at what points in our different coordinate systems the event horizon is located.

For the Kerr black hole, the event horizon can be most easily found using Boyer-Lindquist coordinates and considering the point in spacetime where the radial coordinate diverges [1]. This point is found by setting $g^{rr} = 0$, which implies $\Delta = 0$ as can be seen from the line element in Eq. (4.6). This equation is easily solved:

$$\begin{aligned}\Delta &= r^2 - 2r + \chi^2 = 0, \\ \Rightarrow r_{\pm} &= 1 \pm \sqrt{1 - \chi^2}.\end{aligned}\tag{4.23}$$

The fact that two solutions exist, defining a so-called *outer* and *inner* event horizon at r_+ and r_- respectively, are a consequence of the spin of the black hole. The behaviour of the metric between these two horizons and inside the inner horizon is very interesting and an active topic of research [52]. For our analysis, we are only interested in the outer event horizon. We can already see some interesting behaviour of the event horizon of a spinning black hole. For higher values of χ , the outer event horizon *decreases*, theoretically allowing a closer approach to the centre³ of the black hole. On the other hand, setting $\chi = 0$ reduces the metric to the Schwarzschild case and sets $r_+ = 2$, which is indeed the Schwarzschild radius.

Using the coordinate transformations provided, we can compute the Kerr outer event horizon in different coordinate systems. From now on, any reference to the event horizon in this thesis should be interpreted as the outer event horizon, the values of which are given in this table:

Radial coordinate	Outer event horizon
r_+	$1 + \sqrt{1 - \chi^2}$
x_+	1
ρ_+	0
ρ_{W+}	0

Note how the location of the outer event horizon in non-Boyer-Lindquist coordinate systems does not depend on the black hole spin. This convenient feature simplifies analysis of black holes in these coordinate systems and is a result of the nature of the coordinate transformations. In fact, this highlights the biggest difference between Boyer-Lindquist coordinates and the other coordinate systems. Boyer-Lindquist radii are measured *relative to the ring singularity*⁴, whereas the other radii are measured *relative to the event horizon*. This is important to keep in mind when making statements about the 'distance from the event horizon' when working with different coordinate systems.

³This 'centre' is actually a ring, as explained in the next footnote, and this is of course a completely coordinate-dependent statement. This is one of the subtleties of trying to characterise the general behaviour of black holes using specific coordinate systems.

⁴In the Boyer-Lindquist formulation, a curvature singularity exists at $r = 0$. When one embeds Boyer-Lindquist coordinates in Cartesian 3-space, for which the transformation will be provided in Eq. (6.33), one finds that if $\chi \neq 0$, this singularity is *not* located at the origin of the coordinate space. Rather, the singularity forms a ring around the origin, which is why spinning black holes are said to possess a ring singularity. Passing through this ring singularity incidentally allows for all kinds of hypothetical, exotic theories on for instance travelling to supposed mirror universes, for details of which an interested reader is referred to Ref. [1].

Chapter 5

Development of an orbital motion framework

As discussed, our search for chaos is built on keeping track of piercings in the Poincaré maps of orbiting test particles. We will model these test particles through geodesic motion in a modified Kerr spacetime. Here, we will discuss the framework used to compute the equations of motion in this dynamical system, using the parametrisations of SAV metrics from the chapter before. Although our considerations in this chapter strongly depend on the form of the SAV metric in a particular coordinate system, we generally do *not* require the coordinate system to be Kerr specifically, unless stated otherwise. This is because we will apply this framework to both the Kerr metric and modified gravity.

5.1 Conserved quantities in SAV metrics

From Chapter 2, we know that it is possible to write the equations of motion of a dynamical system by using the Hamilton-Jacobi equations. By choosing appropriate coordinates, we can use Poisson brackets to compute the equations of motion of geodesics. Recall that the Hamiltonian of the system is given by

$$\mathcal{H} = \frac{1}{2} g^{\mu\nu} p_\mu p_\nu. \quad (5.1)$$

Assume that we are considering an SAV metric. We can apply several properties of SAV spacetimes to provide a more explicit form of the metric.

When looking at the form of the Hamiltonian, one might assume that this problem is four dimensional. However, application of the conserved quantities of an SAV metric can reduce the number of dimensions we need to solve. Firstly, we know a priori that this system is stationary and axisymmetric. These symmetries imply that the momenta of the system in those coordinates should be conserved. This is something which is in fact straightforwardly verified. Let us again write the timelike and axisymmetric coordinates as t, ϕ respectively. From the Hamilton-Jacobi equations, we know that we can then write the equations of motion for the t and ϕ momenta of the Hamiltonian

as follows. Let us denote the index A as running over just t and ϕ . We can then write

$$\begin{aligned}\dot{p}_A(\tau) &= [p_A, \mathcal{H}] \\ &= \sum_i \left(\frac{\partial p_A}{\partial q_i} \frac{\partial \mathcal{H}}{\partial p_i} - \frac{\partial p_A}{\partial p_i} \frac{\partial \mathcal{H}}{\partial q_i} \right).\end{aligned}\tag{5.2}$$

where τ indicates proper time and the dot indicates derivation with respect to proper time. The left term inside this summation is clearly equal to 0, since $\frac{\partial p_A}{\partial x_i} = 0$. The other term must also equal 0, since from Eq. (4.2) we know that the metric line element (and hence the Hamiltonian) does not depend on t or ϕ in SAV metrics. Thus, we can conclude that indeed

$$\dot{p}_A = 0,\tag{5.3}$$

such that we can define the following conserved quantities:

$$p_t \equiv -E, \quad p_\phi \equiv L_z,\tag{5.4}$$

where the sign of E is a common convention. There is a clear physical meaning behind these conserved quantities. E represents the *total energy* of the test particle. Since we are dealing with stationary metrics, it makes sense that this total energy is conserved over time as is required by conservation of energy in any dynamical system. Furthermore, L_z is the *angular momentum* of the test particle, relative to the central black hole. Indeed, we would expect this quantity to be preserved as well, since the metric also has a symmetry in this direction, combined with our more general intuition of conservation of angular momentum.

Apart from proving the conservation of these quantities, this has also shown us another important aspect of the study of SAV metric geodesics. Due to the symmetries in t and ϕ , we see that the specific values of these coordinates do not give any additional information in our system; they are redundant quantities which do not play a role in determining the dynamics of the system. By proving the conservation of E and L_z , we have reduced the four-dimensional dynamical system to a two-dimensional one. Therefore, we can restrict our studies to analysing the remaining two coordinates of the dynamical system: we will refer to these as the *librational* components¹. These are the components *other* than t and ϕ ; in Weyl coordinates for example, they are ρ_W and z_W . This is the reason why the other parametrisations of SAV metrics generally do not transform t or ϕ . Of course, these coordinates *are* still part of the system. For example, using the Hamilton-Jacobi equations, we can calculate the (nontrivial) equation of motion² corresponding to ϕ . However, it will not give us any additional information about the properties of the dynamical system in question.

The final constraint we can impose on the geodesics of a rotating black hole is that of the *Hamiltonian constant*, which is given by

$$\mathcal{H} = -\frac{1}{2}\mu^2,\tag{5.5}$$

where μ is the rest mass of the particle. This constraint will be employed to construct a quantity which precisely characterises the range of orbits for given values of E and L_z .

One might wonder why we are not considering the Carter constant in this analysis, a known conserved quantity in the Kerr solution. This is because we aim for our treatment of SAV solutions

¹We use the word "librational" because the frequencies in these coordinates are sometimes referred to as librational or libration-like due to their behaviour [20].

²Indeed, just one equation of motion: the other ϕ equation of motion is trivially given by $\dot{p}_\phi = \dot{L}_z = 0$, as we have just shown!

in this chapter to hold for *any* SAV metric in the considered parametrisations, not just the Kerr solution (except for Boyer-Lindquist coordinates). Hence, it is not a given that a quantity like the Carter constant exists for all solutions analysed through an effective potential formalism. In fact, one might recall that the existence of chaotic behaviour in modified Kerr metrics depends precisely on the *absence* of a fourth conserved quantity like the Carter constant. Thus, we will for now ignore the existence of the Carter constant and come back to its conservation in Chapter 6.

5.2 Defining an effective potential

Using the conservation of the Hamiltonian constant, it is possible to compute a quantity which expresses one of the librational momenta in terms of the other. To this end, we will construct an *effective potential*. This is a convenient method of implementing this boundary condition in the dynamical system and has will also prove itself useful for the characterisation of an orbit's properties, as will become evident shortly.

In a Newtonian context, the effective potential is the result of considering all forces in a dynamical system and relates directly to the equations of motion of a particle [1]. For dynamical systems in general relativity, the derivation of such a quantity is more subtle. Note that there exist many different forms of the effective potential, depending on definitions and conventions as chosen by different authors. However, these conventions naturally do not affect the actual dynamics of the system [25]. We will follow a definition similar to the one used in Ref. [26].

The effective potential is a very important tool in characterising the motion of our system and will be employed to test for and validate the physical meaning of orbits for a given value of E and L_z . The effective potential is, much like the equations of motion, a *coordinate dependent* quantity, depending on the chosen parametrisation of the metric. We will now define our effective potential in several coordinate systems and see how they relate to the equations of motion of the system.

5.2.1 Weyl coordinates

Weyl coordinates allow for a straightforward definition of an effective potential [26]. Let us write the Hamiltonian as

$$\mathcal{H} = \frac{1}{2}g^{\mu\nu}p_\mu p_\nu = \frac{1}{2}(g^{AB}p_{APB} + g^{CD}p_{CPD}), \quad (5.6)$$

where $A, B \in t, \phi$ and $C, D \in \rho_W, z_W$. We can separate the Hamiltonian like this due to the form of SAV metrics in this coordinate system: we always have $g_{AC} = g_{CA} = 0$, as seen in Eq. (4.4). Applying the Hamiltonian constant then yields

$$-\frac{1}{2}\mu^2 = \frac{1}{2}(g^{AB}p_{APB} + g^{CD}p_{CPD}), \quad (5.7)$$

which can be rearranged as

$$-\mu^2 - (g^{AB}p_{APB}) = g^{CD}p_{CPD}. \quad (5.8)$$

Let us now explicitly write out the components. We find:

$$\begin{aligned} -\mu^2 - (g^{tt}p_t^2 + g^{t\phi}p_t p_\phi + g^{\phi t}p_\phi p_t + g^{\phi\phi}p_\phi^2) &= -\mu^2 - (g^{tt}E^2 - g^{t\phi}EL_z - g^{\phi t}L_z E + g^{\phi\phi}L_z^2) \\ &= g^{\rho_W\rho_W}p_{\rho_W}^2 + g^{z_W z_W}p_{z_W}^2, \end{aligned} \quad (5.9)$$

which can be recast using $g^{t\phi} = g^{\phi t}$ as

$$-\mu^2 - (g^{tt}E^2 - 2g^{t\phi}EL_z + g^{\phi\phi}L_z^2) = g^{\rho_W\rho_W}p_{\rho_W}^2 + g^{z_W z_W}p_{z_W}^2. \quad (5.10)$$

Here is where the greatest advantage of Weyl coordinates can be applied. Define

$$\begin{aligned}
 G &\equiv -(g^{tt}E^2 - 2g^{t\phi}EL_z + g^{\phi\phi}L_z^2) \\
 &= -g^{AB}p_A p_B, \\
 \frac{1}{V_W} &\equiv g^{\rho_W\rho_W} = g^{z_W z_W}.
 \end{aligned} \tag{5.11}$$

Note that since there are no cross terms present between the ρ_W and z_W components of the metric tensor, we immediately have $V_W = g_{\rho_W\rho_W} = g_{z_W z_W}$. Using these definitions, we can rewrite Eq. (5.10) and define the effective potential J_W as

$$p_{\rho_W}^2 + p_{z_W}^2 = V_W(G - 1) \equiv J_W(\rho_W, z_W, E, L_z), \tag{5.12}$$

where we set $\mu = 1$. J_W has several important properties, which we will now discuss.

Simplicity of the equations of motion

By using the definitions of G and V_W , we can write the *reduced Hamiltonian* $H(\rho_W, z_W, p_{\rho_W}, p_{z_W})$ from Eq. (5.6) as

$$\begin{aligned}
 H &= \frac{1}{2}g^{\mu\nu}p_\mu p_\nu \\
 &= \frac{1}{2}(-G + g^{\rho_W\rho_W}p_{\rho_W}^2 + g^{z_W z_W}p_{z_W}^2) \\
 &= \frac{1}{2}\left(-G + \frac{1}{V_W}(p_{\rho_W}^2 + p_{z_W}^2)\right).
 \end{aligned} \tag{5.13}$$

The reduced Hamiltonian is equal to the original Hamiltonian, except that we explicitly require that p_t and p_ϕ have been fixed such that the function depends purely on the librational components and momenta. The reduced equations of motion then become

$$\dot{q}_C = [q_C, H], \quad \dot{p}_C = [p_C, H], \tag{5.14}$$

which when evaluated give the following lovely expressions [26]:

$$\begin{aligned}
 \dot{\rho}_W &= [\rho_W, H] \\
 &= \frac{\partial \rho_W}{\partial \rho_W} \frac{\partial H}{\partial p_{\rho_W}} - \cancel{\frac{\partial \rho_W}{\partial p_{\rho_W}} \frac{\partial H}{\partial \rho_W}} + \cancel{\frac{\partial \rho_W}{\partial z_W} \frac{\partial H}{\partial p_{z_W}}} - \cancel{\frac{\partial \rho_W}{\partial p_{z_W}} \frac{\partial H}{\partial z_W}} \\
 &= \frac{p_{\rho_W}}{V_W},
 \end{aligned} \tag{5.15}$$

$$\begin{aligned}
 \dot{p}_{\rho_W} &= [p_{\rho_W}, H] \\
 &= \cancel{\frac{\partial p_{\rho_W}}{\partial \rho_W} \frac{\partial H}{\partial p_{\rho_W}}} - \frac{\partial p_{\rho_W}}{\partial p_{\rho_W}} \frac{\partial H}{\partial \rho_W} + \cancel{\frac{\partial p_{\rho_W}}{\partial z_W} \frac{\partial H}{\partial p_{z_W}}} - \cancel{\frac{\partial p_{\rho_W}}{\partial p_{z_W}} \frac{\partial H}{\partial z_W}} \\
 &= \frac{1}{2V_W} \frac{\partial J_W}{\partial \rho_W}.
 \end{aligned} \tag{5.16}$$

One similarly finds

$$\begin{aligned}\dot{z}_W &= \frac{p_{z_W}}{V_W}, \\ \dot{p}_{z_W} &= \frac{1}{2V_W} \frac{\partial J_W}{\partial z_W}.\end{aligned}\tag{5.17}$$

These equations of motion are not just easy to write down; they can be read off straight from the line element itself by using the definitions of J_W and V_W . Clearly, this is a desirable property when working with these dynamical systems. However, this property is unfortunately of limited use to us. This is because we do not have the Kerr line element as expressed in Weyl coordinates, because this coordinate system is not suited to this problem. Altogether, this exercise demonstrates the earlier assertion that Weyl coordinates are very useful for computing field equations.

Constraint on the librational momenta

The effective potential is used to translate the Hamiltonian constraint to a constraint on the librational momenta (p_{ρ_W}, p_{z_W}) of the system. In fact, J_W proves that the initial conditions $p_{\rho_W}(0)$ and $p_{z_W}(0)$ are not independent, since we can write

$$p_{z_W}(0) = \sqrt{J_W(\rho_W(0), z_W(0), E, L_z) - p_{\rho_W}^2(0)}.\tag{5.18}$$

Hence, setting the initial conditions for ρ_W , z_W and one of the librational momenta automatically determines the initial condition of the remaining librational momentum.

Analysing the range of orbital motion

Due to the fact that J_W is a sum of squares, we see that any physical solution must have $J_W \geq 0$. Hence, J_W provides a means of analysing the full parameter space of geodesics for a given E, L_z , without having to solve the equations of motion for all possible orbits. The area where $J_W \geq 0$ is called the *physical region* or *allowed region* of the physical space. We also note that $J_W = 0$ implies $p_{\rho_W} = p_{z_W} = 0$. For this reason, the border of the physical region where $J_W = 0$ is called the *curve of zero velocity* [25]. As we will show later, we can infer several important characteristics of the orbit from this property, including for example the boundedness, maximum allowed eccentricity and closest allowed approach of different classes of geodesics.

5.2.2 Prolate spheroidal coordinates

Weyl coordinates provide a convenient framework to compute equations of motion; however, we cannot use this form of those equations, because we cannot rephrase the Kerr black hole in this coordinate system. However, we *can* try to formulate an effective potential J_{PS} in a similar fashion to J_W and recreate as many of its useful properties as we can in this spheroidal coordinate system.

Let us again start from the Hamiltonian of an SAV metric. This time, it is given by

$$\mathcal{H} = \frac{1}{2} g^{\mu\nu} p_\mu p_\nu = \frac{1}{2} (g^{AB} p_{APB} + g^{EF} p_{EPF}),\tag{5.19}$$

where $E, F \in x, y$. Because the transformation from Weyl to prolate spheroidal coordinates does not affect t or ϕ , this separation of the Hamiltonian is again allowed. Now we will similarly to the Weyl case apply the Hamiltonian constant to obtain

$$-\mu^2 - (g^{AB} p_{APB}) = g^{EF} p_{EPF}.\tag{5.20}$$

Writing out the metric components and using $g_{xy} = g_{yx} = 0$ then gives

$$-\mu^2 - (g^{tt}E^2 - 2g^{t\phi}EL_z + g^{\phi\phi}L_z^2) = g^{xx}p_x^2 + g^{yy}p_y^2. \quad (5.21)$$

One notices that the left hand side of Eq. (5.21) is exactly the same as in the Weyl case. This makes sense: we have not transformed t or ϕ . The same quantity $G = -g^{AB}p_Ap_B$ has appeared in the reformulation of the Hamiltonian. We see that the quantity G is *independent of the chosen SAV parametrisation* and maintains its structure as displayed in the LHS of Eq. (5.21), under the condition that t and ϕ are not transformed in such a way that cross terms with the librational components of the metric tensor appear. Since all physical information of these systems is encoded in the librational components however, most coordinate transformations employed in the study of EMRIs seem to satisfy this condition already. In this thesis, this is the case for all but one transformation: in Chapter 6, we will use an embedding of Boyer-Lindquist in Cartesian coordinates for visualisation purposes. Since this transformation couples ϕ to the (formerly) librational coordinates, this coordinate system is an example of a system not well suited to this kind of analysis.

Upon setting $\mu = 1$ we can rewrite the expression as

$$G - 1 = g^{xx}p_x^2 + g^{yy}p_y^2. \quad (5.22)$$

Of course, Eq. (5.22) and Eq. (5.10) are equivalent, due to the invariance of the left hand side of Eq. (5.10). This can also be shown by explicitly transforming Eq. (5.10) to prolate spheroidal coordinates. Recall that we had $C, D \in \rho_W, z_W$. Since g^{CD} transforms as contravariant 2-tensor and p_C, p_D as vectors, we can write

$$g^{CD} = \left(\frac{\partial q^C}{\partial q^E} \right) \left(\frac{\partial q^D}{\partial q^F} \right) g^{EF}, \quad (5.23)$$

and

$$p_C = \frac{\partial q^E}{\partial q^C} p_E, \quad (5.24)$$

using which we can write

$$\begin{aligned} g^{z_W z_W} p_{z_W}^2 + g^{\rho_W \rho_W} p_{\rho_W}^2 &= g^{CD} p_C p_D \\ &= \left(\frac{\partial q^C}{\partial q^E} \frac{\partial q^D}{\partial q^F} g^{EF} \right) \left(\frac{\partial q^{E'}}{\partial q^C} p_{E'} \right) \left(\frac{\partial q^{F'}}{\partial q^D} p_{F'} \right) \\ &= g^{EF} \underbrace{\frac{\partial q^{E'}}{\partial q^E} p_{E'}}_{\delta_E^{E'}} \underbrace{\frac{\partial q^{F'}}{\partial q^F} p_{F'}}_{\delta_F^{F'}} \\ &= g^{EF} p_E p_F, \end{aligned} \quad (5.25)$$

where primes were used to distinguish repeated indices. Writing out the last expression like in Eq. (5.21) we then obtain

$$g^{z_W z_W} p_{z_W}^2 + g^{\rho_W \rho_W} p_{\rho_W}^2 = g^{xx}p_x^2 + g^{yy}p_y^2, \quad (5.26)$$

which shows the consistency between the derivations.

In the Weyl case, we were able to find the common prefactor in the momenta p_{ρ_W} and p_{z_W} and

move it to the other side of the equation, because we had $g^{\rho_W \rho_W} = g^{z_W z_W}$. This time, we are not so lucky. Because $g^{xx} \neq g^{yy}$, it is not possible to isolate a prefactor such that only a square of momenta remains on the right hand side of the equation. However, we have a different symmetry which we can exploit. Recall that in prolate spheroidal coordinates we have

$$\frac{g_{xx}}{x^2 - 1} = \frac{g_{yy}}{1 - y^2}. \quad (5.27)$$

By defining

$$V_{PS} \equiv g_{xx} \cdot (x^2 - 1) = g_{yy} \cdot (1 - y^2), \quad (5.28)$$

we can write Eq. (5.22) as

$$G - 1 = \frac{1}{V_{PS}} \left(\frac{p_x^2}{x^2 - 1} + \frac{p_y^2}{1 - y^2} \right) \quad (5.29)$$

where, in a similar fashion to the Weyl case, we used $g_{xy} = g_{yx} = 0$ and $g_{AE} = g_{EA} = 0$ to write $g_{xx} \cdot g^{xx} = g_{yy} \cdot g^{yy} = 1$. We can now finally define the prolate spheroidal version of the effective potential as

$$J_{PS} \equiv V_{PS}(G - 1) = \frac{p_x^2}{x^2 - 1} + \frac{p_y^2}{1 - y^2}. \quad (5.30)$$

Of course, this quantity is inherently different from its counterpart in Weyl coordinates. It is tempting to take the equations of motion in Weyl coordinates and replace V_W with V_{PS} ; however, this will get you into trouble, because V_W is defined specifically in that coordinate system.

This actually brings us to an important consideration in the theoretical framework behind the analyses. The just-performed computations require highly specific and coordinate-dependent definitions and this creates room for a potential (typographical) errors to slip into the computations. Indeed, during the development of this framework, it has become evident that some small errors in the equations of motion can pass under the radar, because they produce solutions which *look* right at first and only turn out to be incorrect when compared to independent but equivalent formulations of geodesics in the Kerr solution. In order to catch such a mistake before it propagates throughout the analyses in this thesis, we will always derive the equations of motion of the system from the Hamiltonian *directly* via the Hamilton-Jacobi equations, rather than as a derived set of equations constructed from the effective potential. Although the latter option can be easier to implement, our method has the advantages of reducing its dependence on the specific definition of the effective potential by finding the equations of motion directly from the line element, as well as providing an additional sanity check on the framework. Furthermore, if one would like to use another form of the effective potential, it should still be compatible with the equations of motion as derived from the Hamiltonian directly, since no definition should ever change the underlying physical processes.

Because our effective potential is defined by dividing the momenta by particular quantities, we should check where our potential is well defined in the domain of x and y . Recall that the domains of these variables in this coordinate system are $x \in [1, \infty)$ and $y \in [-1, 1]$. From this, we draw two important conclusions:

- The effective potential J_{PS} is well defined in the *open* ranges of $x \in (1, \infty)$ and $y \in (-1, 1)$.
- Within these ranges, we note that $\frac{1}{x^2 - 1}$ and $\frac{1}{1 - y^2}$ are both greater than zero.

Let us now summarise the properties of J_{PS} which we will use in the orbital analysis, similarly to the J_W case.

Constraint on the librational momenta

We can reformulate Eq. (5.30), which much like in the Weyl case is in essence just a reformulation of the Hamiltonian constraint, to prove the interdependence of the initial conditions of the librational momenta. Rewriting Eq. (5.30) gives for instance

$$p_y(0) = \sqrt{1 - y^2(0)} \cdot \sqrt{J_{PS}(x(0), y(0), E, L_z) - \frac{p_x^2(0)}{x^2(0) - 1}}, \quad (5.31)$$

which shows that setting the initial librational components and one of the momenta automatically fixes the other initial librational momentum. Note that setting the initial y and p_x value to 0 in Eq. (5.31), which is equivalent to letting orbits start in the equatorial plane with initial momentum out of this plane, happens to yield the same relation between $p_y(0)$ and J_{PS} as one would find between $p_{z_W}(0)$ and J_W by filling in Eq. (5.18). However, this is only true for this special case of the initial conditions and underlines how subtle the differences between effective potential definitions are when converting to and from different coordinate systems.

Analysing the range of orbital motion

Similarly to J_W , J_{PS} provides a bound on the range of allowed orbits in (x, y) space. Because $\frac{1}{x^2-1}$ and $\frac{1}{1-y^2}$ are positive, we see that J_{PS} must always be a non-negative quantity for physically allowed orbits. Therefore, a region plot of $J_{PS} \geq 0$ illustrates the range of orbits for a given set of E, L_z . Furthermore, we again note that $J_{PS} = 0 \iff p_x = p_y = 0$, such that $J_{PS} = 0$ denotes the curve of zero velocity. Hence, we can use J_{PS} much like we would use J_W when it comes to characterising the allowed region of geodesics around black holes.

We have shown that the quantity J_{PS} as defined above is a useful quantity in analysing geodesics in SAV metrics, despite the fact that it does not reproduce the field equations as beautifully as J_W would. Note that these calculations hold for any SAV metric in prolate spheroidal coordinates, not just the Kerr solution. In the next chapter, we will apply our findings to the Kerr solution to obtain an explicit form of J_{PS} . First however, we will see whether it is feasible to define an effective potential in Boyer-Lindquist coordinates as well, since much of the literature on the Kerr solution employs this form of the metric.

5.2.3 Boyer-Lindquist coordinates

In order to derive an effective-potential-like quantity J_{BL} in Boyer-Lindquist coordinates, we will again start from the Hamiltonian in an SAV metric, which now looks like

$$\mathcal{H} = \frac{1}{2} g^{\mu\nu} p_\mu p_\nu = \frac{1}{2} (g^{AB} p_A p_B + g^{GH} p_G p_H), \quad (5.32)$$

where $G, H \in r, \theta$. The Boyer-Lindquist form of the metric also has the properties $g_{AG} = 0$ and $g_{r\theta} = 0$, such that this separation of the Hamiltonian is allowed. Performing the same decomposition of the Hamiltonian constant as before, we this time arrive at

$$-\mu^2 - (g^{AB} p_A p_B) = g^{GH} p_G p_H, \quad (5.33)$$

which, using the invariance of G and setting $\mu = 1$, becomes

$$\begin{aligned} G - 1 &= g^{GH} p_G p_H \\ &= g^{rr} p_r^2 + g^{\theta\theta} p_\theta^2. \end{aligned} \quad (5.34)$$

This time, we will employ the symmetry between g_{rr} and $g_{\theta\theta}$ derived from the Kerr line element³ Eq. (4.6), which is

$$\frac{g_{\theta\theta}}{\Delta} = g_{rr}, \quad (5.35)$$

where we recall that $\Delta = r^2 - 2r + \chi^2$. We can thus define

$$\boxed{V_{BL} \equiv g_{rr} \cdot \Delta = g_{\theta\theta}}, \quad (5.36)$$

such that, using $g_{rr}g^{rr} = g_{\theta\theta}g^{\theta\theta} = 1 \Rightarrow 1/V_{BL} = g^{\theta\theta} = g^{rr}/\Delta$, we find

$$G - 1 = \frac{1}{V_{BL}} (\Delta \cdot p_r^2 + p_\theta^2), \quad (5.37)$$

from which we define an effective potential J_{BL} as

$$\boxed{J_{BL} \equiv V_{BL}(G - 1) = \Delta \cdot p_r^2 + p_\theta^2}. \quad (5.38)$$

Let us take a moment to consider for what range of r, θ this definition is well defined. Since we divide by Δ , we need $\Delta \neq 0$. Note, however, that $\Delta = 0$ is precisely the condition which determines the radius of the event horizon in Boyer-Lindquist coordinates. Combined with the knowledge that the Kerr solution is not relevant to our analysis inside the event horizon, we can safely state that this definition is well defined for all r outside the event horizon.

Much like for J_{PS} , there is no simple way to read off the equations of motion from the line element for J_{BL} . However, we still maintain the following properties:

Constraint on the librational momenta

Through a similar treatment as with J_W and J_{PS} , one can show using Eq. (5.38) that

$$p_\theta(0) = \sqrt{J_{PS}(r(0), \theta(0), E, L_z) - p_r^2(0) \cdot \Delta(0)}. \quad (5.39)$$

J_{BL} hence provides a similar solution to the initial momenta problem as J_W and J_{PS} .

Analysing the range of orbital motion

Since $\Delta > 0$ outside the event horizon, we can again conclude that J_{BL} is a strictly non-negative quantity. Hence, it also provides a bound on physical orbits in (r, θ) space. Furthermore, since $J_{BL} = 0 \iff p_r = p_\theta = 0$, the contour $J_{BL} = 0$ also denotes the curve of zero velocity.

Since we have been able to construct a quantity with similar properties to J_{PS} , it is certainly possible to perform our analysis in this coordinate system. Indeed, working in Boyer-Lindquist coordinates directly has the advantage of making the analysis directly compatible with black hole solutions given in these coordinates, without requiring a coordinate transformation. However, we should also discuss some of the downsides of this formulation. Firstly, unlike the prolate spheroidal and Weyl case, this derivation depends on using the Kerr solution specifically, rather than a general SAV solution. Fundamentally, this dependence on the Kerr solution specifically is encoded in Eq. (5.35), since the functional Δ is inherently a Kerr-specific quantity. In the prolate spheroidal

³One might notice that, unlike in the Weyl and prolate spheroidal case, we now *are* performing this calculation specifically for the Kerr metric, rather than general SAV metrics. We touch upon this at the end of this section.

case however, as encoded in Eq. (5.27), the proportionality factors are just a result of the coordinate system; the actual solution is encoded in the functionals listed in Eq. (4.18), of which Eq. (5.27) is independent. Hence, our definitions in the prolate spheroidal case are stronger than in Boyer-Lindquist coordinates, which were derived specifically to denote just the Kerr solution [52]. Furthermore, the symmetric form of solutions in prolate spheroidal coordinates and its derivative coordinate system, factor structure coordinates, compactifies the expressions of some of the equations of motion and makes it easier to analyse some properties of these geodesics. Nevertheless, they are both useful tools in understanding the Kerr solution and its modifications and of course yield the same orbital dynamics around black holes. However, as was also pointed out throughout Chapter 4, it is important to pick the right tool for the job when performing a coordinate-dependent analysis.

Chapter 6

The Kerr solution

Now that we have a framework to calculate and analyse geodesic motion in, it is time that we apply it to black hole solutions. Before we investigate a modified gravity theorem, it is important that we build a good understanding of the Kerr solution. This is because we expect the effects of any modifications to gravity to be very small. Hence, we will not just compute orbits in modified gravity, but also compare them to their counterparts in the Kerr solution. This will put our earlier derived framework to the test and grant us more insight into the effect of employing different coordinate systems.

6.1 Conservation of the Carter constant

The integrability of the Kerr metric is due to the conservation of the Carter constant, which was first formulated in 1968 by Brandon Carter [53], in addition to the conserved quantities of energy, angular momentum and Hamilton's constant. Here, we will provide an outline on how this quantity is constructed and why it is conserved.

A priori, it is not at all obvious that the Kerr metric has another constant of motion. After all, the 'low-hanging fruit' in the form of the Killing vectors is already encoded in E and L_z . However, by considering the separability of the Kerr metric in Boyer-Lindquist coordinates, Carter found a fourth constant of motion, which we will now introduce.

In order to construct the Carter constant, we will follow the method as outlined in Ref. [1] and Ref. [2]. First, it is instructive to introduce *Killing tensors*. A Killing tensor is the generalisation a Killing vector. We define a rank n Killing tensor $K_{\mu_1 \dots \mu_n}$ as a symmetric tensor satisfying

$$\nabla_{(\lambda} K_{\mu_1 \dots \mu_n)} = 0, \tag{6.1}$$

where λ is an affine parameter. If one can show that a tensor exists which satisfies this condition in some spacetime, that tensor corresponds to a conserved quantity in that spacetime. In fact, Killing vectors are just rank 1 Killing tensors.

Let us now employ Boyer-Lindquist coordinates and use its representation of the Kerr line element as given in Eq. (4.6). One can then define the rank 2 tensor $\sigma_{\mu\nu}$ as

$$\sigma_{\mu\nu} \equiv 2\Sigma l_{(\mu} n_{\nu)} + r^2 g_{\mu\nu}, \tag{6.2}$$

where we recall from Eq. (4.6) that $\Sigma = r^2 + \chi^2 \cos^2 \theta$. Here we have introduced the vectors l_μ and n_μ , which are given by

$$\begin{aligned} l^\mu &\equiv \left(\frac{r^2 + \chi^2}{\Delta}, 1, 0, \frac{\chi}{\Delta} \right), \\ n^\mu &\equiv \frac{1}{2} \left(\frac{r^2 + \chi^2}{\Sigma}, -\frac{\Delta}{\Sigma}, 0, \frac{\chi}{\Sigma} \right), \end{aligned} \quad (6.3)$$

where Δ was also defined in Eq. (4.6) as $\Delta = r^2 - 2r + \chi^2$. When performing calculations with these vectors, one should keep in mind the raised index in this definition. l_μ and n_μ are *principal null vectors*, which means that they satisfy the relations

$$l^\mu l_\mu = n^\mu n_\mu = 0, \quad l^\mu n_\mu = -1, \quad (6.4)$$

which can be verified from their definitions and the form of $g_{\mu\nu}$ in Eq. (4.6). By substituting $\sigma_{\mu\nu}$ in Eq. (6.1), we can verify that it is in fact conserved. One can write

$$\nabla_{(\lambda} \sigma_{\mu\nu)} = \frac{1}{6} \left(\nabla_\lambda \sigma_{\mu\nu} + \nabla_\mu \sigma_{\nu\lambda} + \nabla_\nu \sigma_{\lambda\mu} + \nabla_\lambda \sigma_{\nu\mu} + \nabla_\mu \sigma_{\lambda\nu} + \nabla_\nu \sigma_{\mu\lambda} \right). \quad (6.5)$$

Now we could confirm that each of the 16 components of this tensor reduces to zero. If one wishes to do the full calculation, using a symbolic programming language is advisable, since the covariant derivatives cause this calculation to quickly get out of hand. The conclusion of this calculation, however, is that $\sigma_{\mu\nu}$ is indeed a Killing tensor. With this information and by applying the conservation of energy and angular momentum, one can construct a conserved scalar by contracting $\sigma^{\mu\nu}$ with two four-velocities u_μ to obtain [2][53][54]

$$C \equiv \sigma^{\mu\nu} u_\mu u_\nu = \left(\chi^2 (1 - E^2) + \frac{L_z^2}{\sin^2 \theta} \right) \cos^2 \theta + p_\theta^2, \quad (6.6)$$

which is the Carter constant in Boyer-Lindquist coordinates. Since functions consisting of just conserved quantities are still conserved, an alternative version is often defined as [2]

$$Q = C + (L_z - \chi E)^2. \quad (6.7)$$

Q has the advantage of always being non-negative¹, which can be desirable in some applications. This quantity is also often referred to as "the" or "a" Carter constant.

Whereas energy and angular momentum have a clear physical interpretation, it is much less obvious what the Carter constant "is" exactly. Indeed, the extent to which it is non-obvious has led to it being referred to as a "hidden symmetry" in the Kerr spacetime. Mathematically, it is clear what it means; it is the conserved quantity related to the hidden symmetry $\sigma_{\mu\nu}$. If one insists on finding a physical analogue, there exist reformulations of the Carter constant which relate it to (among other things) the total angular momentum of the system (not just L_z) [55] and as well as the Newtonian analogue of a particle travelling through a non-relativistic dipole potential [56].

Carter himself found this conserved quantity by studying the separability of the Kerr Hamiltonian in Boyer-Lindquist coordinates. This underlines how some problems are best solved in a coordinate-dependent fashion, where one has to make a careful choice between the different parametrisations

¹It is only zero when $\mu = 0$, i.e. when the test particle is massless [2].

available for SAV metrics. For our purposes, it is important to realise how subtle this conserved quantity was to find and that therefore it is not an easy task to determine whether modified gravities definitively do or do not possess a similar conserved quantity using an analytical approach. This is part of the reason why indirect investigations into integrability like the one in this thesis are necessary to provide indications on whether other theorems possess a fourth constant of motion.

6.2 Calculation of some curvature invariants

In order to quantify specific aspects of a spacetime, it is useful to compute some invariant quantities from the line element. There are many different quantities which one can construct and compute in the study of black hole spacetimes. One common example is the Ricci scalar. In the case of the Kerr metric, we have $R = 0$. This can be verified using a symbolic programming language, which is also how we will compute the other invariants in this section. In fact, the Kerr metric also is "Ricci flat": $R_{\mu\nu} = 0$. This is required for it to be a solution to the vacuum Einstein field equations [52].

Since R is invariant, one sanity check on any proposed parametrisation of Kerr is that one should have $R = 0$, regardless of the parametrisation. However, the implication does not hold the other way; not every $R = 0$ solution is actually the Kerr solution. Indeed, small typos in the metric tensor could still result in a spacetime where $R = 0$, despite not representing the Kerr solution accurately. In light of this, another useful quantity to consider is the *Kretschmann scalar*. It is computed from the Riemann tensor via

$$\mathcal{K} = R_{\mu\nu\rho\sigma}R^{\mu\nu\rho\sigma}. \quad (6.8)$$

In Kerr spacetime expressed in Boyer-Lindquist coordinates, the Kretschmann scalar is given by

$$\mathcal{K} = -\frac{48(\chi^6 \cos^6(\theta) - r^6 + 15r^4\chi^2 \cos^2(\theta) - 15r^2\chi^4 \cos^4(\theta))}{(\chi^2 \cos^2(\theta) + r^2)^6}. \quad (6.9)$$

Another invariant we can compute is based on the *Weyl tensor*, which is computed from the Riemann tensor by removing its contractions [1]. In four dimensions, it is given by

$$C_{\rho\sigma\mu\nu} = R_{\rho\sigma\mu\nu} + \frac{1}{3}g_{\rho[\mu}g_{\nu]\sigma}R - g_{\rho[\mu}R_{\nu]\sigma} + g_{\sigma[\mu}R_{\nu]\rho}. \quad (6.10)$$

More invariants can be used to check whether a line element truly parametrises a black hole spacetime. For instance, the contraction of the Weyl tensor with itself is another invariant which can be used to characterise a spacetime in (numerical) investigations of modified gravity [57]. The Weyl tensor contraction is in four dimensions related to the Kretschmann invariant via

$$\mathcal{K} = C_{\rho\sigma\mu\nu}C^{\rho\sigma\mu\nu} + 2R_{\mu\nu}R^{\mu\nu} - \frac{1}{3}R^2. \quad (6.11)$$

In the Kerr case, the contraction of the Weyl tensor with itself takes the form

$$C_{\rho\sigma\mu\nu}C^{\rho\sigma\mu\nu} = -\frac{48(\chi^6 \cos^6(\theta) - r^6 + 15r^4\chi^2 \cos^2(\theta) - 15r^2\chi^4 \cos^4(\theta))}{(\chi^2 \cos^2(\theta) + r^2)^6}. \quad (6.12)$$

Note that this expression is exactly the same as what we found for the Kretschmann invariant. This is no surprise: since in the Kerr case we have $R = 0$ and $R_{\mu\nu} = 0$, Eq. (6.10) reduces to

$$C_{\rho\sigma\mu\nu} = R_{\rho\sigma\mu\nu}, \quad (6.13)$$

such that

$$\mathcal{K} = C_{\rho\sigma\mu\nu}C^{\rho\sigma\mu\nu}. \quad (6.14)$$

This relation may no longer hold in modified gravity theories and can be used as a sanity check on parametrisations of the Kerr solution. The invariants discussed are easily converted to other coordinate systems; since they are scalars, one can directly apply the transformation rules as outlined in Chapter 4 without need for a Hessian.

6.3 Innermost stable circular orbits

In the study of orbital motion around black holes, one can characterise the closest allowed *circular* orbits around a black hole. A thorough analysis of these orbits was performed by Bardeen and Teutolsky [58]. The radii corresponding to these *innermost stable circular orbits* (ISCOs) are of great importance in understanding the orbital dynamics of a given spacetime. By using a potential formalism, one can define three such radii, which we will introduce here.

Let us employ Boyer-Lindquist coordinates for the following. By considering the smallest possible value of r at which a photon is able to orbit, one can find the innermost boundary for any circular orbit around a black hole. This radius describes the so-called *photon sphere* and is given by

$$r_{ph} = 2 + 2 \cos \left(\frac{2}{3} \cos^{-1}(\mp\chi) \right). \quad (6.15)$$

The upper sign corresponds to a *prograde* orbit (in the same direction as the black hole spin) and the lower sign to a *retrograde* orbit (against the black hole spin). For example, for a Schwarzschild black hole, we have $r_{ph} = 3$, since the spherical symmetry does not distinguish between prograde and retrograde orbits.

Although circular orbits are hence possible if $r > r_{ph}$, these orbits are not necessarily bound orbits. The innermost radius where a bound circular orbit can exist for a massive particle is called the radius of *marginally bound* orbits and is given by

$$r_{mb} = 2 \mp \chi + 2\sqrt{1 \mp \chi}. \quad (6.16)$$

It turns out that even these bound orbits are not necessarily stable. The smallest radius at which stable and bound circular orbits can exist defines the true innermost stable circular orbit and is given by

$$r_{ms} = 3 + Z_2 \mp \sqrt{(3 - Z_1)(3 + Z_1 + 2Z_2)}, \quad (6.17)$$

where

$$\begin{aligned} Z_1 &= 1 + (1 - \chi^2)^{1/3} \left[(1 + \chi)^{1/3} + (1 - \chi)^{1/3} \right], \\ Z_2 &= \sqrt{3\chi^2 + Z_1^2}. \end{aligned}$$

These radii correspond to equatorial, circular orbits, which we will not use in our analysis. However, we will use these radii to gain further intuition on the orbits we find in Kerr spacetime, in particular when we compute the three-dimensional representations of these orbits.

6.4 The Kerr effective potential

Using the definitions in Chapter 4 and 5, we are able to construct and analyse the effective potential of the Kerr black hole in several coordinate systems. Recall that the effective potential gives us information on the allowed region of orbits as well as other important orbital information and is crucial in the study of orbital motion in Kerr spacetime and beyond.

6.4.1 Computing J_{BL} and J_{PS}

We have defined an effective potential for three coordinate systems, two of which allow parametrisation the Kerr solution: prolate spheroidal and Boyer-Lindquist coordinates. In order to calculate the full form of these potentials, it is instructive to first calculate the inverses of the line elements of the Kerr solution in both coordinate systems. Let us start with the Boyer-Lindquist case, since this form of the metric is most often encountered in other literature.

Computing J_{BL}

From Eq. (4.6), we see that the Kerr metric tensor in Boyer-Lindquist coordinates can be written in matrix form as

$$g_{\mu\nu, BL} = \begin{pmatrix} \frac{2r}{\chi^2 \cos^2(\theta) + r^2} - 1 & 0 & 0 & -\frac{2r\chi \sin^2(\theta)}{\chi^2 \cos^2(\theta) + r^2} \\ 0 & \frac{\chi^2 \cos^2(\theta) + r^2}{r^2 - 2r + \chi^2} & 0 & 0 \\ 0 & 0 & \chi^2 \cos^2(\theta) + r^2 & 0 \\ -\frac{2r\chi \sin^2(\theta)}{\chi^2 \cos^2(\theta) + r^2} & 0 & 0 & \frac{\sin^2(\theta) \left((r^2 + \chi^2)^2 - \chi^2 \sin^2(\theta) (r^2 - 2r + \chi^2) \right)}{\chi^2 \cos^2(\theta) + r^2} \end{pmatrix},$$

which can be inverted to obtain

$$g_{BL}^{\mu\nu} = \begin{pmatrix} -\frac{4r(r^2 + \chi^2)}{((r-2)r + \chi^2)(\chi^2 \cos(2\theta) + 2r^2 + \chi^2)} - 1 & 0 & 0 & -\frac{4r\chi}{((r-2)r + \chi^2)(\chi^2 \cos(2\theta) + 2r^2 + \chi^2)} \\ 0 & \frac{(r-2)r + \chi^2}{\chi^2 \cos^2(\theta) + r^2} & 0 & 0 \\ 0 & 0 & \frac{1}{\chi^2 \cos^2(\theta) + r^2} & 0 \\ -\frac{4r\chi}{((r-2)r + \chi^2)(\chi^2 \cos(2\theta) + 2r^2 + \chi^2)} & 0 & 0 & \frac{\csc^2(\theta) (\chi^2 \cos(2\theta) + 2(r-2)r + \chi^2)}{((r-2)r + \chi^2)(\chi^2 \cos(2\theta) + 2r^2 + \chi^2)} \end{pmatrix}.$$

This inversion is most easily validated through the librational components of the metric tensor. Using the above expression, it is possible to explicitly compute J_{BL} . By filling in Eq. (5.11) we find

$$\begin{aligned} G &= -(g^{tt} E^2 - 2g^{t\phi} E L_z + g^{\phi\phi} L_z^2) \\ &= -E^2 \left(-\frac{4r(r^2 + \chi^2)}{((r-2)r + \chi^2)(\chi^2 \cos(2\theta) + 2r^2 + \chi^2)} - 1 \right) \\ &\quad - E L_z \left(\frac{8r\chi}{((r-2)r + \chi^2)(\chi^2 \cos(2\theta) + 2r^2 + \chi^2)} \right) \\ &\quad - L_z^2 \left(\frac{\csc^2(\theta) (\chi^2 \cos(2\theta) + 2(r-2)r + \chi^2)}{((r-2)r + \chi^2)(\chi^2 \cos(2\theta) + 2r^2 + \chi^2)} \right), \end{aligned} \tag{6.18}$$

using Boyer-Lindquist coordinates. From Eq. (5.36) we similarly compute

$$\boxed{\begin{aligned} V_{BL} &= g_{\theta\theta} \\ &= \chi^2 \cos^2(\theta) + r^2, \end{aligned}} \quad (6.19)$$

which are then combined to yield

$$\boxed{\begin{aligned} J_{BL} &= (G-1)V_{BL} \\ &= \frac{\chi^2 \cos^2(\theta) + r^2}{((r-2)r + \chi^2)(\chi^2 \cos(2\theta) + 2r^2 + \chi^2)} \\ &\times \left[-E^2 \left(-4r(r^2 + \chi^2) - ((r-2)r + \chi^2)(\chi^2 \cos(2\theta) + 2r^2 + \chi^2) \right) \right. \\ &\left. - EL_z(8r\chi) - L_z^2 \left(\csc^2(\theta)(\chi^2 \cos(2\theta) + 2(r-2)r + \chi^2) \right) - 1 \right]. \end{aligned}} \quad (6.20)$$

The above expression encodes a great deal of information on orbits in Kerr spacetime. Before we analyse it however, let us compute its counterpart in prolate spheroidal coordinates.

Computing J_{PS}

In Chapter 4, we saw that the Kerr solution has an exact formulation in prolate spheroidal coordinates. Before we compute J_{PS} , let us verify that form by directly transforming the line element in the Boyer-Lindquist case to prolate spheroidal coordinates. There are two main reasons to perform this transformation ourselves:

- By computing both the Boyer-Lindquist and prolate spheroidal form of the metric from the same first principle, any potential ambiguity on their physical equivalence is removed.
- Modified gravity theorems are often computed in Boyer-Lindquist coordinates. Having the transformation to prolate spheroidal coordinates ready and proven will serve us well when tackling modified gravity.

From the transformation rules given in Eq. (4.19), we see that x only depends on r and y only on θ . Combined with the transformation rule of the metric tensor given in Eq. (5.23), the Hessian matrix needed for the transformation takes the form

$$\mathbf{H} = \begin{pmatrix} 1 & 0 & 0 & 0 \\ 0 & p^2 & 0 & 0 \\ 0 & 0 & \frac{1}{1-y^2} & 0 \\ 0 & 0 & 0 & 1 \end{pmatrix}, \quad (6.21)$$

since t and ϕ are not transformed. The transformation is then performed as

$$g_{\mu\nu,PS} = \left[\mathbf{H} \cdot g_{\mu\nu,BL} \right]_{(r,\theta) \rightarrow (x,y)}$$

$$= \begin{pmatrix} \frac{2(px+1)}{(px+1)^2+q^2y^2} - 1 & 0 & 0 & \frac{2q(y^2-1)(px+1)}{(px+1)^2+q^2y^2} \\ 0 & p^2 \frac{(px+1)^2+q^2y^2}{p^2(x^2-1)} & 0 & 0 \\ 0 & 0 & \frac{1}{1-y^2} ((px+1)^2 + q^2y^2) & 0 \\ \frac{2q(y^2-1)(px+1)}{(px+1)^2+q^2y^2} & 0 & 0 & \frac{(1-y^2)(q^2(y^2-1)(p^2x^2+q^2-1)+((px+1)^2+q^2)^2)}{(px+1)^2+q^2y^2} \end{pmatrix} \\
 = \begin{pmatrix} -\frac{p^2x^2+q^2y^2-1}{(px+1)^2+q^2y^2} & 0 & 0 & -2\frac{q(1-y^2)(px+1)}{(px+1)^2+q^2y^2} \\ 0 & \frac{(px+1)^2+q^2y^2}{x^2-1} & 0 & 0 \\ 0 & 0 & \frac{(px+1)^2+q^2y^2}{1-y^2} & 0 \\ -2\frac{q(1-y^2)(px+1)}{(px+1)^2+q^2y^2} & 0 & 0 & \frac{(1-y^2)((px+1)^2+q^2)^2 - p^2q^2(1-y^2)(x^2-1)}{(px+1)^2+q^2y^2} \end{pmatrix},$$

which is indeed precisely what one finds when using Eq. (4.4), Eq. (4.17) and Eq. (4.18)². Note how the symmetry between g_{xx} and g_{yy} is clearly visible here. The contravariant form of the metric tensor is then found via matrix inversion:

$$g_{PS}^{\mu\nu} = \begin{pmatrix} g_{PS}^{tt} & 0 & 0 & -\frac{2(pqx+q)}{(p^2x^2+q^2-1)((px+1)^2+q^2y^2)} \\ 0 & \frac{x^2-1}{(px+1)^2+q^2y^2} & 0 & 0 \\ 0 & 0 & \frac{1-y^2}{(px+1)^2+q^2y^2} & 0 \\ -\frac{2(pqx+q)}{(p^2x^2+q^2-1)((px+1)^2+q^2y^2)} & 0 & 0 & -\frac{p^2x^2+q^2y^2-1}{(y^2-1)(p^2x^2+q^2-1)((px+1)^2+q^2y^2)} \end{pmatrix},$$

where

$$g_{PS}^{tt} = -\frac{1}{p^2(x^2-1)((px+1)^2+q^2y^2)} \left[-4pq^2x^3 + 4pq^2x + 4px^3 + 4px + q^4x^4 - q^4x^2y^2 - q^4x^2 + q^4y^2 - 2q^2x^4 + q^2x^2y^2 - 5q^2x^2 - q^2y^2 + 3q^2 + x^4 + 6x^2 + 1 \right]. \quad (6.22)$$

We see that we have managed to remove the goniometric functions that we had in the Boyer-Lindquist form of the metric, at the cost of an unwieldy g_{PS}^{tt} component.

We can now calculate J_{PS} by filling in Eq. (5.28) and Eq. (5.30). One finds

$$G = \frac{1}{p^2(x^2-1)((px+1)^2+q^2y^2)} \left[E^2 \left(1 + 3q^2 + (4p + 4pq^2)x + (6 - 5q^2 - q^4)x^2 + (4p - 4pq^2)x^3 + (1 - 2q^2 + q^4)x^4 + (q^4 - q^2)y^2 + (q^2 - q^4)x^2y^2 \right) + EL_z \left(4q(1 - px) \right) + L_z^2 \left(\frac{q^2(y^2 - x^2) + x^2 - 1}{y^2 - 1} \right) \right], \quad (6.23)$$

and

$$\begin{aligned} V_{PS} &= g_{yy} \cdot (1 - y^2) \\ &= (px+1)^2 + q^2y^2, \end{aligned} \quad (6.24)$$

²For the sceptical reader: the equality of the (t, t) and librational components of our form of the metric and the one shown in Ref. [48] are relatively straightforward to check.

to finally arrive at

$$\begin{aligned}
 J_{PS} &= (G - 1)V_{PS} \\
 &= \frac{(px + 1)^2 + q^2y^2}{p^2(x^2 - 1)((px + 1)^2 + q^2y^2)} \left[E^2 \left(1 + 3q^2 + (4p + 4pq^2)x + (6 - 5q^2 - q^4)x^2 \right. \right. \\
 &\quad \left. \left. + (4p - 4pq^2)x^3 + (1 - 2q^2 + q^4)x^4 + (q^4 - q^2)y^2 + (q^2 - q^4)x^2y^2 \right) \right. \\
 &\quad \left. + EL_z \left(4q(1 - px) \right) + L_z^2 \left(\frac{(q^2(y^2 - x^2) + x^2 - 1)}{y^2 - 1} \right) \right] - ((px + 1)^2 + q^2y^2). \tag{6.25}
 \end{aligned}$$

In the next section, we substitute the orbital parameters in the above equations to gain insight on what orbits in Kerr spacetime look like.

6.4.2 Visualising the effective potential

As was stated during their definitions in Chapter 5, J_{BL} and J_{PS} are not simply transformations of one another, but coordinate dependent definitions based on specific parametrisations of the Kerr solution. However, they have some of the same properties which can give us insight in how the Kerr spacetime behaves. Now we will see what the Kerr spacetime looks like in different coordinate systems.

Let us begin by choosing some values for our spacetime parameters. In our framework, allowed orbits in Kerr spacetime are characterised by three numbers: E , L_z and χ . One should remember that E and L_z are properties of the *class of geodesics*, whereas χ is a property of the *metric*. The reason we refer to a class of geodesics is that for a given E and L_z , we can still vary the initial conditions of individual orbits. On the other hand, the fact that the metric is fully determined by χ is in line with the no-hair theorem, since we do not consider charged black holes and have set the black hole mass to unity. For now, let us choose the parameters $E = 0.98$, $L_z = -4.5$ and $\chi = 0.3$ as an example. Using the definitions of p and q from Chapter 4, $\chi = 0.3$ fixes $q = 0.3$ and $p = \sqrt{0.91}$ for the prolate spheroidal case. The negative value of the angular momentum indicates that the test particle is in a retrograde orbit around the black hole.

In Fig. 6.1, we see a three-dimensional plot of the value of J_{BL} and J_{PS} . One can see that for this set of parameters, there is a divergence of the effective potential near the event horizon³. The physical intuition behind this should be noted: if one orbits close enough to a black hole, the gravity is strong enough to allow for any physical (that is, timelike) orbit to be pulled into the event horizon despite ones energy and angular momentum. One also sees that for this setting of parameters, there is an 'island' of positive effective potential outside the event horizon, which is disconnected from the positive region near the horizon itself. Remembering that geodesics must orbit inside positive regions of the effective potential, as well as that geodesics are continuous functions, this implies that an orbit starting in this outer region will remain in this outer region, no matter how long the orbit is evaluated for. Hence, a disconnected outer region is a guarantee of stability for any orbit originating in that region.

One might wonder whether there exists another positive region further away from the event horizon, outside of the plotting range of these graphs. When one solves for the points at which the second derivative of the effective potential with respect to the radial coordinate is zero, one finds only one solution in the domain of those variables, indicating that the effective potential never becomes

³Please refer to Chapter 4 for the location of the event horizon in all employed coordinate systems.

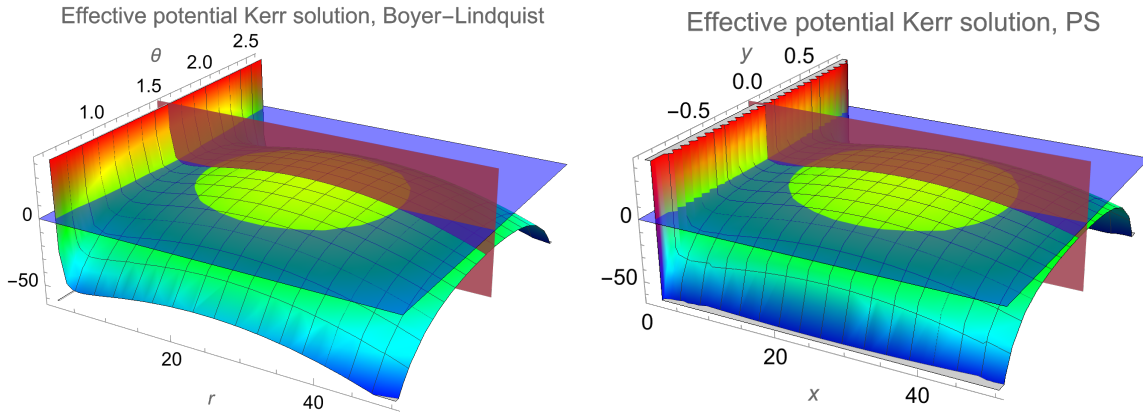


Figure 6.1: Three-dimensional representations of J_{BL} (left) and J_{PS} (right) for a Kerr spacetime with parameters $E = 0.98$, $L_z = -4.5$ and $\chi = 0.3$. The blue horizontal plane indicates where the effective potentials are equal to 0, which means that the part of the potential above this plane is the physical region for this set of parameters. The red vertical plane corresponds to the equatorial plane: $\theta = \pi/2$ or $y = 0$. Notice how the potential jumps to infinity near the event horizon.

positive again at larger values of the radial coordinate. It should also be clear that this does *not* depend on the choice of coordinate system; we reiterate that changing the parametrisation of the Kerr metric does not affect the physics of the orbits.

In Fig. 6.1, a local maximum in the effective potential is clearly visible in both coordinate systems. This maximum is located in the red vertical plane, which corresponds to the equatorial region of spacetime. Indeed, this is what one expects, given the symmetry properties of the Kerr solution. In Fig. 6.2, the equatorial cross-sections of the effective potentials are depicted, with the local maxima indicated with blue dots. These local maxima correspond to the *fixed points* of the dynamical system. Any geodesic in the outer region of the effective potential will orbit 'around' this fixed point. The red dots indicate the roots of the effective potential outer region in the equatorial plane.

Before we study the evolution of the effective potential, we introduce another analysis tool for its study. By plotting the contour $J = 0$, which corresponds to the blue horizontal plane in Fig. 6.1, we find the curve of zero velocity for a particular configuration. The results of such a plot are given in Fig. 6.3. The region inside the curve of zero velocity is the allowed region of the geodesics. Furthermore, we expect that geodesics will always travel from one point of the curve of zero velocity to another, since this contour per definition contains the only points in the outer region where a test particle's librational momenta can both flip sign. This will be further investigated when we plot the actual orbits.

6.4.3 Sensitivity to orbital parameters

By changing the orbital parameters, we can investigate the dependence of the effective potential on E, L_z and χ . Let us use prolate spheroidal coordinates for this analysis. In Fig. 6.4, the allowed region is depicted under variation of these parameters. Here, we can see that even light changes to the parameters of the class of geodesics can lead to greatly different orbits. Of particular interest is the existence of zero, one or two roots of the outer region in the equatorial plane. If only an outer root exists, some geodesics starting in the outer region might fall into the black hole via the

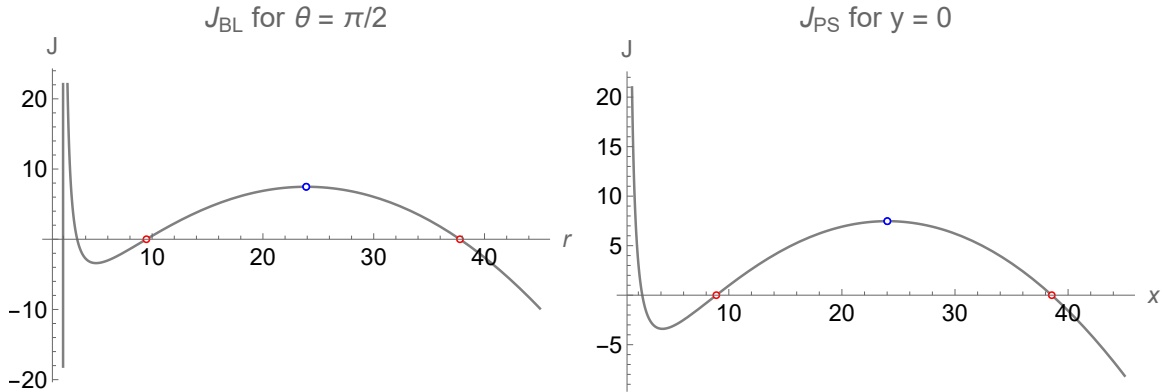


Figure 6.2: Equatorial cross-sections of J_{BL} (left) and J_{PS} (right) for a Kerr spacetime with parameters $E = 0.98$, $L_z = -4.5$ and $\chi = 0.3$. These figures are in one-to-one correspondence with the red vertical planes in Fig. 6.1. The blue dots in this figure indicates the local maximum, i.e. the fixed point. The red dots indicate the roots of the effective potential in the outer region. Note how in the Boyer-Lindquist case, the effective potential behaves erratically for small r . This is because the event horizon in this coordinate system is located at the positive divergence of the potential, rendering values of J_{BL} below r_+ unphysical. Since in prolate spheroidal coordinates the horizon is always at $x = 1$ regardless of spin, one does not encounter this behaviour there.

'neck' in the allowed region. However, if we have both an inner and outer root, we see that they act as bounds on geodesics in that configuration. The existence of these roots is hence an indicator of whether geodesics are guaranteed to be bound⁴, where we should emphasise that bound orbits could still exist if there is only an outer root.

Let us also analyse the effect of the black hole spin on the allowed region. In Fig. 6.5a, we see one case where the spin parameter strongly affects the orbital dynamics of the system. In these examples, increasing the black hole spin causes one of the outer region equatorial roots to vanish. From a physical point of view, this can be understood by realising that these correspond to retrograde orbits. Hence, increasing the black hole spin would make it *more* difficult for a test particle to maintain its orbit. If the particle is orbiting along the black hole spin, as seen in Fig. 6.5b, increasing the spin of the black hole would make it *less* difficult for a test particle to stay in orbit.

If the black hole spin is zero, we see that the effective potentials for prograde and retrograde orbits are identical. This is in line with what one would expect from the complete spherical symmetry of a Schwarzschild black hole.

⁴An unbound orbit is defined as either i) shooting off into radial infinity or ii) falling into the event horizon.

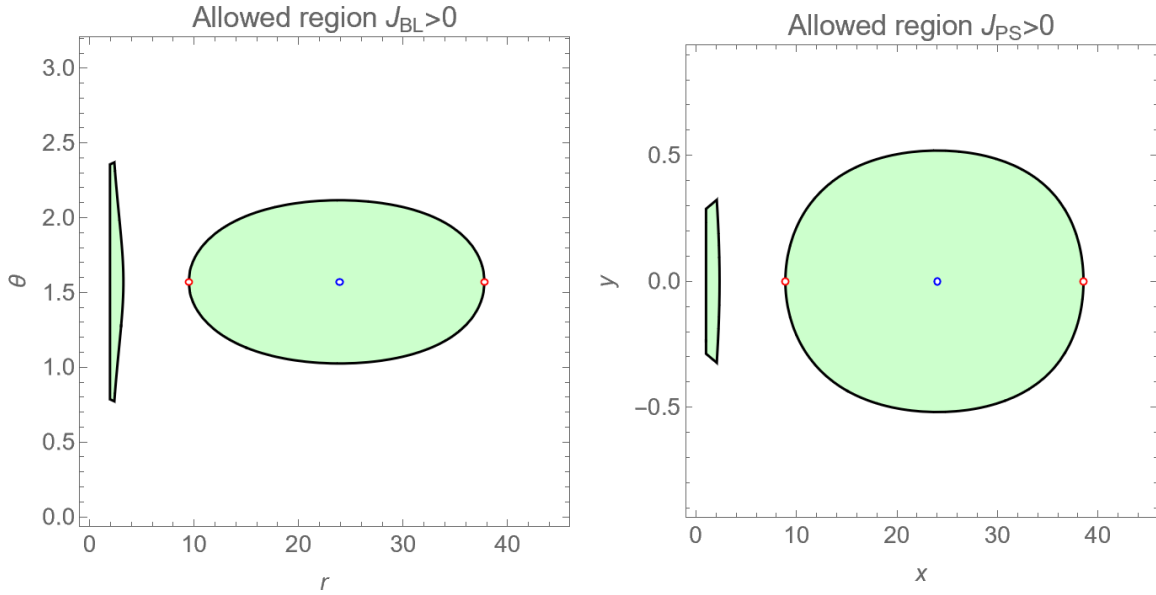


Figure 6.3: Allowed regions of J_{BL} (left) and J_{PS} (right) for a Kerr spacetime with parameters $E = 0.98$, $L_z = -4.5$ and $\chi = 0.3$. Orbits can only exist within the green regions. The black outlines indicate the curves of zero velocity. The blue dots indicate the fixed point and the red dots indicate the equatorial roots of the potential in the outer region.

6.4.4 Keplerian variables in Kerr spacetime

Although orbits in Kerr spacetime are characterised by E , L_z and χ , one can also use standard Keplerian variables to describe orbital motion in Kerr spacetime [1][28][59]. Let r_P indicate the *periapsis* (closest radial distance) and r_A the *apoapsis* (furthest radial distance) of an orbit in Boyer-Lindquist coordinates⁵. One can define the generalised Keplerian variables *eccentricity* e and *semi-latus rectum* p via

$$r_P \equiv \frac{p}{1+e}, \quad r_A \equiv \frac{p}{1-e} \quad (6.26)$$

which one can straightforwardly invert to find

$$e = \frac{r_A - r_P}{r_A + r_P}, \quad p = r_A \left(1 - \frac{r_A - r_P}{r_A + r_P} \right) = r_P \left(1 + \frac{r_A - r_P}{r_A + r_P} \right). \quad (6.27)$$

Using the above equations, we can find the eccentricity and semi-latus rectum of any orbit. In particular, in the case of a separated outer region, we can a priori compute the maximum allowed eccentricity of the class of geodesics. In such a case, the extreme values of r_P and r_A are precisely the inner and outer root of the outer allowed region in the equatorial plane. If the outer region *is* connected to the event horizon, one can take the ISO radius⁶ as r_P . Hence, it is possible to put bounds on the kinds of orbits generated by a set of E , L_z and χ just by analysing their allowed region.

⁵This definition is coordinate dependent; Boyer-Lindquist coordinates are commonly used for this purpose [28][59].

⁶The ISO radius will be defined in section 6.5.2.

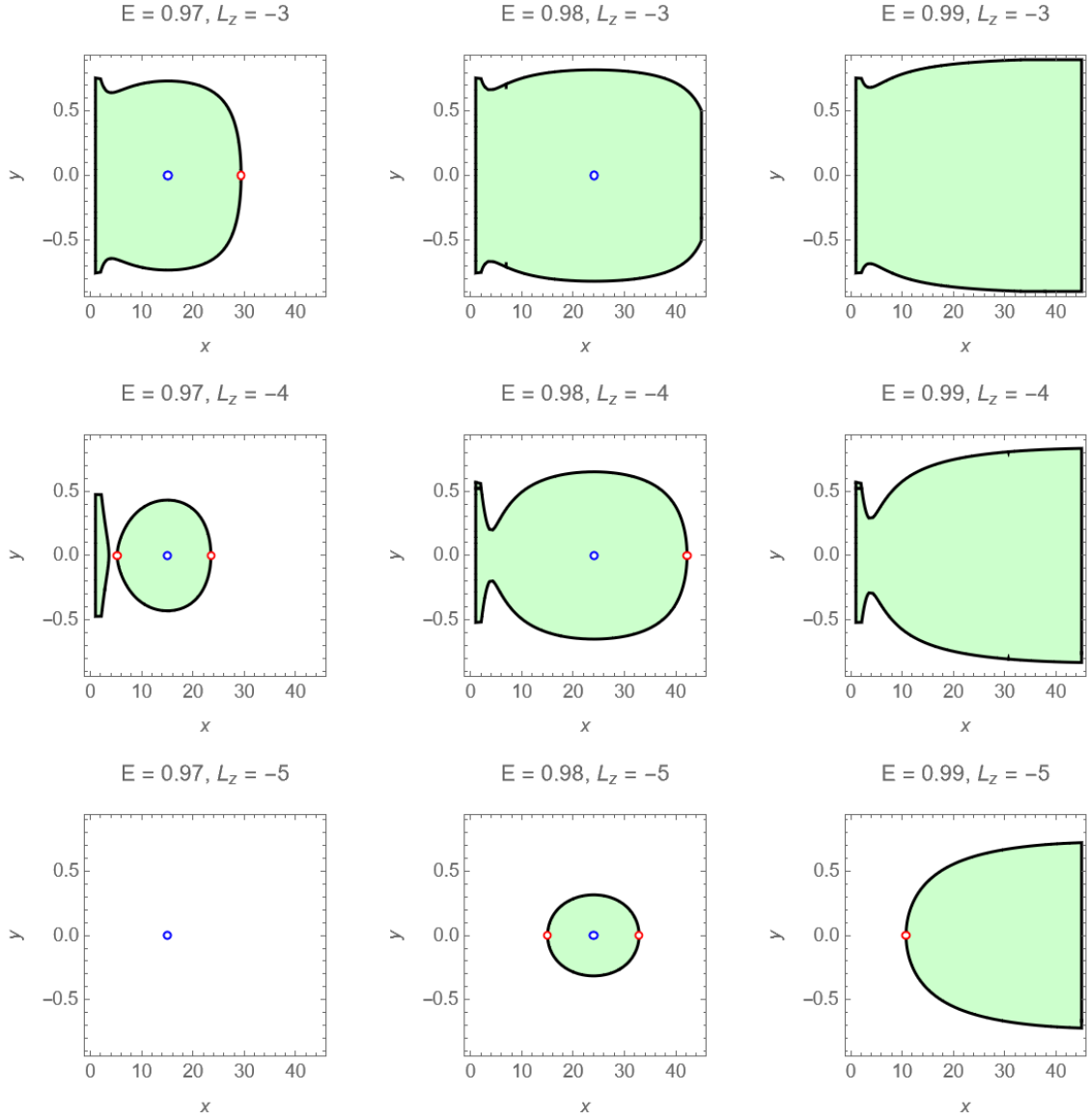


Figure 6.4: Allowed region for different E and L_z at $\chi = 0.3$. One can see that the existence of the inner and outer roots (the red points) are indicators of whether the potential allows for unbound geodesics. Note that for some settings the outer root and fixed point are still present but outside the plotting range. For $E = 0.97, L_z = -5$, no orbits are allowed, since $J_{PS} < 0$ at the fixed point.

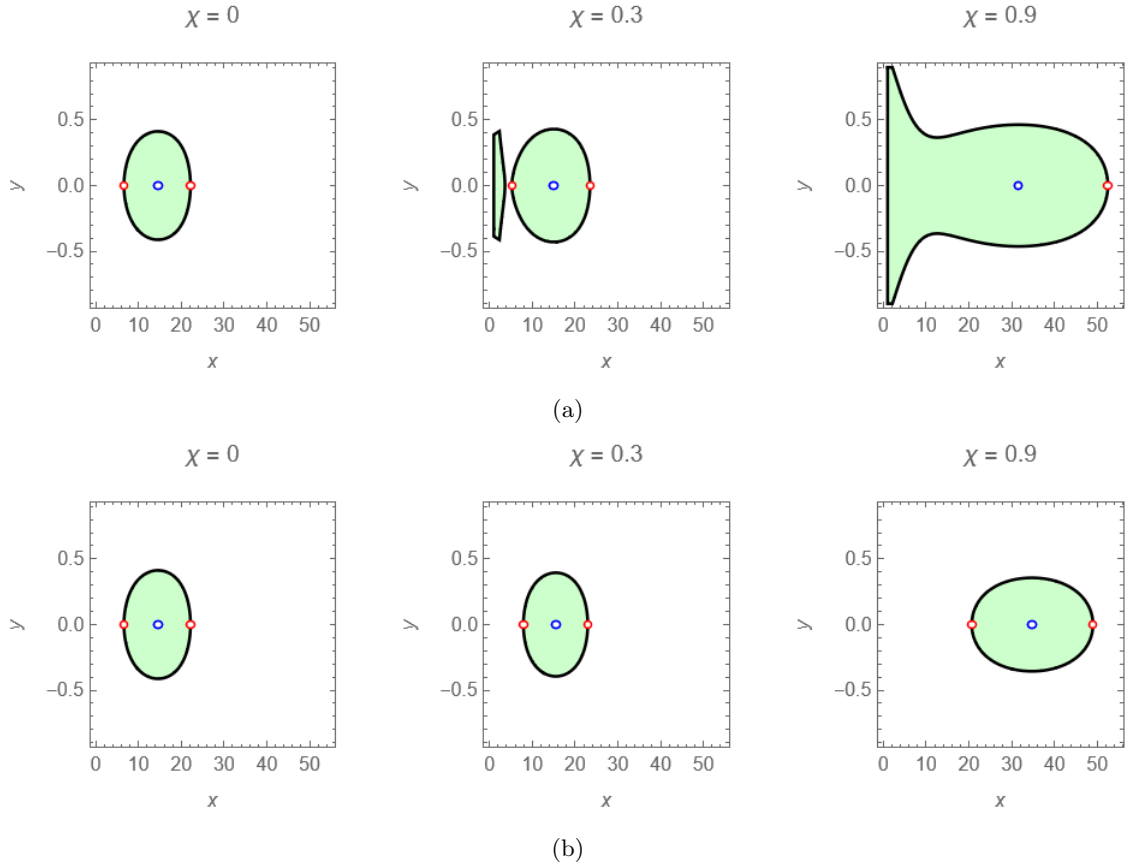


Figure 6.5: Allowed region for different χ at (a) $E = 0.97, L_z = -4$, i.e. a retrograde orbit, and (b) $E = 0.97, L_z = 4$, i.e. a prograde orbit.

6.4.5 Contours of the phase space

In Chapter 5, we found that the librational momenta of the orbits are related via Eq. (5.31) and Eq. (5.39). Using these relations, we are able to construct the Poincaré section of geodesics in Kerr spacetime for a given set of parameters. For our study, we are interested in the phase space of the radial coordinate. As was discussed earlier in this manuscript, one expects to find closed curves around the fixed point in phase space if the spacetime is integrable, each curve corresponding to a unique geodesic. This is indeed what one finds when the radial phase space is computed in either prolate spheroidal or Boyer-Lindquist coordinates. In Fig. 6.6, every contour indicates a different geodesic. During its orbit, a test particle with a particular set of orbital parameters will mark each crossing the equatorial plane on one of these closed curves. If evaluated into infinity, we expect the curve to be completely filled for a non-resonant orbit. Note that this computation of the phase space via contours of the effective potential only is accurate when an analytical expression of the metric is employed; finer features in the phase space will be lost if an expanded form of the metric is employed instead in these contour plots.

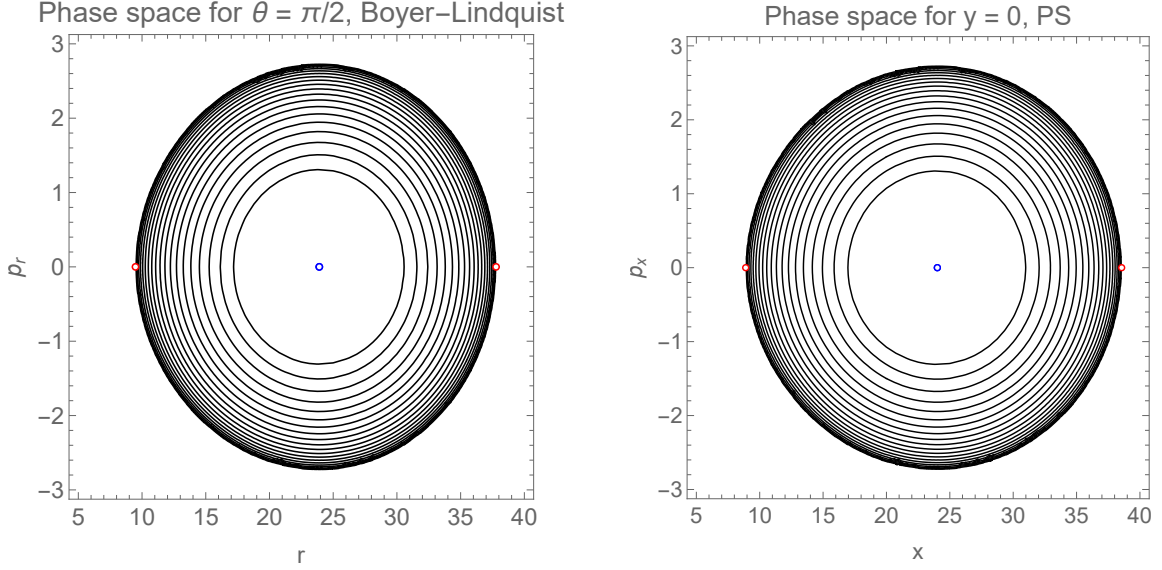


Figure 6.6: Radial Poincaré slice for $E = 0.98$, $L_z = -4.5$ and $\chi = 0.3$ in Boyer-Lindquist coordinates (left) and prolate spheroidal coordinates (right), in the equatorial plane. The fixed point and roots of the effective potential are also depicted.

6.5 Numerical evaluation of geodesics

As was shown in Chapter 5, we are able to construct the Hamiltonian of the Kerr spacetime from the form of the line element. Combined with the stationarity, axisymmetry and Hamiltonian constant, the latter of which formulated through the effective potential, we are able to solve the equations of motion of the system.

6.5.1 Choice of coordinate system

In this section, we will see what orbits look like in different coordinate systems. First, using Eq. (5.32) and Eq. (5.19), we can compute the Hamiltonians corresponding to Boyer-Lindquist and prolate spheroidal coordinates. They are given by

$$\mathcal{H}_{BL} = \frac{1}{2} \left[E^2 \left(\frac{-4r(r^2 + \chi^2)}{((r-2)r + \chi^2)(\chi^2 \cos(2\theta) + 2r^2 + \chi^2)} - 1 \right) + \frac{8EL_z r \chi}{((r-2)r + \chi^2)(\chi^2 \cos(2\theta) + 2r^2 + \chi^2)} \right. \\ \left. + \frac{L_z^2 \csc^2(\theta) (\chi^2 \cos(2\theta) + 2(r-2)r + \chi^2)}{((r-2)r + \chi^2)(\chi^2 \cos(2\theta) + 2r^2 + \chi^2)} + \frac{p_\theta^2}{\chi^2 \cos^2(\theta) + r^2} + \frac{p_r^2 ((r-2)r + \chi^2)}{\chi^2 \cos^2(\theta) + r^2} \right], \quad (6.28)$$

and

$$\mathcal{H}_{PS} = \frac{1}{2} \left[-\frac{\Omega E^2}{p^2 (x^2 - 1) ((px + 1)^2 + q^2 y^2)} + \frac{4EL_z q (px + 1)}{p^2 (x^2 - 1) ((px + 1)^2 + q^2 y^2)} \right. \\ \left. + \frac{L_z^2 (p^2 x^2 + q^2 y^2 - 1)}{p^2 (1 - y^2) (x^2 - 1) ((px + 1)^2 + q^2 y^2)} + \frac{p_x^2 (x^2 - 1)}{(px + 1)^2 + q^2 y^2} + \frac{p_y^2 (1 - y^2)}{(px + 1)^2 + q^2 y^2} \right], \quad (6.29)$$

where

$$\begin{aligned} \Omega = & -q^2 (4p (x^2 - 1) x + x^2 (2x^2 - y^2 + 5) + y^2 - 3) + 4p (x^3 + x) \\ & + q^4 (x^2 - 1) (x - y)(x + y) + x^4 + 6x^2 + 1. \end{aligned} \quad (6.30)$$

Using the Hamilton-Jacobi equations, this provides us with the equations of motion for the spatial coordinates of the system as well as their corresponding momenta. In order to numerically solve the system, we need to add further constraints. In particular, we will choose the following initial conditions in Boyer-Lindquist coordinates:

$$r(0) = r_0, \quad \theta(0) = \pi/2, \quad p_r(0) = 0 \quad \Rightarrow \quad p_\theta(0) = \sqrt{J_{BL} - 0 \times \Delta} = \sqrt{J_{BL}}, \quad (6.31)$$

where r_0 is a parameter we will vary to analyse the full class of geodesics. In prolate spheroidal coordinates, these conditions correspond to

$$x(0) = x_0, \quad y(0) = 0, \quad p_x(0) = 0 \quad \Rightarrow \quad p_y(0) = \sqrt{1 - 0} \sqrt{J_{PS} - 0 \times \frac{1}{x_0^2 - 1}} = \sqrt{J_{PS}}. \quad (6.32)$$

We used Eq. (5.31) and Eq. (5.39) to set the initial momenta in the non-radial coordinates p_θ and p_y to physical values. These initial conditions correspond to letting a particle start on the equatorial plane with some initial momentum out of the plane and no momentum in the radial direction. These kinds of orbits will generate the successive piercings of the equatorial Poincaré slice we need to identify chaotic features. Other classes of orbits also exist; one could for example define perfectly equatorial orbits by setting the non-radial momentum to zero, but these orbits are not relevant to our analysis.

Using these initial conditions, the equations of motion are numerically evaluated using *Mathematica's* NDSolve methods. In the Kerr case, no special considerations for the accuracy are yet necessary; however, for modified gravity, we will need to implement methods designed to maximise the numerical accuracy of the integrator.

In Fig. 6.7, we see an example of orbits in a Kerr spacetime in the case where there is a separated outer region. As expected, all orbits form rectangles in these spheroidal coordinate systems, with corners precisely touching the curve of zero velocity. The centres of these rectangles are always precisely the fixed point of the effective potential. We see that orbits near the fixed point are less eccentric than orbits further away from the fixed point. Indeed: orbits near the fixed point generally experience far less radial motion than orbits closer to the roots of the effective potential. The orbits depicted here are examples of non-resonant orbits. As time continues, these orbits would ergodically fill the rectangles they trace out in this slice of spacetime.

Using the results from Chapter 4, one can straightforwardly transform the prolate spheroidal orbits to be represented in factor structure and Weyl coordinates. In Fig. 6.8, the transformed geodesics of Fig. 6.7 are depicted. One can see that the factor structure coordinates have rescaled the orbits to a more compact form while retaining their spheroidal nature (as seen from the rectangular shape of the orbit space). Weyl coordinates however deform these rectangles. The Weyl representation can be imagined as a section of the torus formed by orbits around the black hole. However, one must be careful when doing this: Weyl coordinates are by their nature measured relative to the event horizon of the black hole (as was shown in Chapter 4) rather than the geometrical centre of the system and are hence *not* a direct analogy of Cartesian space.

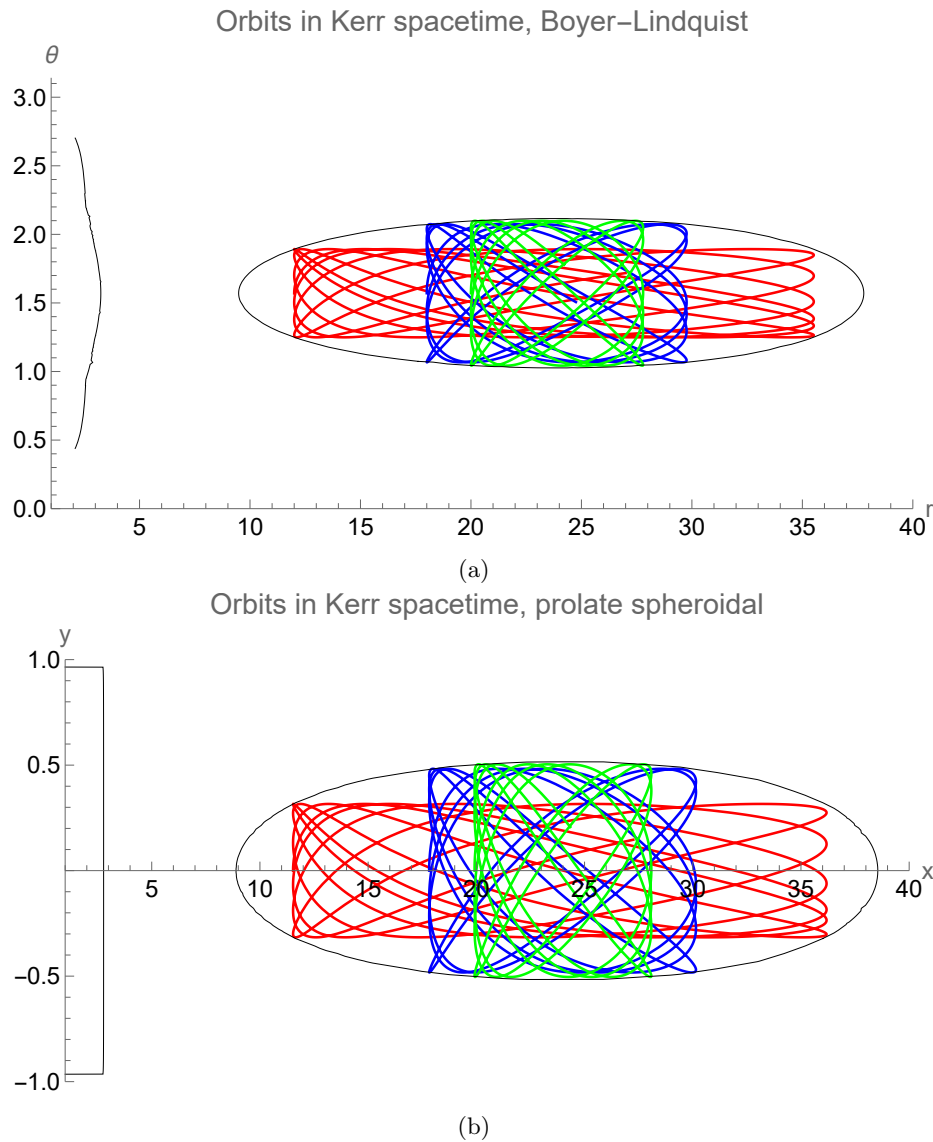


Figure 6.7: Geodesics in the outer region of a Kerr spacetime with $E = 0.98$, $L_z = -4.5$ and $\chi = 0.3$ in Boyer-Lindquist (above) and prolate spheroidal (below) coordinates, evaluated for $\tau = 5000$ time steps. Both plots represent the exact same orbits and initial conditions; the red orbit starts at $r = 12$, the blue orbit at $r = 18$ and the green orbit at $r = 20$ (as expressed in Boyer-Lindquist coordinates). The black line indicates the curve of zero velocity, which is the border of the allowed region. Note the rectangular shape of the orbits in both coordinate systems; this can be attributed to their spheroidal nature.

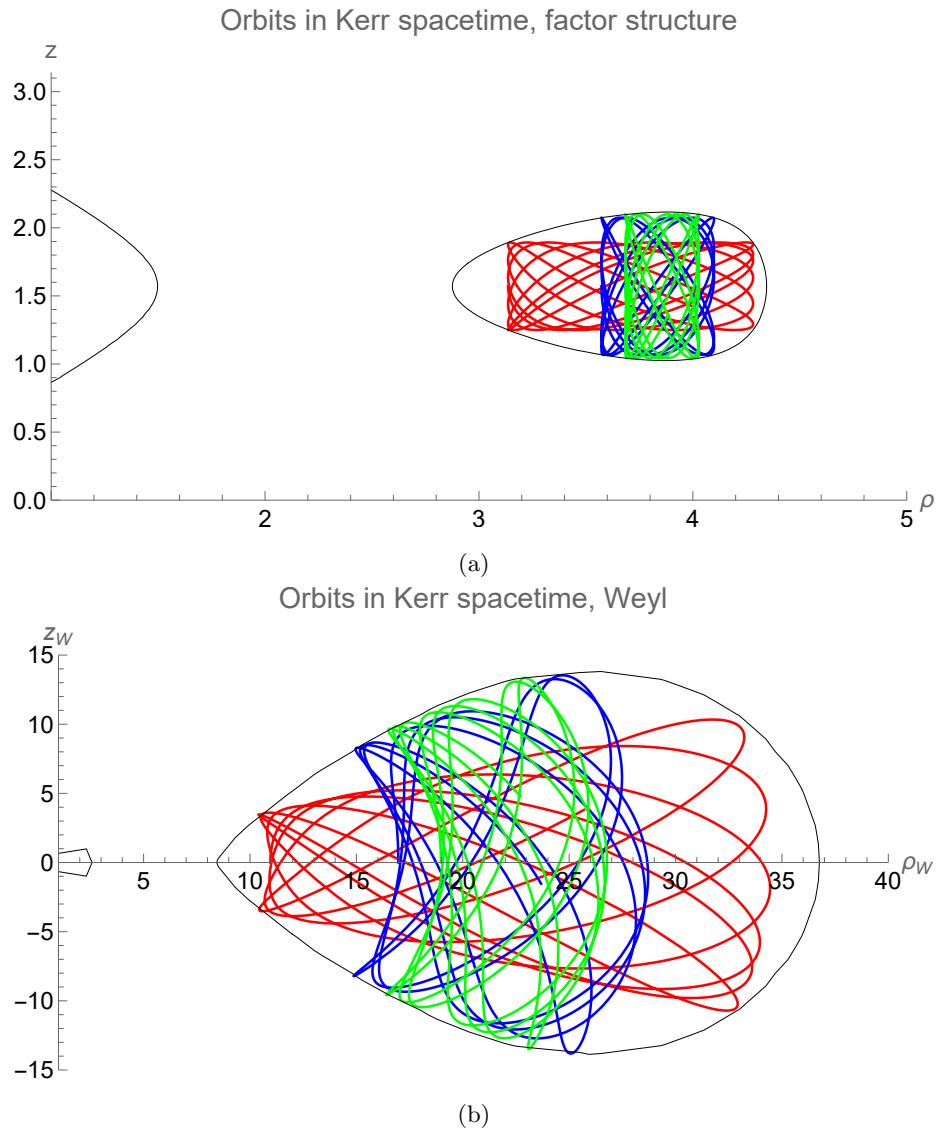


Figure 6.8: Geodesics in the outer region of a Kerr spacetime with $E = 0.98$, $L_z = -4.5$ and $\chi = 0.3$ in factor structure (above) and Weyl (below) coordinates, evaluated for $\tau = 5000$ time steps. These are the same orbits as depicted in Fig. 6.7 and hence use the initial conditions stated there.

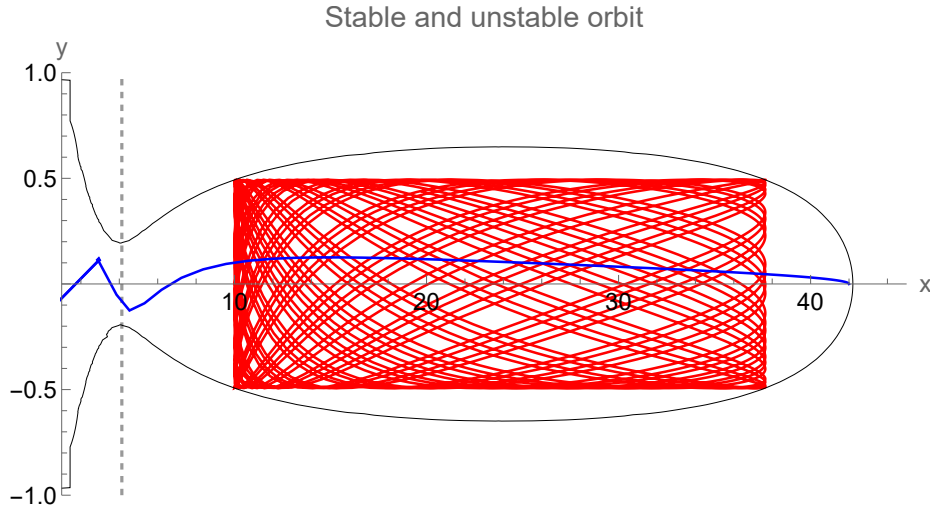


Figure 6.9: Examples of a stable and unstable orbit in Kerr spacetime with $E = 0.98$, $L_z = -4$ and $\chi = 0.3$, using prolate spheroidal coordinates. The red orbit starts at $x_0 = 10$. The blue orbit with $x_0 = 42$ becomes a stiff system after approximately 417 time steps, resulting in the numerical integrator failing to advance the orbit beyond this time. The particle falls into the event horizon, where J_{PS} diverges. The dashed line indicates x_{ISO} .

6.5.2 Orbital stability

We will now consider cases where the outer region is connected to the event horizon of the black hole. This allows some geodesics starting in the outer region to fall into the event horizon. For this part of the analysis, we will employ prolate spheroidal coordinates.

In Fig. 6.9, we see a different parametrisation of the Kerr spacetime which has such a connection between the outer region and the event horizon. In this case, we achieved this by changing L_z from -4.5 to -4 , although there are countless other parametrisations which provide such an allowed region. Fig. 6.9 shows a blue orbit which quickly spirals into the black hole, whereas the red orbit remains stable in the outer region. From the figure, we can see that stable orbits can occur if the non-radial edge of their rectangle is wider than the neck between the outer region and the event horizon. Since orbits initially move towards the fixed point from their starting radius x_0 , one sees that this requirement is directly connected to the initial radial coordinate.

It is desirable to have a more mathematical formulation of this statement. The locus of the thinnest part of the neck is precisely a local minimum in the effective potential. We will hence define the *innermost stable orbit* radius x_{ISO} (equivalently r_{ISO} , ρ_{ISO} , $\rho_{W,ISO}$) as the value of x between x_+ (the outer event horizon) and the fixed point for which J achieves a local minimum. This is precisely the radius for which the potential barrier no longer shields the particle from the black hole singularity [28]. The difference between this radius and the ISCO radii is that we do not require a circular orbit. Together with the ISCO radii, this radial coordinate gives us insight in the closest allowed approaches to the event horizon for a particular set of E , L_z and χ .

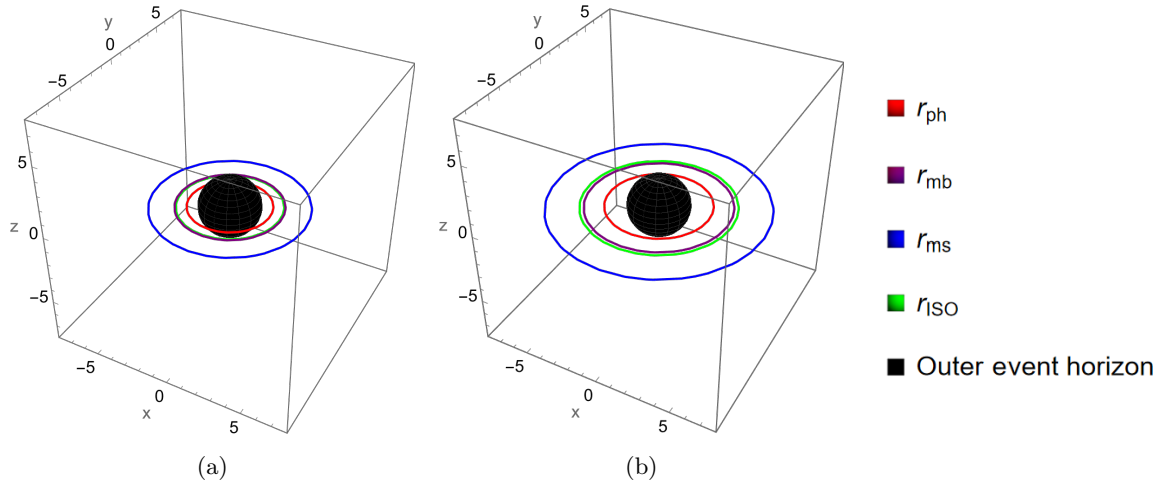


Figure 6.10: Black hole event horizon (black), ISO (green) and ISCO (red for photon sphere, purple for marginally bound, blue for marginally stable) radii for $\chi = 0.3$, $E = 0.985$ and $L_z = \pm 4.5$. Note that only the ISO radius actually depends on the values of E , χ and L_z : the ISCO radii only depend on χ and the sign of L_z and the event horizon only depends on χ . (a) corresponds to the prograde case and (b) to the retrograde case.

6.6 Three-dimensional orbits

Although the Kerr spacetime is fully characterised by a two-dimensional system consisting of spatial coordinates, we can still add the equation of motion for ϕ in order to compute the full orbital motion in Cartesian 3-space around a Kerr black hole. This will give us further intuition in the orbital behaviour of geodesics in these spacetimes. For this section, a representation in Boyer-Lindquist coordinates is the most appropriate, due to its straightforward embedding in Cartesian 3-space. Cartesian coordinates (x_C, y_C, z_C) should not be confused with prolate spheroidal coordinates (x, y) and are related to Boyer-Lindquist coordinates via [1]:

$$\begin{aligned} x_C &= \sqrt{r^2 + \chi^2} \sin \theta \cos \phi, \\ y_C &= \sqrt{r^2 + \chi^2} \sin \theta \sin \phi, \\ z_C &= r \cos \theta. \end{aligned} \tag{6.33}$$

6.6.1 Visualising the black hole

Using the Boyer-Lindquist radius of the event horizon as given in Chapter 4 combined with the transformation rules in Eq. (6.33), we can create a visualisation the Kerr black hole in Cartesian 3-space. Furthermore, we can include the ISO and ISCO radii as discussed earlier in this chapter to build a representation of the most important surfaces of the compact object. In Fig. 6.10, the event horizon of a black hole is presented together with the ISCO and ISO radii for $\chi = 0.3$, $E = 0.985$ and $L_z = \pm 4.5$. Although the black hole looks spherical, the event horizon actually shows a slight bulge on the equatorial plane, which becomes more pronounced as $\chi \rightarrow 1$. We also see a pronounced difference between the prograde and retrograde ISO and ISCO radii.

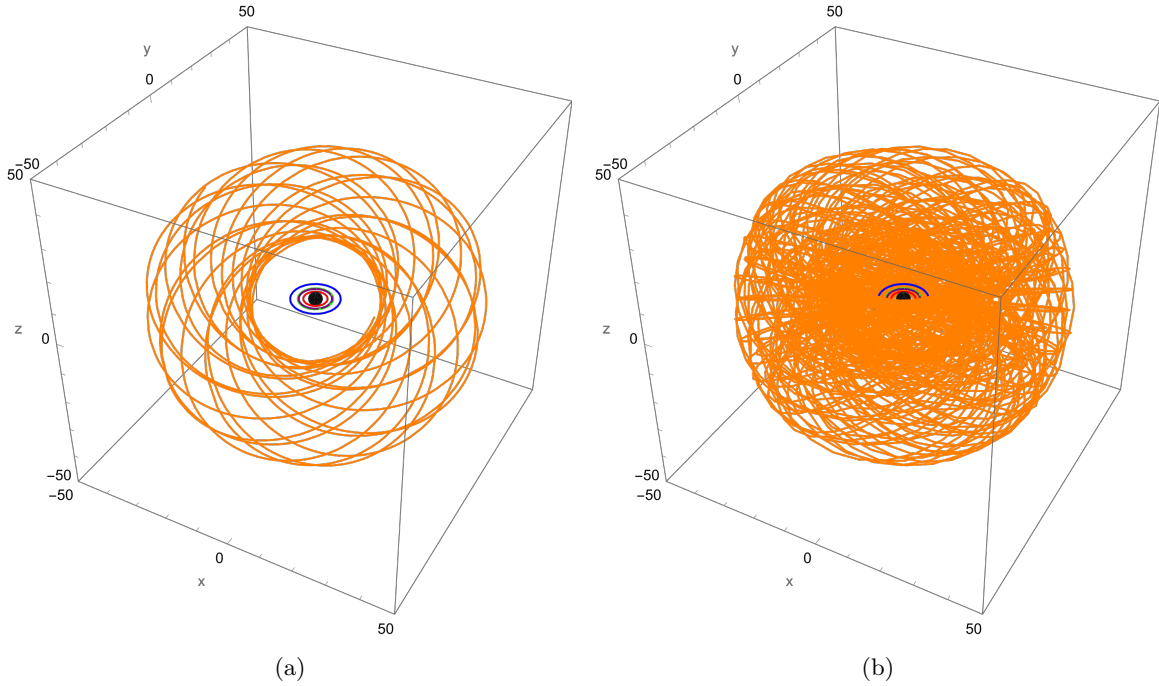


Figure 6.11: An orbit with $E = 0.985$, $L_z = -4.5$ and $\chi = 0.3$ represented in Cartesian 3-space, evaluated for 25 000 time steps (a) and 200 000 time steps (b). The event horizon, ISO and ISCO radii as in Fig. 6.10 are also depicted.

6.6.2 Restoring the ϕ component

Recall that the equations of motion of the system are computed via the Hamilton-Jacobi equations, as outlined in Eq. (2.17). In our framework, we can add the additional spacelike variable ϕ and momentum variable p_ϕ to the list of variables to investigate, in order to generate the full set of equations of motion from the Hamiltonian in three dimensions.

If one takes the Hamiltonian in Boyer-Lindquist coordinates as given in Eq. (6.28) and replaces L_z with p_ϕ , one can apply the Hamilton-Jacobi equations to obtain

$$\dot{\phi} = \frac{1}{2} \left(\frac{8\chi E r}{(\chi^2 + (r-2)r)(\chi^2 \cos(2\theta) + \chi^2 + 2r^2)} + \frac{2p_\phi \csc^2(\theta) (\chi^2 \cos(2\theta) + \chi^2 + 2(r-2)r)}{(\chi^2 + (r-2)r)(\chi^2 \cos(2\theta) + \chi^2 + 2r^2)} \right),$$

$$\dot{p}_\phi = 0, \tag{6.34}$$

along with the previous equations of motion for r and θ . The \dot{p}_ϕ equation reaffirms the conservation of angular momentum. We can then substitute $p_\phi \rightarrow L_z$ in our results to obtain the full set of equations of motion, including the angular component⁷. Using this additional equation, we can plot the three dimensional orbits. In Fig. 6.11, the result of such a computation is shown. The precessive behaviour typical of Kerr orbits is clearly visible in the upper plot. One can also see that for longer evaluation time, the orbit fills out a torus-like region around the black hole.

⁷One might wonder whether this restoration of the ϕ coordinate also works for coordinate time t . In fact, it *does* work like that and this will be revisited in Chapter 7.

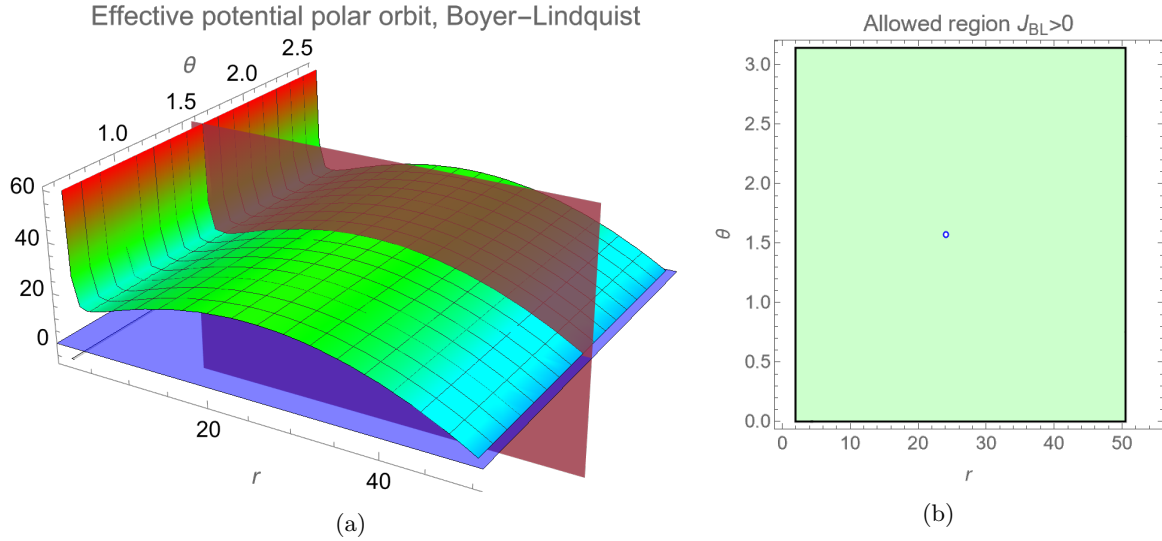


Figure 6.12: Effective potential of polar orbits with $E = 0.98$, $L_z = 0$ and $\chi = 0.3$. The fixed point is indicated in blue. (a) Note how at the ISO radius (the local minimum of the potential) the effective potential has the same value regardless of θ . (b) The effective region is now unbounded in the θ direction.

6.6.3 Polar orbits

By setting $L_z = 0$, one can obtain a special class of orbits: *polar orbits*. Since in this case $p_\phi = 0$, geodesics of this kind do not move in the ϕ direction of spacetime. Given sufficient energy however, they are able to orbit a spinning black hole by repeatedly passing over its poles. In the case of polar orbits, the effective potential takes a different form, as seen in Fig. 6.12. There is no longer a bound on the θ direction, since orbits pass over the poles of the black hole. However, there is still an ISO radius, within which an orbit will plunge into the black hole. Furthermore, the maximum of the effective potential is still in the equatorial plane, as illustrated in a fixed r cross section of the effective potential depicted in Fig. 6.13.

In Fig. 6.14, we see two examples of polar orbits in Cartesian 3-space. If the black hole is non-spinning, the test particle is confined to a plane, in line with the full rotational symmetry of the Schwarzschild black hole. However, if non-zero black hole spin is introduced, an orbiting test particle is dragged along with the black hole spin, despite having no angular momentum relative to the symmetry axis. This is a demonstration of the effect a black hole's frame-dragging has on the path of an orbiting body and grants us insight in the subtle difference between L_z and movement in ϕ in rotating spacetimes.

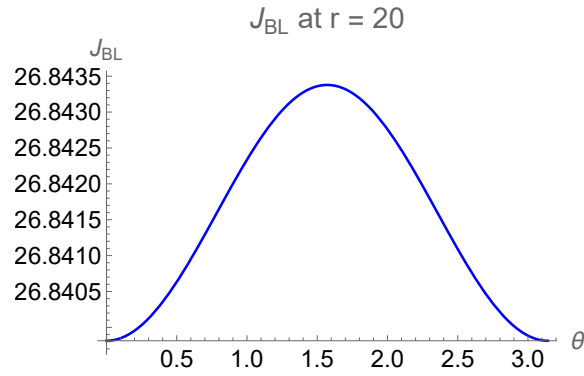


Figure 6.13: Values of the effective potential for an orbit where $E = 0.98$, $L_z = 0$ and $\chi = 0.3$ at $r = 20$. Note that there is a maximum on the equatorial plane, which is also where the fixed point is located, but that the potential varies little under variation of θ .

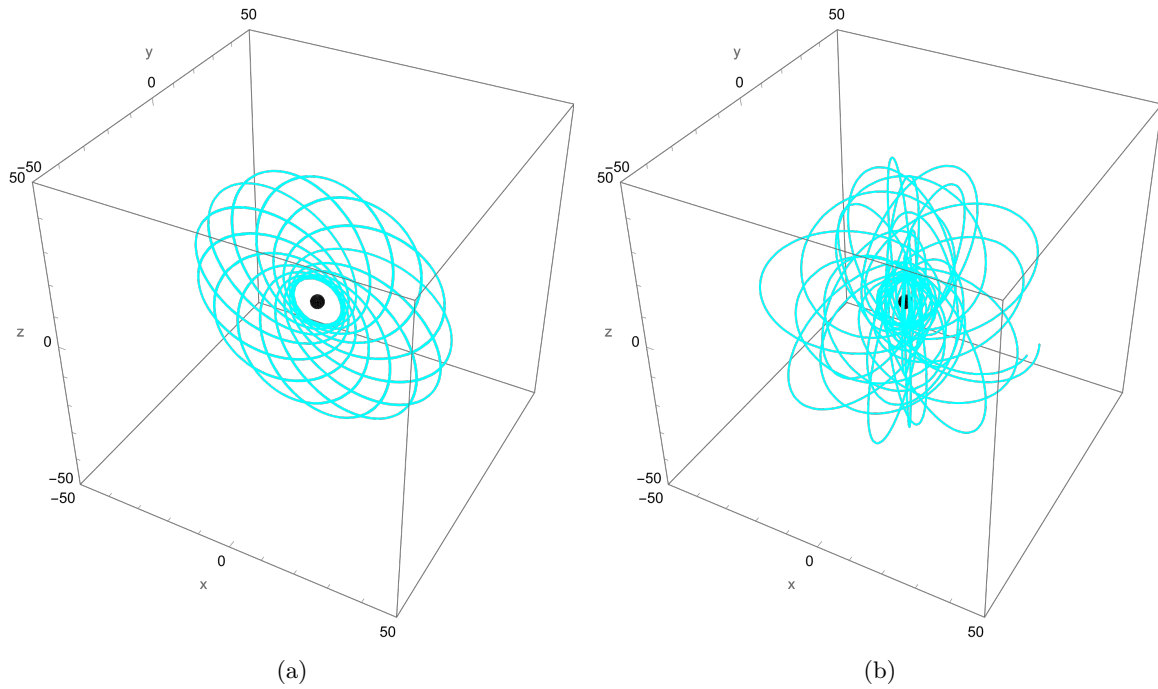


Figure 6.14: Polar orbits with $E = 0.98$ and $L_z = 0$. (a) Here we set $\chi = 0$, which corresponds to a Schwarzschild black hole. Note how the geodesic orbits in the $y = 0$ plane. (b) Here we have $\chi = 0.3$. An orbiting particle is pulled along the black hole spin in the ϕ direction, despite having no angular momentum.

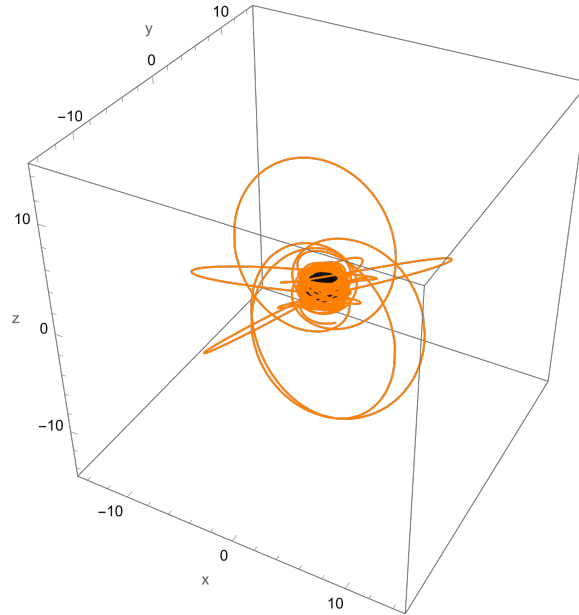


Figure 6.15: A zoom-whirl orbit with $E = 0.93$, $L_z = 1.78$ and $\chi = 0.998$. In this extreme spin case, the geodesic closely hugs the event horizon, which now has a pronounced oblate spheroidal shape.

6.6.4 Zoom-whirl orbits

Besides polar orbits, there exists another special class of orbits which is of interest to us: *zoom-whirl orbits*. This class of geodesics is characterised by its highly erratic motion around the black hole. Specifically, if an orbiting particle approaches close enough to the ISO radius, the radial frequency of the orbit goes to zero, whereas ω_ϕ and ω_θ remain finite [28]. This causes the particle to perform many orbits very close the event horizon (the *whirling* motion), before *zooming* away from the black hole, after which the cycle repeats. In Fig. 6.15, we see one example of such an orbit. In this case, we consider a black hole with almost extremal spin. Hence, the particle is able to come very close to the event horizon without plunging into the black hole. One clearly sees that the particle does not precessively orbit in a slowly rotating plane like in Fig. 6.11, but rather moves around the 3-space in an erratic fashion⁸.

A more relevant parametrisation of such a system is given in Fig. 6.16. In this example, the black hole has a less extreme spin value. However, since the orbit can get very close to the ISO radius, one can again see how the geodesic cycles between whirling behaviour close the event horizon and zooming motion further from the black hole. Some prominent resonances are located near the ISO radius, as we will discuss in the next section.

⁸We should emphasise that this is *not* chaotic motion: the Carter constant is still conserved and hence the system displays periodicity. The seemingly random motion is actually fully determined a priori.

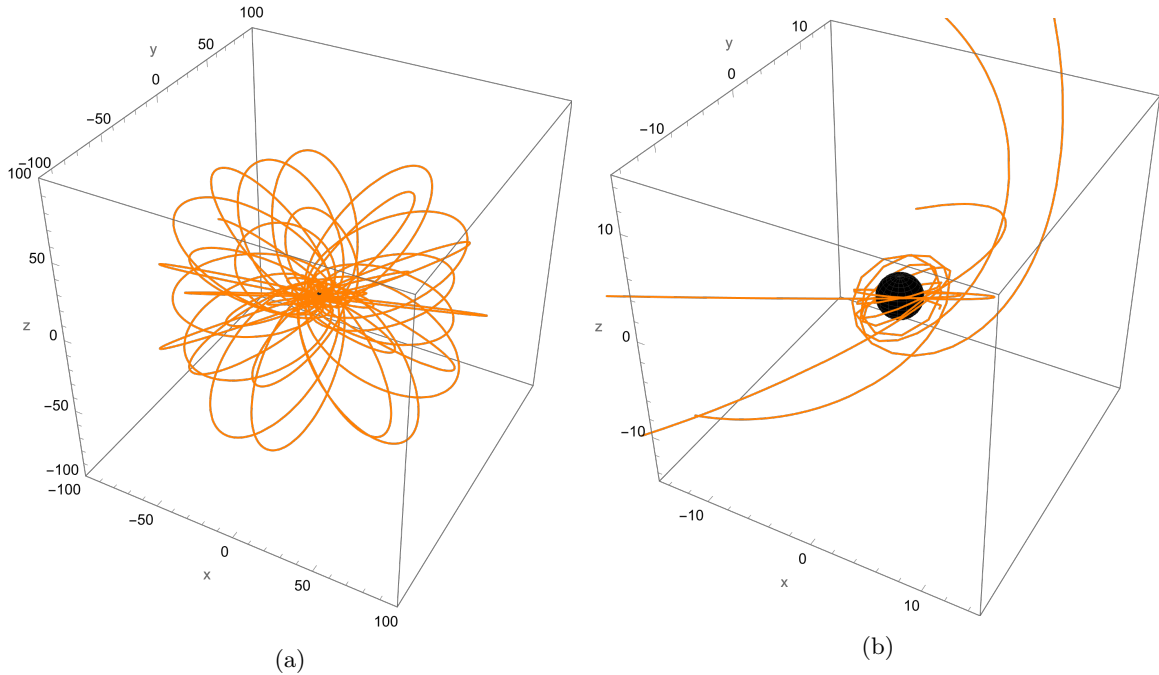


Figure 6.16: A zoom-whirl orbit with $E = 0.99$, $L_z = 3$ and $\chi = 0.3$. Note the differences between the geodesics in (a) and Fig. 6.11. (b) depicts a close-up near the event horizon, where the whirling behaviour is clearly visible.

6.7 Resonant behaviour in Kerr spacetime

The search for chaos in quadratic gravity revolves around the study of resonant orbits. We will now apply the earlier defined theoretical framework to build a concrete characterisation these resonances.

6.7.1 Resonant orbits

As discussed earlier in this thesis, resonant orbits display periodicity in at least two variables. In particular, orbits with rational rotation numbers are resonant orbits. Using our framework for the numerical evaluation of orbits, we are able to keep track of piercings of the Poincaré slice as they happen during the progressive evaluation of the equations of motion. For our computations, we will define the rotation number using piercings of the equatorial plane from below, for example $p_y > 0$ in prolate spheroidal coordinates.

One way of finding resonant orbits is by tuning the initial conditions until the calculated rotation number is equal to a rational value. In particular, we vary the initial radial coordinate until such an orbit is found. In Fig. 6.17, two examples resonant orbits are presented, along with a non-resonant counterexample. From the orbital diagrams themselves, one can see that the non-resonant orbit pierces the equatorial plane at continually differing radial coordinates, progressively filling out the full radial interval between the apoapsis and periapsis of the orbit. This is also seen in the corresponding phase space: as the evaluation time progresses, a full curve around the fixed point is filled. This is in correspondence with an analytical plot of the phase space like Fig. 6.6. In Fig. 6.18, the geodesic solution from Fig. 6.17c is presented in Cartesian 3-space.

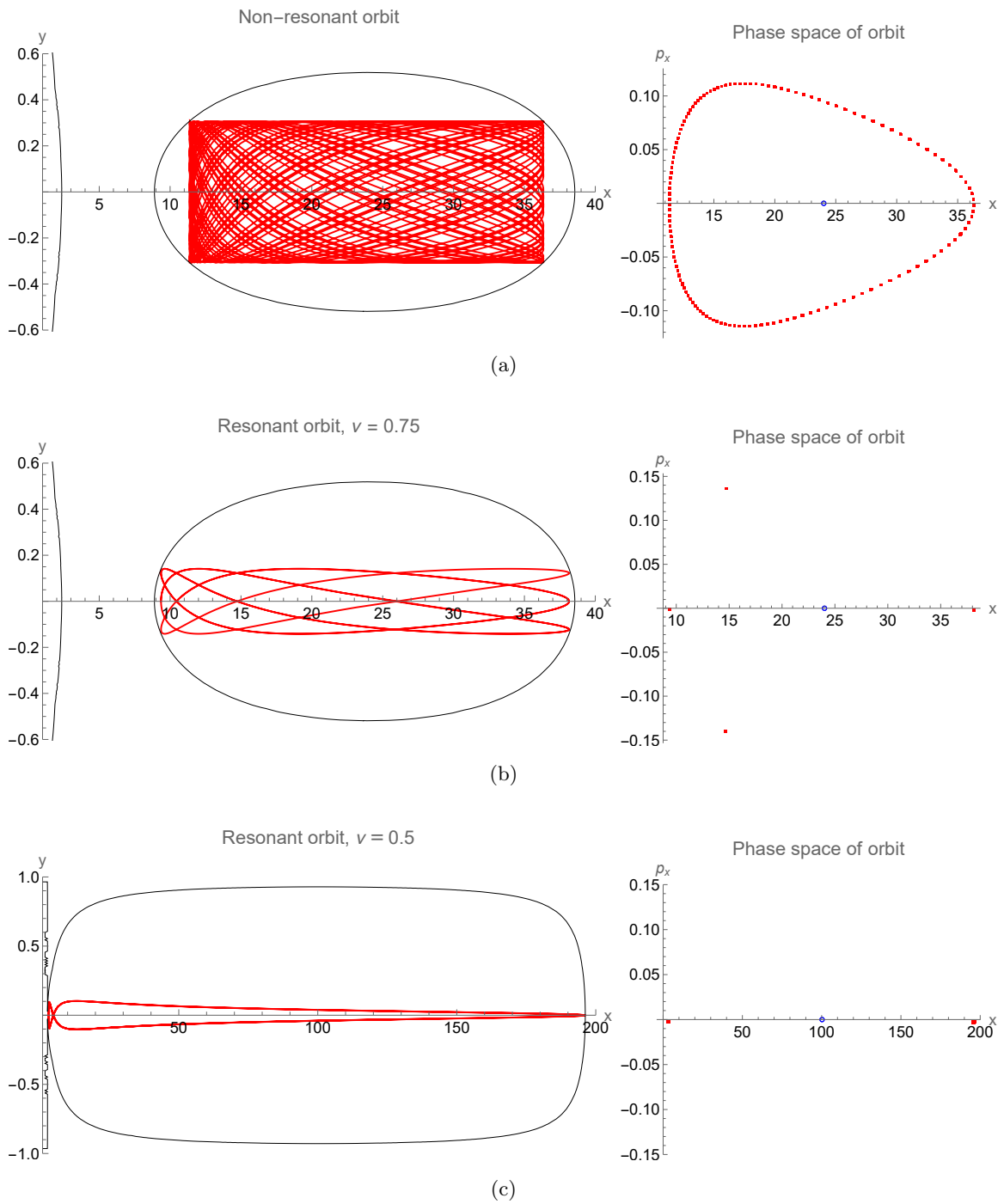


Figure 6.17: Example of non-resonant (a) and resonant (b, c) orbits and the corresponding piercings of the Poincaré slices. For (a) and (b) we have $E = 0.98$, $L_z = -4.5$ and $\chi = 0.3$. For (c), we have $E = 0.995$, $L_z = 3.75365$ and $\chi = 0.2$. The fixed points are indicated in blue.

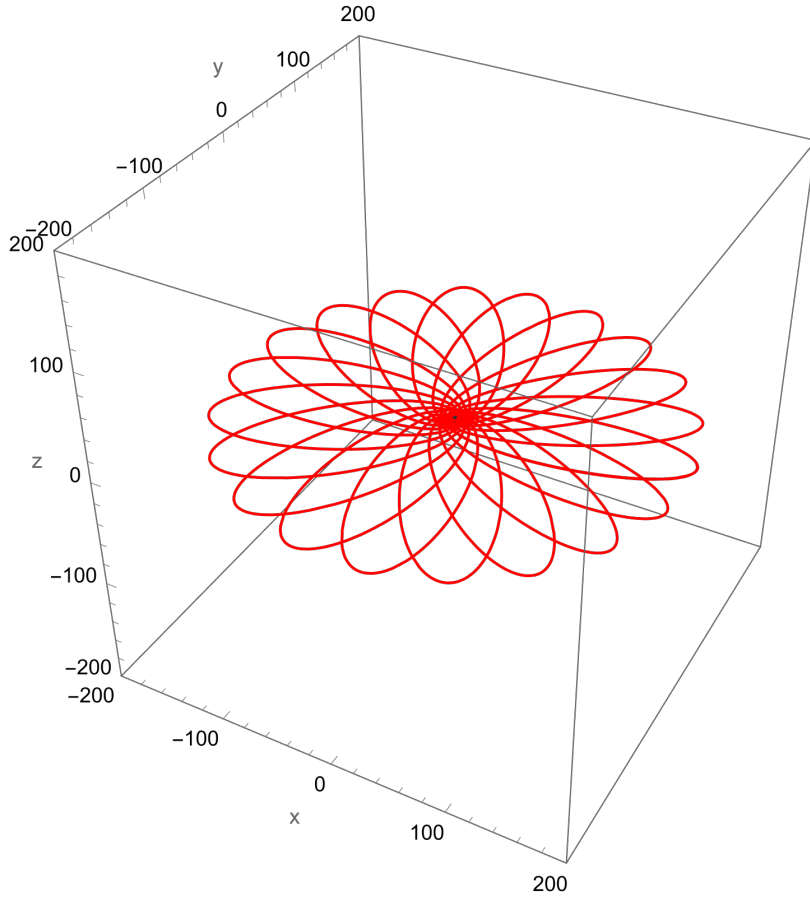


Figure 6.18: The $1/2$ resonance from Fig. 6.17c evaluated in Cartesian 3-space.

In the resonant cases, we see that the orbit traces over itself, causing the equatorial plane to be crossed at the same distinct points in each orbital period. This causes the piercings of the Poincaré slice to be concentrated in the same distinct positions, as seen in the phase space representation of that orbit. This is in one-to-one correspondence with the rationality of the rotation number.

Of the two resonances, we see that the $1/2$ resonance is a much more extreme orbit than the $3/4$ resonance. Lower values of ν are located closer to the event horizon, requiring more extreme orbits to sample them [32]. In particular, the $1/2$ resonance should appear at $r_P \approx 4$ in Boyer-Lindquist coordinates and the $2/3$ resonance at $r_P \approx 5.4$ [28].

6.7.2 Rotation curve

We are now in a position to compute the rotation number of classes of geodesics. For this part of the analysis, we will use prolate spheroidal coordinates and consider a spacetime with parameters $E = 0.995$, $L_z = 3.75365$ and $\chi = 0.2$. We choose this particular parametrisation, since it was shown in recent literature that this allows us to cover several interesting orbital resonances [30]. This parametrisation generates an eccentric class of orbits, as can be seen from their characteristics in Fig. 6.19. The authors of Ref. [30] chose this parametrisation to maximise any deviations from

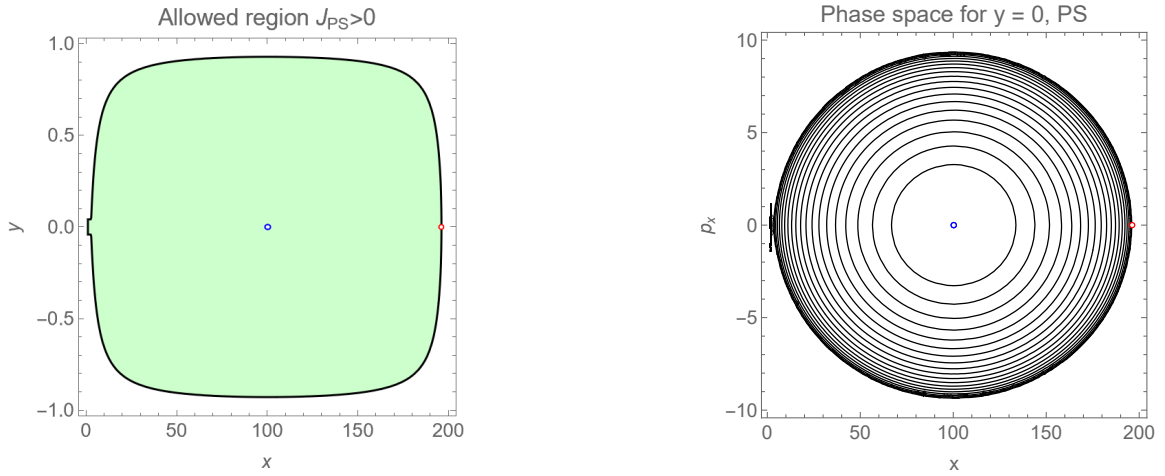


Figure 6.19: Allowed region and phase space of the Kerr spacetime for $E = 0.995$, $L_z = 3.75365$ and $\chi = 0.2$. Note how there is no root of the effective potential between the event horizon and fixed point, indicating that not all orbits in the outer region are by definition stable. The existence of the outer root puts a bound on these orbits; none escape to infinity. Furthermore, many of these orbits are very eccentric compared to previously examined cases, as can be seen in the range of x and p_x .

the Kerr solution arising from a modified gravity action, which is a topic we will discuss in the next chapter.

Using the rotation number calculation, we are able to produce the rotation curve of this spacetime. We set the lowest radial coordinate for the analysis at $x = 3$ and the upper bound at $x = 190$, such that almost the full range of physical, bound orbits in this spacetime is covered. In Fig. 6.20, we see the result of this computation. Starting from the edges of the rotation curve, one can see that the rotation number continuously increases until the fixed point, where a local maximum exists. The curve is then mirrored beyond the fixed point. The latter can be understood by recalling that orbits trace out symmetric rectangles in the physical space, centered around the fixed point.

In the range of the rotation number, one can see that this parametrisation indeed covers several interesting resonances. The $\nu = 1/2$ resonance is located near the event horizon. This resonance is particularly interesting, since the potential effects of chaotic behaviour in spacetimes deviating from Kerr are expected to be the strongest at this resonance value (see for example Ref. [32], where this is applied to Sagittarius A*). Other interesting resonances covered in this Kerr spacetime are for instance at $\nu = 3/5$, $2/3$ and $3/4$. Since this rotation curve was computed for the Kerr case, we know that there are no plateaus or discontinuities in this rotation curve at these values. However, it is around these resonances that we will search for discontinuities in modified gravity.

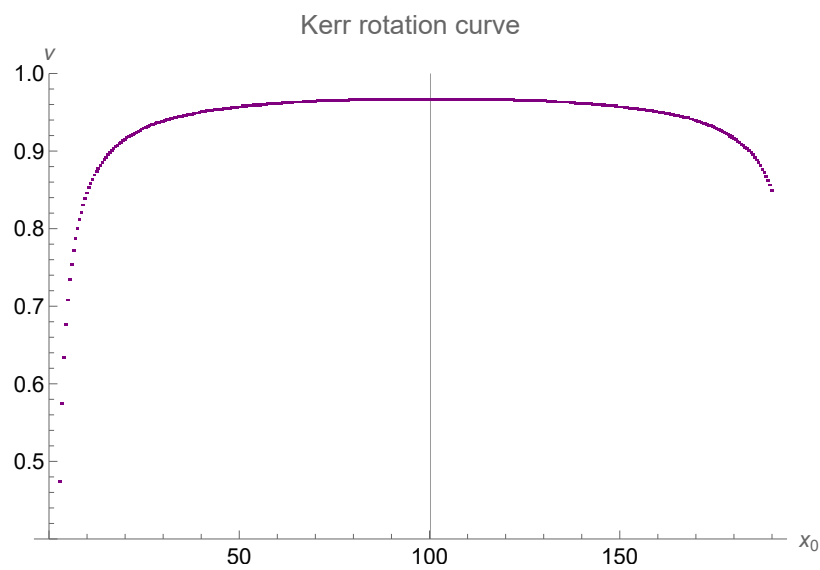


Figure 6.20: Rotation curve for a Kerr spacetime with $E = 0.995$, $L_z = 3.75365$ and $\chi = 0.2$. Initial radial coordinates x_0 are varied from 3 up till 190, with an interval of 0.5. The fixed point is indicated by the vertical line. The graph shows a clear mirror symmetry; if one were to continue evaluating the curve for higher x_0 , one would completely mirror the points on the other side of the fixed point. Since the rotation curve increases monotonically and continuously towards the fixed point, this parametrisation covers the $1/2$ resonance, as well as higher-order resonances.

Chapter 7

Scalar Gauss-Bonnet gravity

Now that we have a solid understanding of the Kerr spacetime, we are in a position to consider modifications to Kerr gravity. As discussed in Chapter 3, there are several ways in which one can make adjustments to general relativity in order to obtain alternate descriptions of gravity. We will now introduce one such theory and analyse how it differs from the regular Kerr solution to the Einstein field equations. We start from modifying the Einstein-Hilbert action itself and then compute part of the black hole solution; after that we will implement known approximate solutions to rotating Scalar Gauss-Bonnet black holes into our numerical methods. These implementations will then allow us to search for discontinuities in the rotation curve at several resonances, providing insight into potentially chaotic behaviour in this spacetime.

7.1 Introduction to Scalar Gauss-Bonnet and Einstein-dilaton Gauss-Bonnet theory

The theory we will study in this chapter is part of a group of theories known as *scalar Gauss-Bonnet gravity* (sGB). sGB gravities are a subclass of quadratic gravity theories, which add quadratic curvature correction terms to the Einstein-Hilbert action. The action corresponding to sGB gravity¹ has the following general form [60][61]

$$S_{sGB} = \frac{1}{2} \int \sqrt{-g} \left[R - \frac{1}{2} \nabla_\mu \phi_s \nabla^\mu \phi_s + \frac{\hat{\alpha} f(\phi_s)}{4} R_{GB}^2 \right],$$
$$R_{GB}^2 = R^2 - 4R_{\mu\nu}R^{\mu\nu} + R_{\mu\nu\rho\sigma}R^{\mu\nu\rho\sigma}, \quad (7.1)$$

where g is the determinant of the metric. R_{GB}^2 is referred to as the *Gauss-Bonnet invariant*, giving this theory its name. ϕ_s is a newly introduced *scalar field* (not to be confused with the ϕ coordinate) and $f(\phi_s)$ is some general coupling function between the scalar field and spacetime curvature. Finally, the coupling strength between the scalar field and the curvature term is encoded in the constant $\hat{\alpha} \geq 0$, where $\hat{\alpha} = 0$ returns the regular Einstein-Hilbert action and a free scalar field. In this formulation, the coupling constant $\hat{\alpha}$ has dimensions of length squared. By defining $\hat{\alpha}/M^2 \equiv \alpha$, we can remove the dimensionality of the coupling constant [60].

¹Different authors might use different conventions for some of the constants in this action. Please keep in mind that we define $\hat{\alpha}$ as the coupling constant, which is defined as α in Ref. [60]. In this thesis, α refers to the dimensionless form of $\hat{\alpha}$, which is the form of the coupling we will actually employ in the numerical calculations later.

This form of the action generates a class of gravities for different functions $f(\phi_s)$. Many forms of $f(\phi_s)$ have been studied and not every form of this function allows a black hole solution. One of the forms for which this is allowed is the following: in this thesis, we will consider a subclass of sGB gravities known as *Einstein-dilaton Gauss-Bonnet theory* (EDGB). Here, we have $f(\phi_s) = e^{\phi_s}$, such that the action takes the form

$$S_{EDGB} = \frac{1}{2} \int \sqrt{-g} \left[R - \frac{1}{2} \nabla_\mu \phi_s \nabla^\mu \phi_s + \frac{\hat{\alpha} e^{\phi_s}}{4} R_{GB}^2 \right]. \quad (7.2)$$

7.1.1 Relation to string theory

This form of the action is one of the best motivated quadratic gravity theories [60], because it arises naturally from string theory. It has its roots in the low-energy limit of heterotic string theory [61]. From a string theory perspective, the coupling constant $\hat{\alpha}$ actually consists of

$$\hat{\alpha} = \alpha' / g_s^2, \quad (7.3)$$

where α' is the *Regge slope* and g_s is a gauge coupling constant. The Regge slope is a well-known concept from string theory: it is a fundamental parameter which is related to *string tension* T via

$$T = \frac{1}{2\pi\alpha'}. \quad (7.4)$$

T has dimensionality of mass per unit length, which is why we refer to it as a tension. A specific choice of α' and hence T corresponds to a particular kind of string. Finding constraints on the value of α' via gravitational wave research is thus related to finding indirect evidence for or against particular versions of string theory on a deeply fundamental level. For further reading on string theory, readers are referred to an introductory book such as Ref. [41] or Ref. [45].

7.2 EDGB as a modified gravity theory

From Chapter 3, we know that there are different categories of modified gravities, each with their own attributes and complications. Let us formulate where EDGB fits in the spectrum of alternate gravity theories.

7.2.1 Quadratic curvature and a scalar field

The action of EDGB as presented in Eq. (7.2) consists of several different terms. The R term corresponds to the original Einstein-Hilbert action. The second term describes a free scalar field. From Chapter 3 one can recall that scalar fields can be introduced in the gravitational action as either being dependent on the curvature or as an extra degree of freedom. In this case, the free term in the action indicates that ϕ_s is in fact independent of R , such that this theory is a scalar-tensor theory.

The final term in the action consists of a coupling between this free scalar field and the Gauss-Bonnet invariant. The Gauss-Bonnet invariant means that this theory is quadratic in curvature. Hence, EDGB is both a higher curvature gravity theory and a scalar-tensor theory.

7.2.2 The scalar-curvature coupling

The coupling constant $\hat{\alpha}$ determines the strength of the perturbation to the Einstein-Hilbert action. By setting $\hat{\alpha} = 0$, one recovers general relativity, as well as a free scalar field which does not interact

with the geometry of spacetime. Furthermore, it is known that the dimensionless coupling α has a theoretical upper bound $\alpha \leq 0.691$ [61], which can be shown from the relation between the scalar field value at the event horizon and the coupling constant. This provides an upper limit on how large the deviation from the Kerr metric can be when testing this theory of modified gravity. There have also been experimental tests on the upper bound of α , which in the case of supermassive black holes are actually tighter than the theoretical limit [60]. However, due to the minuteness of the perturbation from Kerr due to the scalar field (which will become evident in Chapter 8), we will take the extreme scenario of $\alpha = 0.691$ as the maximum perturbation to the Einstein-Hilbert action. After all, we know that for smaller values of α , one has an even smaller perturbation of Kerr and hence one expects that the $\alpha = 0.691$ case provides an upper bound on the feature size. For recent studies on the upper bounds of α , readers are referred to for instance Ref. [62] and Ref. [63].

7.2.3 Instabilities and ghosts

In quadratic gravity, the Ostrogradski ghost modes introduced in Section 3.3 could arise, due to the higher curvature terms. However, sGB and EDGB are constructed in such a way that these ghosts are avoided.

The principle stability problem in gravities with a quadratic curvature term in the action is that variation of the action leads to a fourth order derivative of the metric with respect to time. As was demonstrated in Section 3.3, this is enough for instabilities to occur. However, the incorporation of an auxiliary scalar field in the action can negate this issue, as was shown in for instance Ref. [46]. If one couples a scalar field to the Gauss-Bonnet invariant and also has an independent term in the action for the scalar field (such that $\phi_s \neq \phi_s(R)$), the fourth order time derivatives are dealt with at the level of the equations of motion. This is precisely what we have in sGB gravities. Indeed, one can show that the equations of motion of a general sGB gravity then only contain time derivatives up to second order, as was shown in for instance Equations (23) and (24) of Ref. [46]. Hence, in sGB gravities, these kinds of instabilities do not appear. Since EDGB is a subclass of sGB, EDGB is also free of Ostrogradski instabilities. The lack of ghosts is another motivation for sGB as a candidate for modified gravity, independent of the string theory perspective explained before.

7.2.4 The existence of black holes

One might wonder whether the Kerr solution, which was of course formulated using the Einstein field equations, still holds in EDGB theory. In fact, it does not. One can show that the Kerr solution is not a solution to the EDGB field equations when the scalar field profile is non-trivial [23][64]. From this rises the necessity to find a new metric which parametrises a compact object in EDGB, but which maintains enough similarity to the Kerr solution that it is in line with our observations of gravity at the planetary length scale. It turns out that such solutions indeed exist and have been derived by several authors [60][65][66]. However, these are all non-analytical solutions; as of today there exists no closed-form analogue to the Kerr solution in EDGB spacetime. However, as we will see later, the expansions could be accurate enough to simulate the effect of the scalar field on the integrability of the spacetime.

Even when one finds a spacetime which looks like a rotating black hole, one needs to be careful that these solutions are physically viable. For instance, we require a black hole solution to be stable in order to be an accurate representation of an astronomical object. Studies such as Ref. [67] have shown that these solutions are numerically stable and hence appropriate for analyses representing astronomical events.

Just like in unmodified general relativity, we can vary the action to find the equations of motion of EDGB gravity. Unlike in general relativity however, we will vary not just the metric tensor $g_{\mu\nu}$, but also the scalar field ϕ_s . It is the interplay between scalar field ϕ_s and the curvature components in the action parameterised by $\hat{\alpha}$ which will generate a difference between regular general relativity and EDGB gravity. When varying the EDGB action, it is useful to note that one can rewrite the Gauss-Bonnet invariant in a more compact form; a derivation is provided in Appendix A.

7.3 Finding black hole solutions

For this project, we will mostly use the EDGB black hole spacetime parametrisation as computed by Ref. [60], since this solution goes up to high order in both spin and coupling. In order to find black hole solutions in EDGB spacetime, we will hence follow the line of reasoning in Ref. [60] and Ref. [61]. The authors of Ref. [61] varied the EDGB action and derived the line element of a static black hole, to which correction terms were added by Ref. [60] to generate a rotating black hole solution. We will now perform part of the derivation which yields the static black hole solution in EDGB gravity, in order to build an understanding on how such solutions are found. Specifically, we will present the derivation of the system of coordinate dependent equations of motion which need to be solved to obtain the static black hole line element, after which we discuss how these equations are solved.

7.3.1 Varying the action

From the action, we can identify three different Lagrangians: \mathcal{L}_{EH} , which corresponds to the Einstein-Hilbert term, \mathcal{L}_{ϕ_s} , corresponding to the scalar field, and \mathcal{L}_{int} , corresponding to the interaction term between the scalar field and the spacetime curvature. From Eq. (7.2) one sees that

$$\begin{aligned}\mathcal{L}_{EH} &= \frac{1}{2}\sqrt{-g}R \\ \mathcal{L}_{\phi_s} &= -\frac{1}{4}\sqrt{-g}\nabla_\mu\phi_s\nabla^\mu\phi_s, \\ \mathcal{L}_{int} &= \frac{1}{2}\sqrt{-g}\frac{\hat{\alpha}e^{\phi_s}}{4}R_{GB}^2.\end{aligned}\tag{7.5}$$

The full Lagrangian is then given by $\mathcal{L} = \mathcal{L}_{EH} + \mathcal{L}_{\phi_s} + \mathcal{L}_{int}$. By varying \mathcal{L} with respect to $g_{\mu\nu}$, one can find the metric equations of motion for EDGB:

$$\begin{aligned}
 0 = & -\frac{1}{8}e^{\phi_s}\hat{\alpha}\delta_\mu^\nu R^2 - \frac{1}{2}\delta_\mu^\nu R + \frac{1}{2}e^{\phi_s}\hat{\alpha}R_\mu^\nu R \\
 & - \frac{1}{2}e^{\phi_s}\hat{\alpha}\nabla_\mu(\phi_s)\nabla^\nu(\phi_s)R - \frac{1}{2}e^{\phi_s}\hat{\alpha}\nabla^\nu(\nabla_\mu(\phi_s))R + \frac{1}{2}e^{\phi_s}\hat{\alpha}\delta_\mu^\nu\nabla_\rho(\nabla^\rho(\phi_s))R \\
 & + \frac{1}{2}e^{\phi_s}\hat{\alpha}\delta_\mu^\nu\nabla_\rho(\phi_s)\nabla^\rho(\phi_s)R + R_\mu^\nu - 2e^{\phi_s}\hat{\alpha}R_\mu^\rho R_\rho^\nu + \frac{1}{2}e^{\phi_s}\hat{\alpha}\delta_\mu^\nu R_{\sigma\rho}R^{\rho\sigma} \\
 & + \frac{1}{2}e^{\phi_s}\hat{\alpha}R_\mu^{\rho\sigma\beta}R_{\rho\sigma\beta}^\nu - \frac{1}{8}e^{\phi_s}\hat{\alpha}\delta_\mu^\nu R_{\rho\sigma\beta\gamma}R^{\rho\sigma\beta\gamma} - \frac{1}{2}e^{\phi_s}\hat{\alpha}\nabla_\mu(\phi_s)\nabla^\nu(R) \\
 & - \frac{1}{2}e^{\phi_s}\hat{\alpha}\nabla_\mu(R)\nabla^\nu(\phi_s) - \frac{1}{2}\nabla_\mu(\phi_s)\nabla^\nu(\phi_s) - \frac{1}{2}e^{\phi_s}\hat{\alpha}\nabla^\nu(\nabla_\mu(R)) + e^{\phi_s}\hat{\alpha}\nabla^\nu(\phi_s)\nabla_\rho(R_\mu^\rho) \\
 & + e^{\phi_s}\hat{\alpha}\nabla_\mu(\phi_s)\nabla_\rho(R^{\nu\rho}) + e^{\phi_s}\hat{\alpha}\nabla_\rho(\nabla_\mu(R^{\nu\rho})) + e^{\phi_s}\hat{\alpha}R^{\nu\rho}\nabla_\rho(\nabla_\mu(\phi_s)) + e^{\phi_s}\hat{\alpha}\nabla_\rho(\nabla^\nu(R_\mu^\rho)) \\
 & + e^{\phi_s}\hat{\alpha}R_\mu^\rho\nabla_\rho(\nabla^\nu(\phi_s)) + \frac{1}{2}e^{\phi_s}\hat{\alpha}\delta_\mu^\nu\nabla_\rho(\nabla^\rho(R)) - e^{\phi_s}\hat{\alpha}\nabla_\rho(\nabla^\rho(R_\mu^\nu)) - e^{\phi_s}\hat{\alpha}R_\mu^\nu\nabla_\rho(\nabla^\rho(\phi_s)) \\
 & + \frac{1}{2}e^{\phi_s}\hat{\alpha}\nabla_\rho(\nabla_\sigma(R_\mu^{\nu\rho\sigma})) + e^{\phi_s}\hat{\alpha}\delta_\mu^\nu\nabla_\rho(\phi_s)\nabla^\rho(R) + e^{\phi_s}\hat{\alpha}\nabla_\mu(R_\rho^\nu)\nabla^\rho(\phi_s) \\
 & + e^{\phi_s}\hat{\alpha}R_\rho^\nu\nabla_\mu(\phi_s)\nabla^\rho(\phi_s) + e^{\phi_s}\hat{\alpha}\nabla^\nu(R_{\mu\rho})\nabla^\rho(\phi_s) + e^{\phi_s}\hat{\alpha}R_{\mu\rho}\nabla^\nu(\phi_s)\nabla^\rho(\phi_s) \\
 & - 2e^{\phi_s}\hat{\alpha}\nabla_\rho(R_\mu^\nu)\nabla^\rho(\phi_s) + \frac{1}{4}\delta_\mu^\nu\nabla_\rho(\phi_s)\nabla^\rho(\phi_s) - e^{\phi_s}\hat{\alpha}R_\mu^\nu\nabla_\rho(\phi_s)\nabla^\rho(\phi_s) \\
 & - 2e^{\phi_s}\hat{\alpha}\delta_\mu^\nu\nabla^\rho(\phi_s)\nabla_\sigma(R_\rho^\sigma) + e^{\phi_s}\hat{\alpha}\nabla^\rho(\phi_s)\nabla_\sigma(R_\mu^{\nu\sigma}) + e^{\phi_s}\hat{\alpha}\nabla^\rho(\phi_s)\nabla_\sigma(R_\mu^{\nu\sigma}) \\
 & - e^{\phi_s}\hat{\alpha}\delta_\mu^\nu\nabla_\sigma(\nabla_\rho(R^{\rho\sigma})) + \frac{1}{2}e^{\phi_s}\hat{\alpha}\nabla_\sigma(\nabla_\rho(R_\mu^{\nu\rho\sigma})) - e^{\phi_s}\hat{\alpha}\delta_\mu^\nu R^{\rho\sigma}\nabla_\sigma(\nabla_\rho(\phi_s)) \\
 & - e^{\phi_s}\hat{\alpha}\delta_\mu^\nu R_{\sigma\rho}\nabla^\rho(\phi_s)\nabla^\sigma(\phi_s) + e^{\phi_s}\hat{\alpha}R_{\mu\rho\sigma}^\nu\nabla^\rho(\phi_s)\nabla^\sigma(\phi_s) + e^{\phi_s}\hat{\alpha}R_{\mu\rho\sigma}^\nu\nabla^\sigma(\nabla^\rho(\phi_s)). \tag{7.6}
 \end{aligned}$$

This expression is very messy and we cannot infer much from it. It is worth mentioning that it is possible to rewrite the above expression for vacuum spacetimes as [68]:

$$R_{\mu\nu} = 2\nabla_\mu\phi_s\nabla_\nu\phi_s - 4\hat{\alpha}\left(P_{\mu\rho\nu\sigma} - \frac{1}{2}g_{\mu\nu}P_{\rho\lambda\sigma}^\lambda\right)\nabla^\rho\nabla^\sigma e^{\phi_s}, \tag{7.7}$$

where $P_{\mu\nu\rho\sigma} \equiv R_{\mu\nu\rho\sigma} - 2g_{\mu[\rho}R_{\sigma]\nu} + 2g_{\nu[\rho}R_{\sigma]\mu} + g_{\mu[\rho}g_{\sigma]\nu}R$. How one obtains this result² is shown in Appendix A of Ref. [68]; it involves taking the trace of the equations of motion, which is why the term proportional to R has vanished. However, since we will directly apply a chart to the equations of motion, this simplification is not necessary for us to perform. Furthermore, working further from Eq. (7.6) reduces our dependency on external results. By setting $\hat{\alpha} \rightarrow 0$ and moving down the ν index in Eq. (7.6), we recover the original Einstein field equations as well as some terms of the free scalar field:

$$0 = \frac{1}{4}g_{\mu\nu}\nabla_\rho(\phi_s)\nabla^\rho(\phi_s) - \frac{1}{2}Rg_{\mu\nu} + R_{\mu\nu} - \frac{1}{2}\nabla_\mu(\phi_s)\nabla_\nu(\phi_s), \tag{7.8}$$

which was expected from the form of the action. We can also vary \mathcal{L} with respect to ϕ_s to find the remaining equation of motion corresponding to the scalar field:

$$0 = \hat{\alpha}e^{\phi_s}R_{\mu\nu}R^{\mu\nu} - \frac{1}{4}\hat{\alpha}e^{\phi_s}R_{\gamma\nu\rho\sigma}R^{\gamma\nu\rho\sigma} - \nabla_\gamma(\nabla^\gamma(\phi_s)) - \frac{1}{4}\hat{\alpha}R^2e^{\phi_s}, \tag{7.9}$$

where putting the coupling constant to zero yields the remaining free scalar field term.

²Be very mindful of the differences in conventions for the sGB action as presented in this thesis and in Ref. [68]; these were accounted for in Eq. 7.7.

7.3.2 Derivation of the static black hole equations

Using the equations of motion, one can derive the line element corresponding to a static black hole in EDGB spacetime. In order to find a black hole solution which satisfies these equations of motion, one needs to make an ansatz on the form of the metric and then solve for the unknown components. In particular, we will choose a Boyer-Lindquist coordinate system and make an ansatz of the form

$$\boxed{ds^2 = -e^\Gamma dt^2 + e^{-\Lambda} dr^2 + r^2 d\theta^2 + r^2 \sin^2 \theta d\phi^2}, \quad (7.10)$$

where $\Gamma = \Gamma(r)$ and $\Lambda = \Lambda(r)$ are spherically symmetric functions which need to be determined. We will also assume that the scalar field is spherically symmetric, i.e. $\phi_s = \phi_s(r)$. This is motivated by the fact that the metric should exhibit the same spherical symmetry as general relativity's Schwarzschild solution.

One can now substitute this ansatz in the equations of motion Eq. (7.6) and Eq. (7.9) to obtain the coordinate-dependent form of these equations. These can then be used to solve for the unknown functions Γ and Λ . Once the forms of these functions are known, one has derived a line element corresponding to, in our case, a static black hole in EDGB spacetime. However, this method can also be applied to find solutions to the (modified) Einstein field equations in general. As mentioned before, these computations are best performed by using a symbolic programming language, due to the extensive form of Eq. (7.6) in particular. We will now start the computation of the coordinate dependent equations of motion, starting with the one corresponding to the scalar field variation of the action.

Scalar field equation of motion

By substituting the line element in Eq. (7.9) and performing many simplification steps, we arrive at

$$\begin{aligned} 0 = & \hat{\alpha} e^{\phi_s} (-2(e^\Lambda - 1)\Gamma'' - (3e^\Lambda - 1)\Gamma'\Lambda' - ((e^\Lambda - 1)\Gamma'^2)) \\ & + r(-(\phi'_s(r(\Gamma' + \Lambda') + 4)) - 2r\phi''_s). \end{aligned} \quad (7.11)$$

Let us verify that this result is consistent with what was found by previous researchers. Through some algebraic manipulation, this equation can be recast as

$$\begin{aligned} & \hat{\alpha} e^{\phi_s} (-2(e^\Lambda - 1)\Gamma'' - (3e^\Lambda - 1)\Gamma'\Lambda' - ((e^\Lambda - 1)\Gamma'^2)) \\ & = -r(-(\phi'_s(r(\Gamma' + \Lambda') + 4)) - 2r\phi''_s) \\ \Rightarrow & \frac{\hat{\alpha} e^{\phi_s}}{r} ((1 - e^\Lambda)\Gamma'^2 + (1 - 3e^\Lambda)\Gamma'\Lambda' + 2(1 - e^\Lambda)\Lambda'') = 4 + r(\Gamma' + \Lambda')\phi'_s + 2r\phi''_s \\ \Rightarrow & \frac{\hat{\alpha} e^{\phi_s}}{2r^2} ((1 - e^\Lambda)\Gamma'^2 + (1 - 3e^\Lambda)\Gamma'\Lambda' + 2(1 - e^\Lambda)\Lambda'') = \left(\frac{2}{r} + \frac{\Gamma' + \Lambda'}{2}\right)\phi'_s + \phi''_s \\ \Rightarrow & \frac{\hat{\alpha} e^{\phi_s}}{2r^2} ((2\Gamma'' + \Gamma'(\Gamma' + \Lambda'))(1 - e^\Lambda) - 2e^\Lambda\Gamma'\Lambda') = \left(\frac{2}{r} + \frac{\Gamma' + \Lambda'}{2}\right)\phi'_s + \phi''_s, \end{aligned} \quad (7.12)$$

which is indeed the same result as Ref. [60] and Ref. [61] up to³ $\Lambda \rightarrow -\Lambda$ (and of course $\Lambda' \rightarrow -\Lambda'$). Note that there seems to be a factor $\frac{1}{2}$ different in the scalar field equation of motion presented in

³Please note that in the line element ansatz in Ref. [61] one does not have a minus sign in front of Λ in the exponent, whereas Eq. (7.10), which is based on Ref. [60], does have a minus sign there. However, Ref. [60] does not seem to have taken this difference into account when deriving the static equations of motion and presents the exact results from Ref. [61]. This error does not propagate further into their calculations and is hence most likely a typographical error in the definition of the line element ansatz. In this thesis, we derive the equations ourselves using the line element from Ref. [60] and present the equations of motion one then finds.

Ref. [60]; this is most likely a typographical error, as the equations we derived here are consistent with Ref. [61], on which the authors of Ref. [60] based this part of the computation.

Metric equations of motion

In a similar fashion, we can substitute the line element ansatz in Eq. (7.6) to obtain more constraints on Γ and Λ . In this case, we need to pick several different components of the tensor equation to obtain additional constraints in Boyer-Lindquist coordinates. In particular, the equations resulting from the (r, r) , (t, t) and (θ, θ) components of the tensor equation provide these constraints.

Let us start with the (r, r) equation. By inserting the ansatz and letting $\mu = \nu = r$ in tensor equation Eq. (7.6) and performing several appropriate simplification steps, one obtains the following equation:

$$4(e^\Lambda - 1) = e^\Lambda [r^2 \phi_s'^2 + 2\Gamma' (-2r + e^{\phi_s} (3e^\Lambda - 1) \hat{\alpha} \phi_s')] , \quad (7.13)$$

which can be rewritten as

$$\begin{aligned} \Rightarrow (1 - e^{-\Lambda}) &= \frac{r^2 \phi_s'^2}{4} + \Gamma' \left(-r - \frac{\hat{\alpha} e^{\phi_s}}{2} (1 - 3e^\Lambda) \phi_s' \right) \\ \Rightarrow \Gamma' \left(1 + \frac{\hat{\alpha} e^{\phi_s}}{2r} (1 - 3e^\Lambda) \phi_s' \right) &= \frac{r \phi_s'^2}{4} + \frac{e^{-\Lambda} - 1}{r} , \end{aligned} \quad (7.14)$$

which is consistent with Ref. [60] and Ref. [61] up to $\Lambda \rightarrow -\Lambda$.

Applying the same method to the (t, t) component of the tensor equation, one obtains

$$4(e^\Lambda - 1) = -e^\Lambda [r(4\Lambda' + r\phi_s'^2) - 2e^{\phi_s} \hat{\alpha} ((3e^\Lambda - 1)\Lambda' \phi_s' + 2(e^\Lambda - 1)(\phi_s'^2 + \phi_s''))] . \quad (7.15)$$

This equation is somewhat similar to the (r, r) case in that it can be rewritten as

$$\begin{aligned} \Rightarrow 4(1 - e^{-\Lambda}) + 4r\Lambda' &= -r^2 \phi_s'^2 - 2e^{\phi_s} \hat{\alpha} ((1 - 3e^\Lambda)\Lambda' \phi_s' + 2(1 - e^\Lambda)(\phi_s'^2 + \phi_s'')) \\ \Rightarrow -\Lambda' (4r + 2e^{\phi_s} \hat{\alpha} \phi_s' (1 - 3e^\Lambda)) &= r^2 \phi_s'^2 + 4(1 - e^{-\Lambda}) + 4e^{\phi_s} \hat{\alpha} (1 - e^\Lambda)(\phi_s'^2 + \phi_s'') \\ \Rightarrow -\Lambda' \left(1 + \frac{\hat{\alpha} e^{\phi_s}}{2r} \phi_s' (1 - 3e^\Lambda) \right) &= \frac{r \phi_s'^2}{4} + \frac{1 - e^{-\Lambda}}{r} + \frac{\hat{\alpha} e^{\phi_s}}{r} (1 - e^\Lambda)(\phi_s'^2 + \phi_s'') , \end{aligned} \quad (7.16)$$

which is again consistent with Ref. [60] and Ref. [61] upon flipping the sign of Λ .

Finally, we compute the (θ, θ) component of the equations of motion. We obtain

$$\begin{aligned} \hat{\alpha} e^{\Lambda + \phi_s} [2\Gamma' \phi_s'' + \phi_s' (2\Gamma'' + \Gamma' (\Gamma' + 3\Lambda' + 2\phi_s'))] &= 2(r\Gamma'' + \Lambda') + \Gamma' (r\Lambda' + 2) \\ &\quad + r\Gamma'^2 + r\phi_s'^2 . \end{aligned} \quad (7.17)$$

This expression can be algebraically manipulated as follows:

$$\begin{aligned} \Rightarrow \frac{\hat{\alpha} e^{\Lambda + \phi_s}}{r} \left[\Gamma' \phi_s'' + \phi_s' \left(\Gamma'' + \Gamma' \left(\frac{\Gamma' + 3\Lambda'}{2} + \phi_s' \right) \right) \right] &= \Gamma'' + \frac{\Lambda'}{r} + \Gamma' \left(\frac{\Lambda'}{2} + \frac{1}{r} \right) + \frac{\Gamma'^2}{2} + \frac{\phi_s'^2}{2} \\ \Rightarrow -\frac{\phi_s'^2}{2} + \frac{\hat{\alpha} e^\Lambda}{r} \left[\Gamma' \phi_s'' + \Gamma'' \phi_s' + \phi_s'^2 \Gamma' + \frac{\Gamma' \phi_s'}{2} (\Gamma' + 3\Lambda') \right] &= \Gamma'' + \frac{\Gamma'}{2} (\Gamma' + \Lambda') + \frac{\Gamma' + \Lambda'}{r} \end{aligned}$$

$$\Rightarrow -\frac{\phi_s'^2}{2} + \frac{\hat{\alpha}e^\Lambda}{r} \left[\phi_s' \Gamma'' + \Gamma'(\phi_s'' + \phi_s'^2) + \frac{\Gamma' \phi_s'}{2}(\Gamma' + 3\Lambda') \right] = \Gamma'' + \frac{\Gamma'}{2}(\Gamma' + \Lambda') + \frac{\Gamma' + \Lambda'}{r}, \quad (7.18)$$

which finally shows that all of the equations of motion we found from varying S_{EDGB} mapped to the generalised Boyer-Lindquist chart are indeed consistent with earlier findings, adjusted for conventions.

7.3.3 Solving for Γ and Λ

From the equations of motion derived above, it is possible to find a solution for the unknown functions in the line element corresponding to a black hole. First, by exploiting the fact that these equations are not independent, one can show that the (r, r) equation provides the solution [60][61]

$$e^\Lambda = \frac{-\beta + \sqrt{\beta^2 - 4\gamma}}{2}, \quad (7.19)$$

with

$$\begin{aligned} \beta &= \frac{\phi_s'^2 r^2}{4} - 1 - \Gamma' \left(r + e^{\phi_s} \frac{\phi_s'}{2} \right), \\ \gamma &= \frac{3}{2} \Gamma' \phi_s' e^{\phi_s}. \end{aligned} \quad (7.20)$$

After this, one is left with two independent equations, which take the form of

$$\begin{aligned} \phi_s'' &= -d_1/d, \\ \Gamma'' &= -d_2/d, \end{aligned} \quad (7.21)$$

where d, d_1, d_2 are functions dependent on r given in the appendix of Ref. [61]. Solving these equations leads to the static EDGB black hole; however, only numerical and expanded solutions to these equations exist. The static solution exhibits spherical symmetry by construction; this immediately indicates that the spacetime is integrable [30]. For this reason, as well as the fact that astrophysical black holes practically always exhibit non-zero rotation, we will move on to how one expands around the static solution to obtain a rotating black hole spacetime in EDGB theory.

7.3.4 From static to rotating black hole

Because we do not have a closed-form expression of the equations of motion of the static black hole, it is not difficult to imagine that the rotating case only complicates matters further. The authors of Ref. [60] expanded the static solutions up to high order in spin and coupling in order to obtain an approximate rotating solution. We will now discuss their considerations in constructing this spacetime.

First, one starts by adding spin corrections to the static solution. One starts by writing the spinning line element as a perturbation to the static solution:

$$ds^2 = -e^\Gamma(1 + 2h)dt^2 + e^{-\Lambda}(1 + 2m)dr^2 + r^2(1 + 2k)(d\theta^2 + \sin^2 \theta [d\phi - \hat{\omega}dt]^2), \quad (7.22)$$

where $\hat{\omega}, h, m, k$ are functions of θ and r . The axial symmetry of the problem is encoded in the dependencies of these functions. One can recognise that this kind of symmetry allows us to reformulate

these functions in terms of Legendre polynomials, such that one obtains

$$\begin{aligned}
 \hat{\omega} &= \sum_{n \text{ odd}}^{N-q} \sum_{l \text{ odd}}^n \chi^n \omega_l^{(n)}(r) S_l(\theta), \\
 h &= \sum_{n \text{ even}}^{N-p} \sum_{l \text{ even} \ \& \ 0}^n \chi^n h_l^{(n)}(r) P_l(\cos \theta), \\
 m &= \sum_{n \text{ even}}^{N-p} \sum_{l \text{ even} \ \& \ 0}^n \chi^n m_l^{(n)}(r) P_l(\cos \theta), \\
 k &= \sum_{n \text{ even}}^{N-p} \sum_{l \text{ even} \ \& \ 0}^n \chi^n k_l^{(n)}(r) P_l(\cos \theta),
 \end{aligned} \tag{7.23}$$

with P_l the Legendre polynomials, $p = 0$ if the spin order expansion N is even and $p = 1$ otherwise, $q = 1$ if N is even and $q = 0$ otherwise and $S_l \equiv -\frac{dP_l}{d\theta} / \sin \theta$. It should be noted that the radial functions in these sums are of order $\mathcal{O}(\chi^n)$. Furthermore, the scalar field is expanded as

$$\Phi_s(r) = \phi_s(r) + \sum_{n \text{ even}}^{N-p} \sum_{l \text{ even} \ \& \ 0}^n \chi^n \phi_{s,l}^{(n)}(r) P_l(\cos \theta). \tag{7.24}$$

By substituting Eq. (7.23) in Eq. (7.22) and inserting the result combined with Eq. (7.24) in the field equations described in Section 7.3.2, one can in principle solve the system to obtain a full set of equations describing the rotation expansion. The linear order expansion turns out to reduce to the static case with a non-zero gravitomagnetic term, whereas the exact form of the higher order terms depends on the parity of N and require contractions with Legendre polynomials. For further details, the reader is referred to the original paper [60]. Using this method, the authors computed spin correction terms up to fifth order.

In principle, one now has a set of equations fully describing the functionals, which when solved for give a line element. However, it turns out that it is not feasible to solve for these equations without further approximations, even numerically. Since the coupling constant is smaller than 1, it can be motivated that one can employ a *small-coupling approximation* in order to make the equations more manageable. This involves expanding the line element with rotation corrections in the coupling constant around 0. However, since the maximum theoretical constraint on α is 0.691, the "small-ness" of the coupling is debatable. Nevertheless, the authors of Ref. [60] compensate for this by computing the correction terms in coupling up to higher order than the spin corrections: up to seventh order. Since the scalar field is assumed to be purely radial, this is just a regular Taylor expansion, without Legendre polynomials. In the end, we are left with a line element which was expanded in spin up to order 5 and in coupling up to order 7.

7.4 Accuracy of the line element at zero coupling

Since this line element was computed by performing two expansions at once, it is evident that it will not be an exact match with the Kerr solution, or even an expansion of the Kerr solution. The authors of Ref. [60] performed several analyses of the accuracy of both the spin and coupling expansion by investigating several interesting points in a rotating black hole spacetime. It is noted that at full order in spin and coupling, the error in for instance the ISCO radius can become up to 2.5%, depending on the spin and coupling values. As expected from the way the expansions were

performed, the solution is the most accurate when both spin and coupling are set to 0. However, any potential effects of modified gravity are the most evident at higher values of spin and coupling. Hence, a compromise needs to be made between the accuracy of the result and the strength of the underlying effect. Before we investigate this however, let us put the line element from Ref. [60] to the test via the effective potential formalism as developed in Chapter 5.

In order to assess the accuracy of the line element, we will compare it to several other theoretically equivalent spacetimes. In particular, we will use the exact Kerr solution and an expansion of the Kerr solution in spin at several orders to see whether the zero-coupling case of the EDGB line element indeed reproduces the Kerr solution, as it should. An alternative EDGB line element is also available, which was provided up to quadratic order [30][65]. This line element of EDGB is particularly interesting since a similar study into EMRIs in EDGB gravity was performed using a higher-order version of this line element. However, it should also be noted that the authors of Ref. [65] use a 'Boyer-Lindquist-like' coordinate system, which seems to be slightly different from the usual Boyer-Lindquist coordinates, presumably via a particular coordinate transformation. Because this parametrisation of the Kerr solution hence might have been based on different assumptions than ours, we will proceed with the line element of which the derivation was outlined in the previous sections. However, we will use the alternative EDGB line element at quadratic order to test our rotation curve framework later when we perform the actual investigation into chaotic motion in EDGB gravity.

7.4.1 Effective potential deviation

For our analysis, the most important metric for the accuracy of the expansion is how the effective potential is changed by using a different line element. After all, the initial conditions of the geodesics depend on this quantity, as well as the allowed region of orbits in spacetime. By performing a spin expansion of the Kerr solution and computing J_{BL} for both the Kerr expansion and the line element from Ref. [60], we can see how well the EDGB line element reduces to the Kerr solution for different parameter settings. The reason we use the Kerr expansion in addition to the exact Kerr solution is that performing an expansion will always introduce an error in the calculations; we are interested in whether the EDGB line element possesses an additional inaccuracy due to the spin and coupling expansions relative to the spin expansion of the Kerr solution.

In Fig. 7.1, we see a comparison of the allowed region of both the EDGB line element at zero coupling and the Kerr solution expanded to fifth order in spin. One can qualitatively already see that the solutions look very similar in the outer region of the effective potential, whereas there are significant differences near the event horizon, particularly inside the ISO radius. Furthermore, around the equatorial plane the solution seems to be the most accurate. This can be explained by the fact that many terms in both expansions likely reduce to zero when $\theta = \pi/2$ due to the presence of trigonometric functions in both spacetimes. This is of particular importance for us, since we will track piercings of the equatorial plane in order to construct a Poincaré slice from which to compute the rotation curve. This feature of the spacetime approximations holds for different settings of E and L_z , as seen in Fig. 7.1.

A more quantitative comparison can be made by comparing the location of the first root of the effective potential using different line elements. As introduced in Chapter 6, this was defined as the innermost root of the outer region of the effective potential, i.e. the closest allowed stable approach if the outer region is separated from the event horizon. In Fig. 7.2 we see the location of this point for the EDGB solutions at fifth spin order, compared to the expanded Kerr and exact Kerr

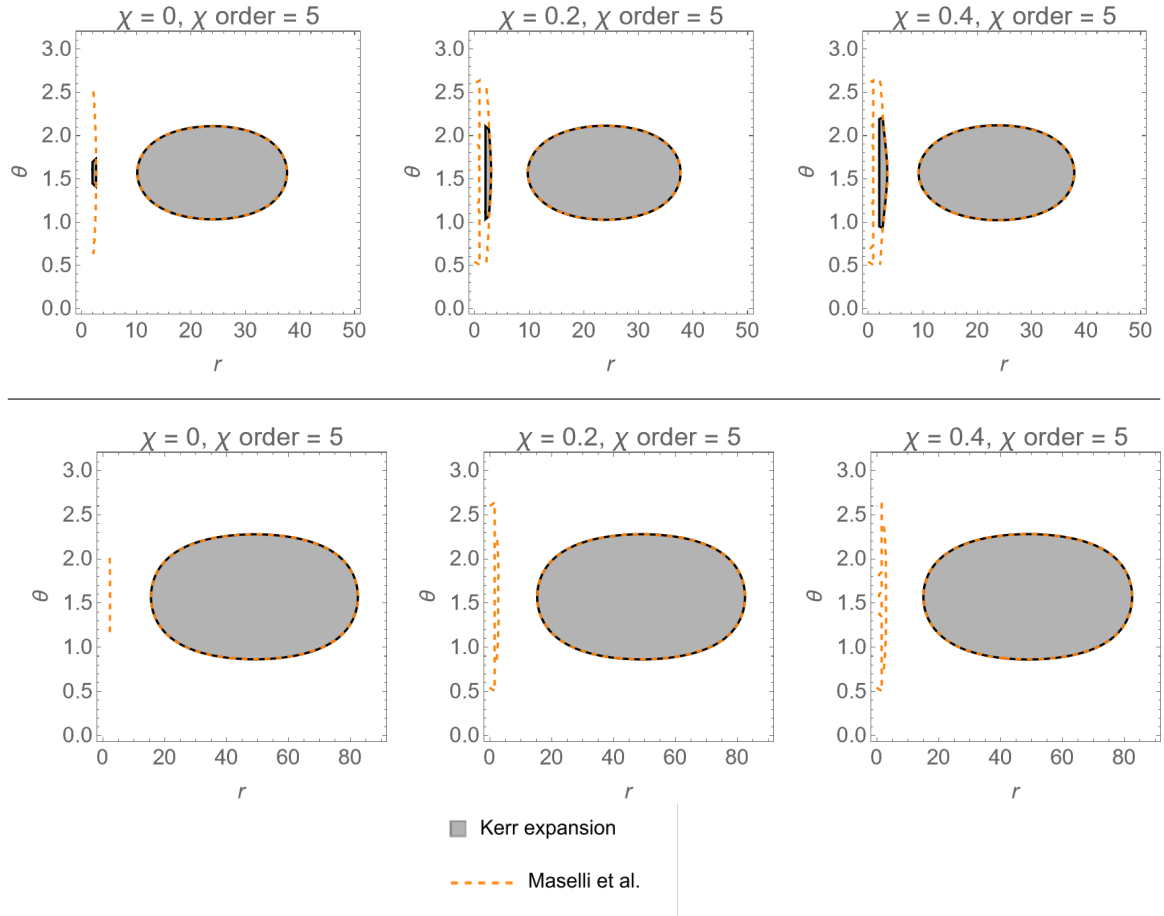


Figure 7.1: Allowed regions of J_{BL} using the fifth order expansion in spin of the Kerr metric and the EDGB line element, the latter at zero coupling. *Above*: $E = 0.98$, $L_z = -4.5$. *Below*: $E = 0.99$, $L_z = -5.5$.

solutions. The coupling to the Gauss-Bonnet invariant was set again set to zero. We see that a slight difference between the exact and the EDGB solution appears as spin is increased, which warrants a more precise investigation. After all, we expect to obtain exactly the Kerr solution when $\alpha = 0$.

In order to more precisely determine how much the EDGB solution with no coupling differs from the Kerr solution, we compute the relative deviation of the first root location of the EDGB spacetime compared to the Kerr expansion. In Fig. 7.3a, we see the relative deviation between the Kerr expansion and the EDGB line element first root locations for the same parameters. For these settings, the deviation is small. However, the error does exponentially grow as spin increases. This means that for larger spin, even small increases in value will cause much larger deviations from the Kerr solution. As demonstrated in Fig. 7.3b, the Kerr expansion also has this inaccuracy with respect to the exact Kerr solution, but it is much smaller. These deviations are potentially larger than those caused by the scalar coupling, clouding our potential results. Hence, it is imperative to choose the black hole spin such that the error is still reasonable whilst maximising the Kerr perturbation.

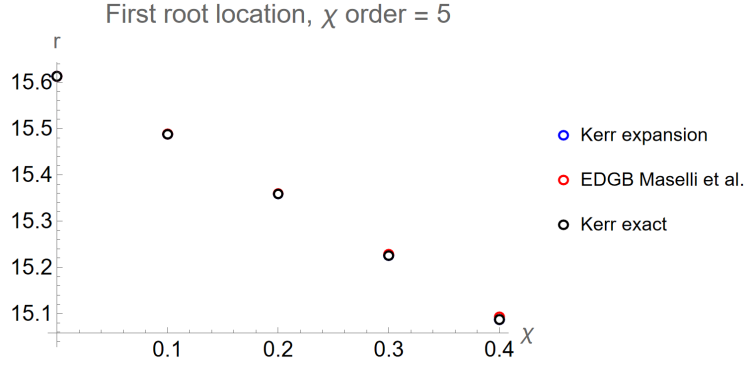
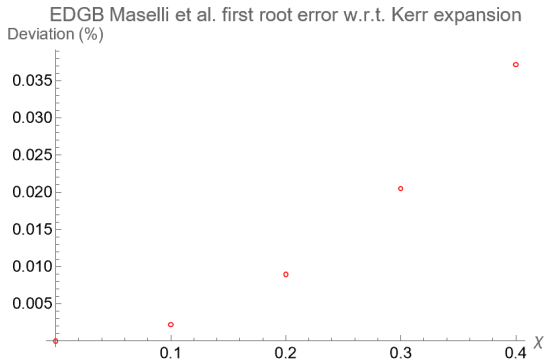
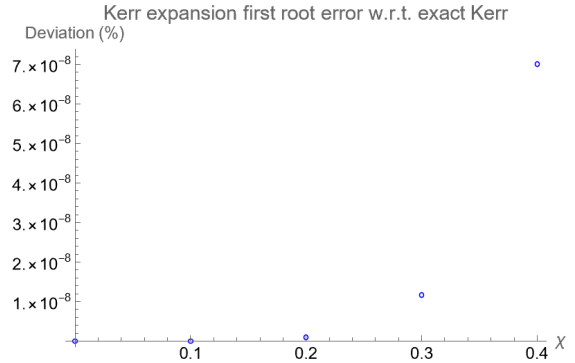


Figure 7.2: Locations of the first root in the effective potential for several different versions of the different Kerr-like line elements. The two expansions are up to fifth order in spin. For the EDGB line element, the coupling set to zero and the chosen parameters were $E = 0.99$, $L_z = -5.5$. A slight deviation from the exact Kerr solution appears as χ increases.



(a) Error of the EDGB line element at fifth order in spin as compared to the fifth order **expansion** of the Kerr solution for $E = 0.99$, $L_z = -5.5$. The error gets exponentially larger as the black hole spin is increased, but remains small in this range of spin values.



(b) Error of the Kerr line element at fifth order in spin as compared to the **exact** Kerr solution for $E = 0.99$, $L_z = -5.5$. We see that the error is much smaller than in Fig. 7.3a, as expected.

Figure 7.3: First root errors of the EDGB and Kerr approximations. NB: the EDGB line element is compared to the expanded Kerr line element, whereas the expanded Kerr line element is compared to the exact Kerr solution.

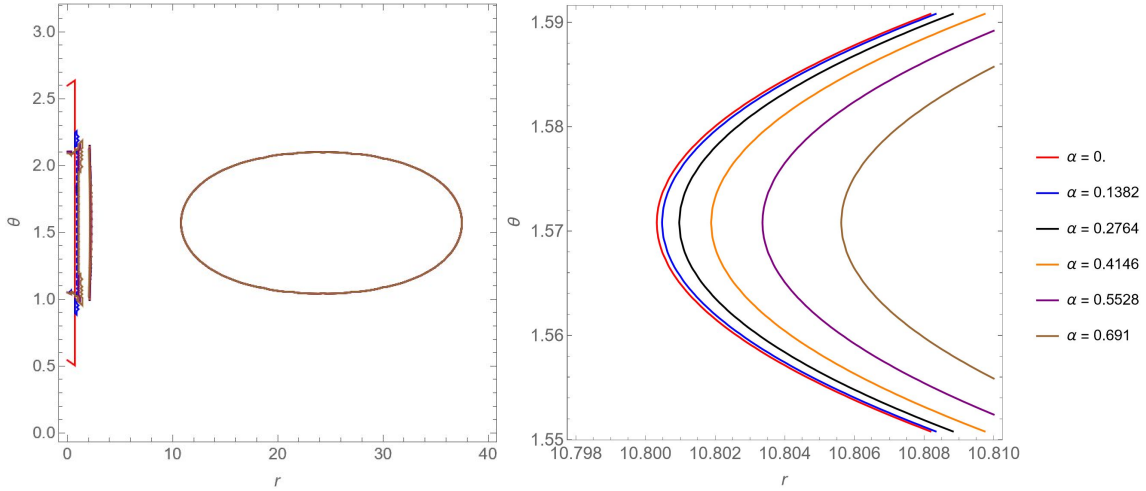


Figure 7.4: Dependency of the roots of the effective potential of an EDGB spacetime with $E = 0.98$, $L_z = 4.5$ and $\chi = 0.3$ on the value of α . On the right, we see a zoomed-in version of the plot on the left. Note the subtlety in the difference of the first root radius. The erratic behaviour of the plot near the event horizon should be interpreted as numerical inaccuracy, rather than physical effects.

7.5 The effect of α on the innermost root radius

It is interesting to investigate how much the value of the coupling parameter α affects the effective potential and hence allowed region of orbits in EDGB spacetime. One method to investigate this dependency is by analysing the position of the first root of the effective potential. We will investigate this dependency in an $\mathcal{O}(\chi^5, \alpha^7)$ EDGB spacetime with $E = 0.98$, $L_z = 4.5$ and $\chi = 0.3$, with several values of $\alpha \in [0, 0.691]$. The results are shown in Fig. 7.4.

We note that the shape of the effective potential changes only very slightly due to the value of α . Nevertheless, there is a discernible effect this has on the allowed region of orbits; the location of the first root is pushed very slightly outward when α is increased. However, as we will see in Chapter 8, this does not directly imply that the resonant orbits are also pushed outward; in fact, the resonance radii are actually pushed inward. The pushing out of the first root is in line with the findings as presented in Ref. [30].

7.6 Conserved quantity deviation

In the Kerr spacetime, we know that there exist four conserved quantities. Hence, these parameters should remain constant as the orbit evolves. However, numerical inaccuracies could cause these quantities to deviate from their preset values. In order to assess the existence and severity of this effect, we can reconstruct the conserved quantities during the numerical evaluation of an orbit and compute their rate of change as the orbit evolves. In particular, we will compute the percentage deviations of the conserved quantities from their original values for both the Kerr line element spin expansion and the EDGB line element at zero coupling. As said, the zero coupling case of the EDGB line element should reproduce the Kerr metric and hence we expect all four conserved quantities to remain conserved when the coupling is disabled.

Numerically, this is achieved by starting from the software infrastructure used to compute the orbits in the three spacelike Boyer-Lindquist coordinates r, θ and ϕ . In the same fashion in which the ϕ coordinate was restored, one then adds t as an additional coordinate, with corresponding conjugate momentum p_t . Naturally, since the spacetime is stationary, \mathcal{H} does not depend on t and hence $p_t = -E = \text{constant}$ (as we pointed out in Chapter 5). However, numerical inaccuracies might arise, causing the momentum in the t coordinate to change very slightly. By plotting p_t over time relative to $-E$, we can compute the numerical error in this conserved quantity. One can similarly compute the error between p_ϕ and L_z over time.

The two remaining conserved quantities are the Hamiltonian constant and the Carter constant. The Hamiltonian constant is equal to $-1/2$, since $\mu = 1$. Hence, we will compute the relative error of the Hamiltonian reconstructed from the values of t, r, ϕ, θ and their conjugate momenta over time by using Eq. (5.32). Similarly, we can employ Eq. (6.6) to compute the relative error of the Carter constant; the initial value of C can be reconstructed from the initial values of the other conserved quantities of a particular orbit.

One might wonder why the analysis is not always performed over the full coordinate space of t, r, θ, ϕ , since it is a trivial exercise to compute their equations of motion from the Hamiltonian. Apart from the algebraic and intuitive simplifications gained from reducing the problem to a two-dimensional one, including the other redundant coordinates significantly slows down the numerical integrator. Optimising the speed of the integrator will become an important consideration in this analysis when we compute the rotation curve of the EDGB spacetime.

In Fig. 7.5, the deviation of the conserved quantities from their initial values are depicted for the expanded Kerr spacetime up to fifth order in spin, whereas Fig. 7.6 shows the same plot for the zero coupling case of the EDGB line element at the same spin order. The errors in energy and angular momentum are zero within machine precision in both cases. The Hamiltonian gains an error which steadily increases as the iteration proceeds; however, it remains very small even after millions of time steps. Importantly for this comparison however, we see that the Kerr expansion and EDGB line element perform similarly. The Carter constant does show a difference in behaviour however. The Kerr expansion shows a deviation which is similar to the Hamiltonian case, although greater in magnitude. Much like the Hamiltonian, the error grows with time. The EDGB case however shows that although the error is much greater, it stays approximately constant around some mean value which is still very close to C at $\tau = 0$. This difference shows that although the line elements are inherently different due to the methods used to obtain them, the EDGB line element is a reasonably accurate approximation of the Kerr solution at this order, since it shows near-integrable behaviour in its conserved quantities.

One should note that the exact Kerr solution also displays numerical errors in the conserved quantities; these are shown in Appendix B. They are of a similar magnitude to the errors in the Kerr expanded case.

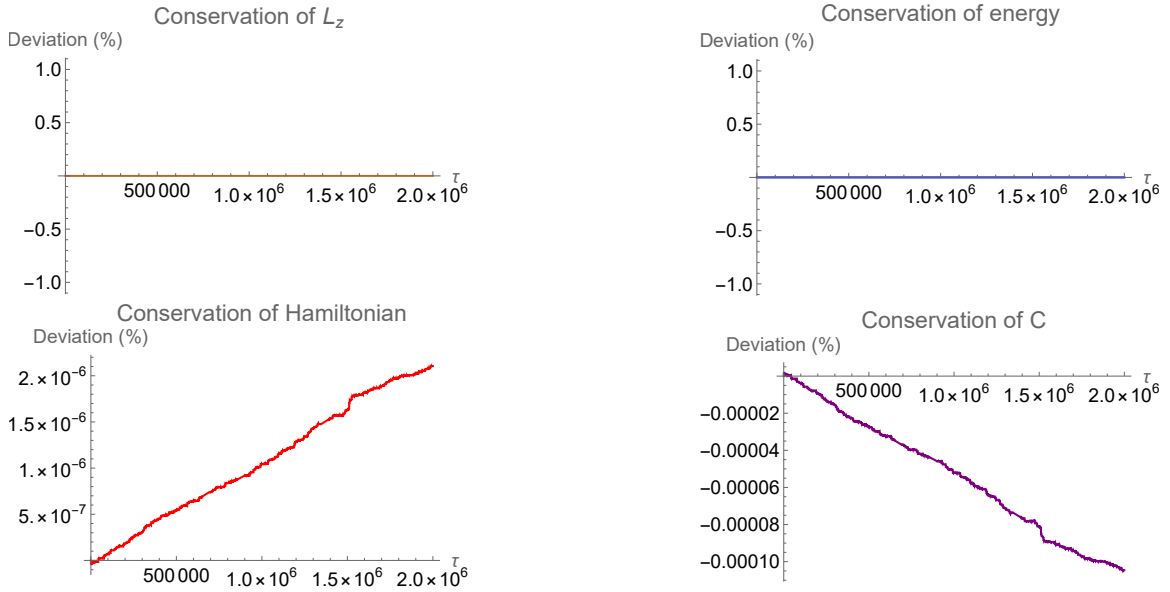


Figure 7.5: Numerical errors in conserved quantities for an orbit evaluated for 2 million time steps using the Kerr expansion up to fifth order in χ , with $E = 0.98$, $L_z = -4.5$ and $\chi = 0.3$. Energy and angular momentum are conserved within machine precision; the Carter constant C and Hamiltonian constant accumulate an error as time continues.

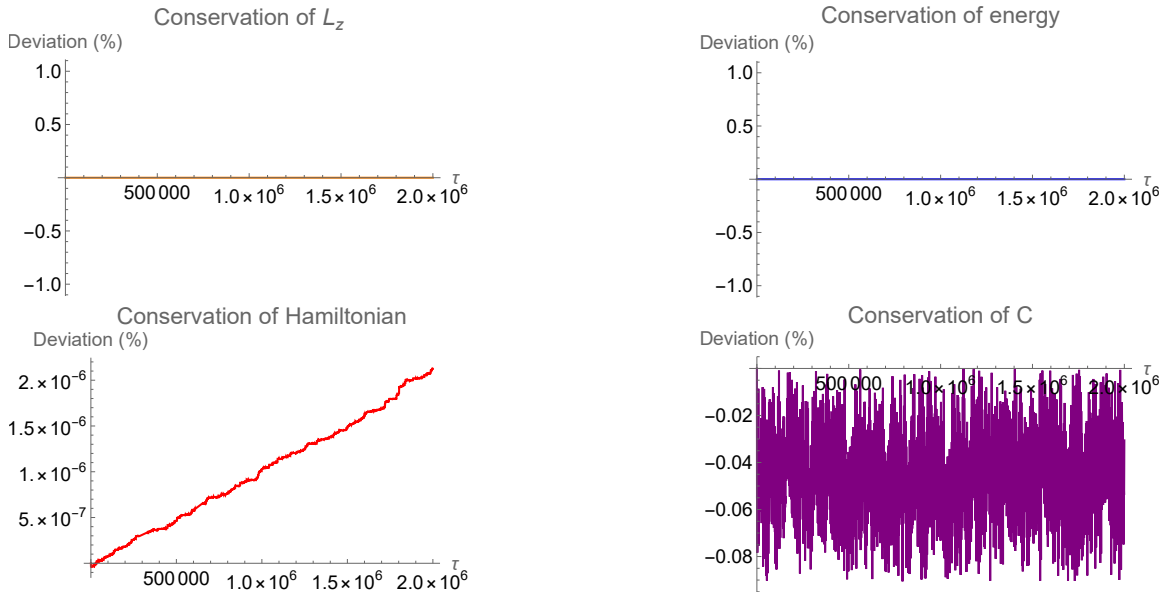


Figure 7.6: Numerical errors in conserved quantities for an orbit evaluated for 2 million time steps using the EDGB expansion up to fifth order in χ at zero coupling, with $E = 0.98$, $L_z = -4.5$ and $\chi = 0.3$. Unlike in Fig. 7.5, the error in the Carter constant C does not increase steadily. Rather, it fluctuates around a constant mean value close to the initial value.

Chapter 8

The search for chaos

Having established the validity of the EDGB line element, we can now perform a numerical analysis on this spacetime to see whether detectable signatures of chaos exist. This will be achieved by applying the framework as tested and validated through the Kerr solution in Chapter 6 to the EDGB line element. Due to the nature of this expansion and the small magnitude of the perturbation, special considerations need to be made when performing such an analysis, as outlined in this chapter.

8.1 Goals and considerations

Recall from Chapter 2 that chaotic features resulting from broken tori in modified gravity manifest as stable and unstable points in the rotation curve corresponding to a particular set of conserved E, L_z, χ . Furthermore, in Chapter 4 we learned that the conservation of the t and ϕ conjugate momenta allows us to find all the information we need in the remaining two coordinates. This particular fact will serve us well; whereas the closed-form Kerr solution is relatively easy to integrate numerically, the full $\mathcal{O}(\chi^5, \alpha^7)$ EDGB line element as obtained from Ref. [60] is cumbersome to work with. To give an impression of the algebraic complexity of the fully expanded metric tensor, it is worth noting that whereas a *Mathematica* script containing the quadratic spin and coupling expansion of the EDGB line element is a file of 3 kilobytes, the full $\mathcal{O}(\chi^5, \alpha^7)$ file has a size of more than a megabyte. As we will see, this poses a significant challenge to the numerical integration methods employed to evolve the equations of motion and hence it is imperative to perform as few calculations as possible. Reducing the problem to two dimensions roughly halves the required number of computations.

Apart from the computational considerations, one also needs to consider what kind of system settings could potentially reproduce interesting results. We will cover these and other ideas in the following sections.

8.1.1 Choice of coordinate system

In Chapter 4, we developed effective potential formalisms for several coordinate systems. In particular, Boyer-Lindquist and prolate spheroidal coordinates were found to be natural coordinate choices for SAV metrics in general and are hence also applicable to Kerr solutions with perturbative terms. Since both coordinate systems will produce precisely the same physical results, the choice of coordinates is purely made based on the convenience of their application. For that reason, we will in principle perform the numerical evaluation of EDGB geodesics in Boyer-Lindquist coordinates. This is because several earlier studies have used this coordinate system for this purpose [25][28][30],

which allows us to more closely compare our results to previous findings. Furthermore, the physical intuition is more easily formed in Boyer-Lindquist coordinates than prolate spheroidal coordinates, which is an advantage when trying to interpret potential results from the numerical calculations.

At a later stage, we will analyse how the results are affected by changing coordinates, as well as whether there are potential numerical gains to be had from performing the computation in prolate spheroidal coordinates rather than Boyer-Lindquist coordinates.

8.1.2 Choice of parameters

By varying E , χ and L_z , we can generate different classes of geodesics, of which we can compute the rotation curve by varying the initial radial coordinate r_0 . Hence, a choice should be made in what class of geodesics to investigate. Naturally, one should ideally vary all of these parameters to see in what regime potential chaotic features are the most prominent. However, due to the intensive nature of the computations, it is not realistic to do a full sweep of the parameter space. For the first set of computations, we should therefore determine values of these quantities in such a way that chaotic features are most likely to present themselves, whilst making sure that the orbits are likely to appear in physical systems.

The first consideration is the presence of resonant frequencies. Indeed, not all orbital configurations allow geodesics to take on a full range of rotation numbers. In order to investigate the low-order resonances, it is necessary to define relatively eccentric orbits. As can be seen in for instance the phase spaces depicted in Fig. 6.17, the $1/2$ resonance for example occurs close to the event horizon. We can best sample this regime by allowing the geodesic to become highly non-circular, such that the orbits are still stable. The $1/2$ resonance is for most parameter settings close to the ISO radius, but not quite close enough to generate truly erratic zoom-whirl orbits discussed in Chapter 6. Furthermore, since astrophysical objects orbiting supermassive black holes would most likely have been captured by the black hole, it is likely that one encounters eccentric orbits through experimental observations as well. A real example of a star orbiting a supermassive black hole with very high eccentricity will be discussed in Chapter 9.

The other aspect to take into account is the strength of potential deviations from the Kerr solution. Indeed, the EDGB line element differs the most from the Kerr solution at higher spin values as well as higher coupling values. However, we also note that the (unjustified) deviation of the EDGB line element at zero coupling from the Kerr expansion grows exponentially worse for increasing spin values, as was shown in Fig. 7.3a. Finally, several observed supermassive black holes show high spin, although some higher-mass examples show more intermediate values of χ [69]. Striking a compromise between these factors, we perform our analysis with $\chi = 0.3$. Varying the spin parameter to find a relation between the black hole spin and the deviation from the Kerr metric is an interesting avenue for future research, although one must then find a way to distinguish between the effects from the increasing error in the expansion and actual gravity scalarisation effects. In addition to this value of χ , we maximise potential deviation from the Kerr metric by computing the plateaus at the maximum allowed value of $\alpha = 0.691$. We also search for plateaus at $\alpha = 0$; since in that case no perturbation should exist at all, we can take potential plateaus in the zero-coupling case as a baseline error of our analysis method. If the plateaus at maximum coupling are significantly larger than the zero-coupling plateaus, we can attribute this effect to the presence of the scalar field and hence a feature of modified gravity, rather than numerical inaccuracy.

When setting $\chi = 0.3$, one can obtain the required eccentric orbits by setting $E = 0.995$ and

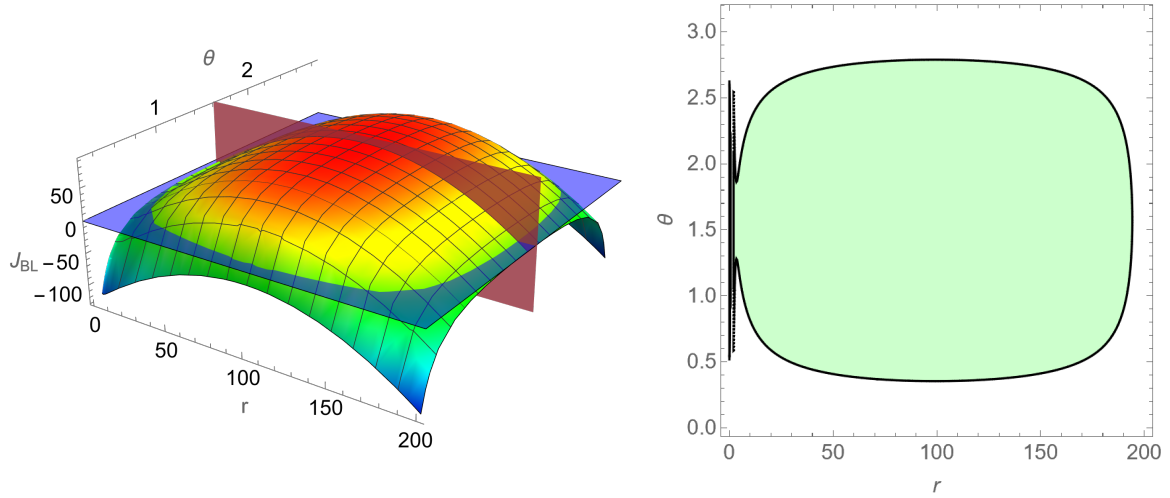


Figure 8.1: *Left:* The EDGB spacetime effective potential for $E = 0.995$, $L_z = 3.5$ and $\chi = 0.3$, at $\alpha = 0$. The red plane indicates the equatorial region and the blue plane indicates $J_{BL} = 0$. *Right:* Allowed region where $J_{BL} \geq 0$. Note how the outer region is connected to the event horizon.

$L_z = 3.5$. The effective potential one obtains with these parameters in Boyer-Lindquist coordinates is depicted in Fig. 8.1. These parameters provide access to geodesics which are interesting for this analysis, but much like with the value of χ , an investigation of the correlation between E , L_z and the plateau size could grant insight in the behaviour of these systems. Due to time constraints, this particular investigation is left to future researchers.

8.1.3 Choice of resonances

Since modified gravity effects are expected to be small in comparison to the Einstein-Hilbert contribution, one is unlikely to find Birkhoff islands by performing a low-resolution sweep of the rotation curve corresponding to the allowed region of a class of orbits. Hence, it is necessary to predetermine in what region chaotic features are most likely to appear, such that small effects due to the scalar field and Gauss-Bonnet invariant in the action can be detected through highly accurate computations around these regions. As pointed out in Chapter 2, the tori which are most likely broken via the Poincaré-Birkhoff theorem are situated around low-order resonances. Hence, the most interesting places to look for islands of stability or discontinuities in the rotation curve are near these resonances. In particular, one generally expects the $1/2$ resonance to experience the strongest deviation from the Kerr solution [32]. However, in our particular case, the curvature modification to the Kerr metric is quadratic in nature. This could cause chaotic effects to be more prominent in the $2/3$ resonance, despite being higher order than the $1/2$ resonance [28]. Heuristically, this can be understood by noting that the EDGB line element is mostly a quadrupole modification to the Kerr solution, which means that it is proportional to $\cos(2\theta)$ in Boyer-Lindquist coordinates. This in turn should cause strong effects in resonances where the numerator of the rotation number is 2, of which the $2/3$ resonance is the lowest order in the modified Kerr case due to our definition of the rotation number as ω_r/ω_θ . Because of this, we will investigate the $1/2$ and $2/3$ resonances for the EDGB line element at both zero and maximum coupling.

8.1.4 Numerical considerations

As mentioned before, the potential effects due to modified gravity are expected to be very small. Previous studies such as Ref. [30] have shown that the scale at which these plateaus occur in EDGB gravity are orders of magnitude smaller than for instance in Manko-Novikov spacetime [31]. The effects are expected to be so small that special care must be taken when computing rotation curves. Here, we will outline the settings used in this analysis to obtain the rotation curves for the EDGB line element. However, it should be noted that specialised numerical integrators for this task could be developed [30], which is indeed warranted in our view due to the high accuracy and slow speed of these analyses. It was beyond the scope of this project to develop a specialised programme for this, but the author recommends employing a fast programming language such as *C++* for this purpose or *Python* packages such as NumPy which employ such languages. For our purposes, *Mathematica* was an appropriate choice due to the advanced nature and ease of use of the NDSolve method integrated in this software framework as well as the advantages it has over other programming environment when it comes to symbolic equation manipulation.

For the following studies, the integrated numerical methods of *Mathematica*'s NDSolve function were employed. In particular, NDSolve has a sub-function called WhenEvent, which is well suited to compute the rotation curve. On the highest level of our computation, NDSolve takes the r, θ equations of motion with the predetermined parameters and starts evolving them over proper time τ by automatically choosing an integration method suited to the particular equations¹. In this analysis, we found that it was necessary to set the machine precision of the algorithm to at least 20 digits to prevent rounding errors from the averaging of Poincaré slice piercings. Furthermore, the AccuracyGoal and PrecisionGoal of the algorithm were set to 10 digits each². The maximum step size was set to 1, where it should be noted that NDSolve is adaptive, meaning that it decreases the step size around points of interest dynamically while integrating. Whereas NDSolve usually generates its solutions as InterpolatingFunction objects, for extreme integration times, it is far too memory-intensive to save these objects in full. This is where the WhenEvent method can be applied. WhenEvent allows NDSolve to locate points of interest at high accuracy once they appear during the integration. In our case, these points of interest are moments where the equatorial plane is pierced from below. Once NDSolve determines that such a piercing has happened, WhenEvent uses the Brent method to accurately locate the proper time of the piercing [70]. Once the piercing is accurately located, the corresponding r, p_r values are saved and the NDSolve evaluation is resumed. Every 200 piercings, the integrator is restarted. Through this approach, many points in the Poincaré slice can be generated without memory problems. Indeed, as we will discuss in the next section, we need a large number of points in the Poincaré section to compute an accurate rotation curve in which chaotic features are distinguishable.

Despite these memory considerations, memory usage is still high, with some long-duration runs requiring close to 5 GB of memory for a single rotation number. Hence, a dedicated computing cluster was employed for the computation of rotation curves in EDGB gravity.

¹NDSolve can use for example implicit, explicit or even symplectic Runge-Kutta based methods to advance the equations of motion; however, the expanded form of the EDGB line element at maximum did not allow for the specified use of the more specialised methods of NDSolve due to compatibility issues resulting from the large size of the equations (several megabytes). This did in all likelihood not significantly affect the accuracy of the result, since the event locator used by WhenEvent applies a separate and highly accurate method to determine the location of piercings of the equatorial plane. Nevertheless, this further underlines the advantages of developing a specialised numerical integrator for these analyses.

²Accuracy and precision settings essentially provide the same desired effect in this study. They are however generally different measures; accuracy is more appropriate than precision for near-zero values. To ensure accurate results in all cases, we set both parameters at our desired level.

Because the effect we are looking for is very small, changing any of these integration settings has an effect on the properties of the result. In particular, changes to the accuracy settings of the integrator cause the exact locations of the resonant orbits to shift very slightly. However, these shifts can be orders of magnitude larger than the potential plateau sizes, in particular in the higher order line elements. Because of this, every highly accurate investigation of a resonant region in the rotation curve is preceded by one or more zoomed-out runs used to determine the precise location of the point of interest. This means that it can be a time-intensive process to determine the existence and magnitude of a plateau in EDGB gravity, although by far the strongest contributing factor to this is of course the integration time.

8.1.5 The importance of iteration time

Since the rotation number is theoretically the average result from an infinite number of points in the Poincaré slice, one needs to integrate the equations of motion for as much time as possible to obtain accurate results. The accuracy required is in turn dependent on the scale of the feature one wishes to find. If for example an island of stability has a width of $r \approx 0.01$, integrating for $\mathcal{O}(10^6)$ time steps typically provides enough accuracy to find the feature in the rotation curve. However, the effects we are looking for are small enough that the integrations must run for at least $\mathcal{O}(10^9)$ time steps, which is both time- and memory-intensive. If one tries to find these features at lower integration time, artifacts in the rotation curve due to low numbers of piercings are much larger than the effect one is trying to quantify, as illustrated in Fig. 8.2. Hence, one needs to keep increasing the integration time until the feature of interest is distinguishable in the rotation curve. However, just like changing the settings of the integrator, the *location* of the resonance shifts slightly when integration time is changed. This means that for every change in integration time *or* settings, one has to redetermine the precise location of the feature of interest.

The method to find features in the rotation curve can hence be summarised as follows:

1. Determine integration settings and physical parameters.
2. Perform a run for a wide interval in r to determine the location of the resonance.
3. Perform progressively zoomed-in runs around the resonance region.
4. If one encounters averaging artifacts such as in Fig. 8.2, increase the iteration time and revert to step 1.
5. If one encounters a potential plateau or discontinuity, perform a high resolution run to determine its magnitude.

One can now appreciate the time it takes to locate and characterise a small plateau or discontinuity in the rotation curve. For example, computing the rotation number of a geodesic at maximum coupling and $\mathcal{O}(\chi^5, \alpha^7)$ for $\tau = 2 \cdot 10^9$ at the required accuracy settings takes 125 CPU hours³, or roughly 5 CPU-days. In addition, it typically takes multiple such runs of zooming in along the radial axis to determine either the existence of a chaotic feature or the need to further increase the integration time. By parallelising the computation of the rotation curve (i.e. assigning one CPU to each geodesic), a full rotation curve can be computed in the time it takes to compute one rotation number. Unfortunately, NDSolve is a linear process which itself does not allow for further parallelisation. Hence, available CPU cores and the CPU clock speed are the primary bottlenecks of this analysis.

³Using an Intel Xeon Gold 6252N at 2.3GHz, this translates to roughly an equal amount of wallclock time.

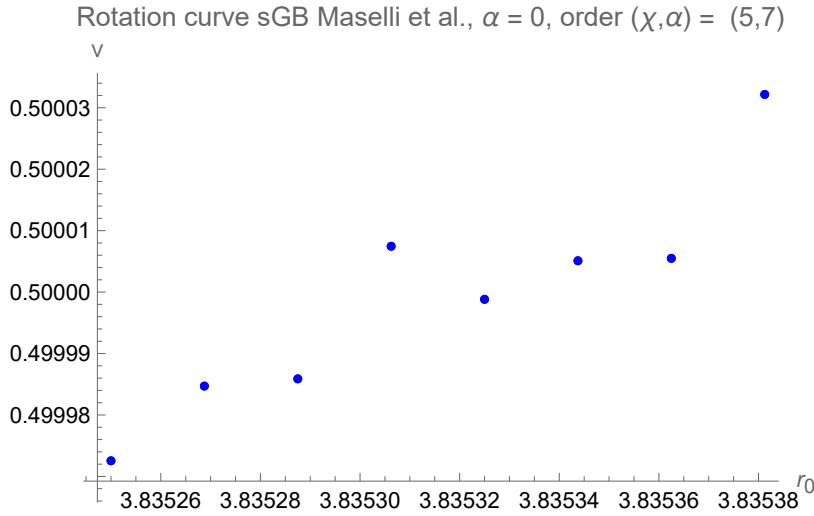


Figure 8.2: Rotation curve around the $1/2$ resonance for EDGB spacetime at zero coupling and $\mathcal{O}(\chi^5, \alpha^7)$. This run was computed for an integration time of $\tau = 4 \cdot 10^9$. At this integration time, there is too little consistency in the distribution of the rotation numbers to conclude anything about the nature of the underlying chaotic feature, since it could be a result of numerical errors rather than a true Birkhoff island.

8.2 Verifying the framework

Before we analyse the EDGB line element at several orders and search for chaotic features, it is imperative to verify that our method of integration produces physical results. To this end, we will apply the aforementioned method to a spacetime obtained from another source. In particular, we will use the line element from Ref. [65], a higher order version of which was used in a similar rotation curve analysis [30]. This line element was provided in 'Boyer-Lindquist-like' coordinates, defined in Ref. [30]⁴ If we are able to reproduce the plateau at the $1/2$ resonance, it serves as a validation of the analysis methods employed in this thesis.

In Fig. 8.3, we see the result of such an analysis. In Ref. [30], the conserved quantities were set at $E = 0.995$, $L_z = 3.75365$, $\chi = 0.2$, and the coupling⁵ to the Gauss-Bonnet invariant was set at $\alpha = 0.001$. In Ref. [30], at second order in spin, a plateau with a width of approximately 0.001 is presented for this resonance, which was also found using our framework. The precise location of the resonance is slightly different; however, it is very close to the expected $1/2$ resonance location of $r = 4$. The deviation is most likely a result of the integration time or accuracy settings; recall that differences in these parameters shift the observed radius of the resonance.

⁴We were unable to identify precisely which transformation from conventional Boyer-Lindquist coordinates such as presented in for instance Ref. [48] provides the coordinate system depicted in Ref. [65]. It is hence difficult to perform a one-to-one comparison between the results in this system and from the version of the line element from Ref. [60] we will be using. Nevertheless, we can still reproduce the results from Ref. [30], under assumption that this Boyer-Lindquist-like coordinate system allows the same definition of the effective potential.

⁵Due to differences in conventions, the coupling parameter is not necessarily in one-to-one correspondence with the one as defined in Chapter 7. However, care was taken to set the parameters in this line element to the precise values presented in their paper, to ensure an accurate comparison.

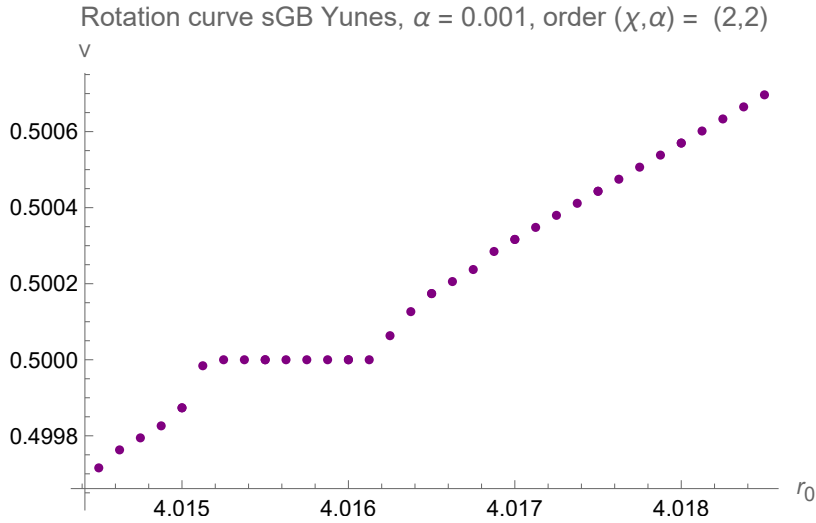


Figure 8.3: Rotation curve around the $1/2$ resonance for the EDGB spacetime from Ref. [65] at $\mathcal{O}(\chi^2, \alpha^2)$, using the same conserved quantities as in Ref. [30]. This run was computed for an integration time of $\tau = 10^8$. There is a distinct plateau present at precisely $\nu = 1/2$, indicating the crossing of a stable point in a Birkhoff chain.

8.3 Chaotic features at $\mathcal{O}(\chi^2, \alpha^2)$

Having confirmed the validity of the algorithm employed, it will now be applied to the spacetime investigated in Chapter 7. As motivated earlier, we set the orbital parameters at $\chi = 0.3$, $E = 0.995$ and $L_z = 3.5$.

In this spin expansion regime, we expect that the perturbation to the Kerr solution measured through the rotation curve will primarily be a result of the spin expansion rather than the scalar effect of the line element. Nevertheless, we will compute the rotation curves at both zero and maximum coupling around the $1/2$ and $2/3$ resonance, to verify that the line element behaves as expected. Furthermore, if a discernible difference between the zero and maximum coupling cases can be determined at this order, it would save a great deal of time in the analysis, since the full-order expansion of the line element is very cumbersome to numerically integrate.

8.3.1 $1/2$ resonance

Recall that a significant number of broken tori is expected to form around the $1/2$ resonance, since this we know from Arnold's criterion that tori near low-order resonances are more likely to break. Furthermore, we note that the other line element reproduced a plateau at this resonance value. Hence, one expects *a priori* to encounter such a plateau in the second order expansion of the EDGB line element as well. Following the outlined analysis methods, an iteration time of $\tau = 2 \cdot 10^8$ was determined to be great enough to determine the nature of the chaotic features in this spacetime.

Zero coupling

Through some runs of a relatively large range in r , the point where $\nu = 1/2$ was determined to exist around $r \approx 3.82$ for these settings. A follow-up run around this region at a closer zoom level

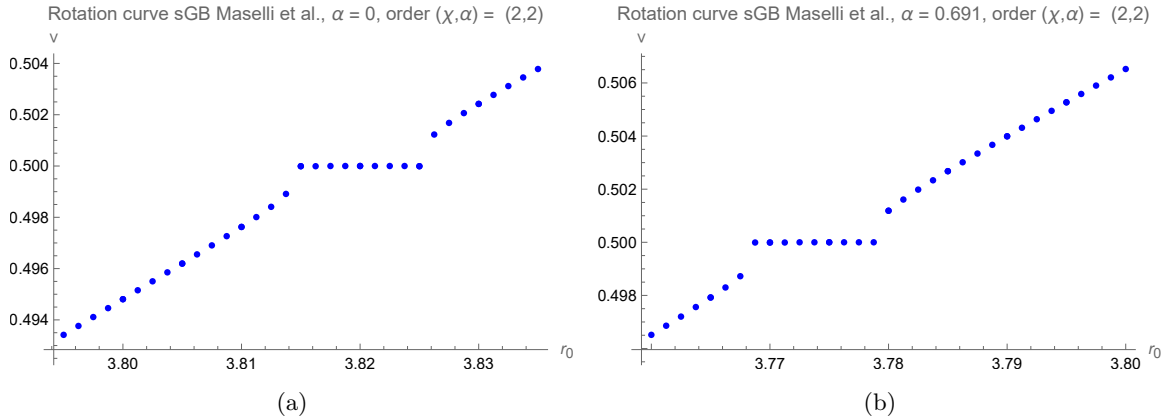


Figure 8.4: (a) The EDGB spacetime rotation curve near the $1/2$ resonance at $\mathcal{O}(\chi^2, \alpha^2)$ for $E = 0.995$, $L_z = 3.5$ and $\chi = 0.3$, at $\alpha = 0$. A clear plateau at $\nu = 1/2$ is present, indicating an island of stability in the phase space as part of a Birkhoff chain. (b) The $1/2$ resonance for the same settings, except that $\alpha = 0.691$, the maximum allowed value. We see that the plateau is still present, albeit very slightly pushed towards the event horizon.

was performed and yielded a distinct plateau, depicted in Fig. 8.4a. We should reiterate that at zero coupling, we expect to be dealing with the (expanded) Kerr solution; hence this feature is *not* a physical plateau due to the form of the EDGB action. We will compare this result to the same resonance in the expanded Kerr solution in Section 8.3.3.

Maximum coupling

Similarly, the location of the $1/2$ resonance in the maximum coupling case was determined to be at $r \approx 3.775$. Interestingly, it seems that the scalar field at this order in spin and coupling actually pushed the resonant orbit closer to the event horizon and hence further into the strong-field regime of gravity, when compared to the resonance radius found in the zero coupling case. This is in contrast with Ref. [30], where the authors state that increasing the scalar field coupling pushes the orbit further away from the event horizon. We find that even though the first root of the effective potential *is* pushed away from the event horizon under increasing α (as was shown in Fig. 7.4 as well as Ref. [30]), the resonant initial radii are actually pulled closer towards the event horizon. A zoomed-in analysis yielded another plateau, depicted in Fig. 8.4b.

From the rotation curves in Fig. 8.4, we see that the perturbations to the Kerr metric seem similarly sized in both the zero and maximum coupling cases. This suggests that the effect of the spin expansion dominates the generation of these plateaus, drowning out the effect of adding a scalar perturbation. Before this can be concluded however, it is desirable to perform a high accuracy run to determine the plateau sizes more precisely. The results of such runs are depicted in Fig. 8.5.

Since it is known where the plateaus are, for these high accuracy runs, we only need to compute the transition regions to and from the island of stability. This saves a significant amount of computation time. From these figures, it is now possible to compute the radial size of the plateaus found. We find that the radial plateau width in the zero coupling case ($\equiv \mathcal{W}_0$) is given by $\mathcal{W}_0 = 0.011125 \pm 0.000125$, where the uncertainty stems from the resolution of the rotation curve. Similarly, we find that in the maximum coupling case, the width is given by $\mathcal{W}_{max} = 0.010375 \pm 0.000125$.

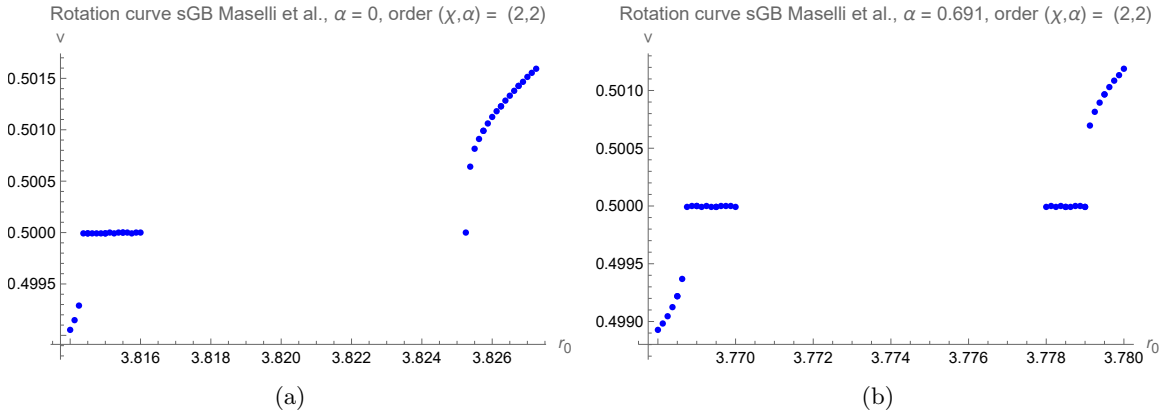


Figure 8.5: Higher accuracy runs of the edges of the plateaus depicted in Fig. 8.4. The very slight deviations in the plateau itself are due to numerical inaccuracies. (a) The zero coupling case. (b) The maximum coupling case.

Although it might seem paradoxical that maximum coupling case seems to have slightly decreased the plateau size, the broader conclusion which we draw from this is that the error in truncating the spin expansion at second order makes it impossible to formulate any precise conclusions on the effect of the spin coupling on the rotation curve. At this order in spin and coupling, the line element is not accurate enough to reproduce meaningful physical results in terms of the observable effects of EDGB gravity specifically and is hence inappropriate for this purpose. However, we *can* conclude that the scalarisation effect we are attempting to consider will be much smaller than the perturbation from the second order spin expansion, since we have not found any distinguishable scalarisation effect at this scale. This finding confirms the necessity of using a (much) higher order expansion in spin and coupling when looking for measurable effects in the rotation curve, as well as the necessity to perform the analysis at a much further zoomed-in radial resolution.

Phase space picture of plateaus

Although the rotation curves provide an indication of the size and location of the Birkhoff islands of the analysed spacetime, it is helpful to actually realise these islands as they appear in the phase space itself. This will help us understand the physics behind these points and build more fundamental insight in its effect on the orbital mechanics of an EMRI.

In Fig. 8.6, sections of the phase space corresponding to the regions near the $1/2$ plateaus from Fig. 8.4 are depicted for both zero and maximum coupling. In this figure, we see that around the centre of the rotation curve, closed curves form in line with what was expected from the Poincaré-Birkhoff theorem. The local fixed point is precisely the point around which these curves coalesce, and this point corresponds precisely to the centre of the plateau. In the phase space, the full plateau area can be identified by the higher density of curves; this is due to the fact that a closed curve in the plateau effectively results in a doubling in the number of $p_r = 0$ crossings in the plot. This is of course an artifact of the discrete nature of computational analysis, but also points to a real physical phenomenon.

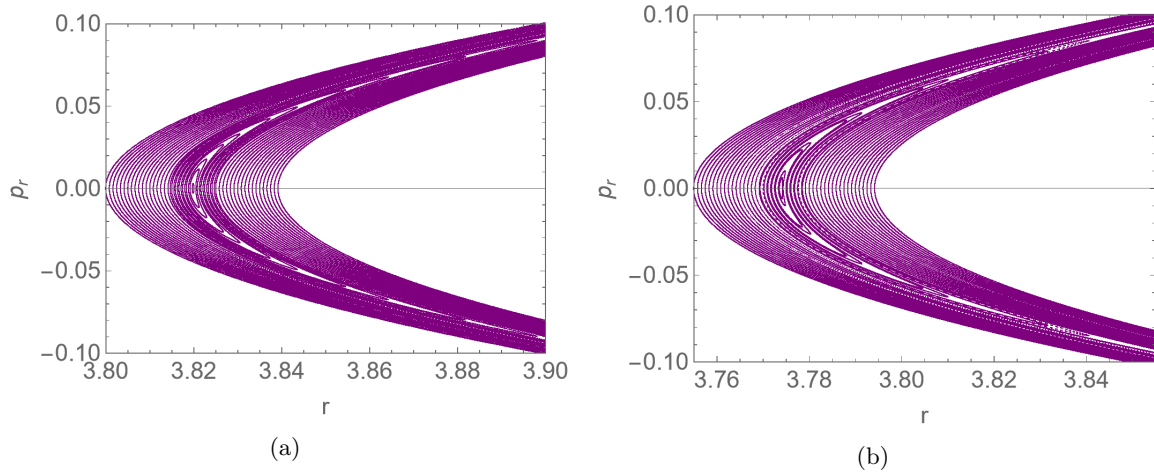


Figure 8.6: Phase space representations of the chaotic features in second order EDGB gravity near the $1/2$ resonance, corresponding to the rotation curves in Fig. 8.4, where (a) is the zero coupling case and (b) is the max coupling case. Note the distinct closed curves around the added fixed point, which is precisely the middle of the plateau in the rotation curve. Both cases display similar features, and although the physical effects of the plateau are readily visible at this scale, it is a more cumbersome method of identifying these features than rotation curve analysis.

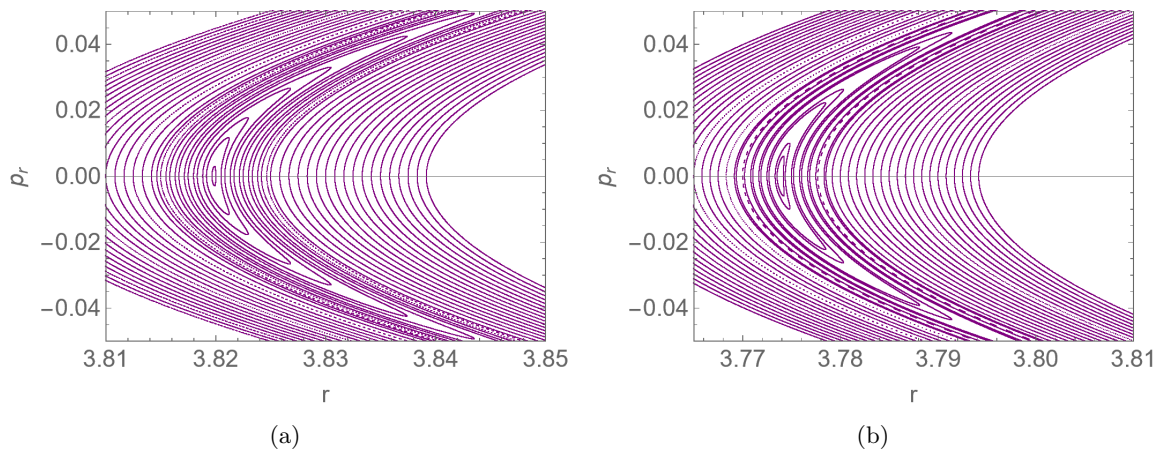


Figure 8.7: Zoomed-in versions of Fig. 8.6 near the fixed point, where again (a) is the zero coupling case and (b) is the max coupling case.

Orbits caught in the plateau are inclined to 'get stuck' in the plateau; one way of interpreting this is that evolving geodesics linger in the $1/2$ resonance region. This is also what one would find through observations; if a geodesic loses energy and progresses through the rotation curve and phase space with decreasing r , it would get 'caught' in the $1/2$ resonance for a short amount of time. This effect is revisited and treated in more detail in Chapter 9.

To provide additional clarity on the nature of the stable points, a zoomed-in version of both phase space plots is provided in Fig. 8.7. Here, the double crossings of $p_r = 0$ at the same resolutions inside the plateau region are more readily visible. There are also several 'dotted' curves in the phase space diagram. To explain their appearance, it is helpful to refer back to Fig. 6.17. If the rotation number of an orbit is rational, the corresponding piercings in the Poincaré section happen at discrete points in the phase space repeatedly, rather than ergodically forming a closed curve. Thus, the occurrence of dotted lines in these plots could be explained by the orbits (nearly) existing at a higher order resonance which is unable to form its own Birkhoff island, but still results in the piercings forming around discrete points at the presented iteration time rather than a full curve.

We should reiterate that in these cases, the perturbations to the integrable Hamiltonian and resulting chaotic features are dominated by the effects of the spin expansion. However, these examples provide some insight in the nature of these chaotic features and how one can expect to find them in the phase space diagrams of orbital motion, rather than purely from the mathematical constructs of fundamental frequencies and rotation numbers.

8.3.2 $2/3$ resonance

After characterising the $1/2$ resonance, the analysis was repeated for the $2/3$ resonance in this second order expansion. The conserved quantities and integration time were kept the same as in the $1/2$ case. The results are depicted in Fig. 8.8.

Zero coupling

Like the $1/2$ resonance, several low resolution runs were performed to locate the radius of the $2/3$ resonance. In this particular case, it was at $r \approx 5.00715$. After performing higher resolution runs, it became apparent that a plateau was not present in this case. Rather, an unstable point in the Birkhoff chain manifested in the rotation curve. This is an interesting result, since most studies on extreme mass-ratio systems focus on the manifestations of plateaus as response to perturbations of the Kerr spacetime; however, it is evidently also possible that unstable points occur at resonant points in these orbits when the Kerr solution is slightly perturbed. The radial size of this feature is not an appropriate quantification of the amount of chaos induced by the modification. The apparent 'height' of the discontinuity is not very well defined either. This is because the discontinuity happens at one particular radius; one can asymptotically zoom in around the unstable fixed point and find an increasingly smaller discontinuous jump in the rotation curve. One could try to create a definition based on the rate of change in ν , but it is more desirable based on this outcome to formulate some coordinate-independent formulation of a perturbation feature from its definition in the phase space. This is an aspect we will address later.

Maximum coupling

In the maximum coupling case, the location of the $2/3$ resonance is $r \approx 4.97382$. Again, the increased value of the scalar coupling has pushed the resonance further into the strong-field regime. The qualitative aspects of the feature are similar to the zero coupling case. This underlines the necessity

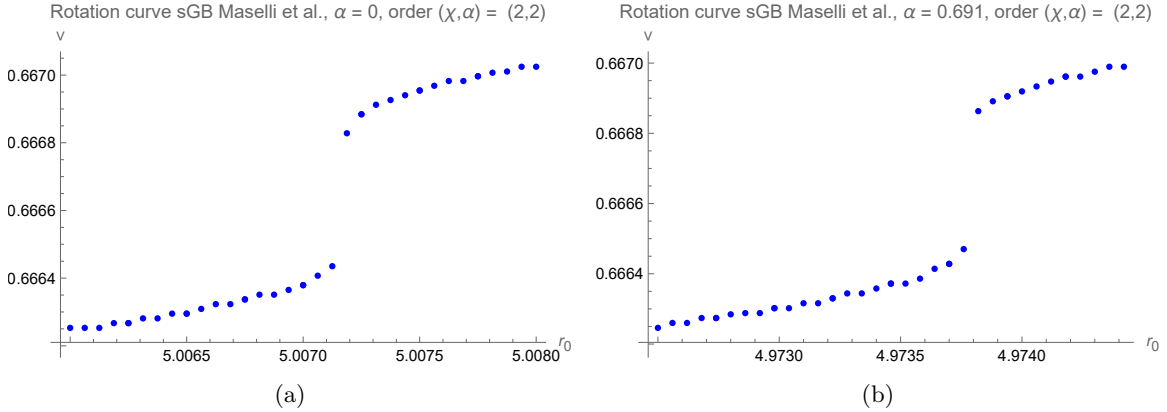


Figure 8.8: (a) The EDGB spacetime rotation curve near the $2/3$ resonance at $\mathcal{O}(\chi^2, \alpha^2)$ for $E = 0.995$, $L_z = 3.5$ and $\chi = 0.3$, at $\alpha = 0$. A discontinuity around $\nu = 2/3$ is present, indicating an unstable island in the Birkhoff chain. (b) The $2/3$ resonance at $\alpha = 0.691$, the maximum allowed value. We see that the discontinuity persists and is again shifted towards the event horizon.

to find an unambiguous method to characterise the 'magnitude' of unstable points in the Birkhoff chain, if one is to infer the effect of the scalar field on potential chaotic motion. Furthermore, much like in the $1/2$ resonance case, we conclude that the second order expansion is not accurate enough to draw conclusions about the effect of the scalar field, due to the effect largely being drowned out by the spin expansion perturbation of the Kerr Hamiltonian.

Phase space picture of discontinuities

The unstable points in the rotation curve are better understood by considering their corresponding phase space. Unlike in the case of islands of stability and plateaus, there are no additional closed curves visible in Fig. 8.9. Indeed, this time, there is a region in the phase space near the $2/3$ resonance where no periodic geodesics can exist. At this point on the $p_r = 0$ line, an X-shape seems to form, which is why unstable Birkhoff islands are also known as X-points⁶ [31]. This behaviour exists in both the zero and maximum coupling cases. In the empty region, no periodic orbits can exist; orbits in this region hence exist in a thin veil of *chaos*. However, the instability of this point means that this chaotic motion will not persist. Interpreting this physically, one can conclude that geodesics moving across such an island would be 'repelled' from the resonance value; like the $1/2$ resonance case, the physical implications of this behaviour will be revisited in Chapter 9. For now, the take-away is that both stable and unstable points in the rotation curve are in one-to-one correspondence to very characteristic features in the phase space, which have clear physical interpretations.

⁶Stable islands are analogously referred to as O-points.

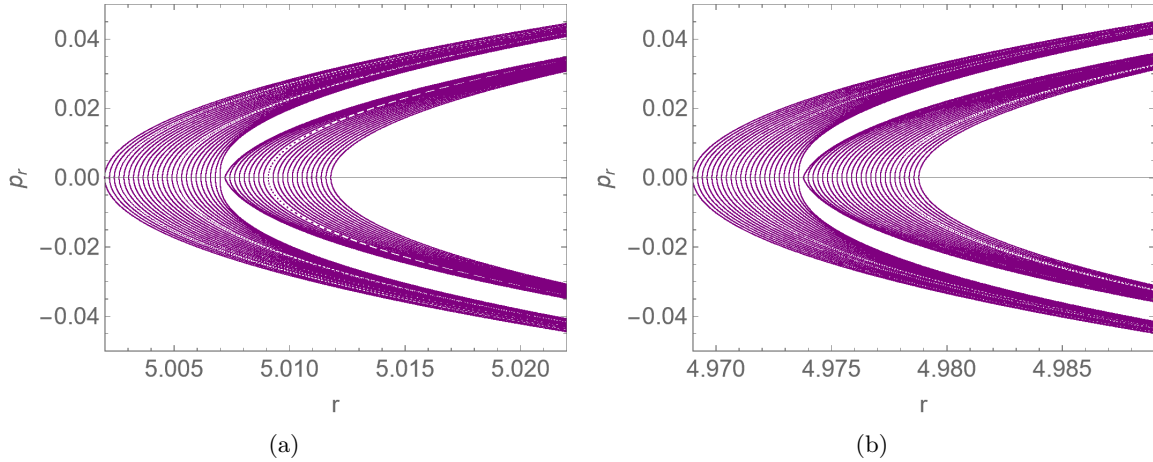


Figure 8.9: Phase space representations of the chaotic features in second order EDGB gravity near the $2/3$ resonance, corresponding to the rotation curves in Fig. 8.8, where (a) is the zero coupling case and (b) is the max coupling case. Unlike with the plateaus corresponding to the islands of stability, a distinct region of the phase space disallows the existence of periodic orbits inside of it.

8.3.3 Kerr expansion

As a control to the above analysis, the rotation curve framework was also applied to the spin expansion of the exact Kerr solution. In this case, the Kerr spacetime was expanded up to second order in spin, as to provide a reasonable comparison with the EDGB line element as used in the results above. A priori, one does not expect to reproduce the zero-coupling EDGB case exactly, because it was already established in Chapter 7 that the line element is not precisely equivalent in that case. However, it is interesting to investigate whether one finds the same chaotic features in the Kerr line element and the EDGB line element, precisely because of this inherent inaccuracy. For the computations, we set the same conserved quantities and run time ($\tau = 2 \cdot 10^8$).

In Fig. 8.10, we see the results of this computation. As expected, the same qualitative features are present in the rotation curve as in the EDGB spacetime at zero coupling; an island of stability around the $1/2$ resonance and an unstable point at the $2/3$ resonance. However, the locations of both features are very slightly shifted compared to the EDGB case at zero coupling. However, one should keep in mind that the precise location also depends on the number of piercings considered. Since the orbital period in proper time depends on the form of the equations and how NDSolve attempts to solve them, the number of piercings in both cases is not necessarily precisely equal. More interestingly, the size of the plateau is smaller in the Kerr expansion than in the EDGB line element. This is also expected, since the Kerr expansion is closer to the Kerr solution than the EDGB expansion, the perturbation to the integrable spacetime is smaller and hence fewer tori are broken. However, the plateaus are still somewhat similar in magnitude, which indicates that the EDGB line element at zero coupling is indeed a reasonable approximation of the Kerr expansion at this order.

We can also compute the phase space representations of the Kerr spacetime at second order in spin, in particular around the resonant values of $1/2$ and $2/3$. The results are depicted in Fig. 8.11. They are of a similar nature to what was found for the EDGB spacetime, with the stable and unstable points manifesting around the new fixed points in the $1/2$ and $2/3$ case respectively.

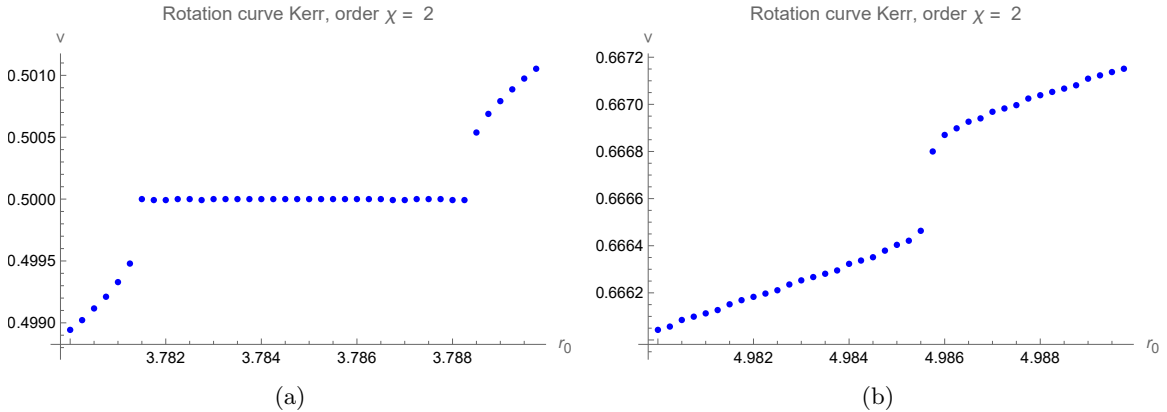


Figure 8.10: The rotation curves near the $1/2$ and $2/3$ resonance of the expanded Kerr spacetime expanded up to $\mathcal{O}(\chi^2)$ for $E = 0.995$, $L_z = 3.5$ and $\chi = 0.3$. We see the same features as in the EDGB case, albeit at slightly shifted radial positions. The magnitude of the plateau is also slightly smaller for the $1/2$ resonance than in the equivalent EDGB case.

One might wonder whether how the plateau size depends on the value of χ . In Appendix C, we investigate this dependency in the expanded Kerr spacetime. We find that smaller spin values in the second order expansion generate smaller plateaus, which is exactly what one expects from an expansion around $\chi = 0$.

8.3.4 Conclusions at second order

We have seen that at second order in spin and coupling, there are clear signatures of chaotic motion to be found in the rotation curve of the EDGB spacetime. However, since there is no objective difference to be found between the zero and maximum coupling cases of the line element, the perturbations measured here are overwhelmingly caused by truncating the spin expansion of the Kerr solution at second order rather than the scalar field effects of the line element. Hence, the potential effects of this scalar field must be orders of magnitude smaller than the effects found in this second order expansion.

These results however did elucidate other aspects of the study of rotation curves in modified gravity. For instance, the appearance of an unstable point at the $2/3$ resonance is interesting, since most research in this field focuses on measuring the magnitude of islands of stability. However, there is a priori no reason to prefer stable points over unstable ones, since the Poincaré-Birkhoff theorem tells us that an equal number of either is generated in the rotation curve in alternating order along the original fixed point in the phase space slice. Hence, the findings at this order indicate the necessity to further develop methods of characterising the scale of both stable and unstable points as they might occur in the rotation curve of modified gravities.

Finally, it is important to note that differentiating between plateau and discontinuity sizes in minimum and maximum coupling is a theoretical consideration needed to provide an expectation of how large possible effects from EDGB gravity compensated for numerical artifacts, if it indeed turns out to be a viable candidate for an alternate theory of gravity. In an experimental setting, finding any sort of plateau or discontinuity from astrophysical observations would immediately show that the

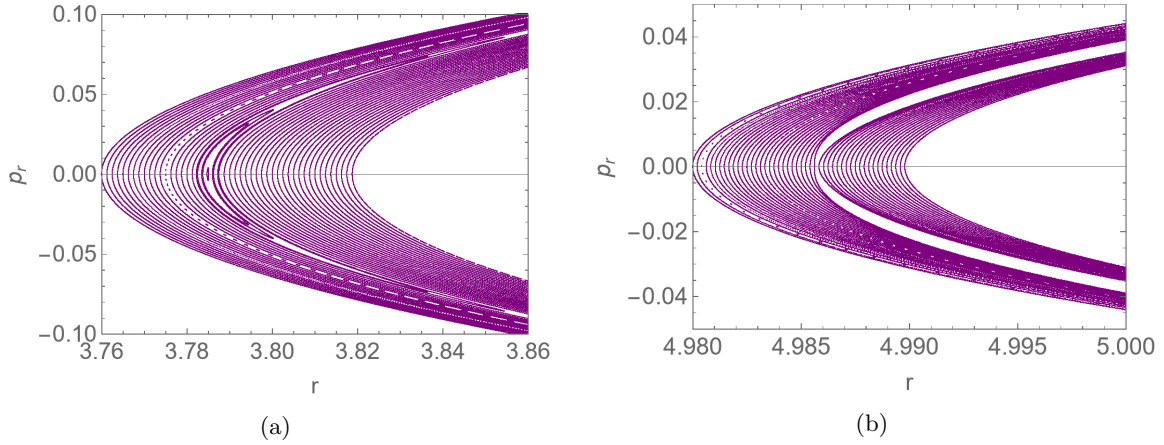


Figure 8.11: Phase space representations of the chaotic features in second order Kerr expansion near the $1/2$ resonance (a) and $2/3$ resonance (b), corresponding to the rotation curves in Fig. 8.10. Their behaviour is analogous to what we found at second order in the EDGB metric.

spacetime analysed is not the Kerr solution, since a true Kerr black hole does not allow for any such islands to appear in the phase space. Hence, the development of a general characterisation of these features is crucial, even beyond the study of EDGB gravity specifically. The features found at second order can be used as a toy model to study different characterisation methods and how appropriate they are, before being applied to rotation curves where the chaotic features might be more difficult to distinguish.

8.4 Chaotic features at $\mathcal{O}(\chi^5, \alpha^7)$

It is now established that although there are clear chaotic features present at second order, a much more accurate formulation of the EDGB line element is needed in order to distinguish between the perturbation as caused by the spin expansion and as caused by the coupling to the scalar field. This is where it becomes critically useful that the provided parametrisation of the EDGB solution is up to $\mathcal{O}(\chi^5, \alpha^7)$. At this level of accuracy, the line element is likely to be close enough to the Kerr solution at zero coupling that a difference in plateau or discontinuity magnitude should become apparent when found in the rotation curve. However, here the numerical considerations become challenging.

In the second order case, an iteration time of $\tau = 2 \cdot 10^8$ was sufficient to provide the chaotic features as presented in the previous section. However, when a line element of the magnitude of the $\mathcal{O}(\chi^5, \alpha^7)$ EDGB parametrisation is fed to NDSolve, the iteration speed of the solver is decreased dramatically. Indeed, the primary issue is that the same amount of iteration time covers less true proper time if the equations to be solved are very extensive. Furthermore, because the features at this order are found to be at least $\mathcal{O}(10^2)$ smaller in radial width (in the case of plateaus) than those at second order, a far greater zoom level in the radial coordinate is required to picture potential chaotic features. At $\tau = 2 \cdot 10^8$, the numerical inaccuracies are still very much dominant, which indicates that more iteration time is indeed required. In order to illustrate this, Fig. 8.12 shows what one finds if one zooms in on the rotation curve of a fully expanded and spacetime at $\tau = 2 \cdot 10^8$ and $\alpha = 0$. Note that since the $\alpha = 0.691$ line element has many more terms than the $\alpha = 0$ case, the problem is exasperated for precisely the case where we expect to find the most interesting chaotic

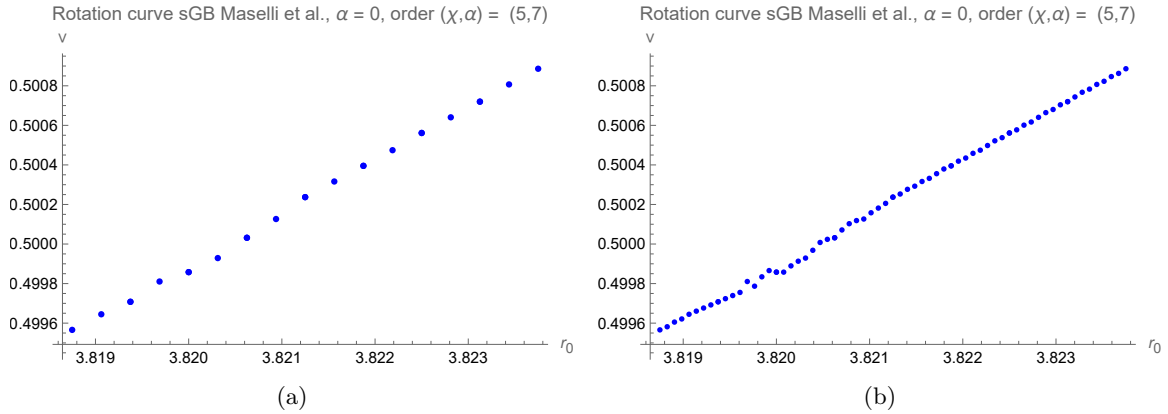


Figure 8.12: Rotation curve of the EDGB line element at $\mathcal{O}(\chi^5, \alpha^7)$ and $\alpha = 0$ near the $1/2$ resonance at $\tau = 2 \cdot 10^8$, with the right plot a high-resolution version of the left. As can be seen by directly comparing these curves to those at second order in Fig. 8.4, this is on a radial scale at which the second order plateaus were evident. In this case, they have vanished, indicating that the effects of the spin expansion have been greatly mitigated. However, increasing the resolution of the plot demonstrates that nonphysical numerical inaccuracies have appeared already. Since these inaccuracies are present at this scale, they dominate any potential plateau or discontinuity. We hence cannot draw definitive conclusions on the size or position of chaotic features.

features relative to the Kerr solution.

In principle, it is no problem to increase the iteration time in order to increase the allowed radial zoom level. However, the potential chaotic features at this order turn out to be so small that the required iteration time and computational resources become a severely limiting factor in the analysis, as well as that the use limits of NDSolve are reached.

Let us first discuss the iteration time and required computing power. Since the maximum coupling case contains more terms in the line element than the zero coupling case, the maximum coupling cases take the longest time to compute. The rotation curve at second order and maximum coupling as depicted in Fig. 8.4 took about half a day to complete on the employed computing cluster, where the job was split over eight cores at once. However, four geodesics were computed per core in this particular case, meaning that these results could in principle be produced in a matter of hours. Indeed, the computation of a single rotation number (which as one might recall is the fundamental speed limit of this analysis due to the non-parallelisation of NDSolve) is in the order of several hours at second order for the maximum coupling case. When moving to $\mathcal{O}(\chi^5, \alpha^7)$, the computations become dramatically slower. When each core is assigned just a single rotation number to compute, completing an iteration of $\tau = 2 \cdot 10^8$ takes approximately half a day at maximum coupling. This means that reproducing a rotation curve with a resolution such as Fig. 8.12b at maximum coupling takes approximately 4 days to complete when using eight cores. Although this still seems somewhat reasonable, the features we are looking for turn out to be so small that iteration times greater than $\tau = 6 \cdot 10^9$ would be needed to unambiguously identify them, which is already 30 times more than what was needed at second order. Indeed, one run at maximum coupling for $\tau = 6 \cdot 10^9$ takes approximately 15 days to run. Combined with the fact that multiple runs are needed to locate and zoom in on the resonance are needed, as was outlined in Section 8.1.5, this makes constructing a high-resolution rotation curve for this line element a process which takes weeks of continuous com-

putations at best. Apart from the time limitations of this thesis, this is also undesirable from a logistical point of view. Due to the limitations on the computing power available, it became difficult to obtain conclusive results on these chaotic features in the time frame of this analysis.

It is not just hardware which is a limiting factor however. At a certain point, NDSolve's integration methods start to break down. Beyond approximately $\tau = 7 \cdot 10^9$, NDSolve detected a stiff system in the zero coupling case of the EDGB line element at high order. Since obviously this is not physically the case, it is a result of the integrator not being able to numerically advance the set of initial conditions further to compute the next step of the calculation. Indeed, if further iteration is required, NDSolve's methods are no longer sufficient. Since at this iteration time the chaotic features are not yet evident, this is the most definitive indication that a specialised numerical integrator is required to further zoom in on the rotation curve. It is beyond the scope of this thesis to develop this software, but it is the next logical step in the investigation of chaotic features in EDGB spacetime.

Despite all of this, the runs which *were* completed successfully provide upper bounds on the potential size of chaotic features. After all, if they do not appear at a particular radial zoom level, we can conclude that the potential features must at least be smaller than the radial resolution employed in those particular computations. Because of this, the results of the highest accuracy runs which finished in time are presented in Fig. 8.13 and Fig. 8.14, despite the conclusive evidence for particular chaotic features at this scale. We find that the potential sizes of the chaotic features in the higher order EDGB line elements all have an upper bound of $\mathcal{W}_{BL} \leq \mathcal{O}(10^{-4})$.

Another aspect of the potential features at this order which could be interesting is the nature of these features one could find. From the second order results, we would expect that the $1/2$ feature one might find is a plateau and the $2/3$ feature a discontinuity. However, it is not necessarily the case that this pattern persists as one increases the order of the line element and hence changes the nature of the perturbation to the integrable dynamics. Although we have provided upper bounds on the radial widths of the potential features in these higher order spacetimes, we are not at present in a position to concretely predict the type of feature one expects to find. This is however an interesting opportunity for future work; it might be possible to analytically predict the nature of a discontinuity based on the nature of the perturbation to the underlying integrable (Kerr) Hamiltonian.

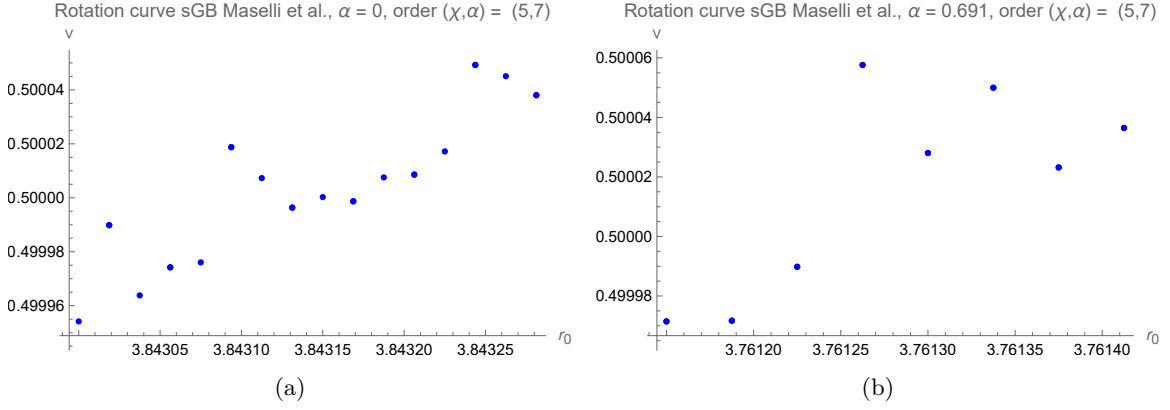


Figure 8.13: EDGB rotation curves at $\mathcal{O}(\chi^5, \alpha^7)$ for (a) zero and (b) maximum coupling near the $1/2$ resonance. They were run for $\tau = 6 \cdot 10^9$. The numerical inaccuracies dominate at this zoom level, but no distinct features are yet present. Based on these runs, we see that the upper bound on radial chaotic feature size is $\mathcal{W}_{1/2, \alpha=0} \leq \mathcal{O}(10^{-4}) \geq \mathcal{W}_{1/2, \alpha=0.691}$.

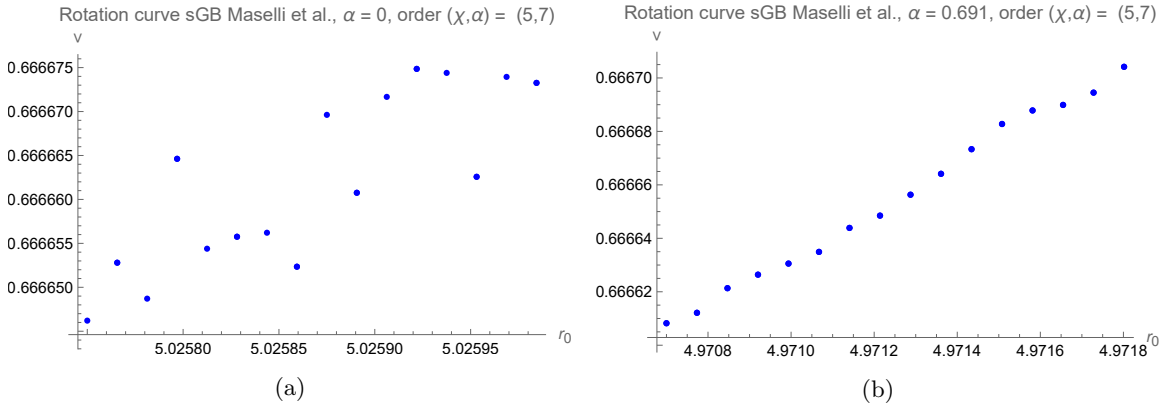


Figure 8.14: EDGB rotation curves at $\mathcal{O}(\chi^5, \alpha^7)$ for (a) zero and (b) maximum coupling near the $2/3$ resonance. Both analyses ran for $\tau = 6 \cdot 10^9$. Again, the numerical inaccuracies dominate. We see that the upper bound on radial chaotic feature size is $\mathcal{W}_{2/3, \alpha=0} \leq \mathcal{O}(10^{-4}) \geq \mathcal{W}_{2/3, \alpha=0.691}$.

8.5 Effects of the chosen coordinate system

In Chapter 5, an effective potential formalism for computations in modified Kerr gravities was developed for both Boyer-Lindquist and prolate spheroidal coordinates. It was already clear that the nature of these coordinate systems is quite different and could have an effect on the magnitude of different features in the orbital rotation curves. In this section, we will investigate some of the effects of changing coordinates to prolate spheroidal coordinates on the study of rotation curves in (modified) Kerr gravity.

8.5.1 The coordinate dependence of plateau size

Many studies on rotation curves aim to predict the potential plateau sizes as detected near resonant orbits. However, the sizes one finds and thus potentially the physical conclusions drawn are strongly dependent on the choice of coordinate system.

From Chapter 4, we recall that most coordinate systems used in SAV metrics maintain the same choice of t and ϕ . For instance, in the transformation from Boyer-Lindquist coordinates to prolate spheroidal coordinates, t and ϕ are left unaffected. Furthermore, x can be obtained solely from r and y solely from θ . Because respectively $x \neq x(\theta)$ and $y \neq y(r)$, x can be interpreted as a radial coordinate and used in direct analogy to r in the construction of the rotation curve⁷. In fact, studies of the Manko-Novikov spacetime often use precisely this coordinate system when constructing rotation curves, or an equivalent compactification in the form of factor structure coordinates [26][31]. Although this might seem like a technicality, we know that these coordinate systems are of inherently different natures. For instance, prolate spheroidal coordinates are measured relative to the event horizon and shift along with the spin of the central black hole.

It is hence a natural step to transform the widths plateaus in rotation curves in Boyer-Lindquist coordinates to prolate spheroidal coordinates and investigate how this changes qualitative conclusions. Recall from Eq. (4.19) that the relation between x and r is given by

$$x = \frac{r-1}{\sigma} = \frac{r-1}{\sqrt{1-\chi^2}}. \quad (8.1)$$

Let us consider the plateaus of the second order expansion of the EDGB line element as an example. Recall that the widths of the 1/2 resonance in Boyer-Lindquist coordinates were $\mathcal{W}_{0,BL} = 0.011125$ and $\mathcal{W}_{0.691,BL} = 0.010375$ at this order. Transforming the r coordinates of the edges of the plateaus to prolate spheroidal coordinates via Eq. (8.1) and recomputing the widths in this coordinate system yields $\mathcal{W}_{0,PS} = 0.011531$ and $\mathcal{W}_{0.691,PS} = 0.010870$ respectively. Of course, since a coordinate transformation does not affect the underlying physics, these are precisely the edges of the plateaus one would find by computing the rotation curve in prolate spheroidal coordinates from first principle, i.e. by transforming the EDGB line element to prolate spheroidal coordinates. If one then computes the relative plateau width in both coordinate systems, one finds that in prolate spheroidal coordinates, the relative difference between the zero and maximum coupling cases is slightly smaller than in Boyer-Lindquist coordinates. This is of course a result of the transformation and also does not change the underlying physics, but should be noted as an important effect which might not be immediately obvious when choosing a coordinate system for this analysis. One of the subtleties inducing this behaviour is the slight shift in resonance location caused by the addition of the scalar

⁷In principle, either non-conserved coordinate could be used. However, the radial coordinate is a natural choice because, as indicated before, orbital decay causes astrophysical orbits to cover the full radial rotation curve in a fashion more intuitive than when an angular choice of coordinate is made.

field coupling. If one chooses a compactified coordinate system such as factor structure coordinates, this radial shift's effect on the ratio between the plateau sizes is amplified, exacerbating the coordinate dependence.

The lack of common agreement between researchers on the characterisation of these chaotic features in general combined with the subtleties in the definitions of some of these coordinate systems can cause these ambiguities to become problematic. After all, it is precisely the relative difference between plateau widths that is often employed to differentiate between the 'amount of chaos' caused by additional terms in the action and by numerical inaccuracies. The fact that conclusions on underlying physics depend on the coordinate system chosen is undesirable at best and confusing at worst. Hence, a common definition for (the magnitude of) chaos in rotation curves of modified gravities should be agreed upon, such that coordinate system artifacts can be excluded as potential sources of errors. Preferably, a coordinate-independent characterisation of rotation curve discontinuities should be developed, such that coordinate choices used in the computation do not affect the final result. We will return to this problem in Section 8.6.

8.5.2 Performance benchmark of different coordinate systems

Since the numerical methods used in the computation of rotation curves are relatively intensive, one could consider using another coordinate system if it is easier to integrate numerically. Indeed, we know that the prolate spheroidal formulation of the Kerr line element for instance contains no trigonometric functions, which can potentially simplify the equations from a computer's point of view. However, since the more intensive integrations in this analysis are based on *expansions* of line elements, these also do not contain any (explicit) trigonometric functions. Hence, the best method to find out whether a particular line element is more efficient is by performing a parallel comparative test using the same conserved quantities and parameters.

For this computation, we compute a single rotation number at $\mathcal{O}(\chi^5, \alpha^7)$ using the same conserved quantities as before. In both cases, we set $\alpha = 0.691$, since the line element in that case is the most cumbersome and hence slow to integrate. An initial radial coordinate of $r = 3.98765$ was chosen since it is somewhat close to the $1/2$ resonance and hence in the relevant regime of these analyses. We avoid choosing a round number such as $r = 4$, because this might unintentionally simplify calculations for the numerical integrator. The radial initial condition $r = 3.98765$ phrased in prolate spheroidal coordinates is then $x = 3.13191$. A computation time of $\tau = 5 \cdot 10^8$ was chosen, which is sufficiently long for significant numerical advantages to manifest at this order in the line element expansion.

The actual analysis was performed by applying these settings to the programming framework using the EDGB line element, which is presented in Boyer-Lindquist coordinates by default. Additionally, the EDGB line element was converted to prolate spheroidal coordinates using the transformations provided in Chapter 4, re-expanding the resulting expression up to $\mathcal{O}(\chi^5, \alpha^7)$. This prolate spheroidal form of the line element was then run through the same software framework, modified for use with prolate spheroidal coordinates. The Boyer-Lindquist and prolate spheroidal analyses were performed in parallel, such that a comparative performance analysis was possible.

In Table 8.1, the results of the comparative run are presented. We see that the prolate spheroidal computation took $\approx 9.5\%$ longer than the Boyer-Lindquist run. This translated into $\approx 9.4\%$ more piercings of the Poincaré slice, which means that both runs compute on average almost the same number of piercings per hour. However, the longer run time indicates that in prolate spheroidal

Performance comparison	CPU time	Memory	# piercings	ν
Boyer-Lindquist	07:11:17	4.621 GB	28667	0.552241
Prolate spheroidal	07:52:47	7.753 GB	31373	0.551719

Table 8.1: Results from the comparative rotation number computation in Boyer-Lindquist and prolate spheroidal coordinates at $\mathcal{O}(\chi^5, \alpha^7)$, $\alpha = 0.691$ and $r = 3.98765$ ($x = 3.13191$). The conserved quantities were the same as for the rotation curve computations and the computation time was $\tau = 5 \cdot 10^8$ in both cases. CPU time should be read as *HH:MM:SS*.

coordinates, a lower setting of numerical proper time corresponds to a greater amount of physical iteration time. The rotation numbers found deviate by $\approx 0.1\%$, which can be attributed to the different number of piercings. The most remarkable difference however is the amount of memory used. Clearly, the prolate spheroidal formulation is much more memory-intensive than the Boyer-Lindquist formulation of the full EDGB line element. When corrected for the number of piercings, prolate spheroidal coordinates are more than 53% more memory intensive than Boyer-Lindquist coordinates. Based on these results, it was concluded that for this project, computing the rotation curves in Boyer-Lindquist coordinates was numerically the most convenient, which complements the other reasons to choose this coordinate system which were mentioned earlier. With that in mind, it might be possible to algebraically simplify the EDGB line element in prolate spheroidal coordinates by for instance performing the double expansion around the Kerr solution in prolate spheroidal rather than Boyer-Lindquist coordinates. However, it is unsure whether this would provide any meaningful numerical gains based on the work done in this thesis.

Since the performance is such an important factor in this analysis, one might wonder whether the computations in this thesis are slow due to the underlying computing cluster employed. Naturally, a faster CPU yields a faster result. For this project, multiple available computing resources were tested; it was found that Utrecht University’s Gemini computing cluster [71] was the best-performing for this analysis, all aspects considered, when compared to SURFsara’s national computing cluster (Lisa) [72]. More details on the differences in performance and logistics between these clusters are given in Appendix E.

8.6 Alternatives to plateau width

As discussed, the coordinate dependence of the plateau width makes it a sub-optimal quantification of the size of a feature, especially since we have shown that it is perfectly possible (and sometimes potentially easier) to compute these features in other coordinate systems. There exist other quantifications of the size of these chaotic features. For instance, the authors of Ref. [30] propose that one could use the area of a feature in the rotation curve for this purpose

$$\mathcal{A} = \int_{\text{plateau}} d\nu dr_0 \quad , \quad (8.2)$$

since it is claimed that certain plateaus near the 1/2 resonance might be warped into different aspect ratios in the rotation curve for different perturbations and orders of the EDGB expansion. However, it is unclear how this could happen from a dynamical-systems point of view, since the Poincaré-Birkhoff theorem implies that the new fixed points are either stable or unstable in nature and occur in alternating patterns around the original fixed point. Indeed, assuming all numerical artifacts have been accounted for via high-precision and long-term evaluations, we believe that it is more likely

that the perceived warped plateaus are indicative of either a plateau at a smaller resolution than measured, since one has an increased gradient in the rotation curve just before and after a plateau, or more likely of an unstable point, which would then mean that the perturbation caused by the scalar field is chaotic in nature at the 1/2 resonance and only becomes apparent as such once the stable point generated by the spin expansion is negated through a higher-order spin expansion.

Apart from all this however, the quantity \mathcal{A} still suffers from the coordinate dependence of r_0 . Indeed, quantitatively comparing plateaus as found in this thesis and Ref. [30] at second order is only possible because both studies employ a Boyer-Lindquist coordinate system, which *should* not matter. Furthermore, Ref. [30] only discusses stable points as they appear in the rotation curve; however, we know that both the second order EDGB and Kerr solution independently have discontinuities in their rotation curves, which means that one also needs to consider X-points when defining a measure of chaos. We are hence motivated to look further for invariant properties which can be used to quantify the magnitude of a chaotic feature, regardless of the coordinate system and appropriate for both plateaus and discontinuities.

8.6.1 Phase space volume as an invariant measure of chaos

It would be beneficial to develop a method by which to characterise the magnitude of a chaotic feature which does not depend on the chosen coordinate system of the underlying line element. That way, researchers do not have to agree on what coordinate system to display their results in when studying rotation curves, but rather use whatever parametrisation is best suited to their situation.

Although rotation curves are intrinsically linked to their underlying parametrisation, we see that a plateau or discontinuity corresponds to qualitatively distinct features which are particularly visible in the phase space of the geodesics. This motivates us to utilise *Liouville's theorem* to formulate an invariant measure of the size of a discontinuity. In our context, Liouville's theorem states that the phase space volume of a trajectory in a Hamiltonian system is invariant under canonical transformations [73], i.e. the quantity

$$\mathcal{V} \equiv \oint dp_\mu dq_\mu \quad (8.3)$$

is independent of the underlying coordinate system, where \oint indicates integration along a given geodesic. Combined with the fact that the SAV metric dynamical system is physically two-dimensional in nature (see Chapter 5), this implies that if we compute the full phase space volume spanned by the librational components of a particular geodesic, we have an invariant characterisation of that geodesic.

Since geodesics are periodic, it is a straightforward exercise to compute the phase space spanned by a geodesic given a set of initial conditions and conserved quantities. Indeed, exploiting the symmetries in $p_r = 0$ and $\theta = \pi/2$ in the Boyer-Lindquist formulation⁸, we can easily construct the phase space volume of a geodesic as follows:

1. Compute the equations of motion of r, p_r, θ, p_θ numerically, for instance via the Hamilton-Jacobi framework built in this thesis.
2. In the Boyer-Lindquist case, we have as initial conditions $p_r = 0$ and $\theta = \pi/2$. Hence, we evaluate the two parametric curves (p_r, r) and (θ, p_θ) over time for half a cycle. This happens

⁸We use Boyer-Lindquist coordinates as an example; for instance prolate spheroidal coordinates would have worked perfectly fine as well. The numerical nature of the analysis means that one always needs to pick *some* appropriate coordinate system. The point of this section is that the result will not depend on the particular parametrisation one has chosen.

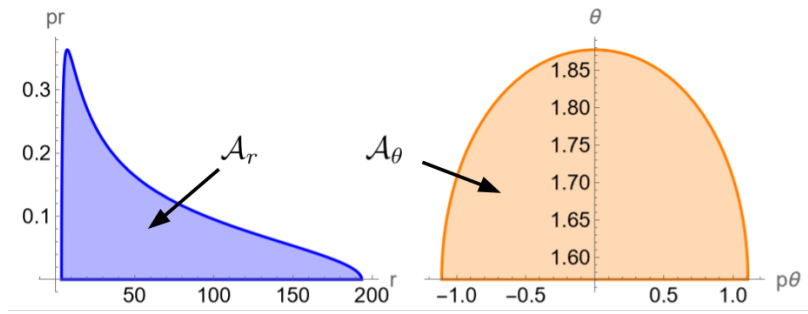


Figure 8.15: Phase space areas as traced out by geodesics for half a cycle in (r, p_r) and (p_θ, θ) space respectively, which we define as \mathcal{A}_r and \mathcal{A}_θ . This particular spacetime is the Kerr line element expanded up to second order in spin with $E = 0.995$, $L_z = 3.5$ and $\chi = 0.3$ starting at $r_0 \approx 3.8$. Note that in the (p_θ, θ) plot, the horizontal axis is located at $\theta = \pi/2$, which is the symmetry axis of that space.

exactly when the geodesics pierce respectively $p_r = 0$ and $\theta = \pi/2$ for the second time⁹. One then has curves such as the examples presented in Fig. 8.15.

3. Because we put the quantities with useful symmetries on the vertical axis in both phase space curves, one can now straightforwardly compute the underlying¹⁰ area numerically. In *Mathematica*, `NIntegrate` has the required functionality. Integrating numerically is preferred over an analytical solution, since it allows application to inexact line elements such as the EDGB solution used in this thesis.
4. The obtained areas \mathcal{A}_r and \mathcal{A}_θ are precisely one half of the full area swept in the respective Poincaré sections. Exploiting the symmetries of the geodesics in p_r and θ respectively, the full volume is then given by $\mathcal{V} = 2 \cdot \mathcal{A}_r \cdot 2 \cdot \mathcal{A}_\theta$, which via Liouville's theorem is then an invariant quantity.

The invariance of \mathcal{V} is only useful if it takes on different values for different geodesics. Indeed, as one would expect, this is the case. Fig. 8.16 shows the evolution of \mathcal{V} within a portion of the allowed region for the expanded Kerr solution with $E = 0.995$, $L_z = 3.5$ and $\chi = 0.3$. We see that \mathcal{V} does indeed vary under changes in the initial radial coordinate and reaches a minimum at the fixed point. The minimum at the fixed point is in line with expectations, since at the fixed point one has a constant radius, which implies that $p_r = 0$ and hence $\mathcal{V} = 0$. This shows that \mathcal{V} encodes information on *where* a geodesic is located with respect to the fixed point. The total area in the phase spaces of r and θ , based on which this quantity was computed, are depicted in Appendix D.

This phenomenon can be exploited in the characterisation of chaotic features. Let us start with the plateaus in the rotation curve. In the phase space depictions of these features, such as Fig. 8.11, we clearly see the closed curves of geodesics around the new island of stability if r_0 is inside the plateau. Hence, there exists some outermost and some innermost radial r_0 for which geodesics do *not* form a closed curve around this fixed island. These 'boundary geodesics' can be determined as precisely as one can meaningfully vary r_0 . Indeed, since there is a one-to-one correspondence between the

⁹Note that this happens at different moments in proper time, since $\omega_r \neq \omega_\theta$.

¹⁰In both cases, one should compute the area between the curve and the initial value. For p_r , the initial zero value means that integrating the area under p_r is fine. However, in the θ case, one should integrate under the function $\theta - \pi/2$ to obtain the correct result.

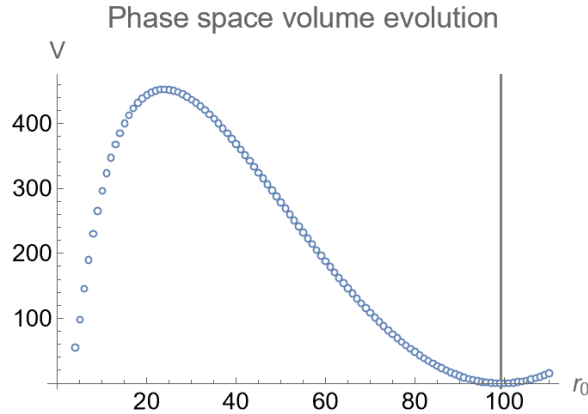


Figure 8.16: Evolution of \mathcal{V} for different values of r_0 , i.e. different geodesics starting in the equatorial plane, in the Kerr spacetime expanded up to second order in spin, with $E = 0.995$, $L_z = 3.5$ and $\chi = 0.3$. The vertical line indicates the fixed point; at the fixed point the volume achieves a minimum where $\mathcal{V} = 0$. In Boyer-Lindquist coordinates, this is due to the fact that those geodesics are paths at constant r .

rotation curves and these phase space depictions, the boundary geodesics can be found by setting r_0 precisely at the two values which are closest to the plateau without being at $\nu = 1/2$ themselves. Having identified the boundary geodesics, one can compute the phase space volumes traced out by these trajectories using the algorithm outlined above and then consider their *difference*. That way, we can define the size of a plateau in terms of the phase space volume as

$$\mathcal{V}_\nu \equiv |\mathcal{V}_{inner} - \mathcal{V}_{outer}|. \quad (8.4)$$

Since \mathcal{V}_{inner} and \mathcal{V}_{outer} are invariant under coordinate transformations, \mathcal{V}_ν is as well. Furthermore, because the low-order resonances are located in the steep incline region of r in the volume curve presented in Fig. 8.16, a more prominent plateau in this region will correspond to a greater difference in volume between the inner and outer boundary geodesics and hence larger \mathcal{V}_ν . This is how one can compute a coordinate-invariant quantity which quantifies the size of a plateau.

This method was applied to the second order results presented earlier in this chapter. In Table 8.2, we see the results corresponding to the various second order metrics considered in this thesis. It should be noted that the main pitfall of this computation is the resolution in r ; if the innermost and outermost geodesics are very close to each other (which is the case for these very subtle features), the error in the accuracy with which one computes r_0 and its propagation into the resulting phase space volume difference could dominate the result. However, this is also a limitation one has when considering the radial width as a metric of the size of a plateau. Thus, this method does not alleviate the numerical challenges of characterising plateaus, but does provide a way of quantifying the results in an invariant fashion, however accurate or meaningful they may be.

In the case one has a discontinuity, it is less obvious what makes a good quantification of the amount of chaos. This is because there is no distinct region in r (or x) where the unstable island exists, but rather one specific disallowed value through which the geodesic is propelled. However, qualitatively looking at the corresponding phase space plots such as Fig. 8.11b can grant us some insight. We see that there exists a region near the resonance where no geodesics are present in the phase space. Indeed, this 'void' is the veil of chaos which surrounds these unstable points, since no periodic

$\nu = 1/2, \mathcal{O}(\chi, \alpha) = (2, 2)$	r_{res}	Inner r_0	Outer r_0	Inner \mathcal{V}	Outer \mathcal{V}	$\mathcal{V}_{1/2}$
EDGB, $\alpha = 0$	$1.25 \cdot 10^{-4}$	3.81425	3.82538	49.7591	50.0517	0.292595
EDGB, $\alpha = 0.691$	$1.25 \cdot 10^{-4}$	3.76863	3.77913	45.6899	45.9755	0.285604
Kerr expansion	$2.5 \cdot 10^{-4}$	3.78125	3.78850	48.0837	48.2780	0.194287

Table 8.2: Results of the computation of the phase space volume of the 1/2 plateau in the three second order spacetimes analysed in this thesis, which are in one-to-one correspondence with their rotation curves as presented earlier in this chapter. r_{res} indicates the resolution in r_0 . Inner and outer r_0 indicate the initial radial coordinate of the innermost and outermost geodesics which are not inside the plateau itself. Inner and outer \mathcal{V} are the corresponding phase space volumes of those boundary geodesics and $\mathcal{V}_{1/2}$ is their difference, which we consider the volume corresponding to the plateau in the rotation curve.

$\nu = 2/3, \mathcal{O}(\chi, \alpha) = (2, 2)$	r_{res}	Inner r_0	Outer r_0	Inner \mathcal{V}	Outer \mathcal{V}	$\mathcal{V}_{2/3}$
EDGB, $\alpha = 0$	$6 \cdot 10^{-5}$	5.00713	5.00719	98.2980	98.3009	0.002836
EDGB, $\alpha = 0.691$	$6 \cdot 10^{-5}$	4.97376	4.97382	95.6952	95.6980	0.002873
Kerr expansion	$2.5 \cdot 10^{-4}$	4.98550	4.98575	97.4604	97.4722	0.011852

Table 8.3: Results of the computation of the phase space volume of the 2/3 plateau in the three second order spacetimes analysed in this thesis, which are in one-to-one correspondence with their rotation curves as presented earlier in this chapter. The quantities have the same meaning as in the 1/2 case, except that the inner and outer geodesic are those closest to the exact 2/3 resonance radius, rather than to the edges of the plateau like in the 1/2 case. The much larger result in the Kerr case is most likely due to the much larger resolution in r , not due to physical effects.

geodesics can exist there. We can also see that the two geodesics which form the boundaries of these voids are those which are the closest to the precise resonance r_0 , which is now a point rather than a plateau. Indeed, we can hence apply the same treatment to the unstable points as to the plateaus, except that we choose the two values of r_0 which are closest to the 2/3 resonance. By computing their volumes and taking the difference, we compute the volume corresponding to the void region visible in the (r, p_r) phase space plots, the results of which are depicted in Table 8.3.

The downside of this approach is that the resolution in r_0 becomes even an more dominant influence on the result near this resonance, since in the case of an X-point, the two boundary geodesics could have arbitrarily close values of r_0 . Hence, although the concept works in principle, the numerical limitations of the rotation curve calculations might make \mathcal{V}_ν more difficult to integrate as a chaos quantification method for the unstable points than for the stable plateaus. Nevertheless, it is again a coordinate-independent quantity and hence worth investigating further as a characterisation tool for chaotic regions as well.

The evolution of the phase space volume as depicted in Fig. 8.16 has another interesting feature we have not considered yet; a maximum before¹¹ the fixed point. Indeed, independent of the chosen parametrisation, there exists a geodesic which has the *maximum phase space volume* \mathcal{V}_{max} . Intu-

¹¹Remember that in spheroidal coordinate systems, this plot is (at least quasi-)symmetric in the fixed point. If one continues the curve in Fig. 8.16 further, one would encounter the same maximum again. However, due to this symmetry, this maximum corresponds to the same geodesic under $\tau \rightarrow -\tau$ and we hence restrict ourselves to the inner half of the allowed region for this section.

$\mathcal{O}(\chi, \alpha) = (2, 2)$	\mathcal{V}_{max}	$\bar{\mathcal{V}}_{1/2}$	$\bar{\mathcal{V}}_{2/3}$
EDGB - $\alpha = 0$	452.348	$6.46836 \cdot 10^{-4}$	$6.270 \cdot 10^{-6}$
EDGB - $\alpha = 0.691$	452.341	$6.31391 \cdot 10^{-4}$	$6.514 \cdot 10^{-6}$
Kerr expansion	452.348	$4.29508 \cdot 10^{-4}$	$2.620 \cdot 10^{-5}$

Table 8.4: The normalised feature volumes of all second order plateaus and discontinuities presented in this section. The consistency of the value of \mathcal{V}_{max} is due to the fact that the line elements are only very slightly different.

itively, we understand that this is analogous to the geodesic for which the area of the rectangle with edges on the curve of zero velocity as spanned out in real space (see for example Fig. 6.7) multiplied by the rectangle in (θ, p_θ) space is maximised.

What makes \mathcal{V}_{max} an interesting quantity is that it provides an invariant benchmark dependent on the given set of conserved quantities, to which one can compare the values of \mathcal{V}_ν as obtained from the rotation curve analysis. That way, we can present the size of a feature as a fraction of the maximum phase space volume, which is a quantity any researcher can reproduce by recreating Fig. 8.16 for their set of conserved quantities and maximising an interpolating function. Furthermore, making \mathcal{V}_ν relative means that for instance choosing more energetic or eccentric orbits, which can inflate the phase space volume, can be accounted for by using this normalisation factor. This motivates us to introduce the *normalised feature volume* $\bar{\mathcal{V}}_\nu$ as

$$\bar{\mathcal{V}}_\nu \equiv \frac{\mathcal{V}_\nu}{\mathcal{V}_{max}} = \frac{|\mathcal{V}_{inner} - \mathcal{V}_{outer}|}{\mathcal{V}_{max}}. \quad (8.5)$$

Let us apply this definition to the second order chaotic features. Using an interpolation method, a set of maximum volumes was found. These maximum volumes were then applied to the results presented in Table 8.2 and Table 8.3, the results of which are shown in Table 8.4. The small values one finds are indicative of the smallness of the features. Indeed, we see that the phase space volumes occupied by chaotic features are small fractions of the maximum volume.

8.6.2 Application to higher order results

The natural next step is to apply this classification scheme to the results of the EDGB line element at $\mathcal{O}(\chi, \alpha) = (5, 7)$. Although no clear plateaus or discontinuities were yet found, we can still compute an upper bound for the normalised feature volume from these plots. After all, if the features were larger than what was depicted in the figures, they would have already been detected. Based on Fig. 8.13 and Fig. 8.14, we pick values of r_0 for the outer and inner geodesics within which it is apparent that the potential features must lie, as far as that can be concluded from those results. The results are then processed in a similar fashion to the second order cases and presented in Table 8.5 and Table 8.6.

There are several interesting conclusions to be drawn from these results. Firstly, it seems that at this order, the zero coupling value of \mathcal{V}_{max} is again equal to the Kerr expansion case presented in earlier results, indicating that the metric seems to be accurate in this respect at this order. Furthermore, we find that the upper bounds on the normalised feature volume are all $\mathcal{O}(\bar{\mathcal{V}}_\nu) \leq 10^{-6}$, with the notable exception of the $\nu = 2/3, \alpha = 0.691$ case; here, the upper bound of the phase space volume of that feature is larger than the other cases at $\mathcal{O}(\bar{\mathcal{V}}_{2/3}) \leq 10^{-5}$. However, it should

$\nu = 1/2, \mathcal{O}(\chi, \alpha) = (5, 7)$	\mathcal{V}_{max}	Inner r_0	Outer r_0	Inner \mathcal{V}	Outer \mathcal{V}	$\mathcal{V}_{1/2}$	$\mathcal{O}(\bar{\mathcal{V}}_{1/2})$
EDGB, $\alpha = 0$	452.348	3.84308	3.84323	50.4974	50.5014	0.0041	$\leq 10^{-6}$
EDGB, $\alpha = 0.691$	452.335	3.76123	3.76138	43.6011	43.6055	0.0045	$\leq 10^{-6}$

Table 8.5: Results of applying the phase space volume characterisation of chaotic features to the rotation curves of $\mathcal{O}(\chi, \alpha) = (5, 7)$ EDGB spacetime near the $1/2$ resonance. The inner and outer radii were selected by considering Fig. 8.13 and looking within what bounds a potential feature can be concluded to exist, taking into account the distortions from numerical inaccuracies. Note that the final result is the order of the *normalised* feature volume, calculated via Eq. (8.5).

$\nu = 2/3, \mathcal{O}(\chi, \alpha) = (5, 7)$	\mathcal{V}_{max}	Inner r_0	Outer r_0	Inner \mathcal{V}	Outer \mathcal{V}	$\mathcal{V}_{2/3}$	$\mathcal{O}(\bar{\mathcal{V}}_{2/3})$
EDGB, $\alpha = 0$	452.348	5.02585	5.02593	99.1659	99.1695	0.0012	$\leq 10^{-6}$
EDGB, $\alpha = 0.691$	452.335	4.97129	4.97143	94.9617	94.9685	0.0068	$\leq 10^{-5}$

Table 8.6: Results of applying the phase space volume characterisation of chaotic features to the rotation curves of $\mathcal{O}(\chi, \alpha) = (5, 7)$ EDGB spacetime near the $2/3$ resonance. The inner and outer radii were again selected by considering Fig. 8.14 and looking within what bounds a potential feature can be concluded to exist. Note that, as with the $1/2$ case, the final result is the order of the *normalised* feature volume, calculated via Eq. (8.5).

be noted that the choice of the inner and outer geodesics in these cases with no clear features was somewhat arbitrary. To conclusively find out what the size of these features is, they must be found and characterised through more high-accuracy runs with as many CPU-cores as one can acquire for this purpose.

Chapter 9

Astrophysical implications

Up till now, the treatment of using EMRIs to detect signatures of modified gravity has been entirely based on theoretical considerations. In this chapter, we will discuss some of the observational implications of the results of the analysis. We will discuss how one uses gravitational waves to couple experimental observations to the theoretical predictions made in this thesis. We then cover some of the observables one can calculate using the EMRI model presented. Furthermore, we will consider whether the effects of astrophysical phenomena such as the presence of an accretion disk change our findings.

9.1 Sagittarius A* and S4714

Before discussing the details of measuring EMRI systems in the universe, it is worth discussing whether the systems analysed in this project are expected to exist in the universe. To illustrate this, we will consider the example of the black hole in the centre of our own galaxy: Sagittarius A*. Sagittarius A* has a mass of $(4.154 \pm 0.014) \cdot 10^6 M_{\odot}$ [74] and is hence considered a supermassive black hole. Sagittarius A* is surrounded by a cluster of stars [75], which due to their stellar masses orbit paths closely resembling geodesics from general relativity in accordance with the EMRI approximation. The innermost of these stars orbit at relativistic velocities and at extremely high eccentricities [76]. Currently, the star with the closest known approach to Sagittarius A* is S4714. S4714 is extreme in its orbital parameters; its eccentricity is 0.985, its orbital period is just 12 years and, importantly, its closest approach is 12.6 ± 9.3 AU. The extremity of these parameters is readily visualised by its orbital trajectory, which is shown in Fig. 9.1. The event horizon of Sagittarius A* corresponding to its mass is $(8.20 \pm 0.03) \cdot 10^{-2}$ AU, assuming $\chi = 0$ (which is a somewhat valid approximation; the spin parameter of Sagittarius A* is probably small [77]). This means that S4714's closest approach could be anywhere between ≈ 40 and ≈ 267 Schwarzschild radii. Although these are not the exact parameters which were studied for the computation of rotation curves, it shows that highly eccentric orbits around central black holes with very close approaches do in fact occur in the universe. Since there are many other supermassive black holes in other galaxies, it is a reasonable assumption that systems similar to the ones modeled in this project could exist and hence be detected observationally. After all, stars such as S4714 are doomed to eventually spiral into the central black hole due to energy loss; at some point, they would pass through the regime of the resonant orbits studied in Chapter 8.

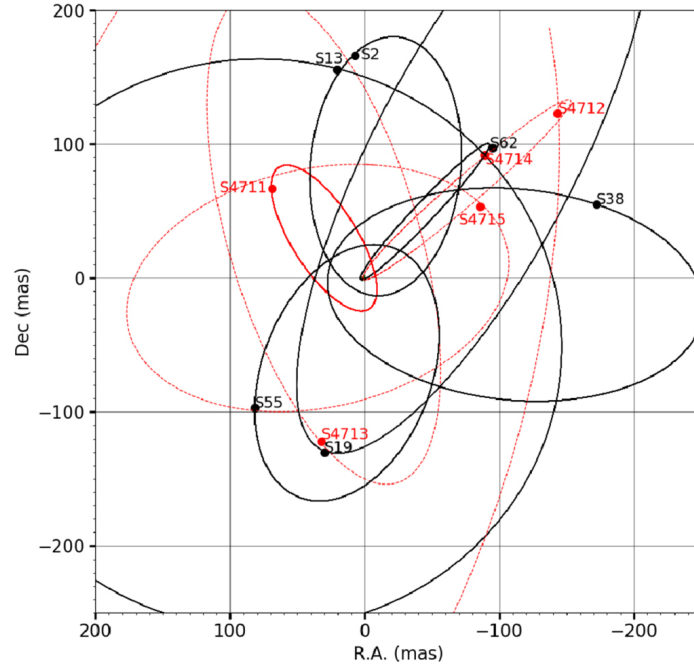


Figure 9.1: Schematic of stars orbiting closely to Sagittarius A*, including S4714 [76].

9.2 Gravitational wave astronomy

Naturally, physical theories have to be tested using experimental setups, which introduces another level of consideration and complication to testing general relativity near black holes. Let us now discuss some of the experiments which will be used to detect the gravitational wave signals generated by EMRI systems in more detail. We will first cover the general principles of gravitational wave astronomy and then apply them to the EMRI case in the context of modified gravity probes.

9.2.1 Measuring spacetime with interferometry

The first confirmed measurement of gravitational wave was performed by the LIGO and Virgo collaborations in 2016 [78], marking the start of the era of gravitational wave astronomy. Both the LIGO and Virgo ground-based experiments use laser interferometry to detect passing gravitational waves. The basic principle behind the machines is best understood with a visual schematic, as depicted in Fig. 9.2. A laser is sent in perpendicular directions along two arms, each 4 km in length. If a gravitational wave passes through the detector, a relative difference in the effective path length covered by the laser in the two arms appears. This difference, which is called the *strain*, causes destructive interference of the laser, which is then measured and reconstructed into a gravitational waveform. The magnitude of this strain is incredibly small: the peak strain measured in this first observation was $1.0 \cdot 10^{-21}$, which corresponds to a length change ≈ 1000 times smaller than the width of a proton. One can now appreciate how minute the measured effect is. Because of this, keeping the *signal-to-noise ratio* (SNR) of a gravitational observatory at acceptable levels is one of the great challenges faced by physicists operating these experiments.

Aside from the resolving power of the experiment, which is determined by the smallest strain it

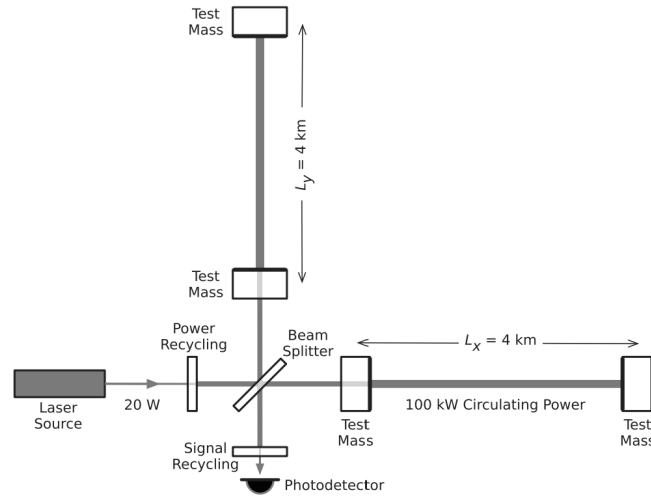


Figure 9.2: Simplified schematic of the Advanced LIGO detector [78].

is able to identify, another limitation of any given gravitational wave experiment is the frequency band of gravitational waves to which it is sensitive. The frequency of a gravitational signal depends on the characteristics of the source. Inspirals of for instance binary neutron stars typically generate a higher frequency signal than EMRIs [79], also depicted in Fig. 9.3. From this sensitivity curve, we can see that the LIGO and Virgo experiments will not be able to measure gravitational waves from EMRIs. However, the EMRI wave frequency sits comfortably in the sensitivity range of LISA. LISA is an upcoming gravitational wave observatory which uses similar principles of interferometry as LIGO and Virgo¹. However, it will consist of several different satellites placed at the Lagrange points of the Earth-Sun orbit. This way, LISA can use 'arms' with a length of 2.5 million kilometres [7], which allows it to measure lower frequency signals than LIGO or Virgo while maintaining a high enough SNR [80]. Since the end points of the arms are freely floating in space, they are not at a fixed length at all times, providing an additional design challenge.

The launch of LISA, which is as of 2022 planned for 2034, will grant us insight into a completely new range of gravitational wave sources, including the EMRIs discussed in this thesis. Hence we are still a decade away from finding experimental data with which to corroborate our theoretical predictions on rotation curves in modified gravity. However, there is another aspect of the experimental testing of EMRIs which must be solved before the data is gathered. A coupling between the physical motion of bodies in spacetime and the gravitational waves generated by that motion need to be computed, since an interferometer naturally does not measure motion directly. The connection between these two aspects of gravitational wave astronomy is provided by gravitational waveforms and it is therefore important to recognise what, in our case, the crossing of a Birkhoff island would look like in terms of gravitational waves.

Besides interferometry experiments such as LISA and LIGO/Virgo, other methods to detect gravitational waves have also been proposed. In particular, *pulsar timing arrays* could be used for this purpose and will be discussed in a later section. Another proposed method is using astrometry to detect gravitational wave sources using ESA's Gaia satellite [81].

¹Although LISA's arms are in the shape of an equilateral triangle, unlike the LIGO/Virgo experiments.

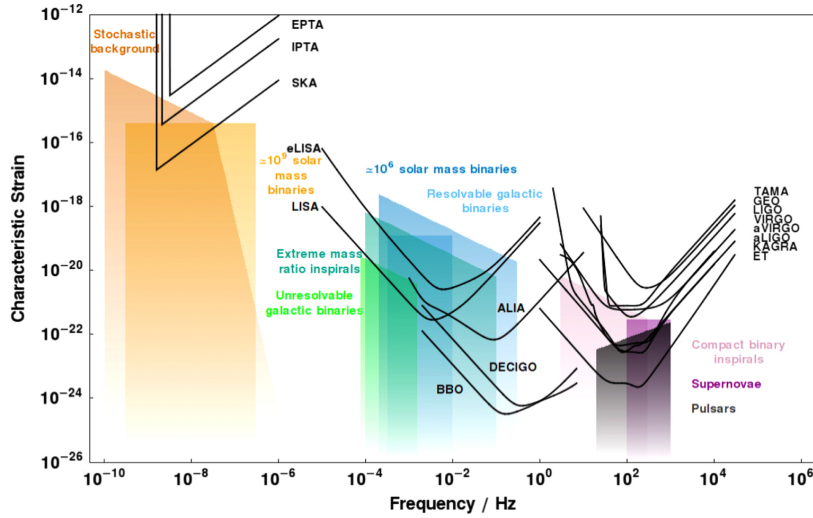


Figure 9.3: Sensitivity curves of different (proposed) gravitational wave experiments [79]. A lower characteristic strain indicates greater resolving power. The coloured regions indicate different sources of gravitational waves.

9.2.2 Orbital response to Birkhoff islands

It is worth investigating the fashion in which the orbiting body in an EMRI crosses the phase space through resonant points from an orbital point of view. This is an important aspect to consider since it couples directly to the detectability of the phenomena. If tori are broken, additional fixed points are created around which the stable and unstable regions form, as is readily visible in the phase space piercings shown in Chapter 8. In this chapter, we briefly discussed the implications of rotation curves features on the orbital mechanics based on their phase space picture; here we will revisit this topic. Let us consider crossing an island of stability first. If a body enters the phase space region near the newly created fixed point, it is effectively caught in a tiny pocket geodesics near the fixed point in terms of orbital frequencies, due to the stable nature of this island. Hence, the orbital frequencies linger slightly on this island of stability, maintaining the rotation number at the resonance in question. The physical manifestation of a stable island is hence the 'attraction' of the orbit to the local fixed point corresponding to a particular resonance, causing the rotation number to stick near the resonant value for a small range of orbits near that fixed point. In the rotation curve, this is indeed seen as a plateau at precisely the resonance in question.

In the case of an unstable point, the behaviour is somewhat opposite. Whereas in an island of stability, the orbit wants to stick close to the resonant value, an unstable fixed point in a certain sense 'repels' the orbit away from that particular resonance. Since unstable resonant points are surrounded by very thin veils of chaos, it is not possible for the orbiting body to maintain a constant ratio of orbital frequencies at precisely the resonant value. Effectively, this results in the orbital frequency ratio being rapidly propelled through the resonant rotation number, as is readily observed in the steep incline in the rotation number evolution near such an island. The orbital behaviour near both stable and unstable points is hence quite different from the consistent evolution along an integrable spacetime's rotation curve, providing a potential avenue of measurement for gravitational wave observatories looking for proofs of modified gravity.

The conclusion from Chapter 8 is that the potential effects of EDGB gravity on the phase space of an EMRI are extremely minute. Although this might suggest that the effects described above are too small to measure, the progression through the phase space could be slow enough that the effects of crossing a stable or unstable Birkhoff island can accrue over the course of many orbits. In a study [82] on the transience of the orbital resonances in Kerr spacetime, it was investigated how long an object stays in the orbital region near different low-order resonant points of the phase space when accounting for adiabatic energy loss to gravitational radiation. Depending on the orbital parameters of the system, the number of orbits spent near a resonant value changes. Generally, several dozens to potentially hundreds of orbital cycles are spent near the important resonances, including the $1/2$ and $2/3$ resonance. If accurate enough measurements can be conducted, the small effect of EDGB gravity could accumulate over many such orbits, allowing its deviation from Kerr to become directly measurable. Indeed, if the non-Kerr effects present themselves as small phase shifts in the gravitational radiation of an orbit, this effect might be able to accumulate over the course of hundreds of orbits and in that way become detectable, under the right circumstances.

9.2.3 Modelling the EMRI signal

The observational data gathered from the LISA experiment will be compared to gravitational waveforms in order to determine the qualities of the source system, as was briefly mentioned in Chapter 2. One might wonder how the chaotic features we have only seen in the phase space up till now are actually measured in gravitational wave signals.

In principle, the gravitational wave signal evolves in the frequency domain as time increases. The full wave signal can, like all periodic data, be decomposed into a Fourier series of (co)sines with different characteristic frequencies. As time moves on and the orbiting body moves closer to the event horizon due to energy loss, the dominant frequency mode of the signal increases, as the stellar body completes full orbits in increasingly shorter time frames [20]. As was alluded to at the start of this chapter, at some point the orbiting body will cover the range of parameters where a resonant orbit can occur. As was shown in Ref. [20], the presence of an underlying non-Kerr spacetime can have a significant impact on the frequency evolution of the gravitational wave signal as detected by LISA, if present. If the underlying spacetime is integrable, the frequency mode of the signal with the highest intensity continuously evolves as the body crosses the resonance. However, if a resonance is crossed in a modified spacetime which is non-integrable, a distinct 'glitch' could appear in the signal caused by the crossing of a Birkhoff island. The authors of Ref. [20] indicate that according to their findings, the $2/3$ resonance depicts the strongest deformation of the signal from the integrable case. This is in line with the assertion of Ref. [28] that the $2/3$ resonance should experience the greatest deviation from the Kerr solution due to the modification of the quadrupole moment.

Besides the detection of these glitches in the case of non-integrable spacetimes, it is also important to construct accurate waveforms of EMRI systems in different gravities, such that useful parameter estimations of the underlying system can be performed using experimental data. This is an active field of research with many challenging aspects [83][84]. There is still much work left to be done; for instance, current frameworks have not yet implemented the full parameter space of orbits. Taking the framework from Ref. [83] as an example: the full waveform models are present for eccentric Schwarzschild orbits, which can be extended to generic Kerr orbits through an augmented analytic Kludge approximation scheme. However, certain parametrisations of the model can introduce problematic signal biasing. In particular, the impact of orbital resonances has not yet been implemented and the authors of Ref. [83] state that it will be a challenge to do so in the current framework. This is a particularly significant problem, since it is around these resonant orbits where a perturbation

from Kerr will be the most detectable. Hence, it is left to future research to continue working on this crucial part of the study of EMRIs, since accurate waveforms will be required for proper data analyses of LISA observations and the potential tests of general relativity these provide.

Although the upshot of this seems to be that being able to properly search for modified gravity using LISA data is still a great challenge, there is one aspect of this search we should highlight. Since the above described effects of Birkhoff islands cannot happen at all in an integrable spacetime, finding *any* non-integrable behaviour is 'smoking gun' evidence against the Kerr spacetime and a direct proof for the non-integrability of the system. Hence, even if one measures a very small manifestation of a Birkhoff island beyond statistical uncertainty, it would already be an highly disruptive discovery. Besides this, there are other methods via which one can test for modified gravity which could corroborate the search for chaotic features, such as the accumulated phasing effect in gravitational waves emitted of the EDGB action as discussed in for instance Ref. [23].

9.3 Time dilation as an observable

In this section, we will investigate whether the evolution of the time dilation experienced by the orbiting body could be used as an additional observable in the investigation of EMRI systems. It is beneficial for the understanding of astronomical phenomena to measure systems using multiple probes; this is an actively developing field of research and is broadly known as *multi-messenger astronomy* [85]. Using the computed numerical solution of an EDGB spacetime where $E = 0.995$, $L_z = 3.5$ and $\chi = 0.3$, it is possible to compute orbital characteristics which one might be able to measure independently of gravitational wave observations. For computational simplicity, we will set $\alpha = 0$. This is warranted because the aim is to build a general understanding of the system, rather than performing a detailed quantitative analysis. By numerically solving for the full 8-dimensional phase space under these conditions, one can construct potentially interesting observable quantities.

9.3.1 Orbital period

One might for instance wonder what kind of orbital period the considered system displays. However, this is not as straightforward to define as one might imagine, due to the highly non-circular behaviour of geodesics around spinning black holes. Indeed, in principle one has an orbital period for each of the three spacelike coordinates. Since the orbits of the class investigated in this thesis contain all interesting physical information in the non-conserved coordinates (r, θ in the Boyer-Lindquist formulation), a natural choice is to take the proper time interval between two crossings of the periapsis as defined in Chapter 6 and name it τ_{orbit} . This is precisely the orbital period in r . Another choice could for example have been to define every full cycle of ϕ as an orbit; however, this fails to exploit the fact that all interesting physics in SAV metrics happens in the r, θ directions. Furthermore, we expect the strength of the gravitational field to be affected mostly by the value of r , making its period a more interesting metric than the θ period.

In Fig. 9.4, τ_{orbit} is illustrated. One finds that the proper time orbital period of the 1/2 resonance in EDGB spacetime at zero coupling and fifth order in spin is $\tau_{orbit,1/2} \approx 6324$, whereas for the 2/3 resonance it is $\tau_{orbit,2/3} \approx 6314$. Although it might seem counter-intuitive at first that an orbit with a closer approach takes longer to complete one cycle, one should keep in mind that a closer approach at the same conserved quantities E, L_z, χ implies more eccentric orbit, indicating a larger apoapsis and hence more time spent in the outer region of the orbit. This results in a longer orbital period, since the radial velocity is smaller further away from the event horizon.

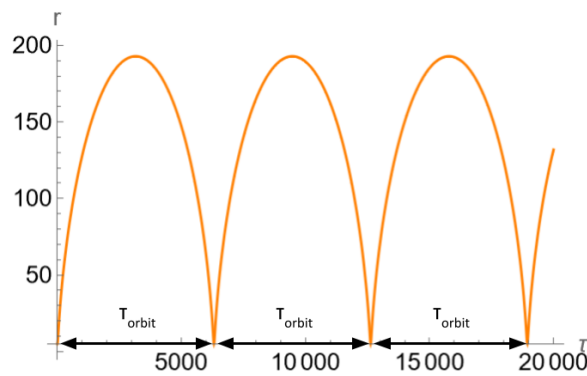


Figure 9.4: Illustration of the periodicity in r over τ , as well as the defined orbital period. This orbit corresponds to the $2/3$ resonance at zero coupling of EDGB spacetime for the given set of conserved quantities. Note that other coordinates, such as the ϕ coordinate, are not (necessarily) oscillating at the same frequency.

9.3.2 The periodicity of time dilation

Another interesting quantity to compute is the *Lorentz factor*. It is defined via

$$\gamma \equiv \frac{dt}{d\tau} \quad (9.1)$$

Physically, this quantity is the time dilation experienced by the orbiting body as observed by an observer at infinity. Since we have the evolution of t over τ for the EDGB line element, we compute γ and track how it evolves over time under our choice of orbital parameters. In Fig. 9.5, we see that on longer timescales, coordinate time evolves linearly along proper time. However, there are distinct changes in the gradient present near the closest approaches of the orbiting body to the black hole. This is expected, since in those regions, the gravitational field is the strongest. To quantify this effect, we compute the evolution of the Lorentz factor over proper time. In Fig. 9.6, one can see that γ is generally close to 1, which is in agreement with the linear evolution of t on large time scales. However, γ peaks strongly when the periapsis is reached. In the $2/3$ resonance orbits depicted in the figure, γ peaks at ≈ 1.637 . For the $1/2$ case, γ can reach values as high as ≈ 2.010 .

One can now truly appreciate that we are indeed in the strong-field regime of gravity with these orbits. Indeed, a star orbiting a black hole near the $1/2$ resonance would experience time twice as slowly as an observer at infinity when it is near its periapsis. If one makes an analogy to special relativity, this is the same amount of time dilation as one would measure between observers moving at a relative velocity of $v \approx 0.866c$. Clearly, the effects of gravity in the analysed systems are extreme. This also opens up interesting potential avenues of research in the characterisation of these systems. For example, the evolution time dilation effect could potentially be used as a way to determine the orbital properties of some object around a supermassive black hole. Since γ and r share the same periodicity, it might be possible to determine ω_r from the periodicity of γ .

Neutron stars are known to have extremely consistent rotation speeds, which is being exploited for gravitational physics research. Pulsar timing array experiments aim to use the remarkably consistent radio frequency emitted by highly-spinning neutron stars (pulsars) to for instance detect gravitational waves [86]. The gravitational waves detectable by these arrays can have extremely low frequencies and could be used to probe for instance galactic mergers, because the effective arm

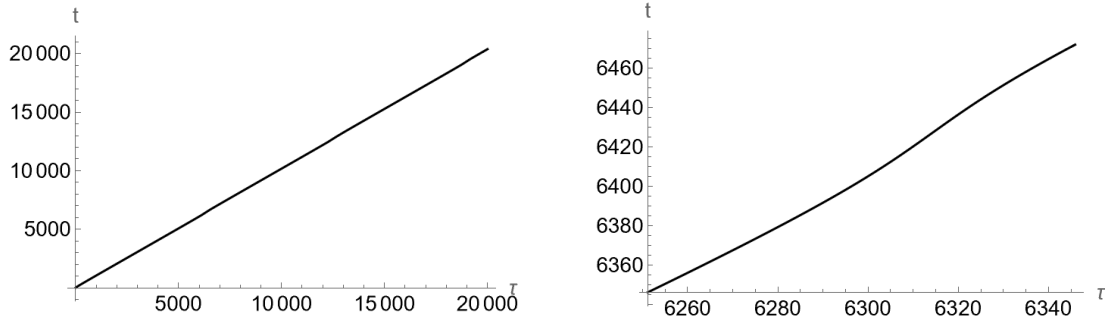


Figure 9.5: The evolution of t over τ around the $2/3$ resonance. On time scales greater than several orbital periods, the relation seems linear. However, upon closer inspection near the periapsis the gradient changes slightly, corresponding to a change in γ . These slope changes happen at multiples of $\tau_{orbit} \approx 6314$, where the gravitational field is the strongest.

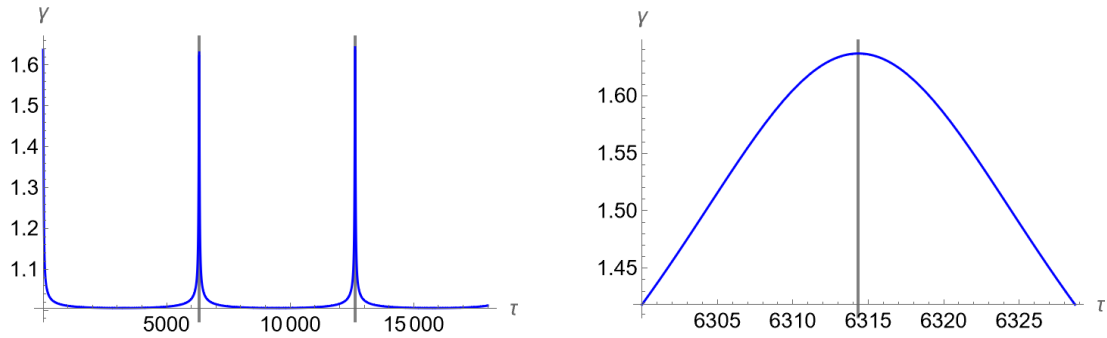


Figure 9.6: The evolution of γ over τ for the $2/3$ resonance. The vertical lines indicate multiples of τ_{orbit} . It might seem as if the maxima in γ are not equal. This is an artifact of the resolution of the plot; the maxima are in fact all located at $\gamma \approx 1.637$.

length of these detectors spans lightyears. One such experiment which is currently in development is the *Square Kilometre Array* (SKA). As its name suggests, the SKA will comprise of a square kilometre sized array of ground-based radio telescopes, containing thousands of dishes and close to a million low-frequency antennae, allowing for a greater image resolution than achieved by for instance the Hubble Space Telescope, albeit in the radio frequency range of electromagnetic radiation [87][88].

Apart from the aforementioned gravitational wave observations, the SKA will be capable of characterising the approximately 1000 pulsars orbiting Sagittarius A*, the supermassive black hole at the centre of the Milky Way [89]. If a pulsar, magnetar or similar compact object with a highly consistent radio signal were to orbit a supermassive black hole such as Sagittarius A* in a highly eccentric configuration, the modulation of its observed radio frequency due to the change in γ could in principle be used to characterise the evolution of its orbit and determine ω_r . Such measurements could corroborate gravitational wave signatures from an EMRI as measured using other experiments, providing an exciting addition to the toolkit of multi-messenger astronomy.

9.4 Environment effects near a supermassive black hole

The extreme-mass-ratio approximation implies that geodesics provide a sufficiently accurate description of a stellar-mass object orbiting a central supermassive black hole for the determination of the very minute effects of a modification to the Einstein-Hilbert action. In Chapter 2, it was established that from a dynamical systems point of view, this assumption is justified due to the relatively slow rate of energy dispersion in the generation of gravitational waves and negligible gravitational influence of the orbiting body on the central black hole. However, the assumption of $T_{\mu\nu} = 0$ might not hold in astrophysical systems. Several objects and features can exist in the area in the near proximity of supermassive black holes, as indicated in the schematic of the central galactic region of the Milky Way in Fig. 9.7.

Around supermassive black holes, one prominent feature one might encounter is an *accretion disk*. Indeed, it is known that Sagittarius A* for example has an accretion disk with a radius of around $2 \cdot 10^4 R_S$ [90]. An accretion disk is comprised of gas rotating around the black hole, in either the co- or counterrotating direction relative to χ , although the rotation axes of the black hole and the disk are not necessarily precisely aligned. Near the event horizon, the matter achieves such extreme orbital velocities that a great deal of electromagnetic radiation is generated from internal friction. When the gas eventually falls into the event horizon, *jets* of extremely relativistic gas are sometimes propelled from either the poles of the black hole or along the rotation axis of the accretion disk [91]. These jets are thought to be generated when the disk and the black hole are strongly magnetised, although building a precise understanding of black hole jets is an active field of research.

The question is then whether these features significantly affect the geodesic orbits analysed in the rotation curve computations. It is safe to assume that the potential presence of a jet does not interfere with the orbital analyses in non-polar orbits². For accretion disks, it is not so obvious; after all, the orbits considered in Chapter 8 exist within 200 Schwarzschild radii, which means that interference with an accretion disk is a possibility. The following phenomena related to the accretion disk could for instance affect the results [92]:

- The mass and spin of the object(s) could change due to the accretion of matter.
- The matter in the accretion disk could influence the stellar-mass object gravitationally³.
- Dynamical friction with the disk could influence the orbital parameters of the stellar-mass object.

Apart from the accretion disk, there are several other factors which might affect the accuracy of the gravitational waveform models and were investigated in Ref. [92]. Some are physically intuitive; for instance, one might wonder whether stars in the cluster around the black hole affect the EMRI system. It is known that this effect is negligible, mostly due to the fact that bodies in an EMRI system interact on a much smaller length scale (and hence generate higher gravitational wave frequencies) than stars in the surrounding cluster. However, there are also effects where physical intuition is less straightforwardly applied. Such effects include for instance the presence of a dark matter halo near the black hole and even the value of the cosmological constant.

By using a Newtonian order estimation, it was determined that at first order these environmental factors in EMRI systems are negligible, and in most cases also up to second order. The exception

²Unless the accretion disk rotation axis is tilted significantly with respect to the black hole spin axis.

³We assume a spherically symmetric matter distribution, such that the potential gravitational pull of the disk on the central body cancels out.

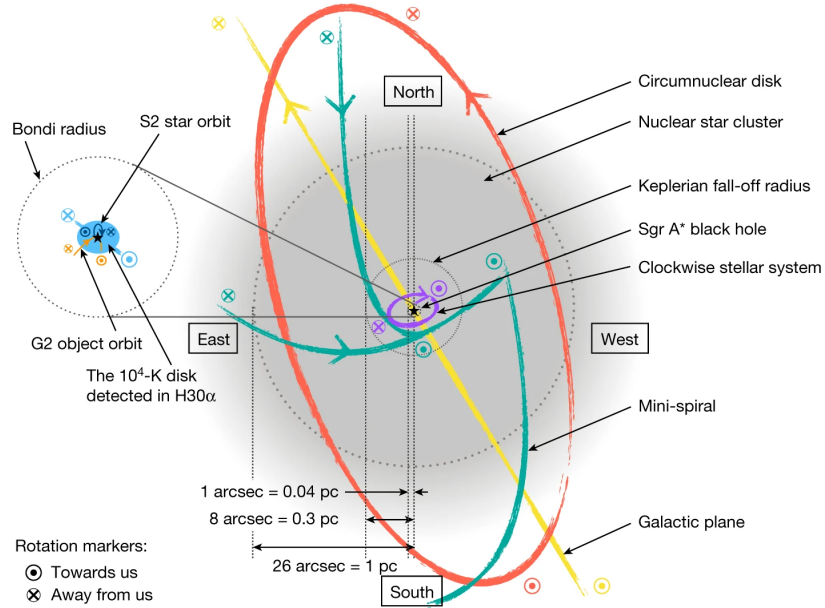


Figure 9.7: Schematic representation of some of the known environmental features near Sagittarius A* [90]. The cyan oval shape indicates the section of the accretion disk where the gas has a temperature of 10^4 K or greater. One can conclude from this example that there are many features near a supermassive black hole which could in principle affect the orbits of surrounding bodies.

at second order is primarily dependent on the dimensions of the accretion disk. If the disk is 'thin', it could become significant. The thinness of the disk depends on the rate of accretion of matter by the central object [93]. Despite this, the authors of Ref. [92] conclude that in most cases, gravitational wave analysis in the EMRI regime is generally not greatly affected by environmental factors. This implies that the system discussed in this thesis can in principle indeed be tested via gravitational wave astronomy and rotation curve analysis, even in active galactic nuclei.

Chapter 10

Conclusions

In this chapter, the main findings of this project are summarised. We provide a succinct and elaborate version of the conclusions, depending on the depth of discussion one is interested in.

10.1 Summarised conclusions

Chaotic features in the form of plateaus and discontinuities in the rotation curves of modified spacetimes provide a method of probing the integrability of EMRI dynamics. By analysing SAV spacetimes in several coordinate systems, we expand a formulation of these dynamical systems which allows for efficient analysis of their properties. Applying this framework to (expansions of) Kerr spacetime and EDGB gravity, we find that high accuracy line elements are required to distinguish between chaotic features arising from the spin expansion inaccuracy and the non-integrability of the underlying spacetime. In particular, we find that the upper bounds of the radial widths of the features in the rotation curve of EDGB spacetime near the 1/2 and 2/3 resonances are of order $\mathcal{O}(10^{-4})$ or smaller in Boyer-Lindquist coordinates. Additionally, we formulate a method of quantifying the size of these features which is invariant under canonical transformations related to the phase space volumes of the geodesics. Application of this method yields upper bounds of $\mathcal{O}(10^{-6})$ on the normalised feature volume of the 1/2 and 2/3 resonances, except the 2/3 resonance in maximally-coupled EDGB spacetime, for which we find an upper bound of $\mathcal{O}(10^{-5})$. Although this indicates that the size of potential chaotic features is very small, since finding any chaotic features experimentally which cannot be attributed to environment effects or inaccuracies would indicate a violation of the no-hair theorem, we believe EMRIs are still a promising probe for GR in the strong-field regime. Other probes such as the phasing of gravitational waves provide further tests of GR and modified gravity, which could support the characterisation of black hole spacetimes via chaotic features. Future work is needed on several aspects of this research. For example, finding waveforms of resonant orbits in EMRIs is a crucial component of studying these systems experimentally.

10.2 Elaborated conclusions

The search for chaotic features in modified gravity theorems is made possible by the results of the KAM theorem and Poincaré-Birkhoff theorem, which predict the existence of plateaus and discontinuities in the rotation curves of non-integrable spacetimes. The rotation curves are hence a probe for general relativity in the strong-field regime, which could in the future be verified by for instance the LISA mission. In the first part of the derivations in this thesis, we established the different

coordinate systems one can use to parametrise SAV solutions to the Einstein field equations. We find that certain coordinate systems are suited only to specific analyses due to their inherent symmetry properties. Weyl coordinates are not useful in the studies of EMRIs due to their cylindrical nature, whereas Boyer-Lindquist, prolate spheroidal and factor structure coordinates are examples of parametrisations well-suited to the characterisation of these systems. The primary difference between the Boyer-Lindquist formulation and the other formulations is that Boyer-Lindquist coordinates are measured relative to the ring singularity, whereas prolate spheroidal coordinates and factor structure coordinates maintain radial coordinates relative to the event horizon.

Due to the conservation of energy and angular momentum in general SAV spacetimes, the usual four-dimensional dynamical system can be reduced to a two-dimensional problem, greatly simplifying the equations of motion one needs to solve. Using the earlier defined spheroidal coordinate systems, it is furthermore possible to define an effective potential formalism which encodes the Hamiltonian constraint as a relationship between the two librational conjugate momenta, the curve of zero velocity and the allowed region of geodesics for given E , L_z and χ . This formalism was derived from first principle independently in Weyl, Boyer-Lindquist and prolate spheroidal coordinates, although only the latter two have a practical application due to the lack of a formulation of the Kerr solution in Weyl coordinates. The prolate spheroidal effective potential holds for any SAV spacetime; the Boyer-Lindquist variant is inherently coupled to the Kerr solution and hence probably only appropriate in close-to-Kerr spacetimes, which are not-so-coincidentally the spacetimes considered in this project.

The effective potential formalism was then applied to the Kerr solution in different coordinate systems. Several aspects of Kerr orbits were considered, such as polar orbits and zoom-whirl orbits. Furthermore, the stability of these orbits was quantified in the form of an ISO radius. The geodesic's relations to the ISCO radii and event horizon were also presented in various coordinate systems. Finally, resonant orbits and their phase space counterparts were computed and analysed.

Next, sGB theory was introduced, as well as the sub-theory of EDGB gravity. A derivation of the static black hole equations was provided, as well as an overview on how one solves these equations and expands the result to the rotating case. Then, several tests were performed on the EDGB line element which was to be used in the zero coupling case to see to what extent the expanded Kerr spacetime re-emerges upon disabling the scalar field contribution to the dynamical system. The EDGB line element was found to be imperfect but sufficiently accurate for the study of rotation curves in this project, within certain parameter restrictions.

Having established the extent of the validity of the EDGB line element, the orbital framework was applied to the second order EDGB spacetime. At the $1/2$ resonance, islands of stability exist in the rotation curve; at the $2/3$ resonance, unstable points are present. After comparing the results in the zero and maximum coupling case, as well as the equivalent features in the expanded Kerr solution and an independent parametrisation of EDGB gravity, we conclude that at this order the chaotic features are dominated by the effects of the spin expansion, such that it is not possible to draw conclusions on the effect of the scalar field at this level of accuracy. However, these features prove the validity of the framework and the predictions of the Poincaré-Birkhoff theorem and provide a useful toy model in the characterisation of chaotic features. Although the results of the higher order expansion require additional runs at higher resolution to their numerical complexity, it was established that the radial magnitude of these features in Boyer-Lindquist coordinates must be smaller than $\mathcal{O}(10^{-4})$, indicating that the effects of scalarisation are indeed minute. The rotation curves were compared to their phase space counterparts, based on which an coordinate-independent

measure of the size of chaotic features was introduced in the form of a normalised differential of the phase space volume of the bounding geodesics of the feature. This quantity encodes the total phase space volume of the chaotic feature, which is an inherently coordinate-independent quantity due to Liouville's theorem. We find that the normalised volumes of the features are smaller than $\mathcal{O}(10^{-6})$, except for the 2/3 resonance at maximum coupling, where the upper bound is $\mathcal{O}(10^{-5})$. Although the features are hence very small in magnitude, future work on for instance their effect on the resonant EMRI waveforms is needed to conclusively determine whether they are observable, where one should keep in mind that other probes of modified gravity are also under development to support these tests, such as via accumulated effects in the gravitational wave phasing as elaborated on in for instance Ref. [23].

Finally, the results of the analysis were put into an astrophysical context. An example of an EMRI which comes close to the analysed regime was presented in the form of a star orbiting Sagittarius A*. The mechanisms behind and recent developments in gravitational wave astronomy were introduced, as well as the possibility of how a pulsar timing array could exploit time dilation to corroborate gravitational wave signals from black hole systems. Finally, the disturbing factors of environmental effects were considered; we reiterate earlier studies indicating that a wide range of potential disturbing factors in high-precision gravitational wave astronomy are not likely to greatly influence the potential results of a rotation curve analysis, since such effects can be accounted for in the waveform models if they become significant.

Chapter 11

Points of discussion

Here, we provide some of the points of improvement of the work done, as well as suggestions for future researchers on which avenues of this aspect of gravity are potentially interesting to pursue in the future.

The primary focus of this thesis was the establishment of a strong and flexible theoretical foundation on which to base calculations in EMRI systems, as well as how one approaches this problem numerically. Because the derivations in this project were largely done from first principle, it was possible to gain a clear overview on the implications, challenges and shortcomings of this study of EMRIs and how they can be addressed in the future. Let us first discuss the implications of the findings of this project and then outline some of the other primary discussion points related to this study.

11.1 Implications of findings

The study of EMRIs in modified gravity theories like EDGB theory is an active field of research. Indeed, discussions on how the findings of this work relate to those of other researchers working in this field are ongoing at the time of writing. Hence, the findings of this project could contribute to the broader study of EMRIs in modified gravity, our understanding of which is evolving as we speak.

Although no definitive feature sizes have been computed yet for the higher order EDGB line element using this framework, the upper bounds on the feature size which *were* found emphasise that any potential research into this topic, whether theoretical or experimental via LISA, needs to employ high-precision methods to seek out differences between the Kerr solution and modified gravity. Indeed, the outer bounds of the phase space volumes can be considered the minimum resolution at which one should look for chaotic features in EDGB gravity at this order. Furthermore, the invariant phase space volume characterisation method introduced in this project could be applied by future researchers investigating nearly-integrable spacetimes, which would simplify comparisons of results in different parametrisations and conventions in Kerr-like spacetimes. Finally, the general conclusions on what makes an appropriate coordinate system and effective potential for the study of SAV systems as well as the numerical (dis)advantages of different formulations could pave the way for others seeking to enter the EMRI field of research for the first time, where we hopefully have given a comprehensive overview of the possibilities and pitfalls for researchers embarking on such a project.

11.2 Sensitivity to line element choice

The behaviour of the geodesics in a spacetime is completely determined by the formulation of the line element. In the case of quadratic gravity theories, oftentimes no closed-form expressions of rotating black hole solutions exist, such that approximations have to be made in order to find a form of $g_{\mu\nu}$ to be used in the numerical analyses. However, as was established in Chapter 2 and confirmed in Chapter 8, this approximation causes a deviation from the integrable case which is larger in magnitude than the potential deviation from the modification of the Einstein-Hilbert action. This fact is the primary challenge in the theoretical findings of EMRI studies in inexact spacetimes.

Furthermore, in this thesis we were largely dependent on the form of the EDGB spacetime as provided by other authors, since we did not derive a black hole solution from first principle. However, steps were taken to address this; the static equations of motion were derived from the action and cross-referenced with earlier work and the provided solution was tested via the effective potential framework in the zero-coupling case. Nevertheless, it would be best if one derives a black hole solution from first principle, such that one does not depend on the findings and possible shortcomings of previous work.

In this point, however, lies also a strength of the framework derived in this thesis. In principle, the framework will accurately compute the equations of motion of any SAV metric in any appropriate parametrisation, exact or approximated, as long as one can provide physical initial conditions. Indeed, the software was written in such a fashion that higher-dimensional dynamical systems can also be analysed, as was demonstrated via the retroactive restoration of the t and ϕ equations of motion. Hence, if one would like to investigate a different line element, for instance a rederived form of EDGB theory or even an entirely different spacetime such as dynamical Chern-Simons theory, the framework would require few to no adjustments.

11.3 Software, hardware and numerical limitations

Even though a significant challenge lies in differentiating between the perturbations to Kerr from the spin expansion and from the scalarisation of the metric, the primary research challenge actually turned out to lie in the numerics behind the project. Because of the tiny effect of the scalar field to the geodesics, out-of-the-box methods for evolving the equations of motion were generally not sufficient in terms of efficiency. In this project, the capacity of *Mathematica* was pushed to its numerical limits, to the point where the integrator was not even able to continue evolving the equations of motion due to software issues beyond $\tau = 7 \cdot 10^9$. Furthermore, the speed of the analysis left much to be desired for; the analyses are intensive to the point that that one needs access to at least 16, but preferably many more, high-speed CPU cores on an external cluster to perform any meaningful analysis in the EDGB EMRI system at higher order.

Although there are most likely points of improvement one could formulate within the *Mathematica* framework, we believe that this language is not well-suited to the heavy calculations it was subjected to in this project, especially for higher order expansions. Although it was a good choice of software for the development of the theoretical framework and the validation of its computations at low order, the sheer amount of computing power required for the higher order cases suggests that a numerical integrator should be developed especially for the identification of chaotic features in a language well-suited for this purpose. Our suggestion for such a framework would be to develop it in *Python*, but keeping all computations inside module environments written in *C* or *Fortran* (such as NumPy). It is also possible to build an integrator in *C++*, but it might be more difficult to incorporate the

symbolic expressions one obtains from the Hamiltonian in this language than in *Python*. Apart from computation speed, developing a numerical integrator also allows one to specify the method and accuracy to precisely match the problem at hand, as well as output diagnostic data to the user on the accuracy and performance of the current computation. It might even be possible to let a computer locate a feature automatically with minimal user input, or parallelise the integrator such that single rotation numbers can be computed much faster than `NDSolve` allows for. Although some work would be required to develop such an environment, the nature of the problem does lend itself to such an approach and we believe that having such software would greatly benefit all researchers looking for chaotic signatures in higher-order EMRI systems. Indeed, developing such a framework and using it to efficiently and precisely characterise the chaotic features at higher order should in our view be a priority for future work in this particular topic.

11.4 Suggestions for further research

Apart from finishing the aforementioned higher order analysis at higher resolution, the study of modified gravity via extreme mass-ratio inspirals still has a great number of aspects which remain unexplored and could provide new insights in the nature of gravity and how to probe it in the strong-field regime. Here, we give some additional suggestions for future researchers intending to study the dynamics of EMRIs in the context of modified gravity, either via the framework provided in this thesis or another mathematical avenue.

11.4.1 Sweep of the orbital parameter space

Due to the numerical challenges of integrating higher order geodesics for tens of thousands of orbits, it was necessary for this project to select a set of orbital parameters E , L_z and χ , under which to investigate the extreme $\alpha = 0$ and $\alpha = 0.691$ cases. However, more could be learned about the effects of these parameters on the size, location and nature of chaotic features. For instance, setting an intermediate value of α and determining the size of the chaotic features could confirm or contradict the idea that maximising the deformation of Kerr also maximises the plateaus or discontinuities observed in the rotation curve. Furthermore, setting different values for E , L_z and χ allows one to both determine which set of parameters is truly optimal for detecting chaotic features and make predictions on a wide range of astrophysical EMRIs as they can be measured, since of course in nature we do not control the values of these conserved quantities.

11.4.2 Alternate definitions of chaos

In different fields of physics, the exact definition of what constitutes chaotic motion can vary significantly. In the study of EMRIs, one generally employs the lack of integrability and hence diffeomorphism to action-angle variables to characterise a spacetime as chaotic or not. Indeed, identifying plateaus and discontinuities is not the only way one can seek out non-Kerr behaviour; there are many other ways in which one can quantify chaotic motion. In principle, we consider motion chaotic if it is non-periodic. However, one can for example also define chaos based on the sensitivity of the orbital shape to very small changes in the initial conditions. These considerations have spurred researchers to work towards generalised and coordinate-independent definitions of chaotic motion. For instance, in a previous report [94], several alternate definitions of chaos which can be applied to general relativity are mentioned. One alternate (and in other fields commonly used) quantification of chaos is in the form of *Lyapunov exponents*, as introduced in for instance Ref. [95]. However, as Ref. [94] shows, this method can not straightforwardly be applied to relativity, due to the concept

of Lyapunov exponents breaking down under particular allowed transformations of the timelike coordinate. Another interesting method comes from employing so-called *fractal dimensions*, which is of particular interest to EMRIs since there exists a one-to-one correspondence between the fractal dimension and a quantity called the Lyapunov dimension, which encodes the Lyapunov exponents, if the dynamical system in question is two-dimensional. As we saw in Chapter 5, SAV metrics can be reduced to two-dimensional systems, making this method potentially very useful in the study of these systems. It is beyond the scope of this thesis to explore these concepts rigorously; for this, readers are referred to Ref. [94] and its references. However, there are clearly other interesting avenues to explore when it comes to the invariant characterisation of chaotic motion in EMRIs, which might be worth investigating in future work.

11.4.3 Predictors of the magnitude of features

One of the aspects of this research which contributed significantly to the numerical challenge of the project is that it was not known beforehand what kind of plateau or discontinuity magnitude we could expect at different resonances for different parameter settings in EDGB gravity. It would be useful to develop a method which allows prediction of the size of these chaotic features in an analytical fashion, based on for example the size of the perturbation from the Kerr solution in the form of the scalar coupling α . Indeed, in Ref. [25] it is pointed out that the expected volume of a chaotic feature is of order $\mathcal{O}(\sqrt{\epsilon})$, where ϵ parametrises the deviation from the Kerr Hamiltonian as in Eq. (2.25). However, this depends on the Hamiltonian being written in action-angle variables; we do not have a closed-form expression of these coordinates for the Kerr case and for modified gravities, this transformation probably does not exist (since we expect non-Kerr spacetime to be non-integrable). It would therefore be very useful if a concretely applicable version of such a relation were constructed, perhaps related to the phase space volumes of features as introduced in Section 8.6. That way, one can predict the size of the potential features one is looking for.

11.4.4 Other gravity theorems

In this project, a theoretical and software framework was developed which can be used to model orbits in general SAV spacetimes. Although the choice was made to investigate the chaotic features in EDGB gravity, there is in principle no limitation on what kind of spacetime one considers. Provided that an expression of $g_{\mu\nu}$ is provided in either prolate spheroidal or Boyer-Lindquist coordinates and that the metric has an SAV symmetry, it is possible to compute the effective potential, black hole orbits and rotation curves in any spacetime through the framework without significant additional development by the user. This opens up the possibility to investigate other theories than EDGB in a similar fashion to this project and compare the features of several different modified gravity candidates. For instance, it would be interesting to perform this study in *dynamical Chern-Simons* gravity, which is another higher-curvature theory with a scalar field, similarly to what was computed in Ref. [30]. Additionally, different forms of the coupling function $f(\alpha)$ in the general sGB class of theories could be considered, or even modified gravities totally unrelated to the ones considered in this project. It would also be possible to investigate the exact dependence of the spin expansion perturbation to the feature size in the rotation curves by varying the spin order of the Kerr expansion and computing the magnitudes of the features for different orders.

In conclusion, this study of EMRIs in EDGB gravity covers just a tiny subset of the potentially interesting physics to be found in supermassive black hole systems, from both a theoretical and experimental point of view. With the advent of gravitational wave astronomy as a novel method to work on the unification of quantum field theory and gravity, it is an exciting time to be working in the field of gravitational physics.

Chapter 12

Acknowledgments

It has been a pleasure to work on this research for the past year and I have several people to thank for this. To start, I would like to thank my first supervisor Dr. Tanja Hinderer for giving me the opportunity to join her research group for a year, as well as for her continual guidance and advice on both research and logistical questions as they arose during the research and writing process. Furthermore, this research project would not have been possible without the thorough and continual daily supervision of Banafsheh Shiralilou, who helped me on countless occasions during the year and provided insightful feedback on the results of the analysis. Additionally, I would like to thank my second supervisor Dr. Tomislav Prokopec for, among other contributions, his helpful questions during the final presentation.

I would also like to thank all participants in the group meetings and journal club for allowing me to develop my research and professional skills, as well as providing a platform for interdisciplinary collaboration within gravitation and cosmology research. Furthermore, the hospitality of Dr. Samaya Nissanke's group at the UvA, who invited me to join them on several occasions, allowed me to interact with researchers from this community as well, from which sprouted several interesting discussions.

Finally, I have had the pleasure of collaborating with a highly motivated and very supportive group of fellow master students during the Theoretical Physics programme. I would like to thank all of them for providing the perfect environment in which to work on the toughest hand-ins of the programme, as well as being great company in the much-needed breaks during these challenges. I am grateful to have shared this experience with this group.

Appendix A

A compact form of R_{GB}^2

One should note that it is possible to write R_{GB}^2 in a more compact form, which can be useful when performing calculations using the EDGB action. We will largely follow the derivation as provided by Ref. [96]. Starting from the Riemann tensor, we can *dualise* the two left indices of the tensor such that

$${}^*R^{\mu\nu\rho\sigma} \equiv \frac{1}{2}\epsilon^{\mu\nu\gamma\lambda}R_{\gamma\lambda}{}^{\rho\sigma} \quad (\text{A.1})$$

where $\epsilon^{\mu\nu\gamma\lambda}$ is the Levi-Civita tensor. We can then take the resulting tensor and dualise the remaining indices on the right to obtain the *double-dual* of the Riemann tensor:

$${}^*R^*{}^{\mu\nu\rho\sigma} \equiv \frac{1}{2}\epsilon^{\mu\nu\gamma\lambda}R_{\gamma\lambda\delta\alpha}\epsilon^{\delta\alpha\rho\sigma} \quad (\text{A.2})$$

The reason we define this form is because of the following useful relation:

$$\begin{aligned} {}^*R^*{}_{\mu\nu\rho\sigma}R^{\mu\nu\rho\sigma} &= R^2 - 4R_{\mu\nu}R^{\mu\nu} + R_{\mu\nu\rho\sigma}R^{\mu\nu\rho\sigma} \\ &= R_{GB}^2 \end{aligned} \quad (\text{A.3})$$

Being able to write the Gauss-Bonnet invariant in this compact fashion can be advantageous when deriving the equations of motion in EDGB and related theories of quadratic gravity. In fact, it allows for a relatively straightforward formulation of the equations of motion obtained when varying S_{EDGB} with respect to the metric [96]:

$$m_{pl}^2 G_{\mu\nu} + \hat{\alpha} \nabla^\rho \nabla^\sigma ({}^*R^*{}_{\rho\mu\nu\sigma} e^{\phi_s}) = 0 \quad (\text{A.4})$$

where we set $T_{\mu\nu} = 0$ since we are interested in black holes, which are vacuum solutions. In this thesis, we vary S_{EDGB} as well; however, we employ a symbolic programming language to compute the equations of motion and then immediately apply a chart to the obtained abstract tensor forms. Because of this, there is not much advantage for us in deriving the abstract equations of motion from S_{EDGB} in any particularly compact abstract form, since converting to a coordinate system will make the equations messy again anyway. However, we use (A.3) to write S_{EDGB} in a more concise fashion, before employing software to vary the action with respect to the metric and the scalar field.

It is important to be aware of the existence of this method of rewriting the equations of motion in abstract form, if one performs a non-coordinate dependent study of these systems or if one is brave enough to perform long calculations on this spacetime completely by hand.

Appendix B

Conserved quantities in the exact Kerr spacetime

As indicated in Chapter 7, the errors in the conserved quantities of the exact Kerr solution when using the default *Mathematica* integrator are depicted in Fig. B.1. Notably, they are very similar to the errors found in the Kerr expansion.

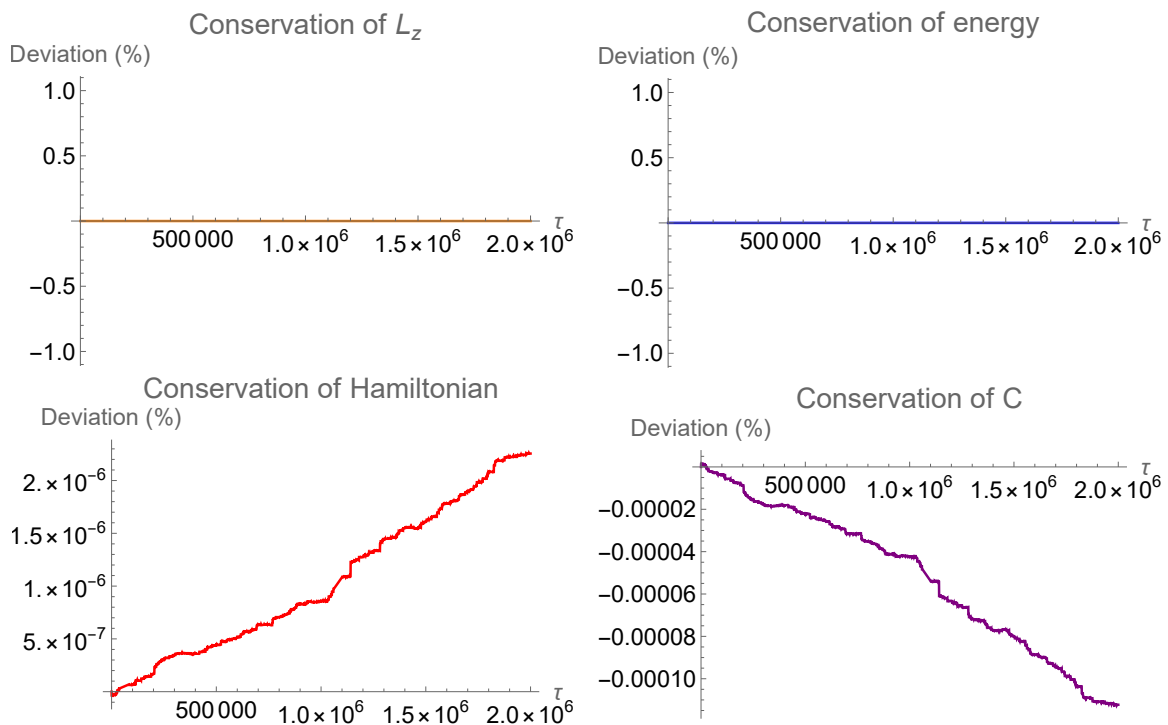


Figure B.1: Numerical errors in conserved quantities for an orbit evaluated for 2 million time steps using the exact Kerr solution with $E = 0.98$, $L_z = -4.5$ and $\chi = 0.3$.

Appendix C

Spin dependence of plateau width in second order Kerr spacetime

Since the magnitude of the perturbation away from the Kerr solution determines the magnitude of the chaotic features one can expect to find, it is interesting to see how the plateau width of the second order Kerr solution evolves under changes in χ . In Figure C.1, we see the result of rotation curve computations at values of $\chi \in [0, 0.3]$. By setting the plot range at the same value for all plots, we can appreciate the evolution of these plateaus under variation of the black hole spin. Indeed, in the no-spin case, the expansion seems to be fully accurate, since no plateau is apparent. This is in line with expectations, since an expansion around $\chi = 0$ was performed such that setting $\chi = 0$ returns exactly the Schwarzschild metric. As we increase χ , the size of the plateau increases, since the error from the exact Kerr solution increases as the Taylor expansion around the Schwarzschild metric loses accuracy. These results do not affect our study, since the potential feature size caused by a scalar coupling in the EDGB action are far smaller than even the 0.1 spin case. However, they could help future researchers with what kind of magnitude of feature they can expect when analysing second order perturbations of a rotating black hole solution.

When one applies the invariant phase space volume quantification from Section 8.6 to these plateaus, one obtains the results shown in Table C.1. We see that the normalised phase space volume of the plateaus evolves in a seemingly exponential fashion as the inaccuracy of the expansion increases under increasing χ .

APPENDIX C. SPIN DEPENDENCE OF PLATEAU WIDTH IN SECOND ORDER KERR SPACETIME

Kerr spacetime at $\mathcal{O}(\chi) = 2$	r_{res}	\mathcal{V}_{max}	$\bar{\mathcal{V}}_{1/2}$
$\chi = 0$ (exact Schwarzschild)	$5 \cdot 10^{-4}$	453.452	0 (no plateau)
$\chi = 0.1$	$5 \cdot 10^{-4}$	453.084	$1.107 \cdot 10^{-4}$
$\chi = 0.2$	$5 \cdot 10^{-4}$	452.716	$2.266 \cdot 10^{-4}$
$\chi = 0.3$	$5 \cdot 10^{-4}$	452.348	$4.442 \cdot 10^{-4}$

Table C.1: Normalised feature volumes of the plateaus in the second order Kerr spacetime near the 1/2 resonance under variation of χ , calculated via the algorithm introduced in Section 8.6. Note that the result could be made more accurate by increasing the resolution; indeed, the result of the $\chi = 0.3$ case shows a small difference with what was shown in Table 8.4 precisely due to the difference in resolution. The results here are mostly intended as an indication on the evolution of this parameter under variation of χ rather than a precise quantification of these features.

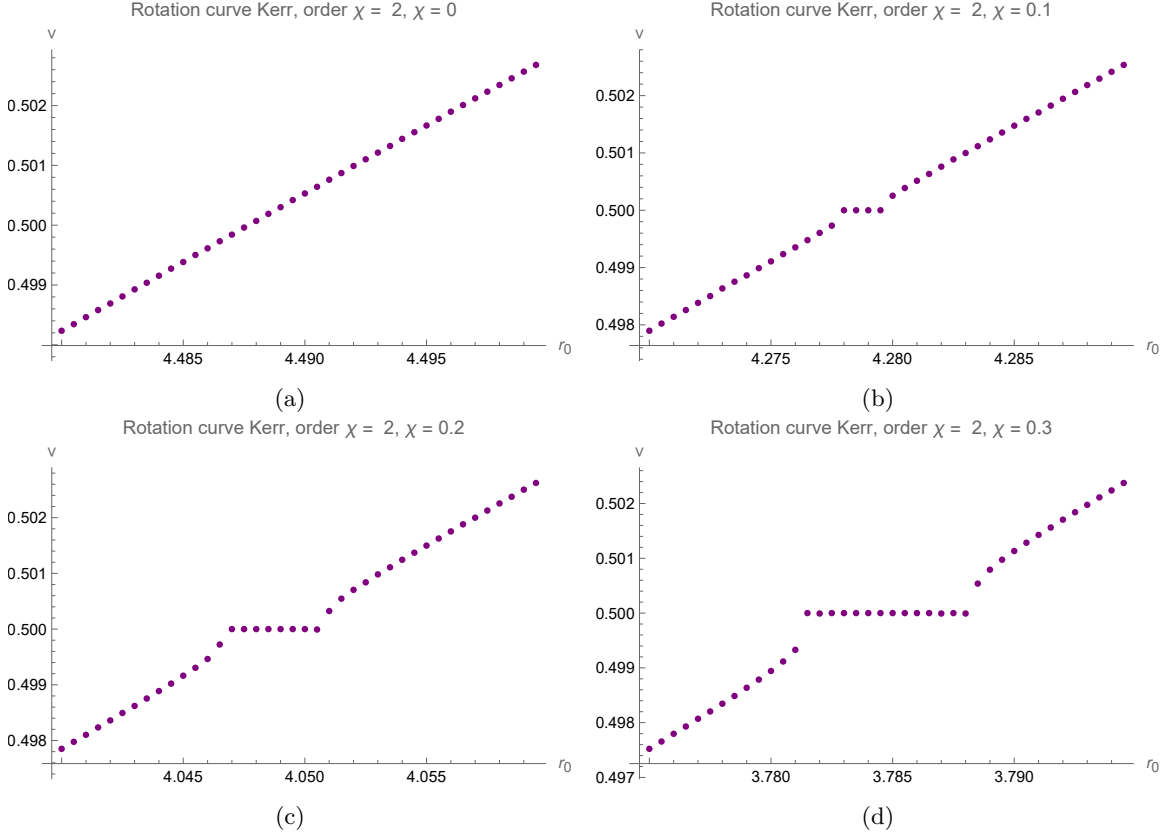


Figure C.1: The rotation curves near the 1/2 resonance of the Kerr spacetime expanded up to $\mathcal{O}(\chi^2)$ for $E = 0.995$ and $L_z = 3.5$, where we vary χ between 0 and 0.3. All rotation curves display the same interval in r , such that we can visually see the evolution of the plateau size. In the $\chi = 0$ (Schwarzschild) case, no plateau is present at all.

Appendix D

Evolution of \mathcal{A}_r and \mathcal{A}_θ

The phase space volume \mathcal{V} is computed by multiplying the phase space areas of the two librational coordinates. In the Boyer-Lindquist case used as an example in Section 8.6, the evolution of the two areas whose product constitutes \mathcal{V} are depicted in Fig. D.1. Note that these areas separately are *not* invariant under canonical transformations, but that their product is.

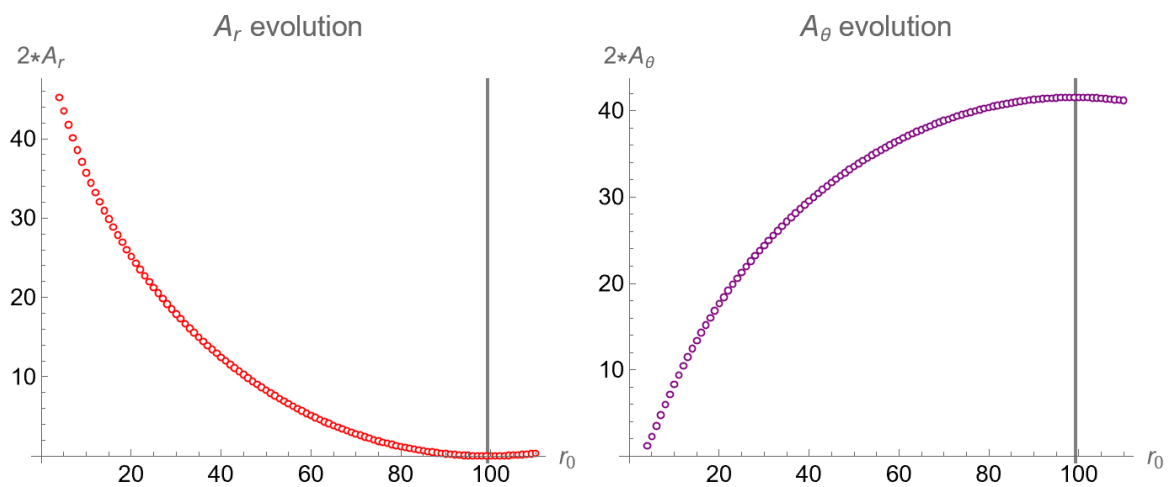


Figure D.1: Areas spanned in the r and θ phase space for different r_0 in a second-order expanded Kerr spacetime with $E = 0.995$, $L_z = 3.5$ and $\chi = 0.3$. The vertical lines indicate the fixed point.

Appendix E

UU Gemini versus SURFsara Lisa computing cluster performance

Since the runs at full coupling were very slow, efforts were made to improve the speed of the analysis. One avenue which was explored was using an alternative cluster to the one provided by the ITP at Utrecht University [71]. The alternative cluster employed was the *Lisa national computing cluster*¹, which is a Linux-based Beowulf computing cluster operated by SURFsara [72]. In particular, an exact copy of the Boyer-Lindquist task from the coordinate system comparison as displayed in Table 8.1 was run on the Lisa cluster. The results of the test run are depicted in Table E.1. Although the exact same results are reproduced, indicating that the software is working correctly, the Lisa cluster used significantly more wall-clock time² to achieve this result. Hence, at default settings, the UU's itf-fat node on the Gemini cluster is faster. Furthermore, the Gemini cluster (as of present) does not have an upper limit on computation time or allowed use, whereas the Lisa cluster does. However, it is still an asset which can be used if the Gemini cluster is not available due to for instance maintenance or lack of capacity.

The performance difference can be explained by the underlying hardware, specifically the processors. The employed partitions of both clusters run on *Intel Xeon* CPUs. However, whereas Lisa uses a *Gold 6130* @ 2.1 GHz in this partition (or even potentially a slower *Silver* model), the Gemini cluster employs a *Gold 6252N* @ 2.3 GHz. Besides clock speed, Gemini's CPU also allows for faster and larger DDR4 RAM memory units than the Lisa CPU. Altogether, Gemini's superior hardware in this node is the reason that it outperforms Lisa in this particular case.

One might wonder whether a faster node on the Lisa cluster could be used instead of the default partition. Although there does exist a "fat" partition on Lisa, its runs are limited to a run time of one day, which means that most computations at higher order cannot be performed on this node. Besides, by default the batch system will on the Lisa cluster automatically insert the job into a particular partition and node, based on its requirements.

It should also be mentioned that the default partition has a maximum run time of five days, which

¹Not to be confused with the Laser Interferometer Space Antenna (LISA) gravitational wave observatory!

²In Chapter 8, we used CPU-time as a metric. This is slightly different from wall-clock time; at its simplest, CPU-time indicates how long the CPU was 'busy', whereas wall-clock time indicates how much real time has passed between start and finish. When comparing two clusters using the exact same algorithm, wall-clock time is more interesting. After all, we would like to know which cluster would complete the same computation the fastest from start to finish. Note that usually, there is not much difference between wall-clock and CPU-time.

APPENDIX E. UU GEMINI VERSUS SURFSARA LISA COMPUTING CLUSTER PERFORMANCE

puts their use for the higher order computations at maximum coupling out of the picture as well. We conclude that the Lisa cluster could be used by UU students as a auxiliary cluster in combination with the Gemini nodes, but that the heaviest computations should be run on the Gemini cluster due to built-in limitations of the Lisa cluster. Finally, we note that the Lisa cluster does not natively support Mathematica; if one wishes to run Wolfram scripts on this cluster, one needs to install the Linux direct file version of Mathematica in their home directory on the Lisa system first.

Performance comparison	Wall-clock time	# piercings	ν
UU Gemini (itf-fat node)	07:12:24	28667	0.552241
SURFsara Lisa (default partition)	09:46:13	28667	0.552241

Table E.1: Performance comparison of the ITP and Lisa clusters for the same task, where time should be read as *HH-MM-SS*. As we see, the wall-clock time of the Lisa cluster was significantly longer than of the ITP cluster, indicating that at default settings, Lisa is slower than the itf-fat node. As a sanity check, we see that indeed the exact same results are reproduced for both runs. For this run, we have $r_0 = 3.98765$, $E = 0.995$, $L_z = 3.5$, $\chi = 0.3$ and $\alpha = 0.691$, just like in Chapter 8. Careful readers might note that the time depicted for the Gemini cluster differs from the time in Table 8.1. This is because wall-clock time is slightly different from CPU-time.

Bibliography

- [1] Sean M. Carroll. *An Introduction to General Relativity: Spacetime and Geometry*. Cambridge University Press, 2019. ISBN: 9781108488396.
- [2] Charles W. Misner et al. *Gravitation*. W.H. Freeman & Company, 1973. ISBN: 0716703440.
- [3] Neil Ashby. “Relativity and the Global Positioning System”. In: *Physics Today* 41 (2002). DOI: 10.1063/1.1485583.
- [4] Matthew D. Schwartz. *Quantum Field Theory and the Standard Model*. Cambridge University Press, 2013. ISBN: 9781107034730.
- [5] Albert Petrov. *Introduction to Modified Gravity*. Springer, 2020. ISBN: 9783030528614.
- [6] The Royal Swedish Academy of Sciences. *Nobel Prize 2017 press release*. URL: <https://www.nobelprize.org/prizes/physics/2017/press-release/>. (accessed: 12.03.2022).
- [7] ESA. *LISA mission summary*. URL: <https://sci.esa.int/web/lisa/-/61367-mission-summary>. (accessed: 31.05.2022).
- [8] John Kormendy et al. “Coevolution (Or Not) of Supermassive Black Holes and Host Galaxies”. In: *Annual Review of Astronomy and Astrophysics* 51.511 (2013). DOI: 10.1146/annurev-astro-082708-101811.
- [9] M. Brockamp et al. “Unveiling Gargantua: A new search strategy for the most massive central cluster black holes”. In: *AA* 585.A153 (2016). DOI: 10.1051/0004-6361/201526873.
- [10] Shigeyuki Morita. *Geometry of differential forms*. American Mathematical Society, 2001. ISBN: 9780821810453.
- [11] Jerry B. Griffiths et al. *Exact Space-Times in Einstein’s General Relativity*. Cambridge University Press, 2009. ISBN: 9781139481168.
- [12] Steven Weinberg. *Cosmology*. Oxford University Press, 2008. ISBN: 9780198526827.
- [13] Karl Schwarzschild. “Über das Gravitationsfeld eines Massenpunktes nach der Einsteinschen Theorie”. In: *Sitzungsberichte der Königlich Preussischen Akademie der Wissenschaften* 7.189 (1916).
- [14] Timothy Clifton et al. “Modified Gravity and Cosmology”. In: *Physics Reports* 513.1 (2012).
- [15] Werner Israel. “Event Horizons in Static Vacuum Space-Times”. In: *Phys. Rev.* 164.1776 (1967). DOI: 10.1103/PhysRev.164.1776.
- [16] Werner Israel. “Event horizons in static electrovac space-times”. In: *Commun. Math. Phys.* 8.245-260 (1968). DOI: 10.1007/BF01645859.
- [17] Brandon Carter. “Axisymmetric Black Hole Has Only Two Degrees of Freedom”. In: *Phys. Rev. Lett.* 26.331 (1971). DOI: 10.1103/PhysRevLett.26.331.

BIBLIOGRAPHY

- [18] Chris Van Den Broeck et al. “Bounding dark charges on binary black holes using gravitational waves”. In: *Phys. Rev. D* 104.063041 (2021). DOI: 10.1103/PhysRevD.104.063041.
- [19] Samuel E. Gralla. “Second Order Gravitational Self-Force”. In: *Phys. Review D* 85.12 (2012). DOI: 10.1103/PhysRevD.85.124011.
- [20] Kyriakos Destounis et al. “Gravitational Wave Glitches in Chaotic Extreme-Mass-Ratio Inspirals”. In: *Phys. Rev. Lett.* 126.141102 (2021). DOI: 10.1103/PhysRevLett.126.141102.
- [21] Eric Poisson. “The Motion of Point Particles in Curved Spacetime”. In: *Living Rev. Relativity* 7.14 (2011). DOI: 10.12942/lrr-2011-7.
- [22] Yasushi Mino. “Perturbative approach to an orbital evolution around a supermassive black hole”. In: *Phys. Rev. D* 67.084027 (2003). DOI: 10.1103/PhysRevD.67.084027.
- [23] Banafsheh Shiralilou et al. “Post-Newtonian gravitational and scalar waves in scalar-Gauss-Bonnet gravity”. In: *Class. Quantum Grav.* 39.035002 (2022). DOI: 10.1088/1361-6382/ac4196.
- [24] Vladimir I. Arnold. *Mathematical methods of classical mechanics*. Springer-Verlag, 1978. ISBN: 0387968903.
- [25] Georgios Lukes-Gerakopoulos et al. “Non-linear effects in EMRI dynamics and their imprints on gravitational waves”. In: *part of the book 'Handbook of Gravitational Wave Astronomy' by C. Bambi, S. Katsanevas, and K. Kokkotas* (2021). DOI: 10.48550/arXiv.2103.06724.
- [26] Jeandrew Brink. “Spacetime encodings. II. Pictures of integrability”. In: *Phys. Review D* 78.102002 (2008). DOI: 10.1103/PhysRevD.78.102002.
- [27] Sidney A. Morris. *Topology Without Tears*. <https://www.topologywithouttears.net/>, 2020 (most recent version).
- [28] Jeandrew Brink et al. “The Astrophysics of Resonant Orbits in the Kerr Metric”. In: *Phys. Rev. D* 91.083001 (2015). DOI: 10.1103/PhysRevD.91.083001.
- [29] Alejandro Cardenas-Avendano et al. “The exact dynamical Chern Simons metric for a spinning black hole possesses a fourth constant of motion: A Dynamical-Systems-Based Conjecture”. In: *Class. Quantum Grav.* 35.16 (2018). DOI: 10.1088/1361-6382/aad06f.
- [30] Alexander Deich et al. “A Tiny Needle in a Messy Haystack: Chaos in Quadratic Gravity”. In: *arXiv preprint* (2022). DOI: 10.48550/arXiv.2203.00524.
- [31] Marisa Geyer. “Geodesics and Resonances of the Manko-Novikov Spacetime”. In: *Master’s thesis at Stellenbosch University* (2013).
- [32] Jeandrew Brink et al. “Orbital Resonances Around Black Holes”. In: *Phys. Rev. Lett.* 114.081102 (2015). DOI: 10.1103/PhysRevLett.114.081102.
- [33] Andrej N. Kolmogorov. “On the Conservation of Conditionally Periodic Motions under Small Perturbation of the Hamiltonian”. In: *Doklady Akademii Nauk SSSR* 98.572 (1954).
- [34] Vladimir I. Arnold. “Proof of a Theorem of A. N. Kolmogorov on the Invariance of Quasi-Periodic Motions Under Small Perturbations of the Hamiltonian”. In: *Russian Mathematical Surveys* 18(5).9 (1963).
- [35] Jürgen Moser. “On invariant curves of area-preserving mappings of an annulus.” In: *Nachrichten der Akademie der Wissenschaften in Göttingen. II. Mathematisch-Physikalische Klasse* 1 (1962).
- [36] H. G. Schuster et al. *Deterministic Chaos: An Introduction, Fourth Edition*. Wiley-VCH Verlag GmbH Co. KGaA, 2005. ISBN: 9783527604807.
- [37] Georgios Lukes-Gerakopoulos et al. “An observable signature of a background deviating from Kerr”. In: *Phys. Rev. D* 81.124005 (2010). DOI: 10.1103/PhysRevD.81.124005.

BIBLIOGRAPHY

- [38] Gerardus 't Hooft. “1999 Nobel Prize lecture”. In: *Nobel Prize archive* (1999). URL: <https://www.nobelprize.org/uploads/2018/06/thooft-lecture.pdf>.
- [39] David Lovelock. “The Einstein tensor and its generalizations”. In: *J. Math. Phys.* 12.498 (1971).
- [40] David Lovelock. “The four-dimensionality of space and the Einstein tensor”. In: *J. Math. Phys.* 13.874 (1972).
- [41] Michael B. Green et al. *Superstring Theory*. Cambridge University Press, 2012. ISBN: 9781107029118.
- [42] Gunnar Nordström. “On the possibility of unifying the electromagnetic and the gravitational fields”. In: *Phys. Z.* 15.504 (1914). DOI: 10.48550/arXiv.physics/0702221(translation).
- [43] Salvatore Capozziello et al. “Non-Local Gravity Cosmology: an Overview”. In: *accepted for Int. J. Mod. Phys. D* (2022). DOI: 10.48550/arXiv.2201.04512.
- [44] Lefteris Papantonopoulos. *The Invisible Universe: Dark Matter and Dark Energy*. Springer, 2007. ISBN: 9783540710127.
- [45] David Tong. “Lectures on String Theory”. In: *arXiv publication* (2012). DOI: 10.48550/arXiv.0908.0333.
- [46] S. Nojiri et al. “Ghost-free Gauss-Bonnet Theories of Gravity”. In: *Phys. Rev. D* 99.044050 (2019). DOI: 10.1103/PhysRevD.99.044050.
- [47] A. Sloane. “The Axially Symmetric Stationary Vacuum Field Equations in Einstein’s Theory of General Relativity”. In: *Austral. J. Phys.* 31 (1978). DOI: 10.1071/PH780427.
- [48] Hans Stephani et al. *Exact Solutions to Einstein’s Field Equations*. Cambridge University Press, 2003. ISBN: 9780511065484.
- [49] Roy P. Kerr. “Gravitational Field of a Spinning Mass as an Example of Algebraically Special Metrics”. In: *Phys. Rev. Lett.* 11.237 (1963). DOI: 10.1103/PhysRevLett.11.237.
- [50] Robert H. Boyer and Richard W. Lindquist. “Maximal Analytic Extension of the Kerr Metric”. In: *J. Math. Phys.* 8.265 (1966). DOI: 10.1063/1.1705193.
- [51] Frederick J. Ernst. “New Formulation of the Axially Symmetric Gravitational Field Problem”. In: *Phys. Rev.* 167.1175 (1968). DOI: 10.1103/PhysRev.167.1175.
- [52] Saul A. Teukolsky. “The Kerr Metric”. In: *Class. Quantum Grav.* 32.12 (2015). DOI: 10.1088/0264-9381/32/12/124006.
- [53] Brandon Carter. “Global Structure of the Kerr Family of Gravitational Fields”. In: *Phys. Rev.* 174.1559 (1968). DOI: 10.1103/PhysRev.174.1559.
- [54] Takahiro Tanaka et al. “Evolution of the Carter constant for a resonant inspiral into a Kerr black hole: I. The scalar case”. In: *Prog. Theor. Exp. Phys.* 063E01 (2013). DOI: 10.1093/ptep/ptt034.
- [55] K. Rosquist et al. “Carter’s constant revealed”. In: *Int. J. Mod. Phys. D* 18.03 (2009). DOI: 10.1142/S0218271809014546.
- [56] Sajal Mukherjee et al. “Carter Constant and Angular Momentum”. In: *Int. J. Mod. Phys. D* 27.01 (2015). DOI: 10.1142/S0218271817501802.
- [57] C. Cherubini et al. “Second Order Scalar Invariants of the Riemann Tensor: Applications to Black Hole Spacetimes”. In: *Int. J. Mod. Phys. D* 11.06 (2002). DOI: 10.1142/S0218271802002037.
- [58] James M. Bardeen et al. “Rotating Black Holes: Locally Nonrotating Frames, Energy Extraction and Scalar Synchrotron Radiation”. In: *Astrophysical Journal* 178 (1972). DOI: 10.1086/151796.

BIBLIOGRAPHY

- [59] Wolfram Schmidt. “Celestial mechanics in Kerr spacetime”. In: *Class.Quant.Grav.* 19.2743 (2002). DOI: 10.1088/0264-9381/19/10/314.
- [60] Andrea Maselli et al. “Rotating black holes in Einstein-Dilaton-Gauss-Bonnet gravity with finite coupling”. In: *Phys. Rev. D* 92.083014 (2015). DOI: 10.1103/PhysRevD.92.083014.
- [61] E. Winstanley et al. “Dilatonic Black Holes in Higher Curvature String Gravity”. In: *Phys. Rev. D* 54.5049 (1996). DOI: 10.1103/PhysRevD.54.5049.
- [62] Scott E. Perkins et al. “Improved gravitational-wave constraints on higher-order curvature theories of gravity”. In: *Phys. Rev. D* 104.024060 (2021). DOI: 10.1103/PhysRevD.104.024060.
- [63] Zhenwei Lyu et al. “Constraints on Einstein-dilation-Gauss-Bonnet gravity from black hole-neutron star gravitational wave events”. In: *Phys. Rev. D* 105.064001 (2022). DOI: 10.1103/PhysRevD.105.064001.
- [64] Helvi Witek et al. “Black holes and binary mergers in scalar Gauss-Bonnet gravity: scalar field dynamics”. In: *Phys. Rev. D* 99.064035 (2019). DOI: 10.1103/PhysRevD.99.064035.
- [65] Dmitry Ayzenberg et al. “Slowly-Rotating Black Holes in Einstein-Dilaton-Gauss-Bonnet Gravity: Quadratic Order in Spin Solutions”. In: *Phys. Rev. D* 90.044066 (2014). DOI: 10.1103/PhysRevD.90.044066.
- [66] Burkhard Kleihaus et al. “Rotating Black Holes in Dilatonic Einstein-Gauss-Bonnet Theory”. In: *Phys. Rev. Lett.* 106.151104 (2011). DOI: 10.1103/PhysRevLett.106.151104.
- [67] Maria Okounkova. “Stability of rotating black holes in Einstein dilaton Gauss-Bonnet gravity”. In: *Phys. Rev. D* 100.124054 (2019). DOI: 10.1103/PhysRevD.100.124054.
- [68] Félix-Louis Julié et al. “Post-Newtonian dynamics and black hole thermodynamics in Einstein-scalar-Gauss-Bonnet gravity”. In: *Phys. Rev. D* 100.104061 (2019). DOI: 10.1103/PhysRevD.100.104061.
- [69] Christopher S. Reynolds. “The Spin of Supermassive Black Holes”. In: *Class. Quantum Grav.* 30.244004 (2013). DOI: 10.1088/0264-9381/30/24/244004.
- [70] Wolfram Research. *Events and Discontinuities in Differential Equations (Mathematica guide)*. URL: <https://reference.wolfram.com/language/tutorial/NDSolveWhenEvents.html>. (accessed: 30.06.2022).
- [71] Utrecht University. *Gemini FAQ (only accessible for UU staff and students)*. URL: https://ict.science.uu.nl/index.php/Gemini_FAQ. (accessed: 30.06.2022).
- [72] SURFsara. *Lisa cluster user information*. URL: <https://userinfo.surfsara.nl/systems/lisa>. (accessed: 20.06.2022).
- [73] Peter Mann. *Lagrangian and Hamiltonian Dynamics*. Oxford University Press, 2018. ISBN: 9780198822370.
- [74] The GRAVITY collaboration. “A geometric distance measurement to the Galactic center black hole with 0.3% uncertainty”. In: *Astronomy and Astrophysics* 625.L10 (2019). DOI: 10.1051/0004-6361/201935656.
- [75] F. Eisenhauer et al. “SINFONI in the Galactic Center: Young Stars and Infrared Flares in the Central Light-Month*”. In: *ApJ* 628.246 (2005). DOI: 10.1086/430667.
- [76] Florian Peißker et al. “S62 and S4711: Indications of a Population of Faint Fast-moving Stars inside the S2 Orbit—S4711 on a 7.6 yr Orbit around Sgr A*”. In: *ApJ* 899.50 (2020). DOI: 10.3847/1538-4357/ab9c1c.
- [77] Giacomo Fragione et al. “An Upper Limit on the Spin of SgrA* Based on Stellar Orbits in Its Vicinity”. In: *ApJL* 901.L32 (2020). DOI: 10.3847/2041-8213/abb9b4.

BIBLIOGRAPHY

- [78] The LIGO Scientific Collaboration and the Virgo Collaboration. “Observation of Gravitational Waves from a Binary Black Hole Merger”. In: *Phys. Rev. Lett.* 116.061102 (2016). DOI: 10.1103/PhysRevLett.116.061102.
- [79] C. J. Moore et al. “Gravitational-wave sensitivity curves”. In: *Class. Quantum Grav.* 32.015014 (2015). DOI: 10.1088/0264-9381/32/1/015014.
- [80] LISA Science Study Team. *LISA Science Requirements Document*. URL: <https://www.cosmos.esa.int/documents/678316/1700384/SciRD.pdf>. (accessed: 31.05.2022).
- [81] Christopher J. Moore et al. “An astrometric search method for individually resolvable gravitational wave sources with Gaia”. In: *Phys. Rev. Lett.* 119.261102 (2017). DOI: 10.1103/PhysRevLett.119.261102.
- [82] Uchupol Ruangsri et al. “A census of transient orbital resonances encountered during binary inspiral”. In: *Phys. Rev. D* 89.084036 (2014). DOI: 10.1103/PhysRevD.89.084036.
- [83] Michael Katz et al. “Fast extreme-mass-ratio-inspiral waveforms: New tools for millihertz gravitational-wave data analysis”. In: *Phys. Rev. D* 104.064047 (2021). DOI: 10.1103/PhysRevD.104.064047.
- [84] Jonathan McCart et al. “Highly eccentric EMRI waveforms via fast self-forced inspirals”. In: *Phys. Rev. D* 104.084050 (2021). DOI: 10.1103/PhysRevD.104.084050.
- [85] Marica Branchesi. “Multi-messenger astronomy: gravitational waves, neutrinos, photons, and cosmic rays”. In: *J. Phys.: Conf. Ser.* 718.022004 (2016). DOI: 10.1088/1742-6596/718/2/022004.
- [86] IPTA Collaboration. *International Pulsar Timing Array home page*. URL: <http://ipta4gw.org/>. (accessed: 26.05.2022).
- [87] SKA TDT team et al. “Pulsar Searches with the SKA”. In: *Proceedings of the International Astronomical Union* 13.174 (2017). DOI: 10.1017/S1743921317009528.
- [88] SKA Collaboration. *Square Kilometre Array home page*. URL: <https://www.skatelescope.org/the-ska-project/>. (accessed: 26.05.2022).
- [89] E. F. Keane et al. “A Cosmic Census of Radio Pulsars with the SKA”. In: *Proceedings of Science* 14.040 (2014). DOI: 10.48550/arXiv.1501.00056.
- [90] Elena M. Murchikova et al. “A cool accretion disk around the Galactic Centre black hole”. In: *Nature* 570.83 (2019). DOI: 10.1038/s41586-019-1242-z.
- [91] Roger Blandford et al. “Relativistic Jets from Active Galactic Nuclei”. In: *Annual Review of Astronomy and Astrophysics* 57.467 (2019). DOI: 10.1146/annurev-astro-081817-051948.
- [92] Enrico Barausse et al. “Can environmental effects spoil precision gravitational-wave astrophysics?” In: *Phys. Rev. D* 89.104059 (2014). DOI: 10.1103/PhysRevD.89.104059.
- [93] N. I. Shakura et al. “Black holes in binary systems. Observational appearance.” In: *Astronomy and Astrophysics* 24.337 (1973).
- [94] Neil J. Cornish. “Time and Chaos in General Relativity”. In: *arXiv preprint CWRU-P14-95* (1996). DOI: 10.48550/arXiv.gr-qc/9602054.
- [95] John R. Taylor. *Classical Mechanics*. University Science Books, U.S., 2004. ISBN: 9781891389221.
- [96] Leo C. Stein. *Note on simple(r) equations for Einstein-dilaton-Gauss-Bonnet and dynamical Chern-Simons theories*. URL: <https://duetosymmetry.com/notes/note-on-simple-eoms-for-edgb-dcs/>. (accessed: 15.04.2022).